

AD-A102 880 AIR FORCE GEOPHYSICS LAB HANSCOM AFB MA
THE MESOSPHERE AND THERMOSPHERE, (U)
1981 K S CHAMPION, G SCHMIDTKE

UNCLASSIFIED AFGL-TR-81-0210

F/G 4/1

NL

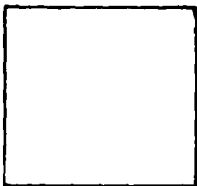
1 of 3
S0080



11

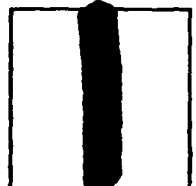
AD A102880

DTIC ACCESSION NUMBER



LEVEL

PHOTOGRAPH THIS SHEET



INVENTORY

The Mesosphere and Thermosphere

DOCUMENT IDENTIFICATION

Rept. No. AFGL-TR-81-0210

30 July 81

DISTRIBUTION STATEMENT A

Approved for public release;
Distribution Unlimited

DISTRIBUTION STATEMENT

ACCESSION FOR

NTIS GRA&I

DTIC TAB

UNANNOUNCED

JUSTIFICATION

BY

DISTRIBUTION /

AVAILABILITY CODES

DIST AVAIL AND/OR SPECIAL

A

DISTRIBUTION STAMP



DATE ACCESSIONED

81 8 06 009

DATE RECEIVED IN DTIC

PHOTOGRAPH THIS SHEET AND RETURN TO DTIC-DDA-2

AEGL-TR-81-0210

THE MESOSPHERE AND THERMOSPHERE

AD A102880

Pergamon Press

DIA
Approved
Distribution Control

ADVANCES IN SPACE RESEARCH

The Official Journal of the Committee on Space Research (COSPAR)
A Scientific Committee of the International Council of Scientific Unions (ICSU)

COSPAR is an interdisciplinary scientific organization concerned with the progress on an international scale of all kinds of fundamental research carried out with the use of balloons, rockets, or rocket propelled vehicles. Operating under the rules of ICSU, COSPAR ignores political considerations and considers all questions solely from the scientific viewpoint.

The COSPAR journal *Advances in Space Research* includes the proceedings of COSPAR organized symposia and other scientific meetings organized by this Committee, containing the latest scientific information in this area. The material published here has been presented to the international community of space scientists and, following discussions at the meetings, edited by eminent scientists in the field.

Fields covered are:

- Space Studies of the Earth's Surface, Meteorology and Climate
- Space Studies of the Earth - Moon System, Planets and Small Bodies of the Solar System
- Space Studies of the Upper Atmospheres of the Earth and Planets, including Reference Atmospheres
- Space Plasmas in the Solar System, including Planetary Magnetospheres
- Research in Astrophysics from Space
- Materials Sciences in Space
- Life Sciences as Related to Space.

EDITORIAL BOARD

Chairman:

Professor J. F. DENISSE, *Mission de la Recherche, Ministère des Universités, 61 rue Dutot, 75015 Paris, France*

Vice-Chairmen:

Professor L. E. PETERSON, *Center for Astrophysics and Space Sciences (CASS) C-011, UCSD, La Jolla, Ca 92093, USA*

Academician R. Z. SAGDEEV, *Head, Space Research Institute, USSR Academy of Sciences, Profsoyuznaya 88, Moscow V-485, USSR*

Members:

Professor V. L. Barsukov, *Moscow, USSR*

Dr. A. Bewersdorff, *Köln, FRG*

Professor S. A. Bowhill, *Urbana, USA*

Dr. W. R. Holmquist, *Richmond, USA*

Professor C. de Jager, *Utrecht, The Netherlands*

Professor S. L. Mandelstam, *Moscow, USSR*

Dr. S. I. Rasool, *Washington D.C., USA*

Dr. M. J. Rycroft, *Cambridge, England*

Professor Yash Pal, *Ahmedabad, India*

ex-officio

Dr. J. I. Vette, *Greenbelt, USA*

Mr. Z. Niemirowicz, *Paris, France*

COSPAR Secretariat: 51 Boulevard de Montmorency, 75016 Paris, France

Subscription rates (inclusive of postage and insurance): Annual subscription (1981) U.S.\$350.00; Two-year subscription (1981-82) U.S.\$665.00.

Microform Subscriptions and Back Issues: Back issues of all previously published volumes are available in the regular editions and on microfilm and microfiche. Current subscriptions are available on microfiche simultaneously with the paper edition, and on microfilm at the end of the subscription year. Prices on request.

Subscription enquiries from customers in North America should be sent to Pergamon Press Inc., Maxwell House, Fairview Park, Elmsford, NY 10523, U.S.A.; and for the remainder of the world to Pergamon Press Ltd, Headington Hill Hall, Oxford OX3 0BW, U.K.

Advances in Space Research is published in individual parts as one volume of approximately 3500 pages per year.

Copyright © 1981 COSPAR.

It is a condition of publication that manuscripts submitted to this journal have not been published and will not be simultaneously submitted or published elsewhere. By submitting a manuscript, the authors agree that the copyright for their article is transferred to COSPAR if and when the article is accepted for publication. However, assignment of copyright is not required from authors who work for organizations which do not permit such assignment. The copyright covers the exclusive rights to reproduce and distribute the article, including reprints, photographic reproductions, microform or any other reproductions of similar nature and translations. No part of this publication may be reproduced, stored in a retrieval system or transmitted in any form or by any means, electronic, electrostatic, magnetic tape, mechanical, photocopying, recording or otherwise, without permission in writing from the copyright holder.

U.S. Copyright Law Applicable to Users in the U.S.A.

The Article Fee Code on the first page of an article in this journal indicates the copyright owner's consent that, in the U.S.A., copies may be made for personal or internal use provided the stated fee for copying, beyond that permitted by Section 107 or 108 of the United States Copyright Law, is paid. The appropriate remittance should be forwarded with a copy of the first page of the article to the Copyright Clearance Center Inc., 21 Congress Street, Salem, MA 01970. If a code does not appear copies of the article may be made without charge, provided permission is obtained from COSPAR. The copyright owner's consent does not extend to copying for general distribution, for promotion, for creating new works or for resale. Specific written permission must be obtained from COSPAR for such copying. In case of doubt please contact your nearest Pergamon Office.

Publishing/Advertising Offices

Pergamon Press Ltd.,
Headington Hill Hall,
Oxford OX3 0BW, England

Pergamon Press Inc.,
Maxwell House, Fairview Park,
Elmsford, NY 10523, USA

UNCLASSIFIED

SECURITY CLASSIFICATION OF THIS PAGE (When Data Entered)

REPORT DOCUMENTATION PAGE		READ INSTRUCTIONS BEFORE COMPLETING FORM
1. REPORT NUMBER ARGL-TR-81-0210	2. GOVT ACCESSION NO.	3. RECIPIENT'S CATALOG NUMBER
4. TITLE (and Subtitle) The Mesosphere and Thermosphere	5. TYPE OF REPORT & PERIOD COVERED REPRINT	
7. AUTHOR(s) K.S.W. Champion and G. Schmidtke*	6. PERFORMING ORG. REPORT NUMBER	
9. PERFORMING ORGANIZATION NAME AND ADDRESS Air Force Geophysics Laboratory (LKB) Hanscom AFB Massachusetts 01731	10. PROGRAM ELEMENT, PROJECT, TASK AREA & WORK UNIT NUMBERS 62101F 66900703	
11. CONTROLLING OFFICE NAME AND ADDRESS Air Force Geophysics Laboratory (LKB) Hanscom AFB Massachusetts 01731	12. REPORT DATE 30 July 1981	
	13. NUMBER OF PAGES 248	
14. MONITORING AGENCY NAME & ADDRESS (if different from Controlling Office)	15. SECURITY CLASS. (of this report) Unclassified	
	15a. DECLASSIFICATION/DOWNGRADING SCHEDULE	
16. DISTRIBUTION STATEMENT (of this Report) Approved for public release; distribution unlimited.		
17. DISTRIBUTION STATEMENT (of the abstract entered in Block 20, if different from Report)		
18. SUPPLEMENTARY NOTES Proceedings of the Topical Meeting of the COSPAR Interdisciplinary Scientific Commission C (Sessions C1 & C3) of the COSPAR 23rd Plenary Meeting, Budapest, Hungary, 2-14 June 1986. *Institut für Physikalische Messtechnik, Freiburg im Breisgau, F.R.G.		
19. KEY WORDS (Continue on reverse side if necessary and identify by block number)		
Energy sources Upper atmosphere Ionosphere Atmospheric models	Stratosphere Mesosphere Thermosphere Exosphere	
20. ABSTRACT (Continue on reverse side if necessary and identify by block number) This publication contains a number of specialized papers on two topics. The first topic is representation of energy sources in the Earth's upper atmosphere and ionosphere. The energy sources include the solar wind and electromagnetic radiation, particle precipitation, joule heating in the electrojets, and energy transfer by gravity wave dissipation. The second topic is concerned with models of the terrestrial upper atmosphere. The subdivisions include the stratosphere, mesosphere, thermosphere and exosphere. Properties considered (cont.)		

SECURITY CLASSIFICATION OF THIS PAGE(When Data Entered)

20. Abstract (cont)

are total mass density, composition, radiative cooling, temperature, winds, diffusion, and turbulence.

SECURITY CLASSIFICATION OF THIS PAGE(When Data Entered)

ADVANCES IN SPACE RESEARCH

The Official Journal of the Committee on Space Research (COSPAR)
A Scientific Committee of the International Council of Scientific
Unions (ICSU)

VOLUME 1, NUMBER 12

THE MESOSPHERE AND THERMOSPHERE

Sponsor

THE COMMITTEE ON SPACE RESEARCH (COSPAR)

in collaboration with

THE HUNGARIAN ACADEMY OF SCIENCES

Organizers

ISC C Session 1

G. Schmidtke

with the collaboration of

S. A. Bowhill

ISC C Session 3

K. S. W. Champion

with the collaboration of

S. A. Bowhill and G. Kockarts

NOTICE TO READERS

Dear Reader

If your library is not already a standing/continuation order customer or subscriber to this series, may we recommend that you place a standing/continuation or subscription order to receive immediately upon publication all new issues and/or volumes. Should you find that these volumes no longer serve your needs your order can be cancelled at any time without notice.

ROBERT MAXWELL

Publisher at Pergamon Press

THE MESOSPHERE AND THERMOSPHERE

*Proceedings of the Topical Meeting of the COSPAR
Interdisciplinary Scientific Commission C (Sessions C1 and
C3) of the COSPAR Twenty-third Plenary Meeting held in
Budapest, Hungary, 2-14 June 1980*

Edited by

G. SCHMIDTKE (Session C1)

Institut für Physikalische Messtechnik, Freiburg im Breisgau, FRG

and

K. S. W. CHAMPION (Session C3)

AFGL/Hanscom AFB, Bedford, Massachusetts, USA

Published for
THE COMMITTEE ON SPACE RESEARCH
by
PERGAMON PRESS

Oxford · New York · Toronto · Sydney · Paris · Frankfurt

U.K.	Pergamon Press Ltd., Headington Hill Hall, Oxford OX3 0BW, England
U.S.A.	Pergamon Press Inc., Maxwell House, Fairview Park, Elmsford, New York 10523, U.S.A.
CANADA	Pergamon Press Canada Ltd., Suite 104, 150 Consumers Rd., Willowdale, Ontario M2J 1P9, Canada
AUSTRALIA	Pergamon Press (Aust.) Pty. Ltd., P.O. Box 544, Potts Point, N.S.W. 2011, Australia
FRANCE	Pergamon Press SARL, 24 rue des Ecoles, 75240 Paris, Cedex 05, France
FEDERAL REPUBLIC OF GERMANY	Pergamon Press GmbH, 6242 Kronberg-Taunus, Hammerweg 6, Federal Republic of Germany

Copyright © 1981 Pergamon Press Ltd.

All Rights Reserved. No part of this publication may be reproduced, stored in a retrieval system or transmitted in any form or by any means: electronic, electrostatic, magnetic tape, mechanical, photocopying, recording or otherwise, without permission in writing from the publishers.

First edition 1981

British Library Cataloguing in Publication Data

The Mesosphere and Thermosphere.- (Advances in space research; vol 1, no. 12)
 1. Mesosphere-Congresses
 2. Thermosphere-Congresses
 I. Schmidke, G.II. Champion, K. S. W.
 III. COSPAR. Plenary Meeting (23rd: 1980: Budapest)
 IIII. Hungarian Academy of Science
 551.5'14 QC881.2.M3

ISBN 0 08 028393 4

In order to make this volume available as economically and as rapidly as possible the authors' typescripts have been reproduced in their original forms. This method unfortunately has its typographical limitations but it is hoped that they in no way distract the reader.

CONTENTS

PART I—*ISC C Session 1—Representations of Energy Sources in the Earth's Upper Atmosphere and Ionosphere*

SECTION 1—*Energy Sources of Solar Origin*

Solar Wind and its Interaction with the Magnetosphere: Measured Parameters <i>R. Schwenn</i>	3
Electromagnetic Field Dissipation and Corpuscular Bombardment and their Implications in Atmospheric Modelling <i>K.D. Cole</i>	19
Particle and Joule Heating of the Neutral Polar Thermosphere in the Cusp Region using Atmosphere Explorer-C Satellite Measurements <i>M. Griffis, J.S. Nisbet and E. Bleuler</i>	27
Thermospheric Signature of Magnetospheric Energy Dissipation <i>G.W. Prölss</i>	31
A Model for Proton Interaction in the Atmosphere Including Fluxes of Generated Electrons <i>H. Karszenbaum and D.A. Gagliajini</i>	35
Representations of Solar EUV Fluxes for Aeronomical Applications <i>H.E. Hinteregger</i>	39
Solar EUV Energy Budget of the Thermosphere <i>M.R. Torr, P.G. Richards and D.G. Torr</i>	53

SECTION 2—*Energy Inputs and Models*

Energy Transfer by Gravity Wave Dissipation <i>K.D. Cole and M.P. Hickey</i>	65
Observations of the Aurora in the Far Ultraviolet from "Cosmos-900" <i>K.I. Gringauz, L. Martini, N.M. Shutte and A.I. Puolokainen</i>	77
Empirical Models of the Thermosphere and Requirements for Improvements <i>L.G. Jacchia</i>	81
Energy Sources for the Ionosphere—A Survey <i>K. Rawer</i>	87

Comprehensive Investigation of the Basic Parameters of the Upper Atmosphere at the Time of the Flight of the Geophysical Rocket "Vertical-6"	101
<i>I. Apáthy, I. Szemerey, P. Bencze, K. Kovács, V. Afonin, V. Bezrukikh, K. Gringauz and N. Shutte</i>	
Experimental Testing of "Corpuscular" Hypothesis of Night-time Mid-latitude Ionosphere—Results of Simultaneous Rocket-Satellite Investigations	107
<i>S.I. Avdyushin, L.L. Bukusova, V.M. Feigin, G.S. Ivanov-Kholodny, T.V. Kazachevskaya, M.A. Savelyev and V.F. Tulinov</i>	
PART II—ISC C Session 3—Models of the Terrestrial Mesosphere and Thermosphere	
SECTION 1—Stratosphere-Mesosphere	
Models of the High Latitude Stratosphere and Mesosphere	113
<i>G.A. Kokin, D.A. Tarasenko and L.A. Ryazanova</i>	
Mesospheric Structure and the D-Region Winter Anomaly	123
<i>D. Offermann, H.G. Brückelmann, K.M. Torkar and H. Widdel</i>	
Dissipation of Temperature Perturbations in the Middle Atmosphere	127
<i>G.E. Thomas</i>	
SECTION 2—Thermosphere - Exosphere	
Properties of the Mesosphere and Lower Thermosphere	133
<i>K.S. W. Champion</i>	
Development of Wind Observational Models for the Upper Atmosphere of the Earth Based on the Joint Analysis of Direct and Indirect Sounding Data	151
<i>S.S. Gaigerov, D.A. Tarasenko, V.V. Fedorov, V.G. Kidiyarova, Yu.P. Koshelkov, M.Ya. Kalikhman, R.A. Britvina and L.V. Scherbakova</i>	
Eddy Diffusion Coefficient and Atmospheric Models	157
<i>K.G.H. Schuchardt and P.W. Blum</i>	
Eddy Mixing and Composition Variations of Earth's Upper Atmosphere	171
<i>L.A. Antonova and V.V. Katjushina</i>	
Thermospheric Model Calculations Based on Turbulence Data	175
<i>K.G.H. Schuchardt and P.W. Blum</i>	
The Influence of Radiative Cooling and Turbulence on the Heat Budget of the Thermosphere	179
<i>B.F. Gordiets, Yu.N. Kulikov, M.N. Karkov and M.Ya. Marov</i>	

Comparison of the Empirical Thermospheric Models and the Self-consistent Model of the Ionospheric Plasma <i>M.N. Vlasov and A.G. Kolesnik</i>	187
SECTION 3—Mesosphere-Thermosphere	
Some Recent Advances in Thermospheric Models <i>G. Kockarts</i>	197
Models of the Geomagnetic Effect in the Earth's Thermosphere <i>J.W. Showey</i>	213
Densities from the CACTUS Accelerometer as an External Test of the Validity of the Thermospheric Models <i>J.L. Falin, G. Kockarts and F. Barlier</i>	221
Variations of Density Scale Height Between 300 and 400 km <i>M.J. III</i>	227
Asymmetrical Structure in the Thermosphere During Magnetic Storms as Deduced from the CACTUS Accelerometer Data <i>C. Berger and F. Barlier</i>	231
Author Index	237

PART I

**ISC C Session 1—Representations of
Energy Sources in the Earth's Upper
Atmosphere and Ionosphere**

SECTION 1

Energy Sources of Solar Origin

SOLAR WIND AND ITS INTERACTION WITH THE MAGNETOSPHERE: MEASURED PARAMETERS

Rainer Schwenn

*Max-Planck-Institut für Aeronomie,
3411 Katlenburg-Lindau 3, FRG*

ABSTRACT

The earth's magnetosphere absorbs only a minor fraction ($\approx 10^{-3}$) of the incident solar wind energy. Variations of the solar wind can often cause lively reactions in the earth's close environment. However, the physical mechanisms involved are not yet understood. It appears now that the combined action of the solar wind momentum flux, the direction of the interplanetary magnetic field as well as its fluctuations might play the dominant role. The behaviour of these parameters is governed in some characteristic way by the solar wind stream structure which reflects the condition of the solar corona and its magnetic field topology. Transients in the sun's atmosphere associated with solar activity cause reactions in the interplanetary medium which also show some typical, though very different, signatures. Taking into account the interdependence of the solar wind parameters in context with the underlying solar phenomena, we may be able to pinpoint the mechanism which controls the action of the solar wind on the magnetosphere.

INTRODUCTION

The possible correlations between certain phenomena on the earth, e.g. geomagnetic activity and aurorae, and processes on the sun have long attracted the attention of scientists. However, even today we are still far from knowing all the links of the long chain of reactions through which energy other than radiation is carried from the sun's atmosphere onto the earth. These ideas have originally been stimulated by the early finding of recurrences in geomagnetic disturbances following the rhythm of the sun's 27 day rotation. (For a historical review and further references, see Wilcox [1], Burlaga and Lepping [2]).

Today we know that the main agent in this chain is the solar wind. In 1932 Bartels [3] had already argued that geomagnetic disturbances might be caused by stationary, though isolated, particle streams ejected from the rotating sun. These stationary sources, which he called M-regions, were thought to be associated more or less with active regions on the sun. Although the solar wind was finally found to be a continuous flow of ionized gas, Bartels' idea was partly confirmed in that the solar wind is highly structured and geomagnetic effects are well correlated with stationary corotating fast streams imbedded in slower plasma (Snyder et al [4]. Even the M-region concept could be verified when the solar sources of those

streams were finally identified: Noci [5] and Krieger et al [6] were the first to argue that regions of diminished brightness at X ray and EUV wavelengths (so-called coronal holes) in the solar corona are the sources of high-speed solar wind streams. Neupert and Pizzo [7] found a direct correlation between coronal holes and recurrent geomagnetic disturbances (For more information see Zirker [8]). The Skylab era finished a longlasting controversy (see Neupert and Pizzo [7]) whether the M-regions are tied to active regions or not: Coronal holes are features typical of the quiet sun, not of the active sun. This is the reason for the well-known fact that recurrent geomagnetic disturbances are found mainly during times around the minima in the solar activity cycles (Sheeley et al [9] [10]). However, even more dramatic geomagnetic effects are caused by active regions on the sun. The major magnetic storms especially can often be uniquely associated with solar flares. These sporadic events are typical features of the active sun, in contrast to the recurrent events which are products of the quiet sun. The occurrence rate of these sporadic events is of course directly correlated to solar activity.

The different sources for geomagnetic activity have unfortunately not always been properly separated. Much of the statistical work done in the past for finding correlations between solar, interplanetary and terrestrial phenomena suffers from the lack of appreciation for this basic difference. It is not the purpose of this paper to review and re-evaluate all those studies. We intend rather to describe our present understanding of the structured and variable solar wind and the processes going on in it. We try to put all those parameters which were suspected or known to be somehow related to geomagnetic activity but were regarded in a more or less isolated fashion into the right context. This way, a bit of new light might be shed on old findings which will then be quoted here without too much regard of their proper historical order.

The earth's magnetosphere absorbs only a minor fraction (10^{-3} to 10^{-2}) of the solar wind kinetic energy flux ($1 \text{ erg cm}^{-2} \text{s}^{-1}$ at 1 AU). The power input into the magnetosphere with an effective radius of $10 R_E$ is of the order of 10^{12} W . This amount appears negligible as compared to the light energy absorbed by the earth's troposphere ($\approx 10^{17} \text{ W}$). There is increasing evidence, though, that the energy absorbed from the solar wind mainly due to its high variability might be able to at least trigger certain mechanisms in the magnetosphere, the ionosphere and even the troposphere (see, e.g. the textbook by Hargreaves [11]). In the first place, the absorbed solar wind energy goes into the magnetospheric and ionospheric current systems, the production of high energy particles in the radiation belt, and the production of auroral particles (Perreault and Akasofu [12]). Changes in the energy input may cause dramatic reactions of these energy consumers by triggering the emptying of other energy reservoirs, e.g. magnetic energy stored in the magnetotail resulting in geomagnetic storms. These phenomena will not be further discussed in this paper. They are mentioned only in order to illustrate that it is the structures and variations in the solar wind which are of basic importance in any solar terrestrial relations.

THE SUN AND THE SOLAR WIND IN TERMS OF THE "BALLERINA" MODEL

The appearance of the solar wind is most adequately described in terms of the "ballerina" model first proposed by Alfvén (for a review see [13]). It is now well established by the aid of several recent findings. Figure 1 is a schematic drawing of the inner heliosphere right before the last solar activity minimum in 1976. The sun's poles are covered by large coronal holes. They are areas of open magnetic field lines, the northern hole being of positive (outward directed) polarity, the southern being negative (inward directed). Some tongue-like extensions of the coronal holes reach well into the equatorial regions and give the sun the appearance of a tilted magnetic dipole (Schulz [14]). The sun's equato-

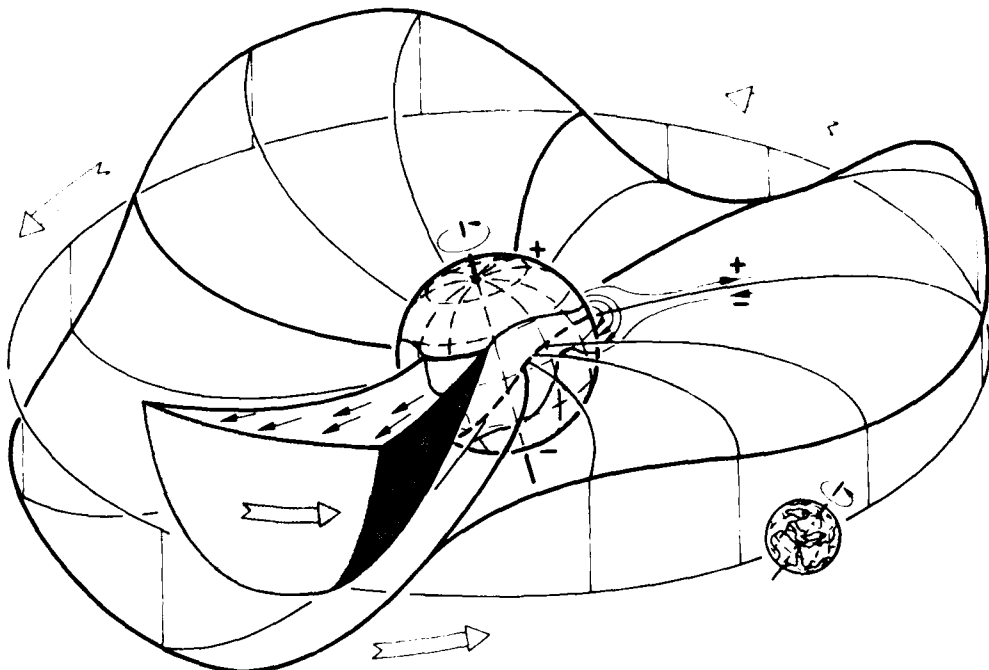


Fig. 1 The "ballerina" model of the heliosphere as proposed by Alfvén [13]. For explanations see text.

rial region is governed by activity centers (e.g. sunspots) and their loop-like and mainly closed magnetic structures. What looks like the skirt of a spinning ballerina is the warped separatrix between positive and negative solar magnetic field lines dragged out into interplanetary space by the radially outflowing conductive solar wind plasma. It is in fact a substantial sheet of azimuthally flowing electric current required for the polarity change of the magnetic field. The sheet is "attached" to the corona on top of closed magnetic structures at the transition between closed and open flux tubes, i.e. generally in the middle of the equatorial "belt" of activity. Any observer north of this current sheet is in a positive magnetic sector, south of it in a negative sector. When the current sheet is swept over the observer he calls this a sector boundary crossing. The size and number of magnetic sectors is closely related to the underlying coronal structure. Around solar minimum the folds in the current sheet do not reach to high latitudes. This is why Pioneer 11, coming to 16° northern heliographic latitude in 1976, spent more than 90 % of the time in positive sectors (Smith et al [15]). The orientation of the solar dipole changes from one solar minimum to the next resulting in a 22 year magnetic solar cycle.

High speed streams

The coronal holes are now known to be the sources of high speed solar wind streams (see Zirker [8]). This explains why high speed streams are always completely enclosed in regions of only one magnetic polarity. Measurements of the solar wind speed at high latitudes using the interplanetary scintillation (IPS) technique indicate that the average speeds are much higher here (Coles and Rickett [16]). This is expected from the existence of the large polar coronal holes. The maximum speed was found to be correlated with the size of the coronal holes (Nolte et al [17]).

However, there is not yet any consistent explanation on how a steady flow of solar

wind can ever achieve speeds often exceeding 700 kms^{-1} . Theoretical studies show some evidence that the degree of divergence of the open field lines plays a major role (Kopp and Holzer [18], Holzer [19]). Furthermore, there is evidence for the importance of wave action for solar wind acceleration (Hollweg [20]) which is not yet fully understood. Observations from the solar probes Helios 1 and 2 approaching the sun as close as 0.29 AU revealed that the often drastic speed differences between α -particles and protons (exceeding 200 kms^{-1} at 0.29 AU) are closely related to the occurrence of Alfvénic fluctuations and their intensities (Marsch et al [21]). Some unexpected features in the particles' velocity distribution functions also show the basic importance of wave-particle interactions (Feldman et al [22], Marsch et al [23]). Generally, the fast solar wind can be characterized by some typical parameters which hardly ever show structural changes within one stream or much difference from one stream to the next (Feldman et al [24]). This reflects the above mentioned fact that the fast streams are expressions of the quiet sun.

Slow solar wind

The slow solar wind has been taken by many authors as representative of the quiet, ambient, and structureless solar wind needed as a reference for comparisons with theoretical models (see, e.g., Hundhausen [25]). However, Feldman et al [24] concluded that "it is reasonable to suggest that the structureless ambient state of the solar wind may be found at high ($> 750 \text{ kms}^{-1}$) flow speeds rather than at low ones". In fact, the slow solar wind is not at all "quiet", since it emerges from those regions in the corona which are situated over the activity centers with all their complicated and highly variable magnetic topologies. The coronal phenomena going on here and the outflow of the slow solar wind from these often loop-like and mainly closed magnetic structures are still far from understood.

Stream-stream interactions

The Helios measurements showed that the longitudinal transitions between plasma streams of different speed are generally much more abrupt closer to the sun than at 1 AU. This led to the impression of a "mesa-like" stream structure (Rosenbauer et al [26] [27]). Comparison of simultaneous Helios 1, Helios 2 and IMP measurements revealed that the latitudinal stream boundaries are also very thin (Schwenn et al [28]). It now appears as if slow and fast streams might represent two states of the solar wind resulting from different acceleration mechanisms.

The hypothetical streamlines of the plasma flowing radially away from the rotating sun are wound up to Archimedean spirals in interplanetary space. Since the spiral angle ($\approx 45^\circ$ at 1 AU) depends on the flow speed, the streams of different speed coming from contiguous sources in the corona start interacting with each other. In the boundary layer between a slow stream and a fast stream coming from behind, the plasma will be compressed. This can lead to high values of density, momentum and energy fluxes within these interaction regions. The density gradients give rise to longitudinal and latitudinal motions of the compressed plasma, i.e. deflections of the streams (Pizzo [29] [30]). As soon as the local sound speed (at the fast magnetosonic mode) at which these density signals can propagate, is less than the corotation speed of the structure, a shock front along the high density region will form, or even a shock pair on both sides on the density ridge. Such corotating shocks were first observed beyond 1 AU (Smith and Wolfe [31]); recently the Helios probes found a few cases inside 1 AU, as close as 0.6 AU from the sun (Burlaga et al [32], Schwenn et al [33]).

Relation of streams and magnetic structure and some terrestrial implications

Figure 1 shows that an observer in the plane of the ecliptic will see alternately

slow and fast streams coming by; their relative number depends directly on the underlying coronal structure, mainly on the occurrence of equatorial coronal holes. From Figure 1 it can be seen that close to the sun the equatorial current sheet forming the magnetic sector boundary can be quite far away from the compression region of the following fast stream, since there is no direct physical dependence between the two. It is only due to the stream interaction processes mentioned above that at 1 AU the sector boundary is found in many cases right in front of the stream interface, preceding it by only 1 1/2 hours to 1 1/2 days (Gosling et al [34]). We emphasize the basic difference between the magnetic sector structure and the solar wind stream structure. This difference is important for any trial of solar terrestrial correlations. Many studies have been published where terrestrial effects were correlated with sector boundary crossings (e.g. Hirshberg and Colburn [35], Shapiro [36], Wilcox et al [37]) inferring the potential significance of interactions between the interplanetary and the earth's magnetic field. On the other hand, from correlations with the solar wind stream structure (e.g. Sawyer and Haurwitz [38]) one might rather conclude that the action of kinematic effects due to momentum and energy fluxes onto the magnetosphere plays the leading role. Regardless of these different aspects, there is no doubt about the key role of the magnetic field in solar-terrestrial relations.

The importance of the interplanetary electric field $\vec{E} = -(\vec{v} \times \vec{B})$ (\vec{v} is the solar wind speed vector, \vec{B} the interplanetary magnetic field vector) for geomagnetic activity has been well known since the pioneering work of Alfvén [39] [13]. Dungey [40] pointed out the possibility of reconnections between interplanetary magnetic field lines if they have a southward directed component B_z , with a northward directed geomagnetic field line. Many observations starting with Fairfield and Cahill [41] demonstrated the significance of B_z for the occurrence of geomagnetic activity. The quality of such correlations could significantly be improved by replacing B_z by the quantity $v \cdot B$ which is the east-west (dawn-dusk) component of the interplanetary electric field (e.g. Rostoker and Fälthammar [42], Alfvén and Fälthammar [43]).

In addition, geomagnetic variability was found to be associated with fluctuations of \vec{B} (e.g. Dessler and Fejer [44], Ballif et al [45], Garrett et al [46]). However, the interdependence of all these quantities due to their common physical basis, which is the expansion of the structured solar wind, has rarely been regarded.

Transients

The most dramatic geomagnetic disturbances are always associated with big solar flares (Chao and Lepping [47]). Part of the flares' action starts as fast as a few minutes later. Especially after very strong flares, the emitted UV and XUV radiation as well as the ejected energetic particles will impinge in the ionosphere and change its electrical conductivity, thus modifying the ionospheric current systems. Another part is due to the interplanetary shock wave which is driven by the flare ejecta (for a review see Dryer [48]) and which does not arrive at the earth until one to four days later. The sudden density and speed increase at a shock front may cause a jump in the solar wind pressure on the magnetosphere by more than one order of magnitude. In addition, the magnetic topology will be drastically changed, in a way that depends mainly on the type of the flare, on the position of the flare site relative to the earth, and on the ambient solar wind structure. It often happens that passage of the shock front is followed some hours later by a tangential discontinuity, which separates the hot, shocked, ambient plasma from the flare ejecta which act like a piston. This driver gas can often be discerned by its increased helium content (Bame et al [49], Hirshberg et al [50]), and frequently also exhibits unusually low proton and electron temperatures (Gosling et al [51], Montgomery et al [52]). This has been interpreted

as being due to topologically closed magnetic structures (like magnetic bottles) which eventually close off and then drift as isolated loops in the post shock flow (Gold [53], Bame et al [54]), see Figure 2. The temperature depression is explained as resulting from the inhibition of thermal conduction due to magnetic cut off, and, in addition, from a greater than r^2 divergence of the flare ejecta. It is clear that any observer during the transition through such a magnetic bottle or "magnetic cloud" (Burlaga and Klein [55]) will see dramatic changes both in the field magnitude and direction.

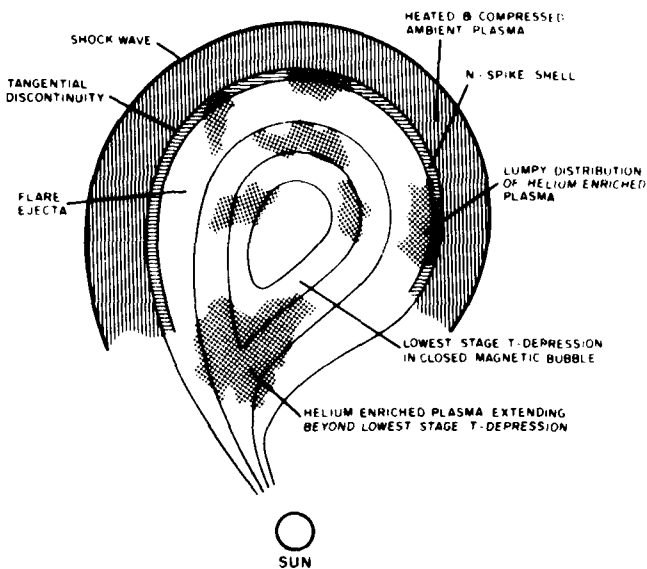


Fig. 2 A possible geometry of flare-expelled plasma driving an interplanetary shock wave. In this extension of the model of Hundhausen [25] the interplanetary field lines threading the shock and compressed ambient plasma have been omitted for clarity; possible magnetic bubble and bottle configurations in flare-expelled gas are shown.
(from Bame et al [54]).

Normally less spectacular than flares and their effects are the coronal mass ejections pushed outwards by eruptive prominences (Gosling et al [56], Hildner et al [57]). Gosling et al [58] conclude that these ejections can be re-identified in the solar wind as "non compressive density enhancements". They are all found imbedded in slow solar wind structures and are characterized by densities greater than 15 cm^{-3} , unusually low proton and electron temperatures, and often by unusual reversals of the magnetic field. Evidence has recently been found that in very rare cases eruptive prominences may themselves eject material, also enclosed in magnetic bottles, and fast enough to act as a piston and drive a shock wave (Schwenn et al [59]). In these cases the existence of singly ionized helium within the piston is suggestive of its chromospheric origin. This is mentioned here in order to indicate that there might well be geomagnetic phenomena which can be associated with neither flare action nor high speed streams. Their sources should rather be sought by means of other types of solar observations, such as H_{α} -spectroheliograms or radio wave measurements.

MEASURED PARAMETERS

In order to illustrate all the main features of the solar wind behaviour as extensively discussed above, we selected measurements covering one complete solar rotation in 1974/1975 as performed by the plasma instruments aboard the Helios-1 solar probe. In Figure 3 the main proton parameters, bulk speed v , density n , and temperature T , are plotted as 1 hr averages (dots denoting α -particles). We also

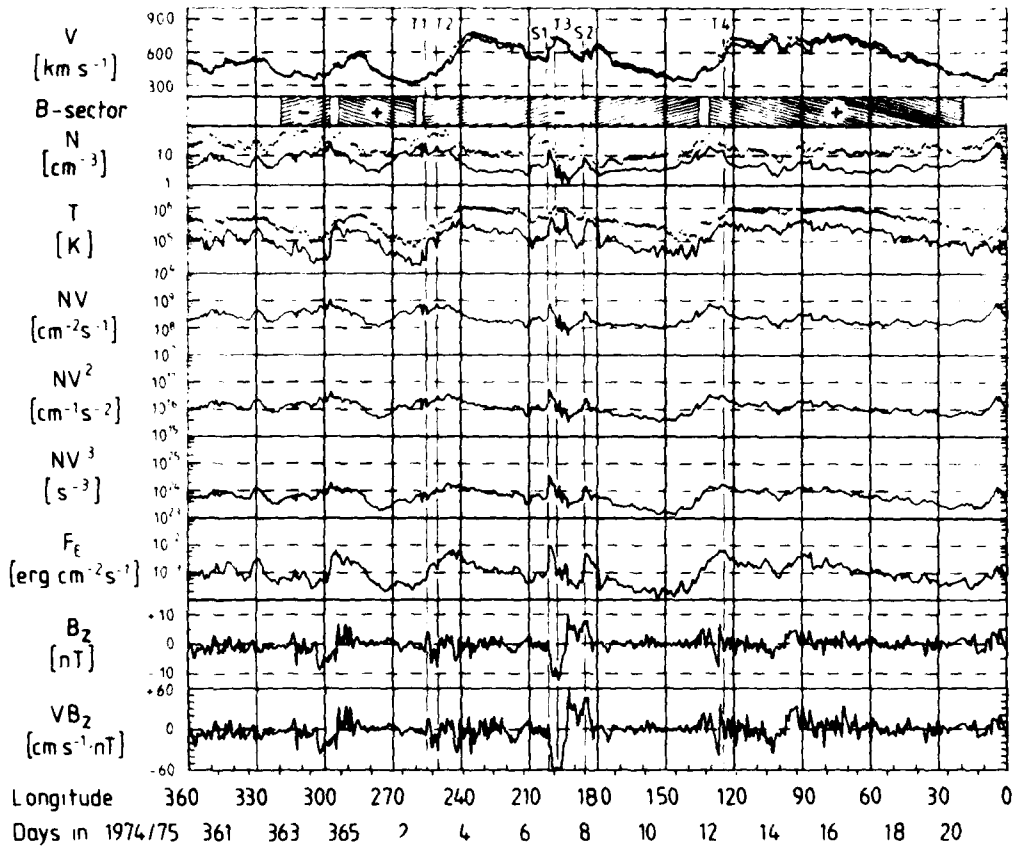


Fig. 3 The main parameters of the solar wind during a complete solar rotation, plotted as 1 hr averages. The dots denote the parameters of the α -particles ($n \times 100$). The data were collected at the Helios-1 solar probe between 0.96 and 0.85 AU. The longitudinal separation between Helios-1 and the earth did not exceed 10° . The solar wind structure shown here is typical for the time period close before solar activity minimum. A detailed description is given in the text.

display some combined quantities deduced from n , v , T which are proportional to the particle flux density $P = nv$, the momentum flux density $M \sim nv^2$, the kinetic energy flux density $F_K \sim nv^3$, the proton enthalpy flux density $F_E \sim nvT$, and the interplanetary electric field component $E_y \sim v \cdot B_z$.

We will concentrate first on the two huge fast stream systems which are both imbedded in magnetic sectors of opposite signs. They had been nearly stationary since at least the end of 1973 (Sheeley et al [9]).

We note a few main points:

- The maximum bulk speed v exceeds 700 km s^{-1} , the speed difference to the ambient slow plasma is $\approx 400 \text{ km}$, the longitudinal extension of each stream is more than 90° . This kind of stream is characteristic for the time right before solar activity minimum (Bame et al [60]).
- The compression of the plasma on both sides of the stream interfaces T_1 , T_2 , and T_4 is clearly visible. The density maximum determined from many more

- interfaces is $\approx 40 \text{ cm}^{-3}$ on the average at 1 AU.
- The proton flux density P reaches maxima at these interfaces ($\approx 10 \text{ cm}^{-2} \text{ s}^{-1}$). The values of P in "quiet" slow plasma (e.g. days 11, 20) and fast streams (e.g. days 4, 5, 13, 16, 17, 18) are surprisingly equal. Other data confirm this trend.
 - The momentum flux density $M = nv (\text{m v})$ reaches its maximum relative to the interfaces several hours later than the density. In addition, the higher power of v causes nv^2 to be generally higher in fast streams than in slow streams.
 - This tendency is even stronger for the flux of kinetic energy $F_K = nv (1/2 m v^2)$.
 - The enthalpy flux density $F_E = nv (5/2 kT)$ is only a few percent of F_K . F_E shows more pronounced fluctuations than F_K . The profile of $\ln (F_E)$ follows quite closely that of v .
 - The sector boundaries as determined by Behannon et al [61] are situated fairly close to the stream interfaces, well within the compression regions.
 - There are significant fluctuations of $E_z = -v \cdot B_z$. Closer inspection and comparison with more cases reveal some recurring trends, especially around sector boundaries.

This last point shall be inspected further, since it might have some terrestrial implications. Rosenberg and Coleman [62] studied the behaviour of B_z around sector boundaries extensively and explained it in terms of the ballerina model: At any sector boundary the current sheet must necessarily be inclined versus the ecliptic implying the existence of non-zero B_z components. At the transition from well within one sector with $B_z = 0$ to well within the other sector with again $B_z = 0$, the observer will see a negative component, $B_z < 0$, first and later $B_z > 0$. This is correct for any sector crossing, positive to negative and vice versa, as long as the general dipole of the sun is oriented as in Figure 1, i.e. the north is positive and the south is negative. Only when the sun's dipole is turned around, e.g. before the previous or after the present solar maximum, an observer will find $B_z > 0$ first and only then $B_z < 0$. This reversal was confirmed by measurements taken between 1966 to 1973 [62]. From Figure 3 one can deduce that during the time of an inverted solar polarity the $B_z < 0$ phase would generally be shifted towards a later time in the stream interface, i.e. into a region where the kinetic energy density flux F_K is already higher. This phase shift between $B_z < 0$ and F_K follows the 22 year magnetic cycle of the sun. We underline the possible importance of this effect, since it might well modulate the recurrent geomagnetic effects. This modulation should follow the 22 year magnetic solar cycle, and be superimposed on the well-known 11 year modulations. Evidence for some 22 year periodicities in geomagnetism was found by Chernovsky [63] and Russell [64].

Another hypothesis explaining these magnetic phenomena as well was given in some previous versions of the paper by Rosenberg and Coleman [62], and was adopted by Pilipp et al [65]. Around several sector boundaries they found significantly decreased values of electron temperature and heat flux indicating a magnetic cutoff from the sun. They inferred the occurrence of magnetic loops resulting from re-connecting field lines at the sector boundary. This idea was supported by the multipoint observations (Schwenn et al [29]) of non-stationary phenomena and multiple stream interface crossings in the vicinity of sector boundaries.

Before further inspection of Figure 3 a summary of the parameters of the typical "quiet" fast and slow solar wind will be given in Table 1. Some of these values were taken from the literature; some of them were calculated from the plasma data of the Helios solar probes. In addition to the features discussed qualitatively above, we find a few more points:

- The electron temperature T_e is less in fast streams than in slow streams, contrary to the protons. T_e in fast streams is even significantly lower than

TABLE 1 Characteristics of "quiet" solar wind at 1 AU.

Quantity	dimension	"slow" streams		"fast" streams	
bulk speed v	km s^{-1}	300 - 325	H	741 ± 49	F
		300 - 400	S	600 - 800	S
proton density n	cm^{-3}	8.7	H	4.4 ± 0.6	S
		9.5 ± 3.8	S		
proton temperature T	10^3 K	40	H	230 ± 30	F
		35 ± 16	S	260 ± 40	S
electron temperature T_e	10^3 K	150	H	90 ± 8	F
magnetic field B	nT	3.45 ± 0.48	M	3.28 ± 0.11	M
proton flux $P = nv$	$\text{cm}^{-2} \text{s}^{-1}$	2.4×10^8	H	$(3.3 \pm 0.5) \times 10^8$	F
momentum flux $M = nv (\frac{m}{p} v)$	$\text{dyn cm}^{-2} \text{s}^{-1}$	2.3×10^{-8}	S	2.5×10^{-8}	S
energy fluxes:	$\text{erg cm}^{-2} \text{s}^{-1}$				
kinetic energy $F_K = nv \cdot (1/2 \frac{m}{p} v^2)$		0.22	H	1.2 ± 0.2	F
		0.34 ± 0.09	S	1.29 ± 0.2	S
proton enthalpy $F_E = nv \cdot (5/2 kT)$		0.008	H	0.024 ± 0.005	F
		0.0045 ± 0.0013	S	0.0032 ± 0.008	S
Alfvén waves $F_A = nv \cdot (5/2 m \langle \delta v^2 \rangle)$				0.0116 ± 0.0047	F
electron heat conduction Q_e		0.007	H	0.0028 ± 0.009	F
proton heat conduction Q_p	$\approx 10^{-5}$		H		

Data sources: F: Feldman et al [24], H: Hundhausen [25],
M: Mariani et al [66], S: Present Work

- the proton temperature (Feldman et al [24]).
- The average magnetic field magnitude B is nearly independent of the stream structure (Mariani et al [66]).
- The energy flux contained in Alfvén waves $F_A = nv (5/2 m \langle \delta v^2 \rangle)$ within high speed streams is only $\approx 1\%$ of the kinetic energy flux (Feldman et al [24]). However, these mainly transverse magnetic fluctuations can obtain high amplitudes up to $|\delta B|/|B| \approx 1$, especially right after stream interfaces and in the front parts of fast streams (Morfill et al [67]). This means that $B_z < 0$ for significant portions of the time. Within slow streams F_A is about two orders of magnitude less than in fast streams.
- The electron and proton heat fluxes appear to be insignificant in the context of this paper.

In addition, Figure 3 gives two typical examples of flare produced interplanetary shocks (denoted S1 and S2) showing some typical features:

- The simultaneous increase of v , n , T and B (not shown here) indicate both

- shocks to be fast forward MHD shocks.
- S1 is followed a few hours later by the driver gas characterized as usual by a discontinuous decrease in n and T . The discontinuity is denoted as T_3 in Figure 3.
- The increase of v and n to such values as never occur during normal conditions, leads to unusually high values of the momentum flux and, even more so, of the kinetic energy flux.
- Right at S1 the magnetic field has a large southward component B_z , which turns northward at the passage of the piston contact surface.

In Figure 4 we show the stream interfaces T1 and T2 and the two shocks S1 and S2 with better time resolution. This time we used plasma data from the IMP 7/8 satellites in order to try correlations with geomagnetic responses. Unfortunately there are no magnetic field data available. Since Helios 1 was only about 8° in longitude away from the earth and the plasma structures found here are very similar, the magnetic field structure can certainly be inferred to be also similar. In Figure 4 we added two panels showing the behaviour of the three hour planetary index K_p and the auroral electrojet index AE, which were adopted from Solar Geophysical Data. Many features described by other authors are also found from Figure 4:

- The K_p -profile around the stream interfaces follows very closely that of the bulk speed, in general agreement with Snyder et al [4] and Sheeley et al [9] [10]. Note that K_p remains high for more than two days behind the interface. Bobrov [68] found it most striking that the recurrent storms do not terminate with the return of the interplanetary magnetic field strength to normal levels but continue for several days. He concluded finally that "the most important of agents responsible for geomagnetic activity at the second stage of a recurrent storm is total interplanetary field variability." In fact, during these second stage phases Alfvénic fluctuations were found to be strongest (Morfill et al [67]). Garrett et al [46] try a series of correlations between empirical functions of combined solar wind parameters and geomagnetic activity indices a_p and AE. They generally confirm Bobrov's [68] result. They infer that "although a static interplanetary electric field is largely shielded from the interior of the magnetosphere by charge distributions in the boundary, a rapidly varying electric field can penetrate the boundary more effectively because of the finite time required for the redistribution of shielding charges."
- Bobrov [68] found also, that for flare produced geomagnetic disturbances there is no relation between K_p and v , since a high K_p is often confined only to the first few hours behind the shock. (In the case of our Figure 4 this does not show up very well). Burlaga [69] finds it "interesting to investigate whether the absence of fluctuations in the trailing part of flare-associated streams is associated with magnetic loops or bottles". Although there is now increased evidence for both the existence of magnetic loops in the piston gas behind shocks as well as the reduced level of Alfvénic fluctuations therein, a systematical analysis is still missing.
- From comparison of Figures 3 and 4 a close correlation between $v \cdot B$ and AE can be inferred for the first part of the fast stream. Only after the speed maximum (after day 5 in Figure 4) the correlation breaks down. This behaviour and similar relations between B and AE have often been observed (e.g. Burlaga and Lepping [2]). Behind the shock S1 AE reaches a maximum, and simultaneously $v \cdot B_z$ is high and negative. The abrupt decrease of AE (as well as K_p and F_K) at the arrival of the piston gas coincides with the reversal of $v \cdot B_z$.

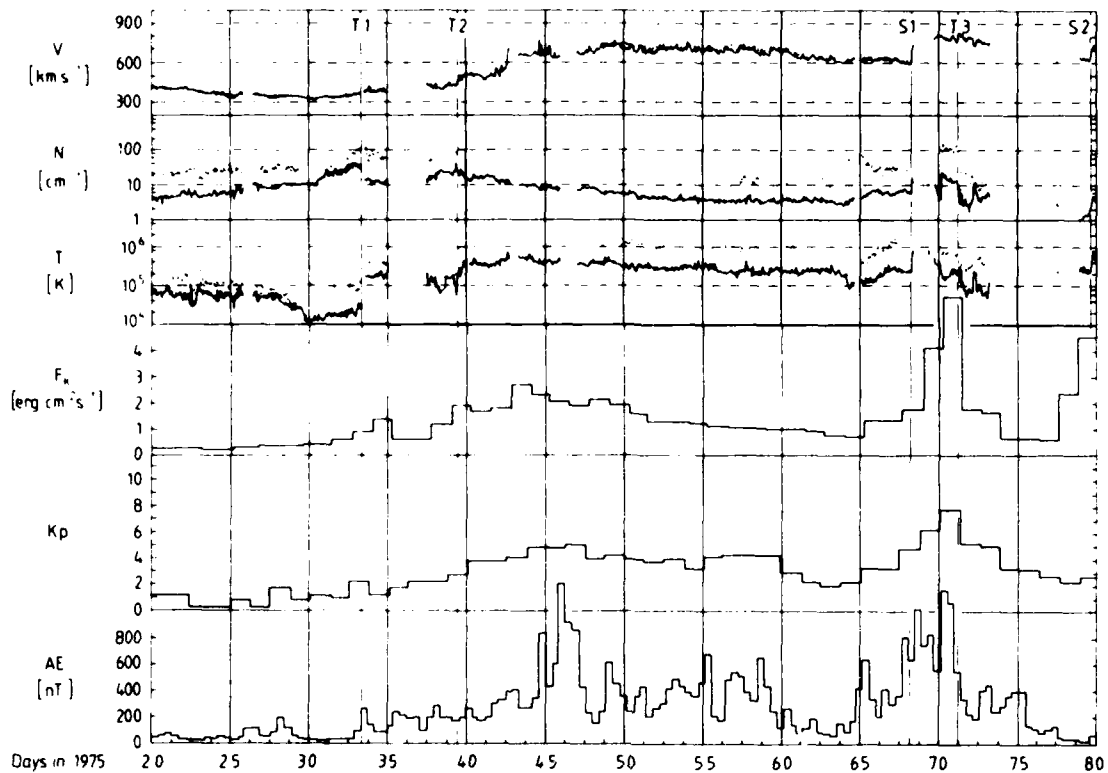


Fig. 4 A detail of the solar wind stream structure from Figure 3, as seen from the IMP 7/8 earth orbiting satellites. These data are plotted as 6 min averages. F_k is the kinetic energy flux density $nv \cdot (1/2 mv^2)$. For comparison, the planetary geomagnetic index K_p and the auroral electrojet index AE are also shown. Since magnetic field data are not available from these satellites the structure of the magnetic field must be inferred from Figure 3.

DISCUSSION AND CONCLUSIONS

In the previous chapters the presently known characteristics of the structured solar wind have been analyzed in some detail in terms of the ballerina model, as well as the features of transients caused by solar activity. From the many trials to correlate interplanetary and geomagnetic activity just a few have been mentioned without too much discussion, mainly in order to illustrate our poor knowledge of the mechanisms involved. The solar wind acts like a huge buffer pushing onto the earth's magnetosphere with a highly variable pressure. Of the energy in the highly variable solar wind reservoir only a tiny fraction is absorbed by the magnetosphere in an obviously very non-stationary way. Theoretical models are still quite controversial. For a long time Dungey's [40] concept of the possible reconnection between interplanetary and terrestrial magnetic field lines favoured by a southward pointing interplanetary field ($B_z < 0$) seemed most promising. It was supported qualitatively by many observed correlations between B_z and geomagnetic indices. However, Alfvén [13] dismisses Dungey's [40] concept of magnetic reconnection as unnecessary and "counterindicated", and introduces his concept of

electric currents driven by the electric field (note the correspondence to the ballerina model!). Alfvén [13] writes: "In fact, what is usually referred to as "bow shock" is a current sheet (as seen from the difference in B on both sides of it). It seems likely that this current connects to the magnetopause current. The tail and magnetopause current systems transfer energy from the solar wind to the magnetosphere. This energy is sufficient ($10^{10} - 10^{11}$ W) to account for all the dissipation in the magnetosphere (Alfvén and Fälthammar [43])."

Perrault and Akasofu [12] estimated the interplanetary energy flux in terms of the Poynting flux $\vec{P} = (\vec{E} \times \vec{B}/4\pi)$. \vec{P} is of the form $v \cdot B^2 \cdot f(\psi, \theta)$, where $f(\psi, \theta)$ is a function of the azimuthal and polar angles between v and B . Empirically they determined an "energy coupling function"

$$\epsilon = v B^2 l_0^2 \sin^4(\theta'/2),$$

where l_0 is a typical linear size of the magnetosphere (taken as 7 earth radii) and θ' is the polar angle between \vec{v} and \vec{B} projected on the yz -plane. It has been demonstrated in several studies (e.g. Akasofu [12], [69], [70]) that ϵ is correlated with the AE index much better than any of the solar wind parameters. In particular the high level of AE in the second phase of recurrent magnetic storms as noted by Bobrov [67] is reasonably well reproduced (Figure 5).

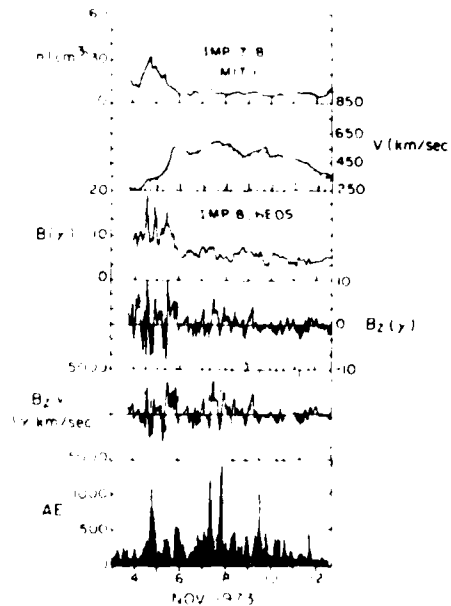


Fig. 5a

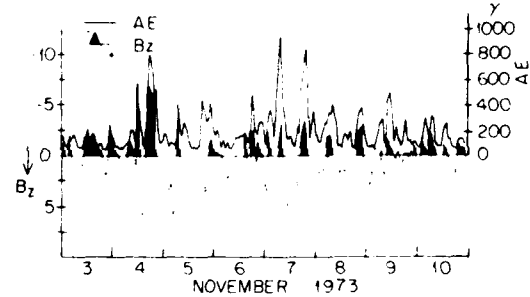


Fig. 5b

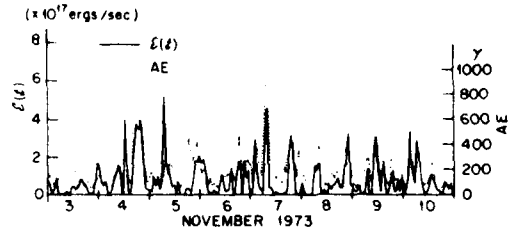


Fig. 5c

Fig. 5 Relations between the interplanetary magnetic field, a corotating stream, and geomagnetic activity for the November 3 - 10, 1973 events. Figures 5a (from Burlaga and Lepping [2]) shows that AE remains elevated during several days during the high speed stream. This is interpreted in terms of fluctuations in $E = v \cdot B$. "These fluctuations occur throughout the stream but are largest in the interaction region, where ambient fluctuations have been compressed." Figures 5b and c (from Akasofu [69]) show the correlation between AE and the "energy coupling function" ϵ .

Based on some geometrical arguments, D'Angelo and Goertz [71] were able to derive a function $f(\gamma, \theta)$ which is very similar to the empirically found $\sin^4(\theta'/2)$ form. In this way ϵ can be interpreted as "that portion of the solar wind electromagnetic power flux which, at any one time, penetrates the magnetosphere."

On the other hand, Perrault and Akasofu [12] find that ϵ can be interpreted as the rate of energy dissipation in terms of the Joule dissipation in the ionosphere, the injection of auroral particles, and finally the injection of the ring current. Akasofu [70] gives a linear relation roughly expressed by $AE(nT) \propto \epsilon (10^7 W)$. This relation is limited to $\epsilon \lesssim 10^{12} W$. For larger values of ϵ the rate of increase of AE decreases. In such cases an abnormal growth of the ring current and the simultaneous development of a large main phase of a magnetospheric storm are observed. Akasofu [70]: "It is of great interest to note that the magnetosphere has such a threshold value." For very low values of ϵ ($\lesssim 10^8 W$), the correlation between ϵ and AE can be further improved by adding some $3 \times 10^8 W$ to ϵ (Rossberg [72]). This amount might represent the minimum fraction of the solar wind kinetic energy entering the magnetosphere continuously and thus maintaining a "ground state" of the magnetosphere.

There is now little doubt that the energy coupling function ϵ may serve as an important tool for correlating geomagnetic phenomena with solar wind properties. D'Angelo and Goertz [71] emphasize the fact that ϵ does not depend on the solar wind density, except implicitly through its weak influence on the magnetospheric radius l . This indicates "that the solar wind electric field may be the primary quantity which determines geomagnetic activity." This conclusion is in general agreement with the ideas of Alfvén [39] [13].

However, one should keep in mind that the parameters v , B and θ' (or B_z) are all interdependent on each other. They vary in some characteristic way according to the underlying solar wind stream structure or, in a very different way, on the nature of the interplanetary transients. Taking all these different features carefully into account one might come to a more detailed understanding of the mechanisms involved in regulating the energy flux from the solar wind into the magnetosphere.

ACKNOWLEDGEMENTS

I am indebted to L. Rossberg for stimulating discussions and to K.-H. Mühlhäuser for skilful processing the data in Figures 3 and 4 and in table 1. The Helios magnetic field data provided to us by F.M. Neubauer (Technische Universität Braunschweig) and the IMP7/8 plasma data provided to us by S.J. Bame (Los Alamos Scientific Laboratory) are gratefully acknowledged. The evaluation of the Helios plasma data was supported by the Bundesministerium für Forschung und Technologie via DFVLR-BPT under grant No WRS 0108.

REFERENCES

- 1 J.M. Wilcox in: Physics of Solar Planetary Environments: Proceedings of the International Symposium on Solar-Terrestrial Physics, vol. 2, edited by D.J. Williams, AGU, Washington, D.C., 1976, p. 947.
- 2 L.F. Burlaga and R.P. Lepping, Planet. Space Sci. **25**, 1151 (1977).
- 3 J. Bartels, Terr. Mag. Atmos. Elec. **37**, 1 (1932).
- 4 C.W. Snyder, M. Neugebauer, and V.R. Rao, J. Geophys. Res. **68**, 6361 (1963).
- 5 G. Noci, Solar Phys. **28**, 403 (1973).
- 6 A.S. Krieger, A.F. Timothy, and E.C. Roelof, Solar Phys. **23**, 123 (1973).
- 7 W.M. Neupert and V. Pizzo, J. Geophys. Res. **79**, 3701 (1974).
- 8 J.B. Zirker, ed., Coronal Holes and High Speed Wind Streams, Colorado Associated University Press, Boulder, 1977.

- 9 N.R. Sheeley Jr., J.W. Harvey, and W.C. Feldman, Solar Phys. 49, 271 (1976).
- 10 N.R. Sheeley Jr., J.R. Asbridge, S.J. Bame, and J.W. Harvey, Solar Phys. 52, 485 (1977).
- 11 J.K. Hargreaves, The Upper Atmosphere and Solar-Terrestrial Relations, Van Nostrand Reinhold Company, New York, 1979.
- 12 P. Perreault and S.I. Akasofu, Geophys. J. R. Astr. Soc. 54, 547 (1978).
- 13 H. Alfvén, Rev. Geophys. Space Phys. 15, 271 (1977).
- 14 M. Schulz, Astrophys. Space Sci. 24, 371 (1973).
- 15 E.J. Smith, B.T. Tsurutani and R.L. Rosenberg, J. Geophys. Res. 83, 717 (1978).
- 16 W.A. Coles and B.J. Rickett, J. Geophys. Res. 81, 4797 (1976).
- 17 J.T. Nolte, A.S. Krieger, A.F. Timothy, R.E. Gold, E.C. Roelof, G. Vaiana, A.J. Lazarus, J.D. Sullivan, and P.S. McIntosh, Solar Phys. 46, 303 (1976).
- 18 R.A. Kopp and T.E. Holzer, Solar Phys. 49, 43 (1976).
- 19 T.E. Holzer, J. Geophys. Res. 82, 23 (1977).
- 20 J. Hollweg, in: Solar Wind 4, to be published in Lecture Notes in Physics, Springer Verlag, Berlin, 1980.
- 21 E. Marsch, K.-H. Mühlhäuser, W. Pilipp, R. Schwenn, and H. Rosenbauer in: Solar Wind 4, to be published in Lecture Notes in Physics, Springer Verlag, Berlin, 1980.
- 22 W.C. Feldman, J.R. Asbridge, S.J. Bame, and M.D. Montgomery, Rev. Geophys. Space Phys. 12, 715 (1974).
- 23 E. Marsch, W.G. Pilipp, R. Schwenn, K.-H. Mühlhäuser, and H. Rosenbauer, in: Solar Wind 4, to be published in Lecture Notes in Physics, Springer Verlag, Berlin, 1980.
- 24 W.C. Feldman, J.R. Asbridge, S.J. Bame, and J.T. Gosling, J. Geophys. Res. 81, 5054 (1976).
- 25 A.J. Hundhausen, Coronal Expansion and Solar Wind, Springer, Berlin Heidelberg New York, 1972.
- 26 H. Rosenbauer, H. Miggenrieder, M. Montgomery, and R. Schwenn, in: Physics of Solar Planetary Environments: Proceedings of the International Symposium on Solar-Terrestrial Physics, vol. 1, edited by D.J. Williams, AGU, Washington, D.C., 1976, p. 319.
- 27 H. Rosenbauer, R. Schwenn, E. Marsch, B. Meyer, H. Miggenrieder, M.D. Montgomery, K.-H. Mühlhäuser, W. Pilipp, W. Voges, and S.M. Zink, J. Geophys. 42, 561 (1977).
- 28 R. Schwenn, K.-H. Mühlhäuser, and H. Rosenbauer in: Solar Wind 4, to be published in Lecture Notes in Physics, Springer Verlag, Berlin, 1980.
- 29 V. Pizzo, J. Geophys. Res. 83, 5563 (1978).
- 30 V. Pizzo, J. Geophys. Res. 85, 727 (1980).
- 31 E.J. Smith and J.H. Wolfe, Geophys. Res. Lett. 3, 137 (1976).
- 32 L.F. Burlaga, R.P. Lepping, R. Weber, T. Armstrong, C. Goodrich, J. Sullivan, D. Gurnett, P. Kellogg, E. Keppler, F. Mariani, F. Neubauer, H. Rosenbauer, and R. Schwenn, J. Geophys. Res. 85, 2227 (1980).
- 33 R. Schwenn, A.K. Richter, and F.M. Neubauer, in: Study of Travelling Interplanetary Phenomena, Reidel, Hingham Mass., to be published, 1980.
- 34 J.T. Gosling, J.R. Asbridge, S.J. Bame, and W.C. Feldman, J. Geophys. Res. 83, 1401 (1978).
- 35 J. Hirshberg and D.S. Colburn, J. Geophys. Res. 78, 3952 (1973).
- 36 R. Shapiro, J. Geophys. Res. 79, 289 (1974).
- 37 J.M. Wilcox, P.H. Scherrer, L. Svalgaard, W.O. Roberts, R.H. Olson, and R.L. Jenne, J. Atmos. Sci. 31, 581 (1974).
- 38 C. Sawyer and M. Haurwitz, J. Geophys. Res. 81, 2435 (1976).
- 39 H. Alfvén, Cosmical Electrodynamics, Oxford Clarendon Press, London, 1950.
- 40 J.W. Dungey, Phys. Rev. Lett. 6, 47 (1961).

- 41 D.H. Fairfield and L.J. Cahill, J. Geophys. Res. 71, 155 (1966).
- 42 G. Rostoker and C.G. Fälthammar, J. Geophys. Res. 72, 5853 (1967).
- 43 H. Alfvén and C.G. Fälthammar, Cosmical Electrodynamics 2, 78 (1971).
- 44 A.J. Dessler and J.A. Fejer, Planet. Space Sci. 11, 505 (1963).
- 45 J.R. Ballif, D.E. Jones, P.J. Coleman Jr., L. Davis, and E.J. Smith, J. Geophys. Res. 72, 4357 (1967).
- 46 H.B. Garrett, A.J. Dessler, and T.W. Hill, J. Geophys. Res. 79, 4603 (1974).
- 47 J.K. Chao, and R.P. Lepping, J. Geophys. Res. 79, 1799 (1974).
- 48 M. Dryer, Space Sci. Rev. 17, 277 (1975).
- 49 S.J. Bame, A.J. Hundhausen, J.R. Asbridge, and I.B. Strong, Phys. Rev. Lett. 20, 393 (1968).
- 50 J. Hirshberg, J.R. Asbridge, and D.E. Robbins, Solar Phys. 8, 313 (1971).
- 51 J.T. Gosling, V. Pizzo, and S.J. Bame, J. Geophys. Res. 78, 2001 (1973).
- 52 M.D. Montgomery, J.R. Asbridge, S.J. Bame, and W.C. Feldman, J. Geophys. Res. 79, 3103 (1974).
- 53 T. Gold, J. Geophys. Res. 64, 1665 (1959).
- 54 S.J. Bame, J.R. Asbridge, W.C. Feldman, E.E. Fenimore, and J.T. Gosling, Solar Phys. 62, 179 (1979).
- 55 L.F. Burlaga, and L. Klein, submitted to J. Geophys. Res. (1980).
- 56 J.T. Gosling, E. Hildner, R.M. MacQueen, R.H. Munro, A.I. Poland, and C.L. Ross, J. Geophys. Res. 79, 4581 (1974).
- 57 E. Hildner, J.T. Gosling, R.T. Hansen, and J.D. Bohlin, Solar Phys. 45, 363 (1975).
- 58 J.T. Gosling, J. Geophys. Res. 82, 5005 (1977).
- 59 R. Schwenn, K.-H. Mühlhäuser, and H. Rosenbauer, Geophys. Res. Lett. 7, 201 (1980).
- 60 S.J. Bame, J.R. Asbridge, W.C. Feldman, and J.T. Gosling, Astrophys. J. 207, 977 (1976).
- 61 K.W. Behannon, F.M. Neubauer, and H. Barnstorff, submitted to J. Geophys. Res. (1980).
- 62 R.L. Rosenberg and P.J. Coleman Jr., J. Geophys. Res. 85, 3021 (1980).
- 63 E.J. Chernovsky, J. Geophys. Res. 71, 965 (1966).
- 64 C.T. Russell, Geophys. Res. Lett. 1, 11 (1974).
- 65 W.G. Pilipp, R. Schwenn, E. Marsch, K.-H. Mühlhäuser, and H. Rosenbauer, in: Solar Wind 4, to be published in Lecture Notes in Physics, Springer Verlag, Berlin, 1980.
- 66 F. Mariani, N.F. Ness, L.F. Burlaga, B. Bavassano, and U. Villante, J. Geophys. Res. 83, 5161 (1978).
- 67 G. Morfill, A.K. Richter, and M. Scholer, J. Geophys. Res. 84, 1505 (1979).
- 68 M.S. Bobrov, Planet. Space Sci. 21, 2139 (1973).
- 69 S.J. Akasofu, Planet. Space Sci. 27, 425 (1979).
- 70 S.J. Akasofu, Planet. Space Sci. 28, 495 (1980).
- 71 N. D'Angelo, and C.K. Goertz, Planet. Space Sci. 27, 1015 (1979).
- 72 L. Rossberg, in: Dynamics of the Magnetosphere, edited by S.J. Akasofu, Reidel, Hingham Mass., 1979, p. 519.

ELECTROMAGNETIC FIELD DISSIPATION AND CORPUSCULAR BOMBARDMENT AND THEIR IMPLICATIONS IN ATMOSPHERIC MODELLING

K.D. Cole

*Division of Theoretical and Space Physics, La Trobe
University, Bundoora, Victoria, Australia 3083*

ABSTRACT

The dissipation of energy of electric fields and currents in the polar auroral atmosphere is a major source of energy for the thermosphere ranging locally up to $100 \text{ ergs cm}^{-2} \text{ sec}^{-1}$ and perhaps more during the most intense disturbance. Globally the input of energy to the thermosphere can often exceed that due to solar EUV radiation. This energy source is always significant in polar regions and its variable strength with respect to that of the solar EUV radiation determines the behaviour of the middle and low latitude thermosphere. It is extremely difficult to model because of its variability in space and time. Nevertheless understanding the dynamics and composition of the global thermosphere is dependent upon incorporation of this source realistically into models. A further important aspect of this energy source is the consequences of its action in changing the density and composition of the thermosphere globally leading to subsequent changes in the absorption of solar EUV radiation. The ring current may also, at times, be a significant source of energy to the low latitude thermosphere.

INTRODUCTION

There is now general agreement that sources of energy other than solar electromagnetic radiation are important to the dynamics and composition of the upper atmosphere [1, 2, 3, 4, 5, 6, 7, 8, 9].

The available sources include (a) dissipation of electric fields and currents [1, 10, 11, 12, 13, 14, 15]; (b) hydromagnetic waves [16]; (c) corpuscular bombardment by electrons, protons, [17], and atoms of hydrogen [18], and oxygen [19]; and (d) heat conduction from the magnetosphere [20, [21]].

In this paper the author wishes not only to stress the direct effects of these energy sources but to draw attention again [22] to consequential effects on the subsequent absorption of solar electromagnetic radiation in an upper atmosphere whose composition has been changed by pre-existing magnetic storms or substorms. It should further be emphasised that these energy sources are important at all times because the geomagnetic field is seldom absolutely "quiet".

Ideally in this problem we would like to solve simultaneously the equation of continuity, momentum, and energy for all species of the atmosphere. Consider first

an atmosphere of one neutral species together with its ions (and equal number of electrons). We have [23]

$$\frac{\delta \rho}{\delta t} + \nabla \cdot (\rho \mathbf{v}) = 0 \quad (1)$$

where ρ , \mathbf{v} = density, velocity respectively of the atmosphere.

$$\frac{dV}{dt} = F + \mathbf{j} \times \mathbf{B} \quad (2)$$

(\mathbf{j} = electric current density, \mathbf{B} - magnetic induction).

$$\mathbf{F} = -\nabla p + \rho g - 2\omega \times \mathbf{v} + \frac{\mu}{3} \nabla \cdot \mathbf{v} + \mu \mathbf{v}^2 \mathbf{v} \quad (3)$$

where p = pressure, \mathbf{g} = acceleration due to gravity, ω = rotation velocity of earth, μ = coefficient of viscosity, $\theta = \nabla \cdot \mathbf{v}$

$$\mathbf{j} = \sigma_0 E_{11} + \sigma_1 E_1 + \sigma_2 \frac{\mathbf{B} \times \mathbf{E}_1}{B} \quad (4)$$

where $\sigma_0, \sigma_1, \sigma_2$ = components of electrical conductivity and E_1, E_{11} = components of electric field (\mathbf{E}) perpendicular and parallel to \mathbf{B} .

$$\mathbf{E} = \mathbf{E}_s + \mathbf{v} \times \mathbf{B} \quad (5)$$

where \mathbf{E}_s = electrostatic field in frame at rest with respect to the earth. Note that the last term in this equation has been misprinted in Cole [23]. It should be as in Cole [1] as it is here. Also [24].

$$\frac{dh}{dt} = \frac{d}{dt} \left(\frac{V^2}{2} + \frac{p}{\rho} + gz + C_v T \right) - \frac{1}{\rho} \frac{\partial p}{\partial t} - \left[\frac{\mu}{3} \nabla \theta + \mu \mathbf{v}^2 \mathbf{v} + \mathbf{j} \times \mathbf{B} \right] \cdot \mathbf{v} \quad (6)$$

$\frac{dh}{dt}$ = rate of heating of unit volume of air from external sources

$$= q_{ph} + q_c + \mathbf{j} \cdot \mathbf{E} - K \nabla^2 T - R_{em} - R_s - R_G - R_{HM} \\ + A_{em} + A_s + A_G + A_{HM} \quad (7)$$

where $K \approx 180 T^{1/2}$ c.g.s. units, is the thermal conductivity of air, R_{em} , R_s , R_G , R_{HM} = the volume rate of emission of electromagnetic radiation, sound (pressure) waves, internal gravity waves, and hydromagnetic waves respectively, and A_{em} , A_s , A_G , A_{HM} , are the volume rates of absorption of electromagnetic waves, sound waves, gravity waves and hydromagnetic waves, q_{ph} , q_c are the rates of heating respectively, from photon and corpuscular sources, viz., energetic electrons, energetic ions and energetic neutral atoms. Also [25]

$$\frac{\partial n_i}{\partial t} = q_i - L_i - \nabla \cdot (n_i v_i) \quad (8)$$

where n_i = ion number density, q_i , L_i = production, loss rate of ions, v_i = ion drift velocity.

In greater generality one could write an equation like (8) for each ion species and for each neutral species for that matter. Given the fact that auroral electric fields and q_c are unpredictably variable in space and time, this means that we can tackle the problem for a short time on a small scale but we must

resort to crude estimations of heating and momentum sources if we are to make progress in understanding their gross effects on the atmosphere.

The problem of the dynamics of the ionised upper atmosphere is clearly a formidable one, much more so than the traditional problem of heating the upper atmosphere by solar photons. In equation (7), q_{ph} means production of heat not only by solar photons but also by photons generated in auroral processes and absorbed in another place. We know that the term $j \cdot E$ can be comparable to and sometimes in excess of heating due to solar photons [1, 23]. It is certainly so at night! An analysis by Cole [25] suggests that in the auroral zones joule heating (i.e. $j \cdot E$) is more important above 100 km altitude than heating by corpuscular bombardment (q_c) because electric fields extend over a greater volume of space than bright auroras which contain high values of q . There is reason also to believe [26] that R_s may be a significant sink of energy.

In order to know the dissipation of energy in the atmosphere from non-solar EUV sources we need continuous measurements of energetic particle spectra, electric fields and currents, winds, temperatures and wave fields all over the thermosphere. This is clearly impossible. The external sources of energy to the thermosphere are q_c , $j \cdot E$, $jxB \cdot V$ and R_{HM} . Of these R_{HM} is the least, and q_c can range up to 300 ergs $\text{cm}^{-2} \text{ sec}^{-1}$ within the narrow confines of bright auroral forms. We do not discuss in detail here all the energy sources and sinks but only those currently considered to be most significant, viz., q_c , $j \cdot E$, and $jxB \cdot V$. Even this discussion is only illustrative and not exhaustive.

CORPUSCULAR BOMBARDMENT

Dalgarno [27] adopted a factor of 1×10^{-3} for the efficiency of conversion of energy of auroral electrons into 3914 \AA° radiation. Rees [28] calculated the altitude profile of emission of 3914 \AA° photons from monoenergetic electron streams and also the penetration depth of monoenergetic electrons into the atmosphere [29]. Such calculations are fundamental to understanding the heating of the atmosphere by energetic electrons. About 1/3 of the energy of energetic electrons interacting with the atmosphere goes to heating the air. Clearly, the energetic electron spectra need to be measured at all times and places before the heating functions appropriate to corpuscular bombardment can be known. This is impossible to achieve, so crude methods of estimating it must be made. According to Dalgarno [27] we may estimate the height integrated recombination heating due to energetic electron streams by $10^{-3}S \text{ ergs cm}^2 \text{ sec}^{-1}$ where S is the number of rayleighs of 3914 \AA° emission. As for the altitude distribution of the heating this would likewise follow the altitude distribution of the 3914 \AA° emission [28] thus $10^{-9}s \text{ ergs cm}^{-3} \text{ sec}^{-1}$ where s is now the number of photons per unit volume emitted per second. There is an approximate ratio of the intensity of emission at 5577 \AA° and 3914 \AA° in auroras [30] of about 2 so that classical observations of the altitude variation of intensity of aurora (in 5577 \AA°) altitude [17] can be used to infer the altitude variation of heating rates. These observations show that for homogeneous arcs the heating per unit volume is greatest in the altitude range 100–120 km suggesting [28] that electrons in the range 2 – 10 kev are dominantly responsible.

AN ($I, \Delta H$) MODEL

Let us compare the recombination heating and joule heating in a model auroral electrojet in which auroras are embedded. Figure 1 represents a meridional cross-section of such a system in which the magnetic field (B) is assumed vertical,

and there are two characteristic regions of east-west auroras of intensity I_1 and I_2 (rayleighs) and width X_1 , X_2 . There is assumed continuity of Pedersen current which, itself, is assumed to be north-south, in the two regions (c.f., [11]).

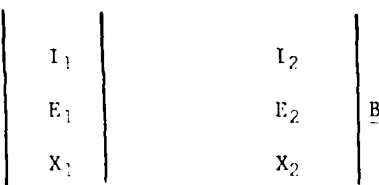


Fig.1 - Model of auroral electrojet

E_1 , E_2 = electric field \perp to B .

$$\text{Now } \Sigma_{P1} E_1 = \Sigma_{P2} E_2 \quad (9)$$

where Σ_p is height-integrated Pedersen conductivity.

The joule heating cm^{-1} of longitude in the meridional section sec^{-1} is given by

$$Q_J = \Sigma_{P1} E_1^2 X_1 + \Sigma_{P2} E_2^2 X_2$$

The particle heating is

$$Q_p = 10^{-3} (I_1 X_1 + I_2 X_2)$$

In practice we are not likely to have all the information regarding E_1 , Σ_{P1} , P_2 , I_1 , I_2 etc. so let us make further simplifying assumptions [11] that the ratio of Hall and Pedersen conductivities is constant throughout the two regions. Then we may relate electric fields to the magnetic disturbance at the ground for a sufficiently broad electrojet. Thus allowing a factor of 50% for induction in the earth

$$\Delta H = 6\pi \Sigma_{H2} E_2 = 6\pi \Sigma_{H1} E_1$$

$$\text{Then } Q_J = \frac{(\Delta H)^2}{(6\pi)^2} \left(\frac{\Sigma_{P1}}{\Sigma_{H1}} \right) \left(\frac{X_1}{\Sigma_{H1}} + \frac{X_2}{\Sigma_{H2}} \right) \text{ ergs cm}^{-1} \text{ sec}^{-1}$$

$$\text{and } Q_p = 10^{-3} I_1 X_1 \left(1 + \frac{I_2 X_2}{I_1 X_1} \right) \text{ ergs cm}^{-1} \text{ sec}^{-1}$$

Another way of expressing Q_p is that about 1/3 of the total energy flux of auroral electrons goes into heating. Observations suggest that the auroral electrojet occupies a much wider latitude range than do bright auroras. Let us assume that $I_2 X_2 \approx I_1 X_1$ i.e. that particle energy flux into bright auroras \approx particle energy flux into other regions. Then approximately

$$\frac{Q_J}{Q_p} \approx \frac{500 (\Delta H)^2}{(6\pi)^2} \frac{\Sigma_{P1}}{\Sigma_{H1}} \cdot \frac{X_2}{I_1 X_1} \cdot \frac{1}{\Sigma_{H2}}$$

In Table 1 we show the ratio of Q_J to Q_p for a range of values of ΔH and I_1 (in Rayleighs) assuming the electron density in the E region in region 2 is 10^4 cm^{-3} and $X_2/X_1 \approx 10$. The table shows that for likely values of ΔH and I_1 , Q_J is likely

to be greater than Q_p . This model is not meant to account for all situations of interest but is illustrative of one commonly occurring condition as during a negative magnetic bay.

$\frac{\Delta H}{I_1(R)}$	10	100	1000	2000
10^{-4}	• 3	30		
10^{-5}		3	300	
10^{-6}		• 3	30	
10^{-7}			3	300

On account of the fact that the $j \times B$ tends to accelerate the atmosphere up to the velocity $E_x B / B^2$ (in the absence of other forces) viscous damping becomes important (see e.g. the model of Wu and Cole [31]).

Another situation which is different is that in which solely dynamo action in the ionosphere is the driving force. This may occur, for example, in the positive bay which frequently follows negative bays (see [10] p.746). There need to be many experimental studies of joule heating and wind fields in a variety of conditions e.g. negative bays, positive bays (day and night), the Harang discontinuity, the polar cusp (sunlit and not). Each needs to be "calibrated" to find empirical relationships between globally measurable parameters e.g. ΔH and the heating.

THEORETICAL ESTIMATES OF HEATING

Numerous theoretical estimates of joule heating by ionospheric currents have appeared in the literature [1, 2, 3, 4, 5, 6, 7, 13]. Commonly it is of order of tens of ergs $\text{cm}^{-2} \text{ sec}^{-1}$. Even at "quiet" times this source of energy may be necessary to account for the dynamics of the thermosphere. Certainly during magnetic storms as much energy may come to the thermosphere from the solar wind as does from the solar EUV.

EFFECTS OF THE HEATING

Electric fields applied to the thermosphere by the solar wind tend to accelerate the neutral atmosphere up to the speed $E_x B / B^2$ in the absence of other forces [1, 23]. Joule [1] and viscous [31] heating take place in approximately equal amounts in some situations. New gradients of pressure build up in the thermosphere which were initially detected by Jacchia [32]. New wind systems are created together with changes in the composition of the thermosphere [33]. The increased heating of the thermosphere raises its temperature also and in localised regions of the auroral zone gives rise to increased loss of helium by the atmosphere.

EXPERIMENTAL STUDIES

Many experimental works leading to estimates of joule heating have now been done employing the Chatanika incoherent radar system [34, 35, 36]; the Scandinavian twin auroral radar [38]. There need to be simultaneous measurements or estimations of currents and electric fields and wind velocities, or simultaneous measurement of ion densities and relative drifts of ions and neutrals in a variety of auroral/magnetic/ionospheric conditions.

An ever present difficulty in relating theory to experiment is the fact that specially in the auroral ionosphere the behaviour of the ionosphere and atmosphere at one place at one instant of time may often be dependent upon conditions at other times and places for which observations are lacking. Only a global observational attack on the dynamics of the auroral thermosphere will produce understanding of its complexities which are hinted at in this review.

EFFECT OF THE MAGNETOSPHERIC RING CURRENT

The ring current decays by charge-exchange [38] and by heat conduction to the ionosphere [20]. Charge-exchange results in the bombardment of the equatorial thermosphere by energetic neutral hydrogen atoms and may constitute an important source of energy for this region in the recovery phase of a magnetic storm [18]. Heat conduction from the ring current leads to an elevation of electron temperatures in the ionosphere but heats the thermosphere very little [20].

CONCLUSION

There is no doubt that the deposition of energy into the polar ionosphere as the result of the action of the solar wind interaction with the magnetosphere is most significant. New wind systems, changes in composition and structure of the thermosphere and ionosphere are produced by it. The change in composition produced by upwelling of gas at the auroral zones and its transport to low latitudes can alter the absorption rates of solar EUV on subsequent days [22]. This post-magnetic disturbance effect deserves more investigation.

In studying mid-latitude effects of the deposition of energy in the auroral zone, one should bear in mind the great asymmetries of the longitude variation of distance of the auroral zone from any particular geographic or magnetic invariant curve [39].

To make significant progress in the field we need to combine observations of many kinds, e.g., (i) global monitoring of the aurora; (ii) global monitoring of magnetic variations; (iii) satellite monitoring of energetic particle precipitation; (iv) "calibration" of the heating rates in various magnetic and auroral situations.

REFERENCES

1. K.D. Cole, Aust. J. Phys. **15**, 223 (1962)
2. J.M. Strauss, S.D. Creekmore, R.M. Harris and B.K. Ching, J. Atmos. Terr. Phys. **37**, 1545 (1975)
3. J.M. Strauss, Rev. Geophys. Space Phys. **16**, 183 (1978)
4. H.G. Mayr and H. Volland, J. Geophys. Res. **78**, 2251 (1973)
5. A.D. Richmond, J. Geophys. Res. **84**, 5259 (1979)
6. S-C. Chang, S.T. Wu and R.E. Smith, J. Atmos. Terr. Phys. **36**, 889 (1974)
7. R.E. Dickenson, E.C. Ridley and R.G. Roble, J. Atmos. Sci. **32**, 1737 (1965)
8. H.G. Mayr, I. Harris and N.W. Spencer, Rev. Geophys. Space Phys. **16**, 539 (1978)
9. G.W. Prölss, Rev. Geophys. Space Phys. **18**, 183 (1980)
10. K.D. Cole, Space Sci. Revs. **5**, 699 (1966)
11. K.D. Cole, Planet Space Sci. **19**, 59 (1971a)
12. K.D. Cole, J. Atmos. Terr. Phys. **19**, 59 (1971b)
13. J.A. Fedder and P.M. Banks, J. Geophys. Res. **77**, 2328 (1965)
14. M.G. Heaps and L.R. Megill, J. Geophys. Res. **80**, 1829 (1975)
15. M.H. Rees and J.C.G. Walker, Ann de Geophys. **24**, 193 (1968)
16. A.J. Dessler, J. Geophys. Res. **64**, 397 (1959)

17. J.W. Chamberlain, Physics of the Aurora and Airglow, Academic Press, N.Y.
(1961)
18. B.A. Tinsley, J. Geophys. Res. 84, 1855 (1979)
19. M.R. Torr, M.C.G. Walker and D.C. Torr, J. Geophys. Res. 79, 5267 (1974)
20. K.D. Cole, J. Geophys. Res. 69, 3595 (1965)
21. M.H. Rees and R.G. Roble, Rev. Geophys. Space Res. 13, 201 (1975)
22. K.D. Cole, Dynamical and Chemical Coupling, B. Grandal and J.A. Holtet eds.,
D. Reidel Pub. Coy, Dordrecht, Holland (1977)
23. K.D. Cole, J. Atmos. Terr. Phys. 37, 939 (1975)
24. S.L. Hess, Introduction to Theoretical Meteorology, Holt Rinehart and Winston,
New York, 1959
25. K.D. Cole, Planet Space Sci. 11, 779 (1963)
26. C.R. Wilson, R.D. Hansucker and G.J. Romich, Planet Space Sci. 24, 1155 (1976)
27. A. Dalgarno, Ann. de Geophys. 20, 65 (1964)
28. M.H. Rees, Planet Space Sci. 11, 1209 (1963)
29. M.H. Rees, Planet Space Sci. 12, 722 (1964)
30. R.J.R. Judge, Planet Space Sci. 2081 (1972)
31. S.T. Wu and K.D. Cole, Planet Space Sci. 24, 727 (1976)
32. L.G. Jacchia, Nature, 183, 526 (1959)
33. H. Trinks, S. Chandra, N.W. Spencer and U. von Zahn, J. Geophys. Res. 81,
5913, (1976)
34. P.M. Banks, J. Atmos. Terr. Phys. 39, 179 (1977)
35. A. Brekke and C.L. Rino, J. Geophys. Res. 83, 2517 (1978)
36. V. Wickwar, M.J. Baron and R.D. Sears, J. Geophys. Res. 80, 4364 (1975)
37. R.A. Greenwald, T.A. Potemra and N.A. Saflekos, J. Geophys. Res. 85, 563 (1980)
38. A.J. Dessler and E.N. Parker, J. Geophys. Res. 64, 2239, (1964)
39. K.D. Cole and P.B. Williams, abstract, IAGA Bulletin No. 43 - to be
submitted for publication (1980)

PARTICLE AND JOULE HEATING OF THE NEUTRAL POLAR THERMOSPHERE IN CUSP REGION USING ATMOSPHERE EXPLORER-C SATELLITE MEASUREMENTS

M. Griffis,¹ J.S. Nisbet¹ and E. Bleuler²

¹ *Ionosphere Research Laboratory; 2 Department of Physics,*
Pennsylvania State University, University Park, PA 16802,
USA

ABSTRACT

Simultaneous measurements taken by instruments on the Atmosphere Explorer - C satellite were used to compare electron and proton particle energy deposition, Joule heating, and neutral density perturbations in the region of the cusp.

Altitude profiles of Joule heating, electron energy deposition, and electron density are derived using measurements taken by the satellite as input to a computer model. Electric fields are calculated using ion drift measurements. Figures are presented for a representative orbital pass.

A peak Joule heating rate of 0.059 Wm^{-2} occurred in the cusp region with a peak of 0.025 Wm^{-2} in the evening auroral electrojet. Peak volume heating rates corresponding to these regions were $1.4 \times 10^{-6} \text{ Wm}^{-3}$ and $7.10^{-7} \text{ Wm}^{-3}$, both occurring at an altitude of 115 km. Particle energy deposition was about an order of magnitude less than Joule heating. Large neutral density perturbations are related to regions of heating.

INTRODUCTION

Thermospheric heating in the auroral zone and polar cap is of great importance to the variations in the high latitude neutral wind and the resulting global temperature and densities. Large horizontal gradients are seen in the densities of nitrogen, argon, atomic oxygen and helium that are correlated with magnetic activity. It was desired to relate in as quantitative manner as possible the energy inputs from the Joule heating and particle inputs with the thermospheric responses. The AE-C satellite provides all the necessary data for such a study and the present paper will discuss some of the results of these analyses in the cusp region and in the region of the eastward auroral electrojet.

The data used in this paper was measured by the Atmosphere Explorer C satellite which was launched late in December of 1973 into an eccentric orbit inclined 68° with respect to the equatorial plane. The orbit was circularized in late 1974 and data presented here is from circular orbits of late December 1974.

METHOD OF ANALYSES

For estimation of the current systems and the Joule heating, it was first necessary to calculate the electric field. The electric field vectors used in this study were derived from measurements made by the retarding potential analyzer system of Hanson et al. [1] on the Atmosphere Explorer - C (AE-C) satellite. This system uses measurements from two planar retarding potential analyzers to obtain three dimensional ion drift velocity vectors. One sensor head supplies information on ion energies and species, from which the ion velocity perpendicular to the collector head can be derived. The second sensor has a segmented collector and gives information on direction of arrival, which, when combined with the velocity derived from the first instrument, supplies velocities in two orthogonal directions in the plane of the analyzer. Corotation of the atmosphere and an assumed cross cap wind of 100 meters per second directed from 1300 hrs. to 0100 hrs. MLT were subtracted from these measured drifts to get ion drifts relative to the neutral atmosphere.

The electric fields were obtained from the ion drift velocities by assuming that at the satellite altitude ion drift is due solely to $\vec{E} \times \vec{B}$ plasma drift:

$$\vec{E}(V/m) = \vec{B}(T) \times \vec{v}(m/sec)$$

The electric fields derived from ion drift velocities at the satellite altitude were assumed to be constant with altitude.

Electron and proton energy spectra were obtained from telemetry data supplied by the Low Energy Electron Experiment on AE-C of Hoffman et al. [2]. This experiment consisted of three detectors: two measuring electron and ion fluxes from 0.2 to 25 keV in 16 logarithmically spaced steps, and one to continuously measure 5 keV electrons. The detectors consist of cylindrical electrostatic energy analyzers with spiraltron electron multiplier sensors. Spectra are obtained from telemetry data by taking into account the geometric factor range of energy acceptance, counting efficiency and accumulation time for each of the 16 energy steps. The system takes one 16 point spectrum per second. The instrument does not measure the spatial distribution in the despun mode and spatial isotropy has been assumed.

Electron spectra taken from the Low Energy Electron Experiment are used as input to a computer program which calculates energy deposition and electron production due to these energetic electrons as a function of altitude in the ionosphere below the satellite. This program is derived from the program TANGLE of Vondrak [3] which uses a technique proposed by Rees [4]. The program calculates $q(z,E)$, the ionization rate per unit volume at altitude z due to electrons of energy E incident on the atmosphere above as:

$$q(z,E) = F(E) \frac{E \rho \lambda(x/R)}{\Delta E_{ion} R}$$

where $F(E)$ is the flux per unit area per unit energy of electrons of energy E incident on the atmosphere, ΔE_{ion} is the average energy per ionization, ρ the mass density at z , R the range in mass per unit area which the electrons penetrate, and λ a function of mass penetrated (x) divided by R , which gives the fraction of E deposited in a given layer. The program uses the MSIS atmospheric model to get ρ and x at each altitude. The function $q(z,E)$ is numerically integrated over E to get the production $Q(z)$ as a function of altitude. These production rates are then combined with EUV production in a modification of the Penn State Mark I ionospheric model of Nisbet [5]. The neutral densities have been revised by using the MSIS neutral density model above 120 km and then the Groves [6] model below

120 km. Photoabsorption cross sections of Kirby et al. [7], as modified by Hinteregger [8] and solar EVU intensities given by Hinteregger [8] were used.

RESULTS

Figure 1 shows the electric fields for an orbit on December 24, 1974 that passed just equatorward of the afternoon sector of the main cusp region at the point marked C and across the region of the eastward electrojet at the point marked E. The electron energy flux and the electric field strengths are shown in Figure 2. The regions of high energy flux which correspond to regions of enhanced electron density and Pedersen conductivity are much narrower than the regions of enhanced electric field. Figure 3 shows the electron density contours as a function of height along the satellite orbit calculated from the model using the measured particle flux spectra. Large electron density enhancements down to 100 km are seen in the cusp region and the electrojet region. Combining the measured electric fields with the Pedersen conductivity calculated from the electron density distribution gives Joule heating. This is shown in Figure 4 compared with the direct energy input from protons and electrons. It can be seen that the peak energy in the region of the cusp traversed is 59 mWm^{-2} and in the evening electrojet region is 25 mWm^{-2} . Because of the localized nature of the cusp, it is difficult to tell if the satellite is in fact traversing the regions of maximum energy input and in this case, it is suspected that energies would be greater poleward of the satellite. It is apparent that the Joule heating exceeds the direct particle heating by more than an order of magnitude in the cusp region and nearly an order of magnitude in the region of the electrojet. The altitude profile of the Joule energy deposition is shown in Figure 5. The neutral densities for this orbit are measured by the satellite as shown in Figure 6. It can be seen that very large density perturbations are related to the regions of heating. In each case the atomic oxygen and helium densities which are sensitive to vertical motion in the heated region are observed to decrease and the argon density which is more sensitive to the scale height in the heated region increases. Care should be taken in attempts to correlate the density perturbations with the heated regions because of the time delay involved between the heating and the time the density changes are seen at satellite altitudes. This causes the densities to be sensitive to the effects of heating that occurred in that geographic region over a period of the order of 12 hours.

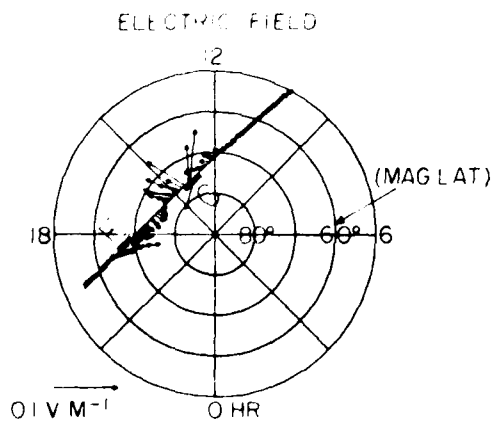


Fig. 1 AE-C orbit 4708 in magnetic coordinates showing electric fields derived from ion drift measurements. Cusp region and auroral electrojet are marked by C and E.

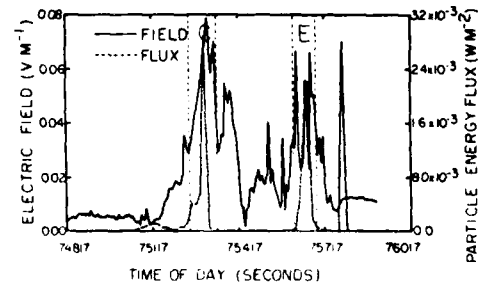


Fig. 2 Electric field strength and particle energy flux measured by the low energy electron experiment for AE-C orbit 4708. Cusp and electrojet regions shown in Fig. 1 are marked by C and E. No attempt is made to interpret the large flux peak near 75780 seconds which is based on a single 15-second average.

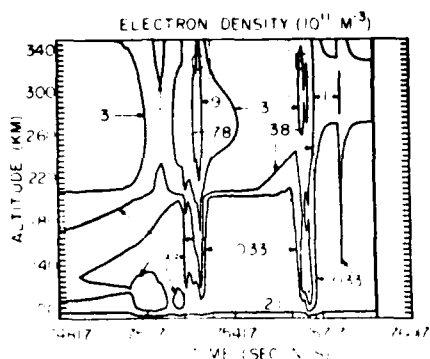


Fig.3 Electron density contours

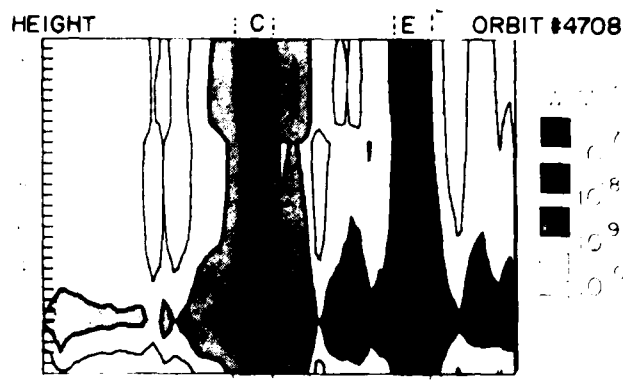


Fig.5 Joule heating contours.

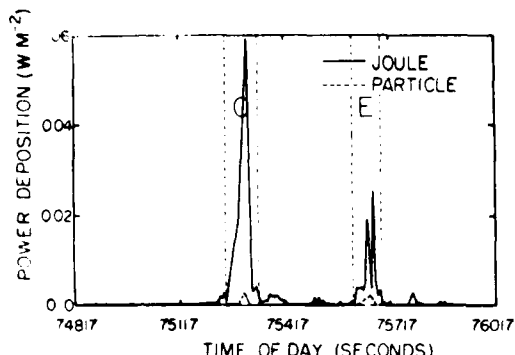
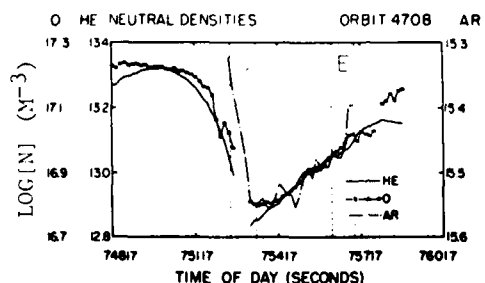


Fig.4 Height integrated Joule heating and particle energy flux.

Fig.6 Log of neutral densities vs. time. He reduced to 300 km, O and Ar reduced to 120 km using N₂ densities and assuming diffusive equilibrium.

Based on the limited number of passes examined so far, it appears that the power deposited by Joule heating in the electrojets is related to the auroral electrojet indices given in nT by the following relation:

$$\begin{aligned} \text{Morning Sector; Peak Power} &\sim 10^{-4} |AL| \text{ Wm}^{-2}; \text{ Average Power} \sim 4 \times 10^{-5} |AL| \text{ Wm}^{-2} \\ \text{Evening Sector; Peak Power} &\sim 1.5 \times 10^{-4} \text{ AU Wm}^{-2}; \text{ Average Power} \sim 6 \times 10^{-5} \text{ AU Wm}^{-2} \end{aligned}$$

ACKNOWLEDGEMENTS: The authors wish to thank W. Hanson, R. Heelis and R. Power for the ion drift data, R. Hoffman for the electron spectra, A. Nier for fifteen second averages of the neutral densities and the entire AE team for many helpful discussions. This research was supported by NASA grants NSG-5212 and NGL-39-009-003.

REFERENCES

1. W. B. Hanson, D. R. Zuccaro, C. R. Lippincott and S. Sanatani, *Radio Science* 8, 333 (1973).
2. R. A. Hoffman, J. L. Burch, R. W. Janetzke, V. F. McChesney, S. H. Way and D. S. Evans, *Radio Science* 8, 393 (1973).
3. R. Vondrak, O. de la Beaujardiere and R. Hoffman, presented at *Atmosphere Explorer Symposium II*, (1978).
4. M. H. Rees, *Planet. Space Sci.* 11, 1209 (1963).
5. J. S. Nisbet, *Radio Science* 6, 437 (1971).
6. G. V. Groves, *COSPAR International Reference Atmosphere 1972*, (1972).
7. K. Kirby, E. R. Constantinides, S. Babeu, M. Oppenheimer and G. A. Victor, *Atomic Data and Nuclear Data Tables* 23, 63 (1979).
8. H. E. Hinteregger, presented at the *Atmosphere Explorer Symposium* (1980).

THERMOSPHERIC SIGNATURE OF MAGNETOSPHERIC ENERGY DISSIPATION

G.W. Prölls

*Institut für Astrophysik und Extraterrestrische Forschung,
Universität Bonn, Auf dem Hügel 71, 5300 Bonn, FRG*

ABSTRACT

Dissipation of magnetospheric energy leads to an upper atmospheric disturbance zone whose extent varies with local time. A statistical analysis of ESRO 4 data reveals that (1) in the afternoon/evening sector the boundary location is determined by the region of electric current dissipation along the auroral oval; (2) in the midnight/early morning sector dynamical effects extend the disturbance zone to lower latitudes; and (3) in the late morning sector direct heating effects are superimposed on the residuals of the early morning disturbance.

INTRODUCTION

There are two principle modes by which solar energy is brought into the earth's upper atmosphere: (1) direct dissipation of solar radiation energy; (2) indirect injection of solar wind kinetic energy via the magnetosphere. Whereas the first mode has long been recognized to be the dominant one, the significance of the solar wind/magnetospheric energy source is more and more appreciated. This study is concerned with the imprint the solar wind energy dissipation leaves in the upper atmosphere. Specifically, the latitudinal structure and extension of the thermospheric disturbance zone generated by the magnetospheric energy source is investigated using density data obtained by the polar orbiting satellite ESRO 4 [1].

DATA ANALYSIS AND RESULTS

The basic latitudinal structure of a thermospheric perturbation observed on a winter afternoon during weakly disturbed conditions is illustrated in Fig. 1. Relative variations in the molecular nitrogen density, in the atomic oxygen density, and in the helium density as measured above the Asian continent are plotted. The density data have been adjusted to a common altitude of 260 km using standard hydrostatic techniques. In addition they have been normalized to suitable density values observed outside the disturbance region (e.g. $R_O = ([O]_{260 \text{ km}})_{\text{observed}} / ([O]_{260 \text{ km}})_{\text{standard}}$ value, with $R_O = 1$ serving as a reference value). Note that whereas molecular nitrogen is plotted on a linear scale, the oxygen and helium data are presented using a logarithmic scale. For comparison, the upper panel also shows the exospheric temperature inferred from the nitrogen data.

The essential feature illustrated in Fig. 1 is a localized disturbance zone at high invariant latitudes. It is characterized by a fairly abrupt increase in the nitrogen

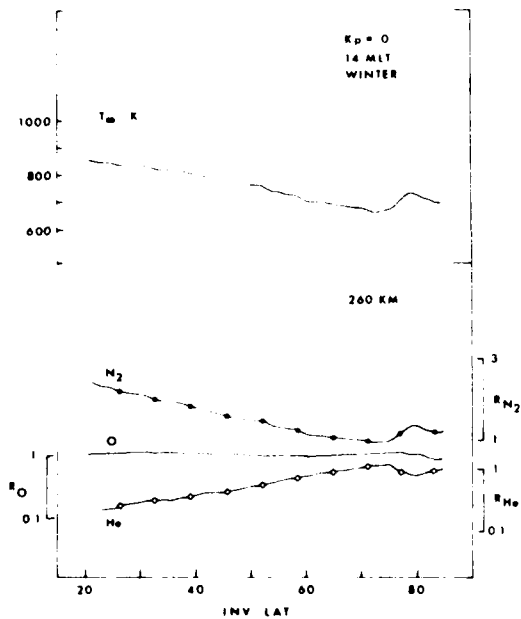


Fig. 1 Latitudinal structure of atmospheric perturbation in the afternoon sector during winter conditions.

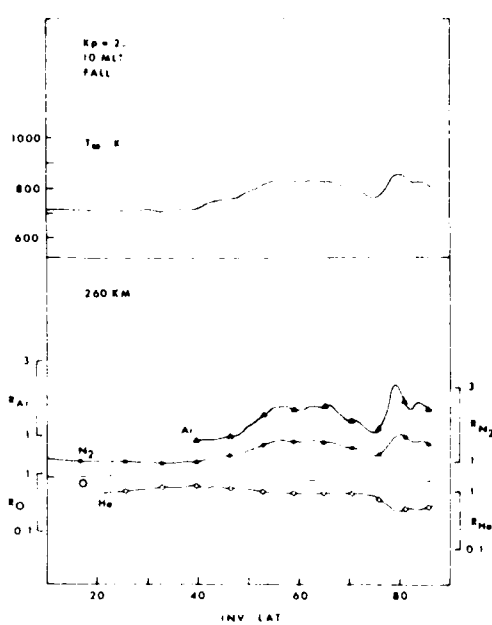


Fig. 2 Latitudinal structure of atmospheric perturbation in the forenoon sector during equinox conditions.

density (and accordingly in the inferred gas temperature), a small decrease in the oxygen density, and a significant V-shaped drop in the helium density. Theoretical studies [2, 3, 4] indicate that these features are the typical thermospheric signature of energy deposition in the lower thermosphere. The most effective energy source at these heights and latitudes are Pedersen currents which heat the ambient neutral gas through Joule dissipation [e.g. 5, 6]. Whereas it is difficult to measure the Pedersen currents (I_p) directly, a sizeable set of data is available on the magnetic signature of Birkeland currents (I_B) which close the current circuit in the magnetosphere. Therefore, to support our interpretation the location of the equatorward portion of the field-aligned currents (= region 2 currents [7]) has been compared to the location of the equatorward boundary of the atmospheric disturbance zone. Figure 3 demonstrates that in the afternoon local time sector (14–16 MLT) and during moderately disturbed conditions ($AE \leq 300\text{ nT}$, $K_p < 4$) both boundaries are approximately collocated. Furthermore, it can be shown that these atmospheric perturbations are always associated with the trapping boundary of 44 keV electrons [8] and, therefore, also with field-aligned currents [9]. We conclude that localized atmospheric disturbances observed at high latitudes are a direct signature of electric field and current dissipation by the magnetospheric energy source.

A very different situation is encountered in the early morning sector where the disturbance boundary is located at middle latitudes and far beyond the electric current dissipation region (Fig. 3). It is suggested that the broad disturbance zone observed at these times is generated by strong winds blowing away from the polar regions and carrying along heated air of perturbed composition. This interpretation is supported by theoretical predictions [e.g. 10] and also by recent measurements which establish the existence of strong equatorward directed winds commencing around midnight [11, 12]. This "midnight surge" is a transient phenomenon lasting a few hours; the disturbance it generates in the mid-latitude thermosphere, however,

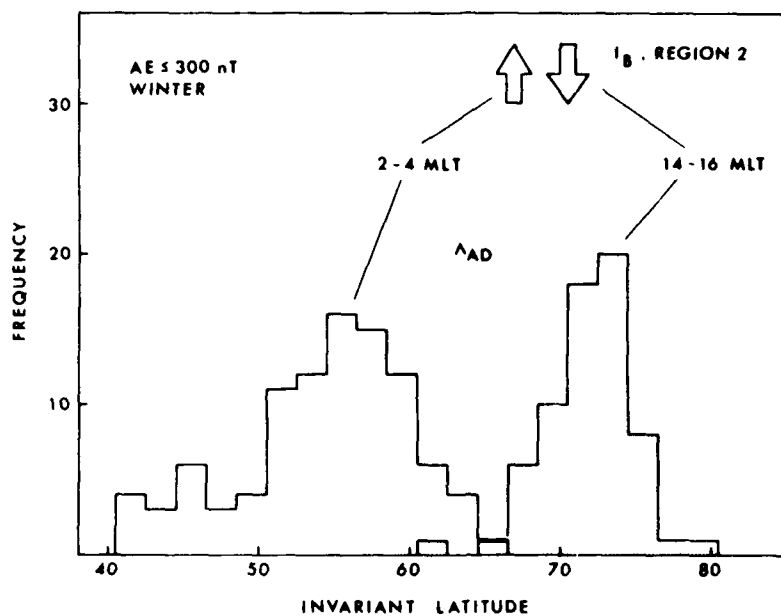


Fig. 3 Distribution of the equatorward boundary of the atmospheric disturbance zone in two different local time sectors during winter conditions. The location of the equatorward portion (Region 2) of Birkeland currents is also shown for comparison [7].

recovers much more slowly, and residuals of it can be clearly seen in the late morning sector. This is illustrated in Fig. 2, which shows the basic latitudinal structure of a thermospheric perturbation in the forenoon local time sector. Here the broad zone of enhanced nitrogen and argon densities and slightly decreased oxygen and helium densities extending all the way to middle latitudes is identified with the residuals of the midnight surge perturbation. In contrast the strong localized disturbance observed at high latitudes is again directly attributed to the dissipation of electric currents in this region. These ideas are summarized schematically in Fig. 4.

CONCLUSIONS

From this model a number of important conclusions can be drawn. For example, even during relatively quiet conditions there should be a continuous energy transfer from the polar to the mid-latitude region in the early morning sector; therefore, the energy budget of this region is not only controlled by EUV radiation but in addition by the dissipation of solar wind energy [13]. Also, the strong local time asymmetry in the observed wind and perturbation structure makes it necessary to revise the currently available models of atmospheric dynamics both during quiet and disturbed conditions. Finally, we note that whereas ionospheric data are consistent with our model [14], explanations of ionospheric storm effects based on large scale wind circulations during daytime hours are not.

ACKNOWLEDGMENTS

I am very grateful to U. von Zahn, who provided all the neutral composition data (ESRO 4 gas analyzer experiment) used in this study. Thanks are also due to M. Roemer

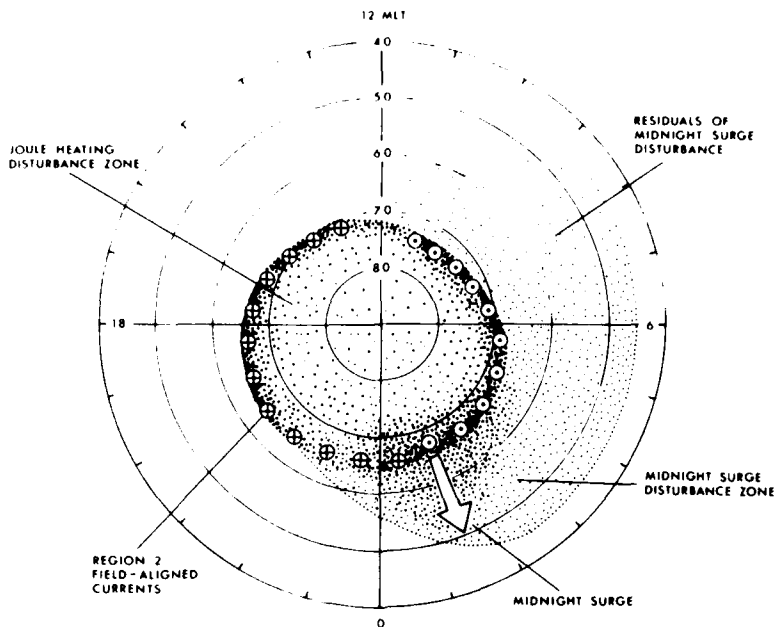


Fig. 4 Phenomenological model explaining the observed latitudinal structure of atmospheric perturbations.

for his continuous support. This research was financed by the Deutsche Forschungsgemeinschaft under grant Ro 446/3.

REFERENCES

1. U. von Zahn, in: Atmospheres of Earth and the Planets, D. Reidel Publishing Company, Dordrecht, Holland, 1975, p. 133.
2. T. Shimazaki, Space Research XII, 1039 (1972).
3. H.G. Mayr and H. Volland, Planet. Space Sci. **20**, 379 (1972).
4. P.B. Hays, R.A. Jones, and M.H. Rees, Planet. Space Sci. **21**, 559 (1973).
5. K.D. Cole, J. Atmos. Terr. Phys. **37**, 939 (1975).
6. H. Volland, J. Atmos. Terr. Phys. **41**, 853 (1979).
7. T. Iijima and T.A. Potemra, J. Geophys. Res. **81**, 2165 (1976).
8. W.J. Raitt, U. von Zahn, and P. Christphersen, J. Geophys. Res. **80**, 2277 (1975).
9. I.B. McDiarmid, J.R. Burrows, and D. Wilson, J. Geophys. Res. **84**, 1431 (1979).
10. P.M. Banks, J. Atmos. Terr. Phys. **39**, 179 (1977).
11. H.F. Bates and T.D. Roberts, J. Atmos. Terr. Phys. **39**, 87 (1977).
12. R.R. Babcock Jr. and J.V. Evans, J. Geophys. Res. **84**, 5349 (1979).
13. D.A. Glenar, E. Bleuler, and J.S. Nisbet, J. Geophys. Res. **83**, 5550 (1978).
14. G.W. Prölss, Rev. Geophys. Space Phys. **18**, 183 (1980).

A MODEL FOR PROTON INTERACTION IN THE ATMOSPHERE INCLUDING FLUXES OF GENERATED ELECTRONS

H. Karszenbaum and D.A. Gagliardini

*Consejo Nacional de Investigaciones Científicas y Técnicas,
Centro Argentino de Estudios de Radiocomunicaciones y
Compatibilidad Electromagnética, Julián Alvarez 1218, 1414
Buenos Aires, Argentina*

ABSTRACT

In this paper we analyse from a new point of view the energy deposition due to precipitated protons when they interact with the atmospheric components. The method described presents a different way of calculating the proton interaction and allows us to obtain the production rate and fluxes of the generated electrons as function of height and energy. Also the model gives the possibility of estimating independently the effects of protons and resulting secondary and tertiary electrons in protons events.

INTRODUCTION

An extensive description of the way protons interact with the atmosphere has been published by Eather [1], [2]. More recent calculations presented by Edgar et al. [3], [4], Sun [5], Singh et al. [6] show the inclusion of new cross section data that can describe quite accurately ionization and excitation processes. All these publications give a detailed description of the behaviour of protons when they penetrate in the atmosphere showing that precipitated energetic particles are the major cause of light emission and enhanced ionization processes. The conclusions emphasize the relevance of secondary electrons in the ion production rate with their contributions being implicitly included in total ionization curves. Several authors [2], [3], [4], [6] also show the energy distribution of secondary electrons created in the total trajectory of the protons, but none of them show the fraction of ionization and energy spectra as a function of altitude resulting from secondary electrons.

It is the purpose of this paper to present a different approach to the problem which allows us to calculate proton ionization, the ionization produced by the generated secondary electrons and the corresponding fluxes as function of height and energy.

PROTON IONIZATION AND ELECTRON FLUXES

The basic processes that a proton beam can undergo in its interaction with the atmospheric components are well known. An incoming proton loses energy primarily by ionization, excitation, electron capture collisions and "stripping" [3], [4]. Therefore, if a proton beam interacts with the atmospheric components, by the

effect of the charge-changing collisions a mixed flux of proton and H atoms is generated, in which the fractional composition is a function of energy. In an equilibrium state the corresponding fractions are given by:

$$F_H = \frac{\sigma_{01}}{\sigma_{01} + \sigma_{10}} \quad \text{and} \quad F_P = \frac{\sigma_{10}}{\sigma_{01} + \sigma_{10}}$$

where 0 and 1 denote the charge state, and σ_{01} is the cross section for stripping and σ_{10} the cross section for capture [7].

The rate of production of ions of species i at height Z by protons and hydrogen atoms of energy E is given by:

$$q_i(E, Z) = \Phi(E, Z) N_i(Z) (\sigma_{I,i}^P(E) F_P(E) + \sigma_{I,i}^H(E) F_H(E)) \quad (1)$$

where $\sigma_{I,i}^P$ and $\sigma_{I,i}^H$ are the ionization cross sections of constituent i by protons and H atoms as described by Green and McNeal [7] and Edgar et al. [3], [4], $N_i(Z)$ is the number density of neutral species i at height Z, and $\Phi(E, Z)$ is the flux of protons and H atoms. For the proton energy variation we follow Banks and Kockarts [8]. We must also consider the contribution from charge exchange processes [9], that is

$$q_{i,10}(E, Z) = \Phi(E, Z) N_i(Z) F_P(E) \sigma_{i,10}^P(E) \quad (2)$$

Therefore the total number of ions for a constituent i will be:

$$q_i(E, Z) = q_{i,I}(E, Z) + q_{i,10}(E, Z) \quad (3)$$

To obtain the ion production in the case of an incident monoenergetic isotropic flux, expression (3) must be integrated over the solid angle, and in the case of a differential flux must be also integrated over the flux energy range.

To calculate the electron fluxes generated by the interaction of protons with the atmospheric components we follow the method presented by Gagliardini et al. [10]. According to it the electron fluxes are given by:

$$\Phi_e(E_s, Z) = \frac{N_{se}(E_s, Z)}{\left(\sum_i \sigma_{EX,ij}(E_s) + \sigma_{I,i}(E_s) \right) N_i(Z)} \quad (4)$$

where $N_{se}(E_s, Z)$ is the total number of secondary electrons, $\sigma_{I,i}(E_s)$ and $\sigma_{EX,ij}(E_s)$ are the ionization and excitation cross sections for element i and process j respectively.

DISCUSSION OF THE RESULTS AND COMPARISON WITH THOSE OF OTHER METHODS

Using the method described above we show in Figure 1 the results obtained for incident isotropic monoenergetic beams of energies $E = 0.3, 1$ and 3 MeV. The ionization due to protons and generated secondary electrons is represented.

Several authors [3], [4], [5] use a continuous slowing down model and an empirical

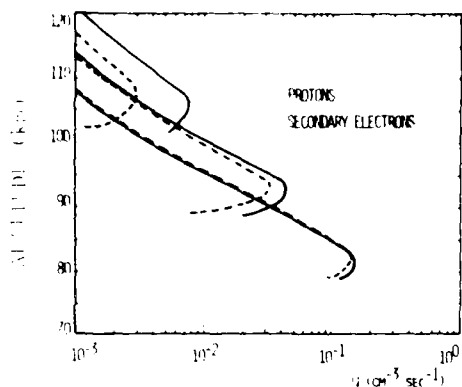


Fig.1 Ionization rates of protons and generated secondary electrons for incident isotropic fluxes of energies $E = 0.3\text{MeV}$, $E = 1\text{MeV}$ and $E = 3\text{MeV}$.

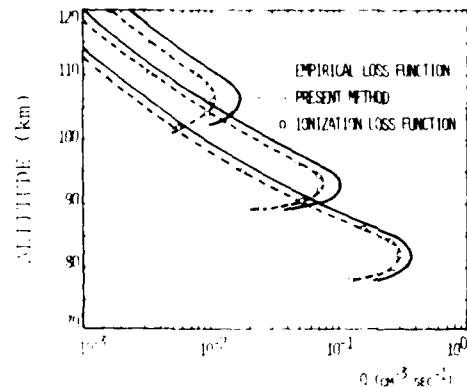


Fig.2 Total ionization rates using empirical loss function, calculated ionization loss function and present method.

energy loss function $L(E)$ [11] to calculate the ion production. Figure 2 in Edgar et al. [3] and Figure 3a, 3b in Edgar et al. [4] show the total loss function for N_2 , O_2 and O following the semiempirical expression given by Green and Peterson [11], together with the loss function due to ionization, charge exchange, elastic and excitation processes and their sum. If one compares the semiempirical loss function with the curve that corresponds to ionization it can be observed that the agreement is good over 1 MeV, but for lower energies the difference increases reaching a factor greater than 2 for 10 KeV. Also, in this region the proton generates the greatest quantity of ions; therefore, for the calculation of the ion production rate it is more precise to use the loss function due to ionization and not the total or the semiempirical one. This can be seen in Figure 2 where the results obtained by our method and by the one described by the authors mentioned above are represented showing a strong agreement, if calculated ionization loss function is used.

Figure 3 shows, as one example, secondary, tertiary and total fluxes of the electrons generated by a proton beam of energy $E = 1\text{MeV}$ at an altitude of 92 km. It can be seen that for energies greater than 35 eV the contribution of the electron created by secondary electrons is negligible. On the other hand, for low energies tertiary electrons become as important as secondaries. Therefore, they have to be taken into account in excitation processes.

CONCLUSIONS

A new method for the calculation of ionization by a proton beam interacting with the atmosphere was presented. In spite of the uncertainty in the cross sections it was possible to obtain separately the proton ion production and the fluxes of generated electrons. This constitutes a great advantage in the study of effects such as emission and excitation processes presented in proton events. Any improvement in the cross section data will also benefit our calculations increasing the possibilities of obtaining a better description of the behaviour of any incoming proton spectrum interacting with the atmosphere.

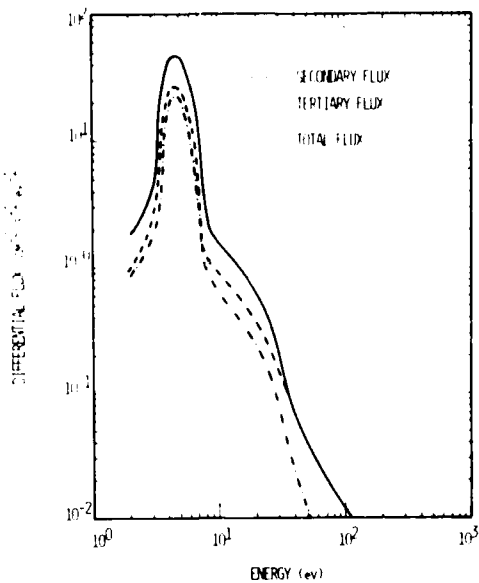


Fig.3 Secondary, tertiary and total fluxes of electrons generated by an incident isotropic beam of protons of energy $E = 1\text{MeV}$.

ACKNOWLEDGEMENTS

We wish to acknowledge the collaboration of the Centre d'Etude Spatiale des Rayonnement Toulouse, France where this work was initiated. We wish to thank also the Ionospheric Research Laboratory in Argentina (L.I.A.R.A.) for their cooperation to use the Argentine Navy's Computer Facilities.

REFERENCES

1. R.H. Eather, Rev.Geophys. Space Phys. **5**, 207 (1967a).
2. R.H. Eather, J.Geophys. Res. **72**, 1481 (1967b).
3. B.C. Edgar, W.T. Miles and A.E.S. Green, J.Geophys. Res. **78**, 6595 (1973).
4. B.C. Edgar, H.S. Porter and A.E.S. Green, Planet Space Sci. **23**, 787 (1975).
5. E. Sum, Ionospheric Research, Scientific Report **396**, University Park, Pennsylvania, 1972.
6. Vir Singh and R.P. Singhal, J.Geophys. Res. **83**, 1653 (1978).
7. A.E.S. Green and R.J. McNeal, J.Geophys. Res. **76**, 133 (1971).
8. P.M. Banks and G. Kockarts, Aeronomy, part A, Academic Press, New York, 1973.
9. R.J. McNeal and J.H. Birely, Rev.Geophys. Space Phys. **11**, 633 (1973).
10. D.A. Gagliardini, H. Karszenbaum and J. Gledhill to be published (1980).
11. A.E.S. Green and L.R. Peterson, J.Geophys. Res. **73**, 233 (1968).

REPRESENTATIONS OF SOLAR EUV FLUXES FOR AERONOMICAL APPLICATIONS

H.E. Hinteregger

*Air Force Geophysics Laboratory, Hanscom AFB, Bedford,
MA 01731, USA*

ABSTRACT

The development of significantly improved representations of solar EUV inputs for computer-aided investigations of the terrestrial thermosphere and ionosphere has become attractive particularly for the present solar cycle which has been covered by reasonably complete and continuous EUV observations from the AE-E Satellite. These representations try to satisfy some rather incongruous requirements of spectral detail, regarding (a) the strong wavelength-dependence in the terrestrial atmospheric cross sections of the various types of EUV photon interactions, (b) the great differences in the relative amplitudes of the various types of variations in the full-disk fluxes of solar emissions at different wavelengths, and (c) the persisting desire to use only a small number of daily indices as actual input variables for computational models supposed to cover the entire EUV wavelength range (remembering the great success of empirical thermospheric models using only two indices). These general physical and specific aeronomical demands indeed outline a very difficult task. The present study, based mainly on AE-E satellite observations during 1976-1979, represents an exploratory step, only clarifying some important developmental aspects, without recommending any specific formulations for immediately practicable adoption in aeronomical modelling at this time.

INTRODUCTION

The crucial qualitative and quantitative role of appropriate data on the incident fluxes of solar EUV radiation for ionospheric physics and for aeronomy in general has been discussed in many individual studies as well as in review articles published over the past ten years [1, 2, 3, 4, 5, 6, 7, 8, 9, 10, 11, 12, 13]. Specific formal representations of incident solar EUV variability adopted in theoretical models of the thermosphere or ionosphere exhibit a variety of important differences in the basic concepts, in the degree of spectral detail, and in the applicability to variable solar conditions. This variety indeed shows a concentration toward two extremes, namely

- (a) the traditional method of representing the EUV variability in terms of Non-EUV parameters such as the solar radio emission at 2800 MHz ($F_{10.7}$) used as input for well-known empirical models of thermospheric structure such as the MSIS model [14, 15] or the Jacchia Models [16].
- (b) the other extreme is that of using a fully detailed reference spectrum of incident solar EUV fluxes such as F74113 [17] which contains over thousand individual wavelength records, but is applicable only to a specific reference date

(e.g. 23 April 1974).

Distribution of Solar EUV Sources and their Variability

The solar EUV fluxes incident on top of the earth's atmosphere, $I_{o\lambda}$ [photons $m^{-2} sec^{-1}$], consist of many different types of emissions stemming from grossly different sources in the solar atmosphere. Hence it is not surprising that both short-term and long-term variabilities of $I_{o\lambda}$ are generally strongly λ -dependent, often even within small wavelength intervals. Furthermore, the brightness distribution of virtually all solar EUV emissions across the visible part of Sun (the solar disk) is generally far from uniform, showing more or less drastic contrasts between quiet-disk areas and active-region areas. The latter are relatively unimportant only under nearly ideal conditions of solar minimum such as those met by AE-E satellite spectrometer observations in the period of 13-28 July 1976.

Both the neutral atmosphere and the ionosphere obviously respond only to the total, so-called "full-disk fluxes" of solar EUV. Therefore, a division of I_o into a "quiet-disk component" and an "active-region component", $I_{o\lambda}^Q = I_{o\lambda}^Q + I_{o\lambda}^A$, might appear superfluous for aeronomical applications. However, it is clearly important to distinguish various types of temporal variations, e.g. the well-known 27-day variation. Even the EUV-variability representations used in the strictly empirical thermospheric models distinguish between a long-term component and daily component in the commonly used index of solar activity, i.e. the 2800 MHz solar radio flux. Using this "Non-EUV Index," one distinguished a daily index, $F_{10.7}$ (same or previous day), from a slowly variable index $\langle F_{10.7} \rangle$ (e.g. defined as 81-day running mean value).

Observations of solar cycle variations. All branches of the physics of the upper atmosphere experienced an enormous enrichment by the advent of rockets and satellites used as powerful new tools of experimental space research. The latter led to a fairly rapid progress in many areas of aeronomy. Unfortunately, the progress toward establishing observational data on full-disk solar EUV fluxes, including all essential spectral detail as well as the various types of temporal variabilities, appears rather painfully slow from the viewpoint of the quantitative requirements of advanced theories of ionospheric physics and aeronomy in general.

The aeronomical significance of this situation has been reviewed by various investigators [1, 4, 7, 9, 10, 11]. Therefore it suffices here to show some diagrams of observed variations of solar EUV irradiance for the last phase of sunspot cycle 20 (Fig. 1) and to illustrate the development of the present cycle 21 (Fig. 2), which appears to have gone through its maximum in November 1979. Fig. 3 gives a simplified overview to serve as a visual aid in our discussions. To avoid costly changes, the original notation of wavelengths in these figures was not converted from Å to the use of nm adopted in the present text only.

EUVS experiment on the satellites AE-C and AE-E. Satellite observations of solar EUV irradiance at wavelengths from 14 to 185 nm, performed by the so-called EUVS experiment [18] on the satellites AE-C (1974-1978) [4, 19, 20] and AE-E (1976 to present) [11, 12, 13], have revealed remarkable differences between the solar cycle 20 and the present cycle 21. Preliminary results were shown as a brief summary (Fig. 3) at the symposium on the Solar Cycle and Dynamics Mission of NASA (Wellesley, Massachusetts, 15 June 1978) and discussed in more detail, including data to June 1979, in a review presented at the XVII IUGG-IAGA meeting (paper 24.01, Canberra, 12 December 1979, informal distribution of extended abstracts not followed by formal publication). A more recently improved data set extended to the end of 1979 is illustrated here as Fig. 2a. Within the scope of the present paper, these diagrams are included merely as a visual aid. A

discussion of observational details and computer data availability through the National Space Science Data Center (NSSDC) and World Data Center A for Solar-Terrestrial Physics will be submitted for publication elsewhere.

REQUIREMENTS OF SPECTRAL DETAILS

The aeronomical (ionospheric) requirements for details of the solar EUV spectrum can be divided into two categories, in accordance with typically different objectives summarized as follows:

- (1) To use a small number of EUV variability indices for approximate representations of the temporal variability of the irradiance, $I_{0\lambda}$, for all known solar emission wavelengths throughout the total range of interest, say for $\lambda \leq 200$ nm, or at least for the range of 14-185 nm, which is most important for thermospheric or ionospheric studies and also represents the range of the now existing long-term observations for the present solar cycle 21.
- (2) To account for the known spectral details of EUV photon-interaction cross sections, at least for the major constituents of the upper atmosphere.

Attempts at approaching the latter objective (2) by the crude substitution of "effective values" of cross sections for a very small number of very wide wavelength intervals, pursued in earlier stages of ionospheric and aeronomical theories, have been rejected in various recent developments of computer-aided, quantitative theoretical models. For the latter, the actual use of known details in cross-section data is obviously much more sensible than any simplistic substitution of poorly defined mean values. A compression, if deemed necessary at all, is now acceptable for quantitative applications only if a relatively large number of wavelength intervals is used. This situation is illustrated by the selection of 37 wavelength intervals offered in a recent paper on ionization frequencies [12] from which examples have been extracted here only in the form of Table 1. The 37 intervals [12] are essentially the same as those used by Heroux and Hinteregger [17] only in their summary table, whereas their detailed aeronomical reference spectrum F74113 includes 1957 different wavelength records [17]. Compared with the latter, the number of 37 intervals is obviously small even though this same number would appear unattractively large with respect to objective (1) above.

Regarding the objective (1) from the viewpoint of thermospheric model developments, one can hardly ignore the very remarkable success of models such as MSIS [14, 15] or the Jacchia Models (e.g. [16]) which have used no more than two variability indices ($F_{10.7}$ and $\langle F_{10.7} \rangle$), noting that the solar 10.7 cm flux indeed penetrates the upper atmosphere without any physical interactions.

Shortcomings inherent in the simple use of $F_{10.7}$ and $\langle F_{10.7} \rangle$ as "EUV" indices have been discussed by many investigators in the past. However, the level of verified inconsistencies between actual aeronomical observations and corresponding model predictions is apparently not serious enough to advocate the use of a very large number of solar variability indices for the practical approach to objective (1). Hence, a subdivision of the EUV spectrum into the 37 intervals of Table 1 (a,b) with 37 interval-peculiar variability indices would not be considered desirable. On the other hand, an even finer subdivision, involving more than 37 intervals, would be needed to avoid the obviously undesirable mixing of solar emissions of significantly different variability character in the same interval. For instance, the interval 3 of Table 1 (a), 15-20 nm, includes emissions of FeVIII through FeXIII which are known to show differences in the relative variability amplitudes by as much as a factor of two that should not be disregarded.

The parts (a) and (b) of Table 1 refer only to ionizing EUV of wavelengths shortward of 102.7 nm, i.e. omitting the D region sources, H Ly- α as well as x-rays of $\lambda < 1$ nm. Results of recent calculations of unattenuated ionization frequencies [12] as a function of solar cycle 21 are abstracted here in Table 1 (c), restricted to show only data averages for 13-28 July 1976 in comparison with the near-maximum conditions of solar activity of 19 February 1979. Table 1 (d) shows the same type of comparison for the unattenuated O_2 -dissociation frequency reported by Torr et al [13].

These considerations lead to the conclusion that the method of subdividing the EUV spectrum into a sufficiently great number of wavelength intervals is indeed a necessity with respect to objective (2), but it is certainly an undesirable approach to objective (1) above.

MODEL REPRESENTATIONS OF EUV VARIABILITY

The various possible representations of EUV variations by models using a certain number of daily indices can be divided into categories depending on the physical nature of the quantities used as indices and on the number of such indices actually used. For instance, one may regard the conventional indices $F_{10.7}$ and $\langle F_{10.7} \rangle$ either as two different indices or as two different quantities based on the same basic index, i.e. $F_{10.7}$. However, the more important distinction is that of identifying both $F_{10.7}$ and $\langle F_{10.7} \rangle$ as "Non-EUV Indices". Other Non-EUV Indices of solar activity, actually used but rarely in aeronomical studies, are the daily values of Zurich sunspot numbers or the CaII plage-area index [22].

The other major category of variability-model parameters is that of "EUV Indices" [9, 21], defined as a set of daily values of the incident solar full-disk flux for some given EUV wavelength(s) or wavelength interval(s).

The basic characterization of any EUV-variability model requires not only a statement of the type of daily indices used as variables but also a detailed statement of the specific formulations converting the input of these daily indices into a sufficiently detailed list of EUV flux values for the given date. The most essential part of the latter statement may be generally described as a list of adjustment constants. The size of this array of constants will of course depend on the degree of spectral detail. Since the latter indeed should involve more than the 37 wavelength groups of Table 1 (for reasons already discussed in the preceding section of this paper), these types of variability models are obviously recommended only for computer-aided investigations. Accepting this fact, one is left with no serious objection against the actual use of a fully detailed reference spectrum.

"Non-EUV Indices" Used "Without EUV-Observation Fits"

The traditional type of EUV variability representation in terms of the daily indices $F_{10.7}$ and $\langle F_{10.7} \rangle$ used in the well-established thermospheric models (e.g. MSIS of Jacchia Models) actually bypasses the entire problem of spectral detail in both solar EUV emission and terrestrial atmospheric absorption. They define specific formulations for the conversion of the daily indices into the desired model values of thermospheric constituent densities and temperatures, using a list of adjustment constants determined empirically by fitting to a very large data base which includes satellite-drag observations and results of in-situ measurements of thermospheric quantities, none of which are formally related to any characteristics of the EUV spectrum.

The recently published simple plage-related model (CBV) of Cook et al [22] expressing variations of irradiance in the range of 117.5-210 nm as a function of

the fractional coverage of the solar disk by active regions was not recommended for any quantitative aeronomical applications by the authors [22].

"Non-EUV Indices" Used "With EUV- Observation Fits"

One of the academically most dissatisfactory aspects of the model treatment of the "EUV-effect" with the solar radio flux at 2800 MHz consisted in the empirical need to use a two-component expression, i.e. $F_{10.7}$ (daily value for the given date, or the previous day) as well as a ± 40 day mean value $\langle F_{10.7} \rangle$, where the latter generally dominates the former in the over-all formulation used to calculate model values of exospheric temperatures.

On many occasions, various authors of thermospheric models have emphasized that they never intended to suggest that the thermospheric structure actually responds to solar conditions over the past 40 days, let alone the nonsensical assumption of any response to 40 days of the future. This means that the use of $\langle F_{10.7} \rangle$ merely expresses a pragmatically justified method of accounting for the long-term variability in solar activity, as distinguished from day-to-day variability or the well-known variations with the 27-day period of solar rotation.

Our preliminary study of AE-E observations during 1976-1979 has included regression analysis for several important solar EUV emissions. These analyses were carried out for two types of associations with 2800 MHz fluxes, i.e. (A) fitting F_{λ} (EUV) data to a linear expression of the type $A_0 + A_1 F_{10.7}$ and (B) fitting to the two-component expression, $B_0 + B_1 \langle F_{10.7} \rangle + B_2 (F_{10.7} - \langle F_{10.7} \rangle)$. Table 2 shows the results for both types, Φ_A and Φ_B [using only the period from June 1977 to August 1979] in comparison with modified types of fitting, Φ_A and Φ_B [forcing Φ_A and Φ_B to reproduce the F76REF fluxes (13-28 July 1976)]. A comparison of the correlation coefficients for fit types Φ_A (Φ_A) versus type Φ_B (Φ_B) leads to the rather illuminating conclusion that EUV fluxes indeed correlate with the parameter $\langle F_{10.7} \rangle$ more strongly than with the daily $F_{10.7}$. This result is not surprising, since any opposite finding would have left us without any sensible explanation for the indisputably great success of thermospheric models such as MSIS or the Jacchia Models.

EUV Class-Variability Model

The purpose of the present model is that of transforming a fully detailed EUV reference spectrum, $F_{0\lambda}$, into equally detailed flux data for some other date, $F_{D\lambda}$, without actually requiring new data for each of the thousand or more individual wavelengths listed. Cycle 21 is the first solar cycle for which the same instrument observed EUV fluxes over the long period from the end of one cycle through the maximum of the next solar cycle. For the analysis of these observations, it seemed most reasonable to select a base-line reference for a suitable period within cycle 21 rather than the aforementioned F74113. Our specific selection of the period 13-28 July 1976 as reference for cycle 21 (F76REF) has been motivated mainly by two considerations. First, the day-to-day variations within that period of spotless sun with no visible active regions were found to be practically negligible, allowing a great enhancement of statistical significance of even weak line signals by averaging all good instrumental scan records obtained during that period. Secondly, it seemed also profitable theoretically to work with a reference spectrum reflecting the simplest possible solar conditions within this solar cycle, where the full-disk fluxes have essentially no active region contributions.

Definition of "variability classes". Letting the subscript $K = 0, 1, 2, \dots$ designate a class identification, defining $F_{0\lambda}$ as the F76REF value of flux and denoting the corresponding updated flux as $F_{D\lambda}$, we use the relation

$$R_\lambda = F_{D\lambda}/F_{O\lambda} = 1 + (R_K - 1)C_\lambda \quad (1)$$

where $K = K(\lambda)$ and C_λ are listed for each λ in F76REF and R_K is the ratio of $F_{D\lambda}/F_{O\lambda}$ for one or more wavelengths listed with $C_\lambda = 1$ and same class K . Hence, the quantity

$$R_K = F_{D\lambda}/F_{O\lambda} \text{ for } C_\lambda = 1 \quad (2)$$

will be briefly called "class ratio" below.

The physical implication of these relations is obvious, i.e. the fluxes in all emissions (1) of the same class (K) and same adjustment constant (C_λ) are assumed to vary identically.

If one were to consider only one specific date outside the reference period, with somehow given values of all fluxes $F_{D\lambda}$, the problem of appropriate classification would be trivial, i.e. we could in principle define any total number of classes. However, in practice observational data for a given date are often incomplete in spectral coverage, the currently available instrumental resolving power of the EUVS experiment falls short of actually separating all separately listed lines (e.g. the "30.4 nm" signal includes both the chromospheric HeII and the coronal SiXI lines which are only 0.03 nm apart), and emissions at $\lambda < 14$ nm, listed in F76REF as well as F74113 [17], are indeed outside the instrumental range of the EUVS experiment. The latter considerations alone would of course not justify the present class-model development outlined here. The primary goal of this model design is to express EUV flux variabilities in terms of a reasonably small number of variable class parameters, R_K , in connection with sets of adjustment parameters, C_λ , treated as constants (over a reasonably limited date range).

The first phase of this development as reported here, was based on the definition of only three variability classes ($K = 0, 1, 2$) with the following "key wavelengths" (defined by setting $C_\lambda \equiv 1$): $\lambda_K(K=0) = 177.5-185$ nm (quasi-continuum); $\lambda_K(K=1) = 58.433$ nm (HeI); $\lambda_K(K=2) = 33.541$ nm (FeXVI); assigning class $K=1$ to the various solar emissions with ionization potentials $E < 200$ eV and $K = 2$ for those with $F_i \leq 200$ eV. The class $K = 0$ consists of those emissions in the range 110-185 nm identified as "quasi-continuum", denoted as QUASI(C) in F76REF (as well as F74113). The latter should be distinguished from various individually identified lines of class $K \neq 0$ listed in the same range of wavelengths. Our preliminary analysis of observations in the range from 135-185 nm suggests that the quasi-continuum of the entire range can be rather well approximated by setting

$$(F_{D\lambda}/F_{O\lambda})_{K=0} \doteq R_0 \exp[0.0076(R_0 - 1)(177.5 - \lambda/\text{nm})] \text{ for } \lambda \leq 177.5 \text{ nm} \quad (3)$$

A similar approximation for the hydrogen Lyman-continuum is given as

$$(F_{D\lambda}/F_{O\lambda})_{H \text{ Ly-Cont.}} \doteq R_1 \exp[0.00032(R_1 - 1)(91.2 - \lambda/\text{nm})] \quad (4)$$

Trade-off between simplicity and accuracy. For some aeronomical studies the use of a fairly accurate representation restricted to a relatively short time period may be more important than the applicability over a much longer period for which the use of a given set of constant values of C_λ in general leads to more significant inaccuracies of the representation for each section of the long period. This "trade-off" condition is inherent in the method of determining best-fitting values of C_λ for some given period of existing observations. If this period is extended over a truly long time span, say 2-3 years, the best-fitting C_λ values indeed differ more or less significantly from those found by fitting a shorter period of observations. Table 3 shows a comparison taken from our exploratory study, given here for illustrative purposes only. The values of C_λ of Table 3 agree only

crudely with those written into F76REF (AE-Computer issue of 10 May 1979). The latter were most heavily weighted toward best accuracy for the representation of the pre-maximum of solar activity of Jan-Feb 1979.

Limitations in Physical Significance. The specific form of equ. (1) might suggest the adoption of an attractively simple physical model, that is to regard the increase of full-disk solar EUV fluxes after 1976 as a straightforward consequence of the increasing number of active regions, with C_A playing the role of products of active-region areas and specific relative contrast ratios of active-region/quiet-disk brightness, i.e. assuming that there is no solar-cycle variation of variability in these contrast ratios. However, these assumptions are justified only as a greatly simplified concept. The apparently significant differences of C_A -values obtained as best-fitting for different time periods within cycle 21 indeed suggest that at least the first, or possibly both of these simplifying assumptions should be abandoned, at least for quantitative applications. The same criticism applies to the recently published CBV model [22].

CONCLUSIONS

Pilot studies performed on AE-E satellite data on solar EUV fluxes for the rising part of the sunspot cycle 21 have demonstrated the feasibility of expressing the variability of solar EUV fluxes in aeronomically attractive terms involving a relatively small total number of date-dependent variables supported by the relatively large number of wavelength-peculiar parameters. The latter can be assumed as a set of conveniently invariant constants only as long as the date range of desired applicability is reasonably limited.

While this is unfortunate from the viewpoint of desiring simplicity for aeronomical calculations, it is clearly not surprising from the viewpoint of solar physics, if one appreciates the great variety of different types of active regions including differences in their evolution over different life times (e.g. recurring after one or more solar rotations with a generally not constant EUV emission spectrum). It is the latter viewpoint from which one can hardly expect that an aeronomically adequate accuracy could be offered by any simple two-component variability model based on either CaII plage area indices of R_Z without involving any massive data base of actual EUV flux observations over the desired period of suggested applicability. Also, it seems hardly surprising that sets of EUV-observation-based model constants, determined for some reasonably limited date range, can give more or less grossly misleading results, if the same set of constants were applied to the description of solar EUV for a different time period of the same solar cycle, or, most drastically, for a different solar cycle.

Discounting the numerical details of our exploratory studies for the moment, one can rather safely conclude the following: (a) Representations of solar EUV for quantitative studies should allow the construction of a date-peculiar detailed spectrum of incident fluxes even if the variability model uses only a few date-dependent variables; (b) Representations using Non-EUV Indices can be improved by restriction to limited parts of a solar cycle for which actual EUV observations allow us to use empirical fitting of the type illustrated in Table 2; (c) Continued use of Non-EUV Indices for various applications may remain a practical necessity still for some time; (d) Ultimate adoption of true EUV Indices is obviously most desirable. However, the realization of this goal will not only require extensive further study of accomplished observations, but it will also require future solar EUV measurements of accommodating aeronomical objectives, to be pursued with more vigor than that reflected in presently approved programs.

Acknowledgements. The EUVS experiment was sponsored by the National Aeronautics and Space Administration (NASA DPR S50030-AG). The author wishes to thank his colleague at AFGL, K. Fukui, for invaluable help in many parts of this study. The work as a whole would have been impossible without the excellent support of scientific data analysis by Computer Sciences Corporation under the expert leadership of B.R. Gilson.

REFERENCES

1. H.E. Hinteregger, Ann. Geophys. 26, 547 (1970).
2. D.E. Knight, E.R. Uribe and B.E. Woodgate, Plan. Space Sci. 21, 253 (1973).
3. L. Heroux, M. Cohen and J.E. Higgins, J. Geophys. Res. 79, 5237 (1974).
4. H.E. Hinteregger, J. Atmos. and Terrestrial Phys. 38, 791 (1976).
5. G. Schmidtke, K. Rawer, H. Norbert and K. Holzer, J. Geophys. Res. 82, 2423 (1977).
6. D. Heath and M. Thekaekara, in The Solar Output and Its Variation, Univ. of Colorado Press (1977), p. 193.
7. J.G. Timothy, in The Solar Output and Its Variation, Univ. of Colorado Press (1977), p. 237.
8. R.G. Roble and J.T. Hastings, Planet. Space Sci. 25, 217 (1977).
9. G. Schmidtke, Planet. Space Sci. 26, 347 (1978).
10. P.C. Simmon, Planet. Space Sci. 26, 355 (1978).
11. H.E. Hinteregger, J. Geophys. Res. 84, 1933 (1979).
12. M.R. Torr, D.G. Torr, R.A. Ong and H.E. Hinteregger, Geophys. Res. Letters 6, 771 (1970).
13. M.R. Torr, D.G. Torr and H.E. Hinteregger, J. Geophys. Res. (submitted, 1980).
14. A.E. Hedin, J.E. Salah, J.V. Evans, C.A. Reber, G.P. Newton, N.W. Spencer, D.C. Kayser, C. Alcayde, P. Bauer, L. Cogger and J.P. McClure, J. Geophys. Res. 82, 2139 (1977).
15. A.E. Hedin, C.A. Reber, G.E. Newton, N.W. Spencer, H.C. Brinton, H.G. Mayr and W.E. Potter, J. Geophys. Res. 82, 2148 (1977).
16. L.G. Jacchia, Smithsonian Astrophys. Observatory, Spectial Report 375 (1977).
17. L. Heroux and H.E. Hinteregger, J. Geophys. Res. 83, 5305 (1978).
18. H.E. Hinteregger, D.E. Bedo and J.E. Manson, Radio Science 8, 349 (1973).
19. H.E. Hinteregger, D.E. Bedo, J.E. Manson and D.R. Skillman, Space Research XVII, 533 (1977).
20. H.E. Hinteregger, Geophys. Res. Letters 4, 231 (1977).
21. J.P. Delaboudiniere, R.F. Donnelly, H.E. Hinteregger, G. Schmidtke and P.C. Simon, COSPAR MANUAL No. 7 (1978).
22. J.W. Cook, G.E. Brueckner and M.E. Van Hoosier, J. Geophys. Res. 85, 2257 (1980).
23. G.H. Mount, G.J. Rottman and J.G. Timothy, J. Geophys. Res. to appear (1980).
24. A. Vidal-Madjar and B. Phissamay, Solar Phys. 66, 259 (1980).

table 1. Examples of Aeronomical Use of Recent Data on Solar EUV Irradiance

(a) SOLAR EUV IRRADIANCE ($10^{10} \text{phot.m}^{-2}\text{sec}^{-1}$) 13-28 JUL 19 FEB				(b) TOTAL AND INDIVIDUAL IONIZATION CROSS SECTIONS FOR ATOMIC OXYGEN(mb)						
Interval	λ nm	Source	1976	1979	Total	4S	2D	2P	4P	4P*
1	5 - 10	various	438	1371	1.06	0.32	0.34	0.22	0.10	0.03
2	10 - 15		169	468	3.53	1.03	1.14	0.75	0.34	0.27
3	15 - 20		1869	5702	3.96	1.62	2.00	1.30	0.58	0.46
4	20 - 25		1395	7145	7.55	1.95	2.62	1.70	0.73	0.54
5	~ 25.6	HeII+bi.	506	1083	8.43	2.15	3.02	1.95	0.82	0.56
6	28, 415	Ly α	77	5723	9.26	2.33	3.39	2.17	0.89	0.49
7	25 - 30	other	1356	12160	8.78	2.23	3.18	2.04	0.85	0.52
8	30, 331	SiIII	600	4691	9.70	2.45	3.62	2.32	0.91	0.41
9	30, 378	HeII	7763	14396	9.72	2.45	3.63	2.32	0.91	0.41
10	30 - 35	other	867	6832	10.03	2.61	3.98	2.52	0.93	0.00
.	.	examples (a) from Table 3 of Ref. [12]	.	.	examples (b) from Table 2 of Ref. [12]
.	which includes weighted data for N ₂ , O ₂ and He
35	102, 572	H Ly- β	4375	11852	0.00
36	103, 191	OVI	1943	6105	0.00
37	100-105	other	2478	6093	0.00

(c) IONIZATION FREQUENCIES (sec^{-1}) FOR MAJOR TROPOSPHERIC SPECIES (from Ref. [12])

	O_2^+	N_2^+	He^+	$O^+(1O_1)$	$O^+(4S)$	$O^+(2D)$	$O^+(2P)$	$O^+(4P)$	$O^+(2P^*)$
13-28 JUL 5.43	3.89×10^{-7}	4.89×10^{-7}	2.80×10^{-8}	1.09×10^{-7}	0.96×10^{-7}	0.56×10^{-7}	1.34×10^{-8}	6.17×10^{-9}	
1976									
1979	1.73×10^{-6}	1.28×10^{-6}	1.93×10^{-7}	0.35×10^{-7}	3.39×10^{-7}	3.25×10^{-7}	1.94×10^{-7}	5.34×10^{-8}	2.45×10^{-8}

(all values are for region of practically unattenuated solar EUV)

(d) O₂- DISSOCIATION FREQUENCY DUE TO UNATTENUATED SOLAR EUV OF $\lambda < 175$ nm

Dates	23 APR 1974	13-28 JUL 1976	14 DEC 1978	22 JAN 1979	19 FEB 1979
Reference	I74113 [17]	I76RLI	[13]*	[13]*	[13]*
$J_O(O_2)/10^{-6} \text{ sec}^{-1}$	1.50	1.50	2.20	2.64	2.80
$J_{10.7}/10^{-22} \text{ km}^{-2}\text{Hz}^{-1}$	74	68	206	234	243

* results based on assumed equality of solar irradiance for the periods of I76RLI (spotless disk, cycle 21) and I74113 (R_Z 18, cycle 20), apparently open to revision.

Table 2. Solar EUV Correlations with 2800 MHz (June 1977-August 1979; prelim.)

 $\psi_a = \phi_o + a_1 F_{10.7}$ and $\psi_b = \phi_o + b_1 F_{10.7} + b_2 (F_{10.7} - F_{10.7})$ "forced"
 $\psi_A = A_o + A_1 F_{10.7}$ and $\psi_B = B_o + B_1 F_{10.7} + B_2 (F_{10.7} - F_{10.7})$ "not forced"

"forced": matching the reference values for 13-28 July 1976 imposed too;
 "not forced": fits are not required to reproduce conditions of F76REF above.

EUV EMISSION LINE Identif. λ (nom.) in nm	ONE-VARIABLE FIT		TWO-VARIABLE FIT	
	Correlation Coefficients for ψ_a	for ψ_A	Correlation Coefficients for ψ_b	for ψ_B
H Ly- α 121.6	0.83	0.84	0.91	0.91
H Ly- β 102.6	0.75	0.90	0.87	0.93
He I 58.4	0.83	0.93	0.93	0.97
He II 30.4*	0.91	0.91	0.95	0.95
O IV Group 55.4	0.31	0.91	0.76	0.97
Fe X 17.5	0.89	0.91	0.96	0.97
Mg X 61.0	0.86	0.92	0.97	0.98
Si XII 49.9	0.88	0.89	0.94	0.94
Fe XVI 33.5	0.93	0.93	0.96	0.96

*) observed fluxes for "30.4 nm" include coronal line of Si XI 30.331 nm

Table 3. C_λ -Determination of simple EUV Class-Variation Model ($K = 1, 2$ only) from Different Date Ranges of fitting to preliminary EUV data

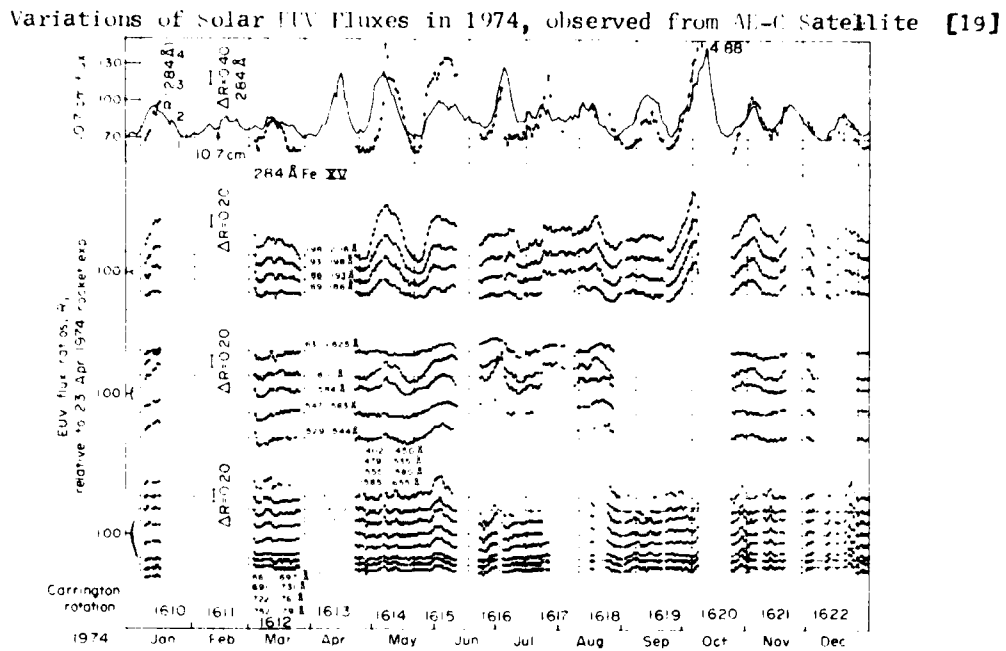
$$\psi_\lambda = \phi_\lambda (F76REF) \cdot [1 + (R_K - 1)C_\lambda] \quad \text{with } R_1 = F_{58.4}/F_{58.4} (\text{F76REF})$$

$$R_2 = F_{33.5}/F_{33.5} (\text{F76REF})$$

EUV EMISSION LINE Identif. λ (nom.) in nm	K	From 77154 to 79226		From 77154 to 77365		From 78001 to 78355		From 79001 to 79226	
		$\langle C_\lambda \rangle$	%dev	$\langle C_\lambda \rangle$	%dev	$\langle C_\lambda \rangle$	%dev	$\langle C_\lambda \rangle$	%dev
H Ly- α 121.6	1	0.915	25	0.763	16	0.711	15	1.139	8
H Ly- β 102.6	1	0.995	12	1.109	8	0.924	12	0.966	8
He I 58.4	1	$C_\lambda = 1$ ("key wavelength" for $K = 1$)							
He II 30.4	1*	0.396	41	0.185	67	0.422	14	0.517	12
O IV Gr. 55.4	1	0.640	16	0.763	8	0.632	10	0.558	7
Fe X 17.5	2	0.018	30	0.021	25	0.020	28	0.014	11
Mg X 61.0	2	0.044	32	0.058	20	0.047	25	0.032	9
Si XII 49.9	2	0.170	20	0.205	19	0.158	16	0.154	9
Fe XVI 33.5	2	$C_\lambda = 1$ ("key wavelength" for $K = 2$)							

*) actually observed is a mixture of $K = 1$ (He II) and $K = 2$ (Si XI)

NOTE: F76REF refers to AE-computer listing of EUV reference spectrum for the date range 13-28 July 1976, based on AE-E observations indicating no significant variations during that period, i.e. allowing the use of average values from all appropriate parts of experiment turnons to obtain meaningful data even for weak emission lines which would be lost in the statistical error of rather small count samples characteristic for a single scan observation turnon. The results shown here in both Table 2 and Table 3 were obtained by accessing the preliminary data base illustrated in the diagrams of Fig. 2b, now considered superseded by a most recently improved and extended data base (see Fig. 2a which illustrates the observed variations for 7 of the 9 wavelengths tabulated above).



Minimum of Solar Chromospheric EUV Fluxes around 20 April 1975

[20]

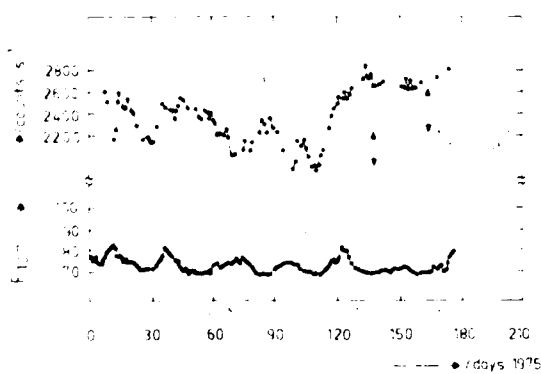


Fig.1 Solar EUV Flux Variations during declining phase of sunspot cycle 20. The upper picture illustrates greatly different 27-day variabilities for the emissions of correspondingly different origin within the solar atmosphere, more or less persisting through the end of the year 1974. The lower picture reproduces the first tentative evidence [20] of the past "solar minimum" for chromospheric EUV fluxes occurring 14 months before July 1976 (lowest value of monthly mean sunspot number), re-asserted with more confidence later [11], and now confirmed by completely independent evidence from AEROS-B observations reported at the 1979 IAGA Session 11-1 in Canberra (Paper 21.12 by G. Schmidtke and N. Bürskens) and OSO-5 satellite observations of H Ly- α published most recently [24].

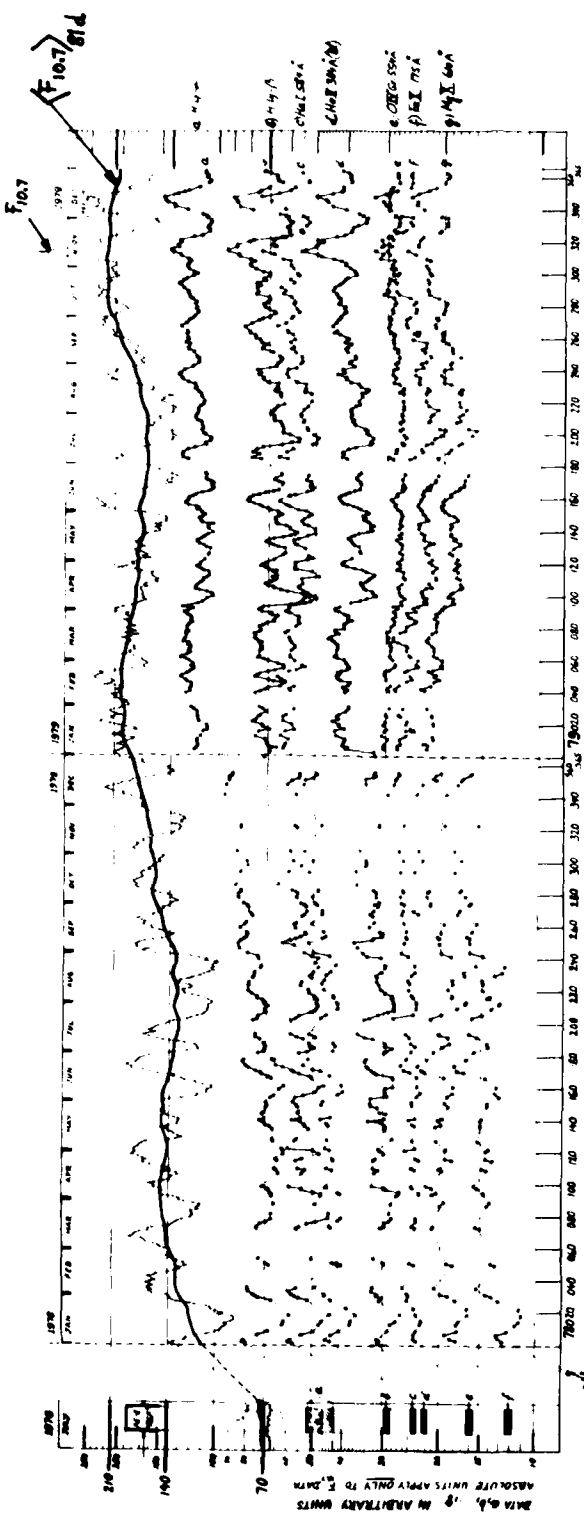


Fig. 2(a) Variations of Solar EUV Irradiance for the Years 1978 and 1979, observed from the satellite AE-E. The development of the solar cycle 21, as viewed in various wavelengths of solar EUV emissions, appears to have passed through its maximum around November 1979, in agreement with ground-based observations of the solar radio flux at 2800 MHz illustrated at the top of the diagram (showing both the daily and the 81-day mean values). All EUV fluxes are plotted as relative values on the same logarithmic ordinate scale used for the absolute values of $F_{10.7}$, to facilitate the visual comparison of the relative variability amplitudes, i.e. showing no organization with respect to the relations of absolute values. Computer-listed data in absolute units for these 7 wavelengths covering all existing AE-E observations of the date range 77154-79364 besides the reference values for July 1976 (indicated graphically at the left side of the diagram), mailed to some colleagues as printouts of the file, namely SEUVFLX, now is part of a data package on magnetic tape released to the National Space Science Data Center for public availability. It should be noted that Fig. 2(a) and SEUVFLX were produced from a most recently improved and extended data base which now supersedes the earlier, preliminary one (ending with date 79226 and including some partially marginal processing) used in the presently reported study as well as in the construction of diagrams such as Fig. 2(b) and Fig. 3 which had been distributed at the occasion of earlier meetings, without any subsequent formal publication. Actual differences for previously covered dates have been found to be quite insignificant.

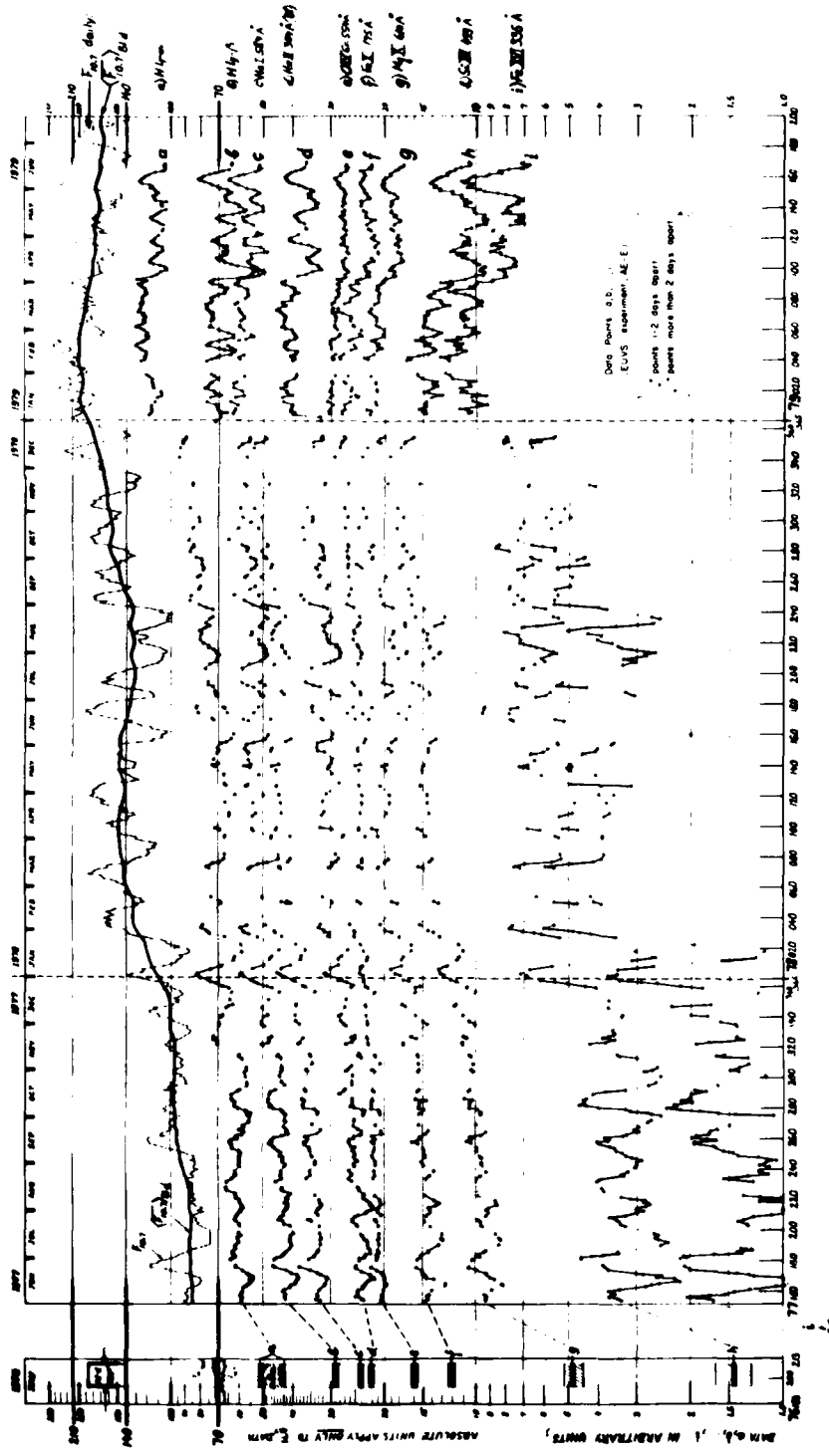
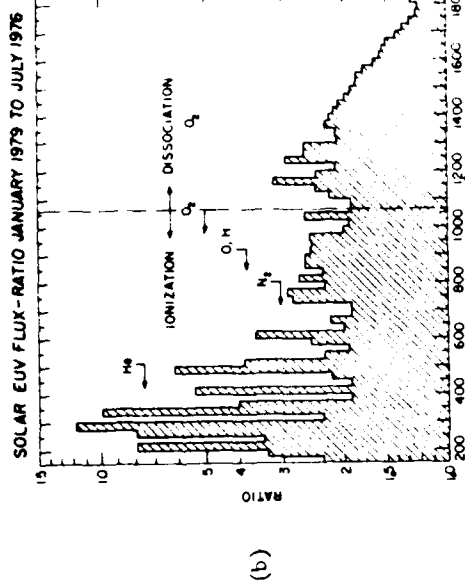


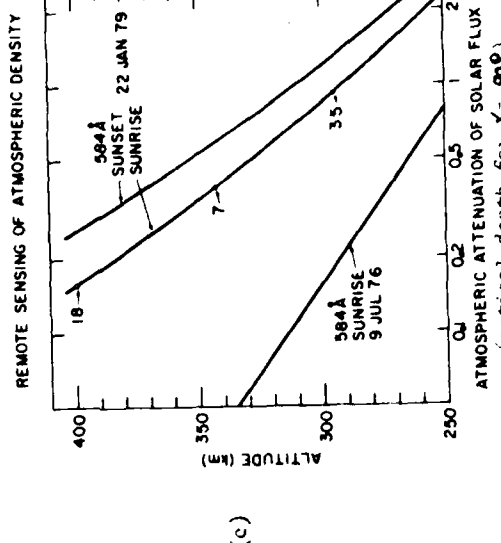
Fig.2(b) Variations of Solar EUV Irradiance from June 1977 through June 1979; preliminary AE-E data base. This illustration of the development of the solar cycle 21 in 9 different wavelenghts of EUV emissions is rather similar to the picture given by Fig.2(a) above. As explained in the legend to Fig.2(a), the diagrams (b) have been created from the same preliminary data base used throughout the presently reported study.

Preliminary Results of EUVS Experiment on AE-E

- (a) EUV fluxes in 25 Å-intervals; absolute values estimated refer to 22 January, 1979
($F_{10.7} = 234$, $\langle F_{10.7} \rangle_{81 \text{ days}} = 198$, $A_p = 10$)
- (b) Ratios of (a) to average of 24 sets of observations obtained during July 1976, on days with $R_z = 0$ and $F_{10.7} \leq 70$ ($\langle F_{10.7} \rangle_{81 \text{ days}} = 71$, $A_p = 9$)
- (c) Diagram of optical depths at points of minimum ray height (90° zenith angle) obtained from occultation measurements at 584 Å; the numbers with arrows express the ratios of mass densities inferred via observed scale heights of optical depths



(b)



(c)

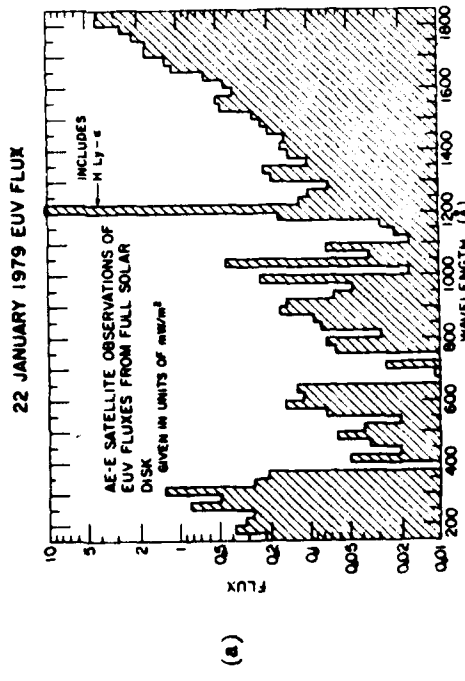


Fig. 3 (a) Overview of Results of EUVS Experiment on the Satellite AE-E, as shown at NASA/VAN SCDM Symposium of 13 June 1979 at Wellesley and discussed in more detail at 1979 IAGA Session II-4 (paper 24.01 by H.E. Hinteregger) in Canberra, without any subsequent formal publication. This illustration is included here merely as a visual aid to a crude overview. For an explanation of data base, see legend to Fig. 2(a).

SOLAR EUV ENERGY BUDGET OF THE THERMOSPHERE

M.R. Torr,¹ P.G. Richards and D.G. Torr¹

*Center for Atmospheric and Space Sciences, Department of
Physics, Utah State University, Logan, UT 84322, USA*

¹*Also affiliated with the National Institute for Telecommunications Research of the C.S.I.R., Johannesburg, South Africa*

ABSTRACT

Using the accumulation of experimental data and theoretical studies conducted on the terrestrial thermosphere since the mid seventies, we have re-evaluated the channels by which solar UV energy is transferred to the atmosphere. As an outcome of this evaluation we have redetermined the solar EUV heating efficiency for the thermosphere and find this to be considerably different from that established in earlier studies. The heating efficiency has strong altitude, solar cycle and diurnal dependencies. The values of this parameter vary from less than 10% to greater than 100%, with peak midday values of 50-55%. In recent papers we have presented the results of this new UV heating efficiency determination using a steady state solution of the ionospheric model. In this paper we present the results obtained solving a time dependent model over a diurnal cycle. The time dependent effects are found to be significant, with certain longlived species acting as temporary reservoirs of latent heat that is released to the neutral atmosphere at later times.

INTRODUCTION

A fundamental parameter in studies of the energy budget of the thermosphere is the efficiency with which solar UV energy is transferred to the neutral atmosphere as heat. The heating efficiency, ϵ , is defined as the ratio of the total heating rate at each altitude divided by the total UV energy deposited at each altitude. A reevaluation of this parameter is timely in view of the relevant new information that has been gained over the past few years, largely as a result of the Atmosphere Explorer satellite program.

In two recent papers we have quantified the thermospheric UV energy partitions for steady state conditions, M.Torr et al, [1 and 2]. From these results we have redetermined the heating efficiency, ϵ , as a function of altitude for selected conditions. The results differ significantly from our previous understanding, and will widely affect models dependent on the thermospheric energy budget. The UV heating efficiency was found in these studies to vary rather dynamically as a function of altitude, season, latitude and solar cycle. In this paper we extend the steady state solution reported earlier, M. Torr et al, [1 and 2] to a time dependent solution over a diurnal cycle.

The basic data set for this study comprises actual measurements of particular

atmospheric parameters and models which have been shown to reproduce observations to an accuracy suitable for these purposes. Thus we use the actual UV flux measurements made by the EUVS instrument on the Atmosphere Explorer (AE) satellites, Hinterberger et al, [3]. The neutral atmosphere as measured by the AE satellites is well represented by the MSIS model, Hedin et al, [4 and 5]. Using our current understanding of the thermospheric photochemistry (see for example, D. Torr and Torr, [6 and 7]) in a comprehensive model of the ionosphere, we are able to reproduce the ionic concentration measurements to a very satisfying degree. This model has been described elsewhere, Young et al, [8, 9 and 10], Richards et al, [11] and solves the ionospheric continuity, momentum and energy equations. It incorporates the Nagy and Banks [12] two stream method of handling the photoelectron transport equations, and the solution is carried out from the E region in one hemisphere to the E region in the other hemisphere. The model takes into account transport of all long-lived species.

For the purposes of this study we solve the diurnal model for conditions appropriate to 14 February 1974 and the northern geographic latitude of Millstone Hill. This is the same day for which the earlier steady state results were presented (D. Torr et al, [1 and 2]). The results shown in this paper incorporate some updates to our earlier study, and we shall discuss such improvements and their impact where appropriate below. Our solutions apply to altitudes of 125 km and above.

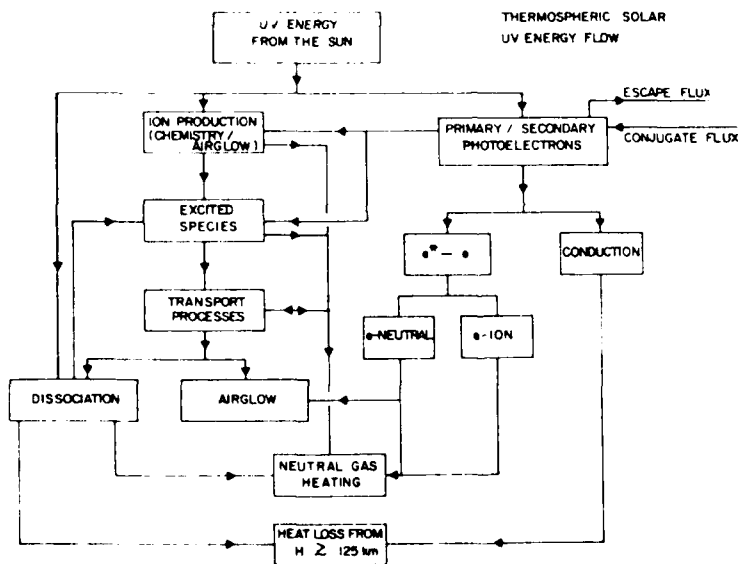


Fig. 1 Schematic of the major solar ultraviolet energy flow channels (from Torr et al, 1980b).

We are concerned here with what happens to an UV photon that is deposited in the atmosphere at a given altitude. The possible channels are illustrated in Figure 1. The initial processes partition the energy into the formation of ions and photoelectrons, and into the photodissociation of molecules. Following these processes, a number of branches can be followed. The photoelectrons formed in the ionization process can in turn result in further ionization and dissociation. Both the photoelectron and ionization channels can reproduce species in various excited electronic states which can in turn channel energy into airglow or heating of the neutral atmosphere. Transport processes play a very significant role in the redistribution of this energy. The remaining energy in the photoelectrons is transferred to the electrons, ions and neutrals.

The various processes discussed above can be divided into heating and cooling mechanisms. The former result in the transfer of energy to the neutral atmosphere as heat while the latter result in the loss of energy from altitudes above 125 km. The major heating processes are the kinetic energy gained by the products of each exothermic chemical reaction, and also electron-electron collisions. Cooling is produced as a result of energy lost in the form of radiation (airglow), and due to the dissociation of molecular oxygen, since the resultant O atoms are transported to lower altitudes before recombining.

Because the model used here solves for the production and loss rates of all the relevant species (ions and neutrals in ground or excited electronic states) we can quantify the role of each process in the energetics of the thermospheric system. We then compute the total heating rate and determine the heating efficiency for a given altitude, local time and set of conditions.

TIME DEPENDENT RESULTS

For purposes of illustrating the magnitudes of these various energy channels, we have run the full diurnal solution for 14 February 1974, and in Figure 2 we show the heating and cooling rates for a local time of 1300 hours. Also shown in this figure is the total solar UV energy deposition rate as a function of altitude. The calculations include solar radiation in the wavelength range corresponding to the O₂ absorption in the Schumann-Runge continuum.

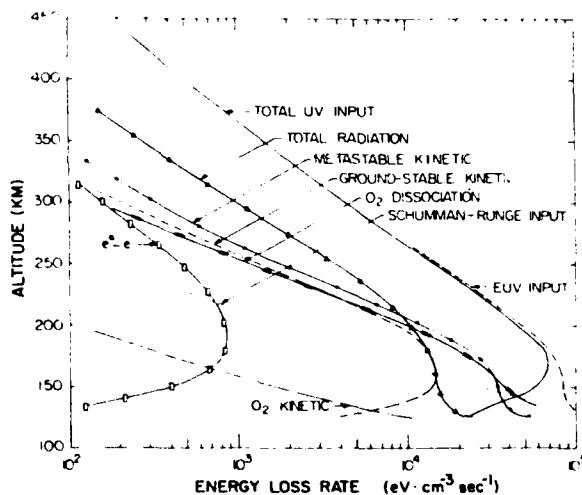


Fig. 2 Comparison of solar UV energy deposition rate and major energy channels. The results shown are from a time dependent solution for 14 February 1974 for a local time of 1300 hours.

As can be seen from the results given in Figure 2, the total energy loss rate at the higher altitudes is less than the total UV energy deposition rate at the same altitude. This is due primarily to two effects. The downward transport of longlived species (primarily O₂, electrons and odd nitrogen) results in the non-local loss of this energy at lower altitudes. Also, at the higher altitudes, where quenching processes are not as dominant, a significant fraction of the deposited energy is lost as airglow.

Each of these energy channels has been examined in detail in our earlier paper, (M. Torr et al, [2]) in which we have quantified the various components for steady state conditions. At the local time that we are considering here, the only

significant differences to the previous steady state solution will be via the longlived species, NO , NO_x and N^{4S} . In the case of the odd nitrogen chemistry, we have also incorporated the photodissociation source of N^{2D} and N^{4D} discussed by Richards et al [13]. The impact of the time dependent effects near noon and the additional production rate is illustrated in Figure 3 in which we show the steady state odd nitrogen concentration compared with those determined in this model. From these results it can be seen that differences from our steady state solution are not pronounced near noon. The time dependent effect of the odd nitrogen are, however, significant over the diurnal cycle as discussed below.

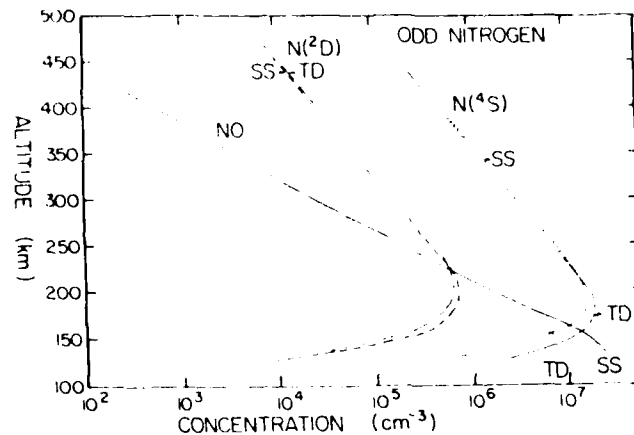


Fig. 3 Odd nitrogen concentrations from the steady state solution (SS) (no photodissociation of N_2) vs time dependent solution (TD) (including photodissociation of N_2).

In Figure 4 we show the diurnal variation of the kinetic heating channels at the altitude of the peak EUV energy deposition i.e. 165 km for 14 February 1974. These are shown compared with to the UV energy deposition rate (for both the EUV and Schumann-Runge components). Also shown is the cooling by 63μ radiation.

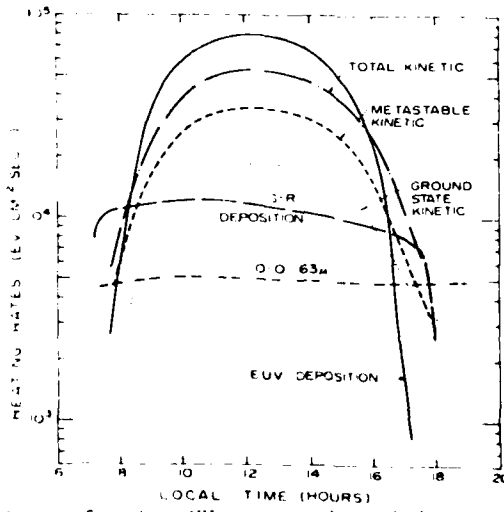


Fig. 4 Comparison of solar UV energy deposition rate and major energy channels as a function of local time at 165 km. (14 February 1974).

HEATING EFFICIENCY

In Figure 5 we show the heating efficiency resulting from the steady state solution for a local time of 1300 hours, as a function of altitude. (The time dependent solution is not significantly different at this local time.) Also shown in the figure, are the results of the study made by Stolarski et al [14] based on the pre-Atmosphere Explorer knowledge of the thermosphere.

Because of the uncertainty that surrounded the solar flux intensities at that time, their calculations were done for an early solar flux compiled by Hinteregger [15] and for a factor of two times these values. In Figure 5 we have shown the Stolarski et al [14] results for the same local time as that for which our data are shown. The Stolarski et al [14] results indicated that the heating efficiency could be approximated by a value of ~30%, regardless of altitude and time of day. By contrast, our results reveal that the UV heating efficiency is a strong function of altitude, with a peak of approximately 55% at the peak EUV deposition altitude, dropping to approximately 10% at higher altitudes (near 400 km).

Several factors contribute to the significant difference found between the results of this study and the study conducted some years ago. We now have the benefit of actual measured solar fluxes and neutral atmospheric concentrations. In addition, there have been substantial advances in the state of knowledge of thermospheric chemistry. Numerous processes and reaction rate coefficients have been identified, quantified or refined over the last few years. This is particularly true of the metastable species, odd nitrogen and vibrationally excited nitrogen.

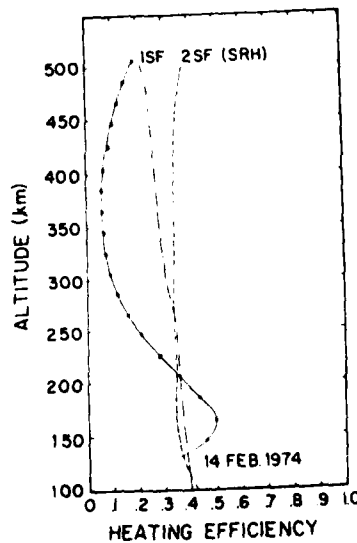


Fig. 5 The heating efficiency vs altitude for a steady state solution for midday conditions. Also shown are the results by Stolarski et al [14] for a factor of two range in solar flux (1SF and 2 SF) (from Torr et al [2].)

The odd nitrogen species play a significant role in contributing to the overall UV heating efficiency and the dependence of ϵ on altitude and local time. It is thus not only important to have a model which includes the correct photochemistry, but also the transport. In Figure 6 we show the heating efficiency altitude profile that would be obtained if transport of odd nitrogen were ignored. The tendency is to flatten the profile, increasing the efficiency at higher altitudes, and reducing

the amplitude of the peak. We have used the steady state solution results to illustrate this effect.

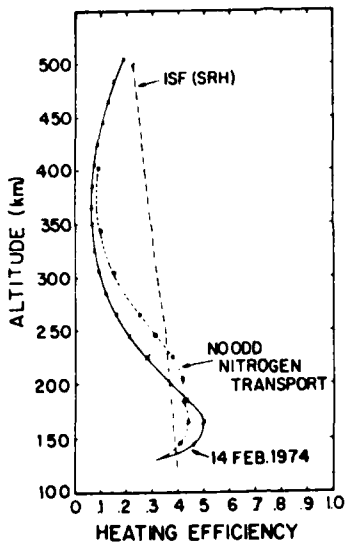


Fig. 6 The effect of neglect of transport of odd nitrogen species on the heating efficiency profile (from Torr et al, [2]).

Altitude profiles of α at three illustrative local times for 14 February are shown in Figure 7. The strong diurnal variation is evident in this figure. Solar UV energy deposited in the morning is released as heat later in the day, via the long lived species. This effect becomes particularly pronounced near sunset, when the rate of energy deposition is falling sharply, while kinetic heating processes (via such reactions as $N + NO$, and quenching of $N(^2D)$) result in significant heating of the neutral atmosphere. The long lived species, mainly odd nitrogen, thus act as latent heat storage mechanisms.

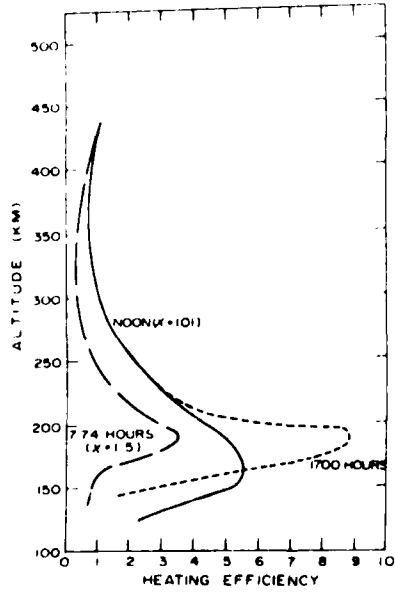


Fig. 7 The heating efficiency as a function of altitude for selected times of day (14 February 1974).

In Figure 8 we show the diurnal variation of ϵ for various selected altitudes. There is an asymmetry due to the fact that solar energy deposited early in the day, is only released in the form of neutral heating at a later time. This becomes particularly dramatic during the evening twilight, where the time dependent effects result in large increases in the heating efficiency at a time when the solar deposition rate is decreasing sharply.

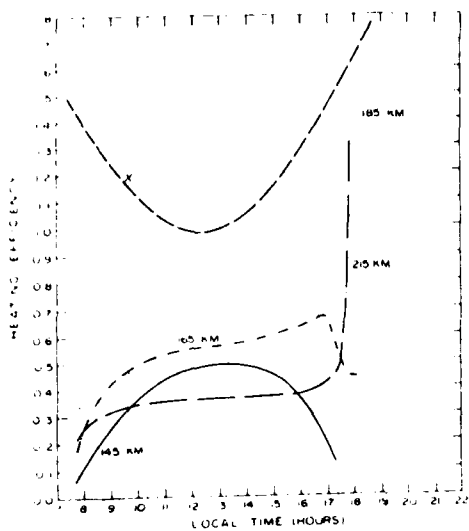


Fig. 8 The heating efficiency vs. local time at selected altitudes (February 14, 1974). Also shown is the relative variation of the solar zenith angle, ϵ .

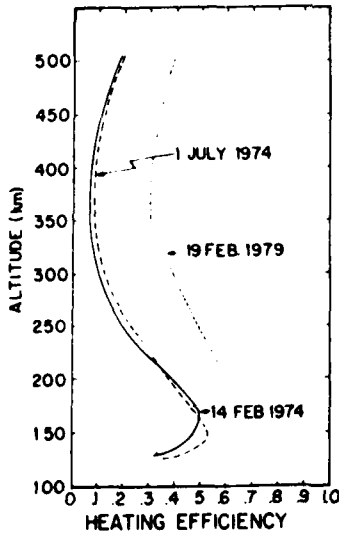


Fig. 9 Comparison of the heating efficiency profile for 14 February 1974 (winter, solar minimum), with results for 1 July 1974 (summer, solar minimum) and 19 February 1979 (winter, solar maximum). The results are all steady state solutions from M. Torr et al [2].

All of the results shown so far have been from the diurnal or steady state solutions for 14 February 1974, i.e. winter and solar minimum. In our steady state study, M. Torr et al, [2] we made a preliminary investigation into the seasonal and solar cycle variability of ϵ . We have not yet run the time dependent solutions for these examples, and so in Figure 9 we show the steady state results.

As can be seen from the results in Figure 9, the seasonal effect over 1974 is not very pronounced. However, ϵ is found to vary strongly over the solar cycle. For the February 1979 case, the maximum in ϵ occurs at a higher altitude due to the higher height of the peak EUV deposition at solar maximum. In addition the heating efficiency at the higher altitudes is a factor of 3 to 4 times as large as it was at these altitudes at solar minimum. M. Torr et al [2] have shown that this is largely due to the increased effectiveness at solar maximum in transferring energy to the neutrals by electron collisions.

CONCLUSIONS

Historically, values adopted for the thermospheric UV heating efficiency have ranged between 0.1 and 1.0. Of the most recent calculations Chandra and Sinha [16] reported a value for ϵ of 0.5 to 0.6 but did not discuss the altitude variation. The value of 0.3 of Stolarski et al [14] has been widely incorporated into thermospheric models. The results reported here will thus require significant revision of thermospheric models. For example, estimates of additional sources such as joule heating obtained from global thermospheric circulation models will require re-evaluation.

As has been shown here, the diurnal phase effects are significant and may eliminate or reduce the problems that have been encountered in reproducing the observed thermospheric temperature over a diurnal cycle.

An impact of the dynamic variability of ϵ that has emerged from this study, is that the incorporation of this parameter into global thermospheric models will not be as simple as it was when a constant of ~ 0.3 value was used. A more complex parameterization as a function of altitude, local time, season, latitude and solar cycle is required. We are currently investigating whether a multicoefficient harmonic fit is a possible solution to this problem.

ACKNOWLEDGEMENTS

This work was supported by NSF grant ATM78005088 and NASA grant NASS-24331. The calculations reported in this paper were carried out under a grant of computer resources from the National Center for Atmospheric Research which is sponsored by the National Science Foundation.

REFERENCES

1. M. R. Torr, D. G. Torr and P. G. Richards, Geophys. Res. Lett. 7, 373 (1980a).
2. M. R. Torr, P. G. Richards, and D. G. Torr, J. Geophys. Res. in press, (1980b).
3. H. E. Hinteregger, D. E. Bedo and J. E. Manson, Radio Sci. 8, 349, (1973).
4. A. E. Hedin, J. E. Salah, J. V. Evans, C. A. Reber, G. P. Newton, N. W. Spencer, D. C. Kayser, D. Alcayde, P. Bauer, L. Cogger and J. P. McClure, J. Geophys. Res. 82, 2130, (1977a).

5. A. E. Hedin, C. A. Reber, G. P. Newton, N. W. Spencer, H. C. Brinton, H. G. Mayr, and W. E. Potter, J. Geophys. Res. 82, 2148, (1977b).
6. D. G. Torr, and M. R. Torr, Rev. Geophys. Space Phys. 16, 327, (1978).
7. D. G. Torr, and M. R. Torr, J. Atmos. Terr. Phys. 85, 783, (1979).
8. E. R. Young, D. G. Torr and P. G. Richards, Air Force Rept. AFGL-TR-79-0125, (1980a).
9. E. R. Young, D. G. Torr, P. G. Richards and A. F. Nagy, Planet. Space Sci. in press (1980).
10. E. R. Young, P. G. Richards, and D. G. Torr, J. Comp. Phys. in press, (1980b).
11. P. G. Richards, E. R. Young and D. G. Torr, Canberra, Australia, (1979).
12. A. F. Nagy, and P. M. Banks, J. Geophys. Res. 75, 6260, (1970).
13. P. G. Richards, D. G. Torr and M. R. Torr, J. Geophys. Res. submitted, (July 1980).
14. R. S. Stolarski, P. B. Hays and R. G. Roble, J. Geophys. Res. 80, 2266, (1975).
15. H. E. Hinteregger, Ann. Geophys. 26, 547, (1970).
16. S. Chandra, and A. K. Sinha, Planet. Space Science 21, 593, (1973).

SECTION 2
Energy Inputs and Models

PRECEDING PAGE BLANK-NOT FILMED

ENERGY TRANSFER BY GRAVITY WAVE DISSIPATION

K.D. Cole and M.P. Hickey

*Division of Theoretical and Space Physics,
La Trobe University, Bundoora, Victoria, Australia 3083*

ABSTRACT

This paper reviews the subject of the dissipation of internal gravity waves in the thermosphere and shows how this is related to propagation. Differences of dissipation and heating rates in quiet and disturbed atmospheres are discussed, and the ranges of waves for different source heights in these atmospheres are calculated. Despite heavy damping of the waves, they may explain T.I.D.'s and related airglow observations in middle and low latitudes.

INTRODUCTION

The energy content of the thermosphere is derived principally from the sun in two ways; firstly by the absorption of radiation (EUV and UV) and secondly by the capture of energy from the solar wind. The EUV radiation will heat only the day-time thermosphere, and appears not sufficient by itself to maintain the observed thermospheric temperatures [1]. The capture of energy from the solar wind leads to a high-latitude heat source due to dissipation of electric fields and currents in auroral regions [2, 3] and occurs both by day and by night [4]. The longitudinal (due to the EUV heating) and latitudinal (due to the heating in auroral regions) anisotropies of these heat sources lead to the so-called diurnal and polar bulges [5] and mean that the distribution of energy of the thermosphere is always far from equilibrium, so that conductive and convective processes will act to re-distribute this energy (see for example [6, 7, 8]).

The main mechanical processes which occur in the thermosphere are winds, tides, acoustic waves and gravity waves. It is well known that energy can be transported in the thermosphere by winds [9, 10, 11], the semi-diurnal tide [12] and acoustic waves [13], but we are interested here only in the transport of energy by gravity waves. We will summarize, in order, the observations, sources, dissipation, thermospheric heating, and propagation of gravity waves. Problems with gravity wave theory in explaining certain observations and ideas concerning the possible resolutions of these problems are discussed. Finally, a conclusion will be given. It will be assumed that the reader has a basic knowledge of gravity wave theory, as discussed for example by Hines [14], Eckart [15], and Tolstoy [16].

OBSERVATIONS

Some of the earliest observations of travelling ionospheric disturbances (T.I.D.'s) were those of Munro [17, 18, 19], which, coupled with the radar observations of drifting meteor trails [20], led Hines [14] to hypothesize that the T.I.D.'s were simply the manifestations of neutral, internal gravity waves in the ionospheric plasma, a generally accepted result today. Since then there have been many observations of T.I.D.'s, of which we can make the following summary.

Heisler [21] and Valverde [22] found that some T.I.D.'s could travel several thousand kilometers with little attenuation. Tveten [23] observed T.I.D. speeds to be usually 40-300 m/sec with only a few up to 1250 m/sec, while Chan and Villard [24] found speeds of 400-750 m/sec with periods of 30-90 mins and horizontal wavelengths of 1300-2000 kms. Bowman [25], by studying world-wide ionograms, found two T.I.D.'s launched by the same event which travelled at speeds of 361 m/sec and 722 m/sec respectively, the former being able to propagate completely around the globe. Thome [26] observed a T.I.D. which propagated some 3000 kms at a speed of 700 m/sec. Georges [27] observed many T.I.D.'s and classed them as large-scale if their speeds were in excess of 300 m/sec (approximately the lower atmospheric sound speed) and medium-scale if their speeds were lower than 300 m/sec. Harper [28] observed a T.I.D. near the equator having a period of about 105 mins and an estimated horizontal wavelength of 4000 kms, while another large-scale wave was observed by satellite by Trinks and Mayr [29], with a period of 2.5 hrs and an apparent horizontal wavelength of 5000 kms. There have been many observations of medium-scale T.I.D.'s with speeds between 50 and 200 m/sec and periods ranging from 20-100 mins [30, 31].

SOURCES

In the lower atmosphere sources of gravity waves can include severe weather systems [27, 32] as well as the meteorological jet-stream [31, 33]. A flux of 10^{-1} watts/m² commonly leaves the troposphere [34] so that significant amounts of energy could reach the thermosphere from the lower atmosphere after absorption and reflection by mesospheric winds. In the middle atmosphere the main sources can include the possible breaking of tidal motions [14], wind instabilities [35] and the supersonic motion of the terminator between $\pm 45^\circ$ latitudes [36, 37], especially in the ozone layer [38].

In the thermosphere the main sources of gravity waves lie in the auroral zones and there is much evidence to support this [24, 39, 40]. The generation here is due to both the Lorentz force ($\underline{F} = \underline{J} \times \underline{B}$) and Joule heating ($Q = \underline{J} \cdot \underline{E}$) and has been studied by many authors (see e.g. [40] and references therein). Testud [41] found that the efficiency of the Lorentz force in creating gravity waves was greater than that due to Joule heating, whereas Richmond [42] has found that waves produced by Joule heating can more easily travel to middle and low latitudes. The total wave energy produced to the total energy input during a magnetic storm can be as high as 15.6% [42], while model calculations comparing the theoretical ionospheric response with the observed response due to the passage of a gravity wave at mid-latitudes show that at times, the total energy input to the auroral zone can be as large as 1.6×10^{23} ergs (1.6×10^{16} J) [43]. Evidence for the trans-polar propagation of waves created during magnetic storms has been given by Potter et al [44]. The dominant force at equatorial latitudes is the Lorentz force in the equatorial electrojet, but Chimonas [45] has concluded that it is inefficient in exciting gravity waves because $\underline{J} \times \underline{B}$ is vertical while long period gravity waves transport energy

predominantly horizontally [27]. The possible evidence for waves produced by the equatorial electrojet can be found in [44].

DISSIPATION

Gravity waves in the thermosphere can be dissipated by viscosity and thermal conduction [46], ion-drag [47], molecular relaxation [48, 49] and diffusive separation [50]. Dissipation leads to the production of a number of dissipative waves [51, 52, 53], but these are usually ineffective in transporting energy very far [54]. Pitteway and Hines [46] showed that the dissipation due to thermal conduction is slightly greater than that due to viscosity, and that if this dissipation is small then only the amplitude of the wave is affected. The dissipation due to viscosity and thermal conduction generally decreases with increasing wavelength [55, 56], whilst that due to ion-drag increases with wave period and is a minimum for waves propagating along the magnetic meridian [55].

The dissipation rates due to viscosity and thermal conduction are inversely proportional to the neutral gas density and so rapidly increase with height. These dissipation rates also depend on the temperature structure of the thermosphere [57], because this affects the wave group velocity (a hotter thermosphere refracts the wave energy up at more oblique angles and thus increases the dissipation rate). Thus gravity wave dissipation depends strongly on local time and solar activity, as well as magnetic activity. For example, it was shown that the dissipation rate due to viscosity increases as the angle of energy flow (θ) from the horizontal increases, because for $\omega^2 \ll \omega^2 g$ and with the asymptotic relation $k^2 z \gg \omega^2 a/C^2$, the loss in vertical energy-flux (ΔF) can be written as

$$\Delta F = nhA^2k^6x \frac{\gamma - 1}{\omega^2} g^4 \tan^2 \theta \quad (1)$$

where all symbols have their usual meanings (see [57]). Their results also show that most waves dissipate within one wavelength for a source at the 120 km level, but that this attenuation distance rapidly decreases as the source height is increased. This can be seen in figures 1 - 4, in which the 'hot' atmosphere refers to the CIRA [58] Model 10 atmosphere at 1400 hrs, and the 'cold' atmosphere refers to the CIRA [58] Model 1 atmosphere at 0600 hrs. The attenuation distance is taken as the distance over which the energy flux is reduced to 30% of its initial value. Figures 1 and 2 show that more energy propagates to greater horizontal distances in the cold atmosphere for source heights less than about 200 kms, while the situation is reversed for source heights greater than this. For a source height of 120 kms, the horizontal range in the cold atmosphere is some 30 - 45% greater than that in the hot atmosphere, the larger number referring to the larger-scale wave. Figures 3 and 4 show that the vertical range is always greater in the hot atmosphere than in the cold atmosphere, a similar result having been obtained by Yeh et al [55]. This means that significantly more energy can be transported to greater altitudes at times of high solar and magnetic activity and during daylight hours than at times when the thermosphere is colder. A further interesting feature seen by comparing figures 3 and 4 is that the vertical range does not seem to depend on the wave parameters as much as the horizontal range does (Figures 1 and 2), which is due to the fact that although the larger scale wave suffers a lower dissipation rate, its energy is transported at an angle much closer to the horizontal than the smaller scale wave, effectively impeding the propagating of energy to high altitudes.

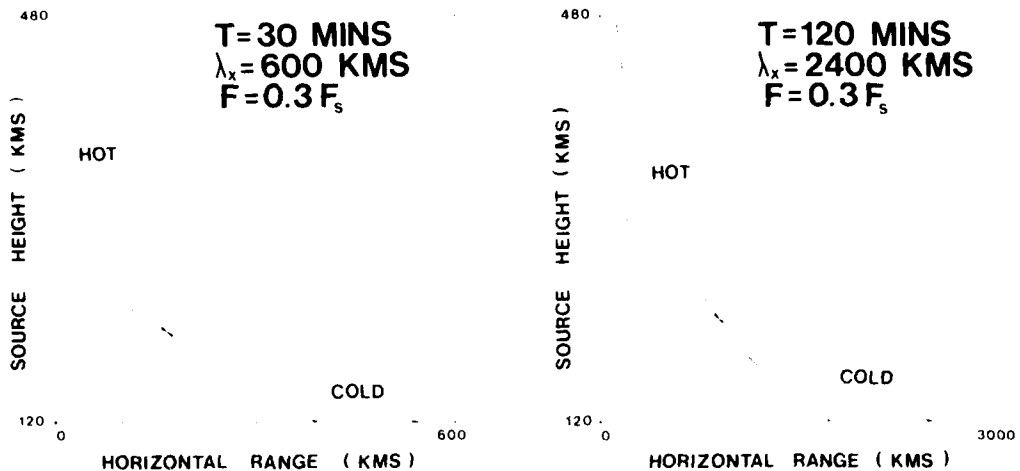


Figure 1

Figure 2

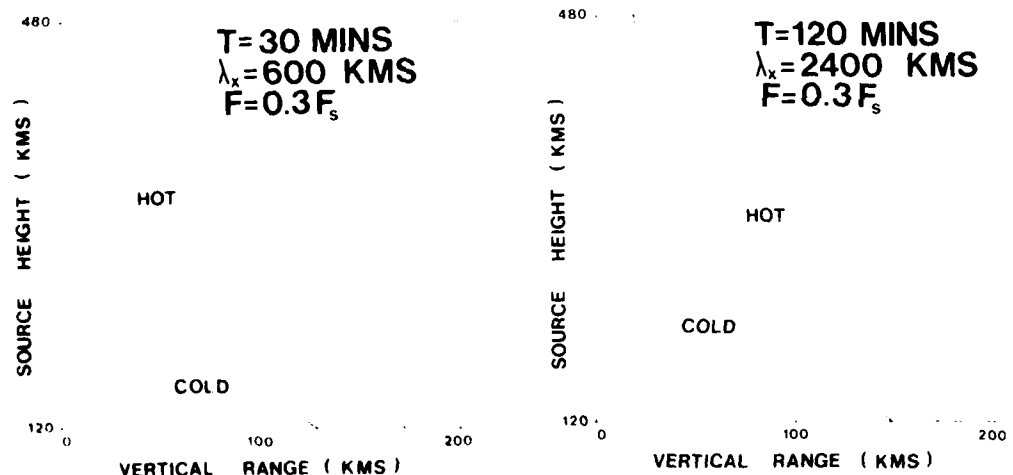


Figure 3

Figure 4

Figures 1 - 4

Attenuation distances defined as the distances over which the energy flux is reduced to 30% of its initial value in both the 'hot' (CIRA (1965) model 10 atmosphere at 1400 hrs.) and 'cold' (CIRA (1965) model 1 atmosphere at 0600 hrs) atmospheres.

There is now theoretical evidence which shows that diffusive separation is an important dissipative mechanism for gravity waves in the lower thermosphere [50], which increases with wave period and decreases with wavelength. For example, a wave of period 60 mins and horizontal wavelength 400 kms will lose 60% of its energy in propagating between the 140 and 240 km levels, whereas in the same altitude range a wave of period 20 mins and the same wavelength will lose only about 10% of its original energy.

HEATING OF THE THERMOSPHERE

Dissipation rates of gravity waves have been estimated to be about 5×10^{-2} watts/kg (5×10^2 ergs/gm sec) near the 95 km level [59], 4×10^{-1} watts/kg near the 105 km level [60], and possibly greater than 1 watt/kg some 50% of the time at the 140 km level [60], giving heating rates of about $4^\circ\text{K}/\text{day}$, $30^\circ\text{K}/\text{day}$ and $100^\circ\text{K}/\text{day}$, respectively. Testud and Vasseur [61] observed a T.I.D. following a magnetic storm and noted that the ion temperature at the 300 km level rose to values of some 50 - 100°K above normal. They explained this by calculating that the vertical energy flux through the 200 km level was 1.6×10^{-5} watts/m² (1.6×10^{-2} ergs/cm² sec) which was about 10% of that thought to be deposited by EUV radiation above the same level (2×10^{-4} watts/m²). Testud [62] and Yeh [30] have estimated that heating rates of the order of 10^{-10} watts/m³ (10^{-9} ergs/cm³ sec) occur at F-region heights due to gravity wave dissipation, and that temperature increases of some 80°K can therefore be expected [62]. Several theoretical studies have calculated the altitude distributions of the energy input rate to the thermosphere due to the dissipation of gravity waves by viscosity, thermal conduction and ion-drag [63, 64, 57], and will now be discussed.

Klostermeyer [63] calculated the energy deposition rate for a wave of period 30 mins, horizontal wavelength 600 kms, and an initial vertical energy flux of 1.25×10^{-4} watts/m² at the lower boundary (170 kms), typical of what one might see following a magnetic substorm. It was noted that although thermal conduction will dissipate wave energy, it will not heat the background gas. His results gave a maximum heat input of 4.5×10^{-10} watts/m³ at the 235 km level, and a height distribution very similar to that of the EUV heat input. The height profile of the irreversible temperature increase was found to be similar to that of the undisturbed temperature profile and to vary logarithmically with time. An exospheric temperature increase of some 40°K was inferred.

Vidal-Madjar [64] studied the dissipation of a wave having its source in the troposphere [31] with a period of 20 mins, horizontal wavelength 150 kms, and a vertical energy flux of 10^{-4} watts/m² at the 120 km level (see [33]). Both the effects of background winds and different azimuths of propagation were included, and all the terms in the equation of heat transfer were retained. In the windless case the maximum energy deposition rate was 7×10^{10} watts/m³ at 160 kms altitude, while the mean value between 120 and 200 kms altitude was 5×10^{-10} watts/m³, roughly 10% of the solar deposition rate for the same region. Vidal-Madjar further showed that certain regions of the thermosphere can actually be cooled by gravity waves, even in the presence of dissipation.

Hickey and Cole [57] have studied the energy deposition to the thermosphere caused by the dissipation of the same two waves which Klostermeyer [63] and Vidal-Madjar [64] studied, under different atmospheric conditions, as discussed in the last section. The results for the 30 minute period wave are shown in figures 5 and 6. As with the dissipation rates discussed previously, the energy deposition rates per unit volume (fig. 5) and per unit mass (fig. 6) depend quite strongly on atmospheric conditions (solar cycle, etc.). The maximum deposition rate per unit volume for this wave ranges from about 7.5×10^{-10} watts/m³ at

245 kms altitude in the cold atmosphere to about 3.8×10^{-10} watts/m³ at 270 kms altitude in the hot atmosphere. The heating rates per unit mass show a much larger variation. Maximum heating rates here are about 35 watts/kg at 265 kms altitude in the cold atmosphere and about 5.5 watts/kg at 325 kms altitude in the hot atmosphere. Significant heating can only occur at high altitudes during times of high solar and magnetic activity and during daylight hours.

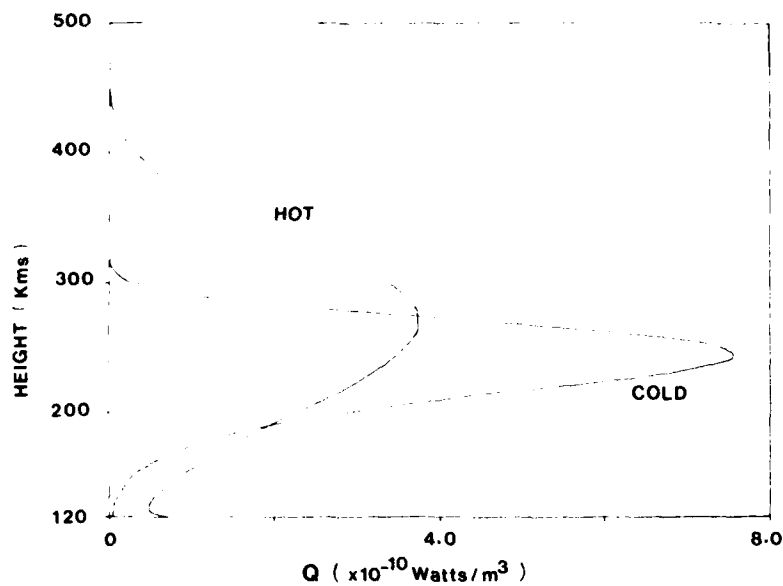


Figure 5

Energy deposition rate per unit volume for the hot and cold atmospheres as defined in the text, for a wave of period 30 mins, horizontal wavelength 600 kms and vertical energy flux at the 120 km level of 1.25×10^{-4} watts/m².

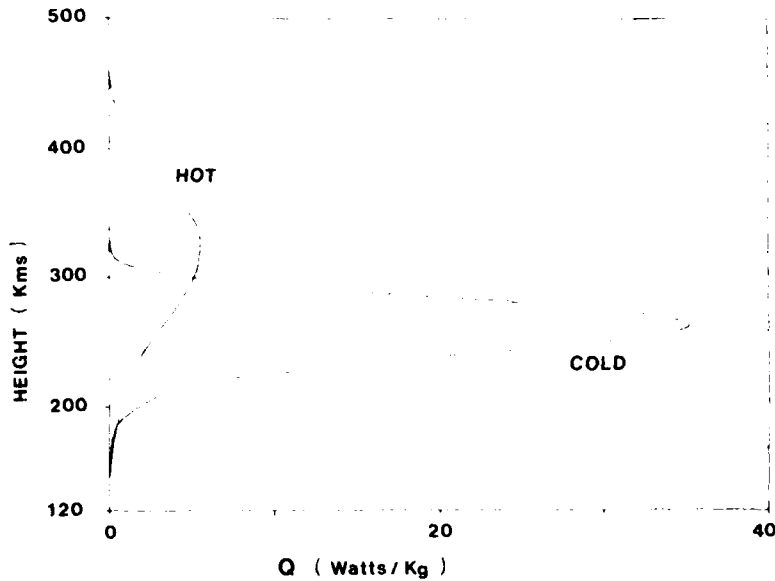


Figure 6

Energy deposition rate per unit mass for the wave as described in Fig. 5.

Richmond [11] has calculated the heating at middle and low latitudes due to both gravity wave dissipation and compressional heating of the meridional circulation set up by auroral heating. He has found that compressional and wave heating are comparable at high altitudes (>250 kms) but the compressional heating is much more important at low altitudes.

Cole [65] has involved the action of internal gravity waves in low latitude conjugate E-regions for the production of field-aligned irregularities in the equatorial F-region. In an extension of this work Cole [66] estimated the joule heating by electric fields associated in equatorial spread-F (at night) to be as much as EUV heating during the day.

PROPAGATION

There have been a number of studies in the past dealing with the ducting of gravity waves [26, 67, 68, 69]. The importance of ducting in the thermosphere is that it keeps most of the waves at low levels where the effects of dissipation are small, and hence allows for certain modes of propagation to travel to large horizontal distances without severe attenuation. However Richmond [69] has strongly criticised the earlier works which dealt with ducting in the thermosphere and shown that these models cannot be legitimately applied to the thermosphere. He has suggested an alternative ducting mechanism which relies on partial reflections at the top of the 'duct' due to dissipative mechanisms [70, 71] and obtained three thermospheric modes with similar properties to those

of Francis [54], but he himself doubts the usefulness of this alternative mechanism. If this is the case, then the only possibility left is that all gravity waves are freely propagating (internal) and subject only to dissipation and small partial reflections as they propagate upward. Some support for a return to the simple idea of freely propagating gravity waves as a cause of T.I.D.'s observed at low latitudes following magnetic storms can be found in the results of Roble et al [39]. They performed a numerical simulation of the ionospheric response to freely propagating gravity waves produced by a substorm and compared these results to observations made at two different sites, and reasonably good agreement was obtained at both sites.

Since, however, internal gravity waves necessarily have speeds less than about $0.9C$ (C = the local sound speed) a difficulty arises when trying to explain observations of high speed F-region T.I.D.'s, when near their source regions (at 120-140 kms in the auroral zone) they would have speeds exceeding the local sound speed. This, as Francis ([72] p.1039) has noted, would require sources to exist at altitudes considerably higher than is usually supposed, where the sound speed is higher. Possible observational evidence in support of high altitude gravity wave sources can be found in [29]. They observed a large-scale gravity wave with a speed of perhaps 550 m/sec, which was generated at high latitudes during fairly quiet magnetic conditions and possibly within the dayside cusp region. They suggested that soft particles may have been the dominant energy source, and from a comparison between experimental results and theory they concluded that thermospheric sources possibly as high as 200 kms altitude were responsible for the excitation of the observed wave phenomena.

Francis [73] showed that a gravity wave source will produce two waves for a given wave frequency and horizontal wavenumber, one propagating energy upwards (the direct wave, for which $kz < 0$) and the other propagating energy initially downwards (the indirect wave). For a source at an altitude of 200 kms the results of Hickey and Cole [57] show that the horizontal range of the direct wave will be less than one half of a wavelength (see figs. 1 and 2) and so would be ineffective in producing observable T.I.D.'s at low latitudes. However, as Richmond [56] has shown, the indirect waves suffer a much lower attenuation rate than the direct waves, so that if a high altitude gravity wave source did exist, only the indirect waves should be capable of transporting significant amounts of energy to low latitudes. An indirect wave having a horizontal phase speed (u) greater than about 250 m/sec will be reflected upward from the lower thermosphere [56], while for $u < 250$ m/sec it will become the earth-reflected wave of Francis [73]. If we imagine a high altitude source at a level where, for example, the local sound speed is 1000 m/sec, then it would be possible to create any indirect wave having a horizontal phase speed less than 900 m/sec. It will travel downwards into regions of ever-decreasing dissipation towards its reflection level, and the lower the speed of the wave, the lower this level will be. It would eventually suffer reflection there so that by the time it has reached mid latitudes, it would be observed as a direct wave. If a high altitude gravity wave source can be shown to exist, then the importance of this postulated mechanism in explaining observations of large-scale, high-speed gravity waves should not be overlooked.

CONCLUSION

Present theory concerning both the propagation and dissipation of gravity waves appears to be limited in explaining some of the large speeds with which, and large distances over which, they are known to travel. The observations of Bowman [25] for example, cannot be explained by gravity wave theory, since gravity waves could not travel such large distances at speeds exceeding the

speed of the Lamb wave. The observations of Titheridge [74] are difficult to explain by standard dissipation theory, for a wave with a horizontal speed of 140 m/sec should not be able to propagate up to the 500 km level. The new theoretical calculations of Del Genio et al [50] show that diffusive dissipation can be large for some of the longer period gravity waves and would further inhibit the transfer of energy from the auroral zones to low latitudes. Heating rates of the thermosphere due to the dissipation of gravity waves appear to contribute significantly to the heat budget of the thermosphere, typically being about 10% of that of the EUV heating rate. While any estimates for the heating rates at low latitudes may require a greater understanding of the propagation characteristics of large-scale waves travelling away from the auroral zone, the resolution of the problem may be as follows.

Despite the heavy damping of internal gravity waves in the thermosphere they may nevertheless be capable of carrying sufficient energy from the auroral ionosphere to the middle and low latitude ionosphere to cause large scale travelling ionospheric disturbances and corresponding airglow fluctuations. Consider the energy flux in a T.I.D. from the auroral zone, in which, for example, the neutral atmospheric velocity is 100 m/sec and the group velocity is 400 m/sec; the horizontal meridional energy flux throughout the F-region would be approximately $5 \times 10^5 \text{ ergs cm}^{-1} \text{ sec}^{-1}$. Allowing for an e^3 decrease of wave energy on account of dissipation during propagation, a decrease by a factor of 5 to allow for geometric spreading of the wave, and also adopting an efficiency of only 10% for the generation of gravity waves by the auroral electrojet, the waves would need to have been produced by an auroral electrojet in which the heating was of order $5 \times 10^5 \times e^3 \times 5 \times 10 \text{ ergs cm}^{-1} \text{ sec}^{-1}$ along its length, i.e. about $6 \times 10^8 \text{ ergs cm}^{-1} \text{ sec}^{-1}$. Assuming an auroral electrojet 300 km wide this requires an energy deposition rate in the jet of order $20 \text{ ergs cm}^{-2} \text{ sec}^{-1}$. Such heating rates can exist in auroral electrojets. Detailed observations and calculations of particular events are necessary to confirm or deny this proposed resolution of an apparent difficulty.

REFERENCES

1. I. Harris and W. Priester, J. Atmos. Sci., 19, 286 (1962)
2. K.D. Cole, Aust. J. Phys. 15, 223 (1962)
3. K.D. Cole, Planet. Space Sci. 19, 59 (1971a)
4. B.K. Ching and Y.T. Chiu, Planet. Space Sci. 21, 1633 (1973)
5. L.G. Jacchia, Nature, 183, 526 (1959)
6. S. Chandra and A.K. Sinha, Planet. Space Sci. 21, 593 (1973)
7. K.D. Cole - Energy balance of the atmosphere under the influence of a disturbed sun and magnetospheric processes, in Dynamical and Chemical Coupling Between the Neutral and Ionized Atmosphere, p. 203, E. Grandal and J.A. Holtet (Eds.), D. Reidel Publ. Co., Holland, (1977)
8. D.A. Glenar, E. Bleuler and J.S. Nisbet, J. Geophys. Res. 83, 5550 (1978)
9. G. Hernandez and R.G. Roble, J. Geophys. Res., 81, 5173 (1976)
10. R.G. Roble - Variations of the mean meridional circulation in the thermosphere, in Dynamical and Chemical Coupling Between the Neutral and Ionized Atmosphere, p. 217, B. Grandal and J.A. Holtet (Eds.), D. Reidel Publ. Co., Holland (1977)
11. A.D. Richmond, J. Geophys. Res., 84, 5259 (1979b)
12. R.S. Lindzen and D. Blake, J. Geophys. Res., 75, 6868 (1970)
13. D. Rind, J. Atmos. Terr. Phys., 39, 445 (1977)
14. C.O. Hines, Can. J. Phys., 38, 1441 (1960)
15. C. Eckart, Hydrodynamics of Oceans and Atmospheres, Pergamon Press, New York, (1960)

16. I. Tolstoy, Rev. Mod. Phys., 35, 207 (1963)
17. G.H. Munro, Nature, 162, 886 (1948)
18. G.H. Munro, Proc. R. Soc., A202, 208 (1950)
19. G.H. Munro, Aust. J. Phys., 11, 91 (1958)
20. J.S. Greenhow and E.L. Neufeld, J. Geophys. Res., 64, 2129 (1959)
21. L.H. Heisler, Aust. J. Phys., 11, 79 (1958)
22. J.F. Valverde, Radio Prop. Lab. Sci. Rept. No.1, Stanford Electronics Labs., Stanford, Cal., U.S.A. (1958)
23. L.H. Tveten, J. Res. Nat. Bur. Standards 65D, 115 (1961)
24. K.L. Chan and O.G. Villard, (Jr.), J. Geophys. Res., 67, 973 (1962)
25. G.G. Bowman, J. Atmos. Terr. Phys., 27, 1247 (1965)
26. G.D. Thome, J. Geophys. Res., 73, 6319 (1968)
27. T.M. Georges, J. Atmos. Terr. Phys., 30, 735 (1968)
28. R.M. Harper, J. Geophys. Res., 77, 1311 (1972)
29. H. Trinks and H.G. Mayr, J. Geophys. Res., 81, 4023, (1976)
30. K.C. Yeh, J. Geophys. Res., 77, 709 (1972)
31. F. Bertin, J. Testud, L. Kersley and P.R. Rees, J. Atmos. Terr. Phys., 49, 1161 (1978)
32. R.J. Hung and T. Phan, J. Atmos. Terr. Phys., 40, 831 (1978)
33. L. Bertel, F. Bertin, J. Testud and D. Vidal-Madjar, J. Atmos. Terr. Phys., 40, 691 (1978)
34. E.E. Gossard, J. Geophys. Res., 67, 745 (1962)
35. I. Tolstoy and C.D. Miller, J. Atmos. Terr. Phys., 37, 1125 (1975)
36. W.J. Raitt and D.H. Clark, Nature, 243, 508 (1973)
37. T. Beer, Nature, 242, 34 (1973)
38. R.N. Datta, Ind. J. Radio Spa. Phys., 6, 9 (1977)
39. R.G. Roble, A.D. Richmond, W.L. Oliver and R.M. Harper, J. Geophys. Res., 83, 999 (1978)
40. R.G. Roble, R.E. Dickinson, E.C. Ridley and Y. Kamide, J. Geophys. Res., 84, 4207 (1979)
41. J. Testud, Ph.D. thesis, Univ. of Paris VI, Paris (1973)
42. A.D. Richmond, J. Geophys. Res., 84, 1880 (1979a)
43. G. Hernandez and R.G. Roble, J. Geophys. Res., 83, 5531 (1978)
44. W.E. Potter, D.C. Kayser and K. Mauersberger, J. Geophys. Res., 81, 5002 (1976)
45. G. Chimonas, Planet. Space Sci., 18, 583 (1970)
46. M.L.V. Pitteway and C.O. Hines, Can. J. Phys., 41, 1935 (1963)
47. C.O. Hines, J. Atmos. Terr. Phys., 30, 851 (1968)
48. C.O. Hines, Planet. Space. Sci., 25, 1045 (1977a)
49. C.O. Hines, Planet. Space. Sci., 25, 1061 (1977b)
50. A.D. Del Genio, G. Schubert and J.M. Straus, J. Geophys. Res., 84, 4371 (1979)
51. H. Volland, J. Geophys. Res., 74, 1786 (1969a)
52. H. Volland, J. Atmos. Terr. Phys., 31, 491 (1969b)
53. J. Klostermeyer, J. Atmos. Terr. Phys., 34, 765 (1972)
54. S.H. Francis, J. Geophys. Res., 78, 2278 (1973)
55. K.C. Yeh, C.H. Liu and M.Y. Youakim, Ann. Géophys., 31, 321 (1975)
56. A.D. Richmond, J. Geophys. Res., 83, 4131 (1978b)
57. M.P. Hickey and K.D. Cole, submitted to J. Atmos. Terr. Phys., (1980)
58. CIRA, Cospar International Reference Atmosphere, North-Holland Publishing Company, Amsterdam, (1965)
59. C.O. Hines, Quart. J. Roy. Met. Soc., 89, 1 (1963)
60. C.O. Hines, J. Geophys. Res., 70, 177 (1965)
61. J. Testud and G. Vasseur, Annls. Géophys., 25, 525 (1969)
62. J. Testud, J. Atmos. Terr. Phys., 32, 1793 (1970)
63. J. Klostermeyer, J. Atmos. Terr. Phys., 35, 2267 (1973)

64. D. Vidal-Madjar, J. Atmos. Terr. Phys., 41, 279 (1979)
65. K.D. Cole, J. Atmos. Terr. Phys., 33, 741 (1971b)
66. K.D. Cole, J. Atmos. Terr. Phys., 36, 1099 (1974)
67. M.L.V. Pitteway and C.O. Hines, Can. J. Phys., 43, 2222 (1965)
68. J.P. Friedman, J. Geophys. Res., 71, 1033 (1966)
69. A.D. Richmond, J. Geophys. Res., 83, 1385 (1978a)
70. M. Yanowitch, Can. J. Phys., 45, 2003 (1967)
71. R.S. Lindzen, Can. J. Phys., 46, 1835 (1968)
72. S.H. Francis, J. Atmos. Terr. Phys., 37, 1011 (1975)
73. S.H. Francis, J. Geophys. Res., 79, 5245 (1974)
74. J. Titheridge, J. Geophys. Res., 74, 1195 (1969)

OBSERVATIONS OF THE AURORA IN THE FAR ULTRAVIOLET FROM "COSMOS-900"

K.I. Gringauz,¹ L. Martini,² N.M. Shuttle¹ and
A.I. Puolokainen¹

¹ Space Research Institute, Academy of Sciences of the
USSR, Moscow, USSR

² Institute for Electronics, Academy of Sciences, GDR

ABSTRACT

The results from observations of auroral emissions within the wavelength band 115 - 135 nm are presented. The experiment was carried out on board the satellite "Cosmos-900", launched on March 30, 1977, to an almost circular polar orbit. We assume that the precipitating fluxes of protons and electrons were the sources of excitation, according to the theory.

INTRODUCTION

The extreme ultraviolet region of auroral emission spectrum (≤ 135 nm) has remained relatively unexplored because of the inaccessibility to ground-based observations, the experimental difficulties of such measurements, and the limited number of rocket and satellite experiments. In this paper results from observations of auroral emissions within the wavelength band 115 - 135 nm are presented. The experiment was carried out on board the satellite "Cosmos-900", launched on March 30, 1977, to an almost circular polar orbit ($h \sim 500$ km, inclination $\sim 83^\circ$).

In order to record the auroral emissions the ionization chamber was installed so that its entrance window was always directed towards the Earth. The ionization chamber consisted of coaxial electrodes and a MgF_2 entrance window [1]. Nitrogen oxide NO was used as a gas filling. It is possible to determine the chamber quantum efficiency within the wavelength band up to $\sim 50\%$ [2]. The ionization chamber spectral sensitivity determined by the potential of the photoionization filling NO and the threshold of radiation absorption by the entrance window of MgF_2 is within the wavelength range 115 - 135 nm. A special collimator consisting of an aluminium tube with a diaphragm system was installed to protect from scattered radiation. Absolute sensitivity characteristics of the ionization chamber is known from pre-flight laboratory calibrations. Table 1 gives basic parameters of the ionization chamber.

TABLE I

Spectral sensitivity	115 - 135 nm
Effective area	31 mm ²
Field of view	22°
Geometric factor	3,6 mm ² sr
Quantum efficiency	3.5

The telemetry data indicating a normal working of the instrument were received up to late April, 1978. It was possible to observe continuously both the day-side and night-side glows of the atmosphere in the ultraviolet wavelength region by a fixed three-axis orientation of the spacecraft which directed the field of view of the ionization chamber to the Earth with an accuracy of several degrees. Taking into account the results of measurements by other authors [3-9] it is evident that the ionization chamber must record auroral emissions at the following wavelengths: atomic oxygen 130.6, 130.5, 130.2 nm, Lyman-alpha 121.56 nm, atomic nitrogen 120 nm, and molecular nitrogen band emissions.

RESULTS OF OBSERVATIONS AND DISCUSSION

The results described refer to September, 20-22, 1977. Figures 1 and 2 give the data for two orbits of the spacecraft during each of which it crossed the auroral latitudes twice. It should be noted that during the flight the level of the scattered radiation background was practically constant. On the illuminated and the dark parts of the orbit in most cases its value was close to that of the noise level. It can be assumed that such a low level of scattered radiation was reached due to the use of an entrance collimator, contrary to the experiments by Unubb and Hicks [4, 5]. As seen from Figs. 1 and 2 the ionization chamber signals exceeded the background only at the auroral oval latitudes along the orbit including the polar cap regions. Spatial characteristics of the emissions extending from 1.5° to 5° in invariant latitudes are rather complicated. It is possible to separate two different structures: large-scale structure with regions of higher intensity extending from ~ 100 km to ~ 500 km, and fine-scale structure with multi-peaks pointing to substantial time and spatial variations with intensities changing rapidly within several fractions of a second. Fig. 3 gives an example of the structure of emissions in the northern hemisphere at the invariant latitudes $\Lambda = 84^\circ - 88^\circ$ at night MLT, with a rate of telemetry data transmission of 5 msec. Two regions of higher intensity are distinguished, recorded during a time interval of 30 sec. The intensity growth from minimum to maximum being rather sharp.

The emissions recorded by the ionization chamber could be caused by Lyman-alpha emission, the nitrogen line at 120 nm, the triplet of oxygen emissions at 130.4 nm, and molecular nitrogen band emissions. The sharp intensity increase is evidence of a discrete character of these auroral arcs. Besides, the display of the

large-scale structure with the distinct maxima of intensity is evidence of not only one but at least two sources of excitation which can differ by the type of particles and by their energy [4, 10]. Considering these regions one can observe some variation in their intensities and extension. It allows us to assume that the precipitating fluxes of protons and electrons were the sources of excitation, according to the theory of Taylor et al. and Sather [11, 12].

We hope that after a more comprehensive investigation of the data we shall be able to distinguish the electron and proton sources of excitations, analyzing the amplitudes of the intensity maxima of these auroral arcs and their relative behaviour.

REFERENCES

1. L. Martini, N.M. Shutte, K.I. Gringauz and B. Stark, Kosm. Issled. **10**, 255 (1972).
2. J.H. Carver, R. Mitchell, E.L. Murray, J. Geophys. Res. **69**, 3755 (1964).
3. R.E. Miller, W.G. Fastie and R.C. Isler, J. Geophys. Res. **73**, 3353 (1968).
4. T.A. Chubb and G.T. Hicks, J. Geophys. Res. **75**, 1290 (1970).
5. G.T. Hicks and T.A. Chubb, J. Geophys. Res. **75**, 6233 (1970).
6. H. Park, P.D. Felman and W.G. Fastie, Geophys. Res. Lett. **4**, 41 (1977).
7. F. Fischer and G. Schmidtke, Space Research XIX, 317 (1979).
8. H.M. Peek, J. Geophys. Res. **75**, 6209 (1970).
9. W.E. Sharp and M.H. Rees, J. Geophys. Res. **77**, 1810 (1972).
10. B. Hultqvist, Ann. Geophys. **30**, 223 (1974).
11. H.E. Taylor and E.W. Hones, Jr., J. Geophys. Res. **70**, 3605 (1965).
12. R.H. Sather, Rev. Geophys. **2**, 207 (1967).

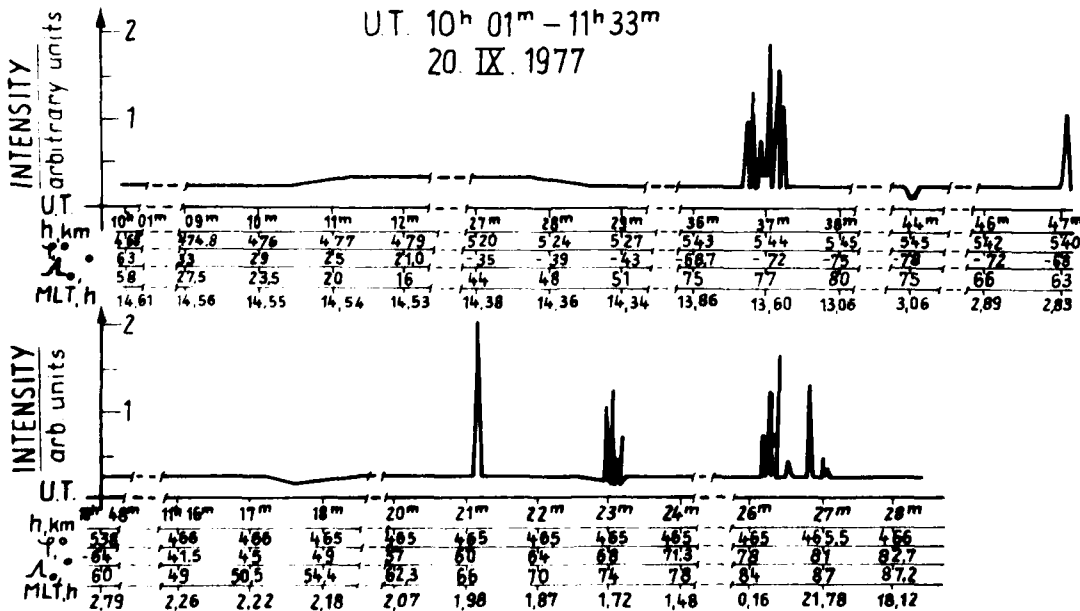


Fig. 1 Observations of aurora within the wavelength band 115 - 135 nm on September 20, 1977

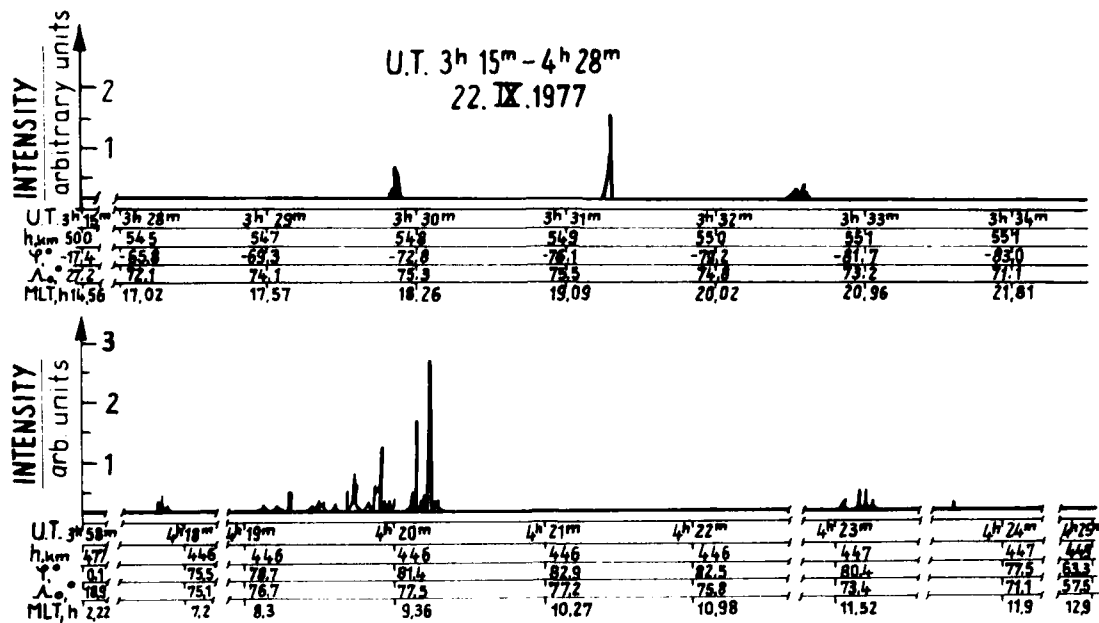


Fig. 2 Observations of aurora within the wavelength band 115-135 nm on September 22, 1977

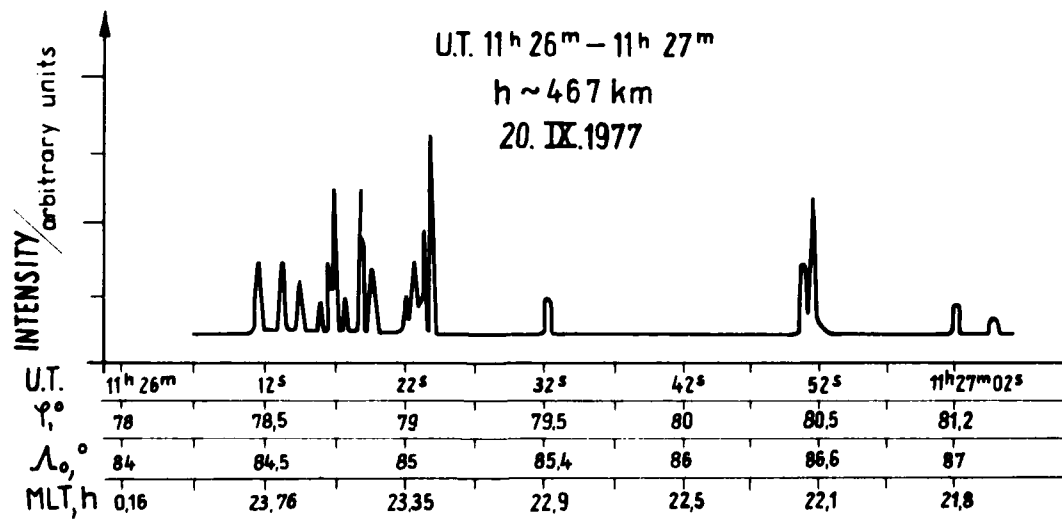


Fig. 3 Ionization chamber record on September 20, 1977;
MLT $\sim 15^{\text{h}}$ and UT $\sim 11^{\text{h}} 30^{\text{m}}$

EMPIRICAL MODELS OF THE THERMOSPHERE AND REQUIREMENTS FOR IMPROVEMENTS

L.G. Jacchia

*Center for Astrophysics, Harvard College Observatory and
Smithsonian Astrophysical Observatory, Cambridge,
Massachusetts 02138, USA*

ABSTRACT

The different types of variation in the thermosphere are briefly examined and the solar-activity effect is singled out for special attention. To this day, empirical models have made use of the decimetric solar flux $F_{10.7}$ as an index of the variable XUV radiation from the sun. To account for the change in the relative intensity of the different types of emissions in the course of the solar cycle, $F_{10.7}$ is made to perform double duty: The daily values are used to represent the day-to-day and "27-day" variations, while its averages over several solar rotations are used to represent the variations with the 11-year cycle. The availability of direct solar XUV data should eventually eliminate the need for such a make-shift procedure. Accuracy and continuity requirements of XUV intensity measurements are discussed and a strategy is outlined for sorting out the relevant features from the observational material and putting them to practical use in thermospheric modeling. It is suggested that future models of the diurnal and the geomagnetic variation use as a guide theoretical models which have achieved considerable success in qualitatively representing the observed phenomena.

EMPIRICAL MODELS

Up to a height of about 90 km the earth's atmosphere is heated mainly by radiation from a region in the solar spectrum where relative variations of intensity are small or insignificant. The radiation that filters through is not energetic enough to cause large-scale molecular dissociation of the main atmospheric constituents and mixing keeps the composition nearly constant. The temperature variations that are observed are mainly related to sun-earth geometry: seasonal-latitudinal and, to a lesser degree, diurnal; the resulting density variations are mostly confined to a factor-of-2 range. Under these circumstances it makes sense to make use of standard models for most homospheric problems.

A dramatic change occurs as we cross the 90-100 km region and enter the thermosphere, where the rarefaction of the air, now unable to sustain mixing, allows the variable, energetic solar XUV radiation to penetrate and do its work. The fluctuations in atmospheric density caused by the variability of the solar radiation grow rapidly with increasing height, to the point where the earth-sun geometry becomes secondary to the conditions of activity on the solar surface. Moreover, an additional, important source of heating, only indirectly related to solar activity, makes its appearance — the energy deposited in the atmosphere by the ionospheric currents that control geomagnetic phenomena. At a height of 600 km the 27-day fluctuation in XUV radiation caused by the rotation of the sun can cause density

variations exceeding a factor of 4, while from sunspot minimum to sunspot maximum the mean density can increase by a factor of 70 or more. In the course of a first-class magnetic storm the density may increase by a factor of 100. From all causes combined the density at 600 km can vary by three full orders of magnitude. And all these variations are accompanied by enormous changes in composition. In these conditions mean or standard atmospheric models have little or no meaning, as sad experience has taught a few forecasters of satellite lifetimes.

The need for good, realistic thermospheric models, capable of predicting temperatures, densities, and compositions for any height and geographic position when solar-activity and geomagnetic data are given, should be pretty obvious to all researchers. Ideally, one should be able to achieve this goal by feeding solar-radiation and ionospheric-current data into a purely theoretical model of the whole atmosphere. Any effort in this direction is certainly highly commendable, even though the present state of the art is so far from the ideal that the results of such efforts cannot be termed very realistic. Not only is the theory wanting, but even the observational data that are supposed to be fed into the model have not been available so far, and necessity has forced the use of empirical models based on second-hand observational data. From the earliest empirical models these second-hand input data have been the decimetric solar flux and the planetary geomagnetic index. As solar XUV data become increasingly available, time seems to be ripe for making plans on how to utilize these data in thermospheric models to replace the decimetric solar flux. The corresponding operation regarding the geomagnetic index would be to go back to the magnetograms of the individual stations that contributed to the planetary index and see if a better parameter could be devised for use in thermospheric models. I assume that with the magnetograms we are as close as we can get to the primary index of the magneto-atmospheric phenomenon.

If we want to tackle the problem of relating the observed XUV radiation with the observed thermospheric variations, it is essential that we carefully examine what are the questions to be asked. If we ask the wrong questions, we are bound to get wrong answers. Thus we must make use of all the experience we have accumulated to date in formulating the questions. We must first list the different types of atmospheric variation related to variations in solar XUV radiation and establish the most likely functional representation for each of them, relying - whenever possible - on physical theory. No computational program can do this for us. A giant least-squares solution will yield only the numerical coefficients of functions that have been preselected. There is no such thing as a "completely objective" thermospheric model. Even those models that have the external appearance of being more objective because they make use of expansions in terms of spherical harmonics rely in ultimate analysis on previously established functional forms, distinct for each type of variation.

At present we can distinguish the following types of thermospheric variation:

1. The solar-activity effect, with its two components:
 - a) the 11-year variation with the sunspot cycle,
 - b) the 27-day variation, connected with solar rotation.
2. The semiannual variation.
3. The diurnal variation, with its daily and annual components.
4. The seasonal-latitudinal variation.
5. The geomagnetic variation.

SOLAR XUV AND THERMOSPHERIC MODELS

The variations of the total 10.7-cm flux F from the sun approximate, in a qualitative manner, those of the solar XUV flux; that is the reason why its use in atmospheric models has been relatively successful. It was soon discovered, however, that the use of a single parameter to replace the complex variations of the XUV flux leads to difficulties: The relation between F and the exospheric temperature is different according to whether the interval considered is one solar rotation, 27 days, or the 11-year cycle of solar activity.

That this should be so is rather obvious. The 27-day variation is caused by the appearance and disappearance on the visible disk of the sun, as a consequence of its rotation, of a particularly extensive active area, and the relative intensities of the various effective XUV emissions do not greatly change during one solar rotation. The situation is radically different if we consider a much longer interval, such as the rise from sunspot minimum to sunspot maximum, when new emissions appear and increase in intensity much more rapidly than other, more permanent emissions. The difficulty was circumvented as best as one could, by splitting F into an instantaneous component to represent the short-term variations, and a smoothed component, the mean over several solar rotations, to represent the long-term variation. The availability of direct XUV observations should eventually eliminate this difficulty altogether; but, for the moment, we still have some obstacles to overcome.

Let us first examine the accuracy that is required of XUV intensity measurements in order to represent atmospheric density variations within their observational errors. A satellite-borne mass spectrometer can measure the number density of a "clean" constituent, such as molecular nitrogen, with a relative error of about 2%. Atmospheric noise, such as that produced by gravity waves, can be considerably larger than that, but can be eliminated within the observational accuracy when longer series of data are analyzed. Systematic errors affecting individual mass-spectrometer experiments can be more serious and more difficult to estimate, since direct *in situ* calibration is not feasible and cannot be replaced with complete assurance by laboratory calibration. Fortunately, densities derived from satellite drag provide an excellent standard against which mass-spectrometer densities can be calibrated, even when the experiments are fragmentary and separated by large gaps in time. The relative error of an individual drag determination decreases with the resolution. While it is much larger than that of mass-spectrometer densities when the satellite acceleration is determined from small time intervals, it decreases as the square of the time interval, until it becomes comparable to, and even smaller than, the mass-spectrometer error for longer intervals; comparisons, then, will have to be made with time-averaged mass-spectrometer densities. The systematic error in the densities from satellite drag is mostly attributable to the drag coefficient and is nearly immaterial in atmospheric modeling, as long as a plausible value for its constant part is assumed throughout.

Ignoring systematic errors, we can assume that atmospheric densities can be determined with an accuracy of 2%. At heights where the density variations are large and well measurable a 2% variation in density corresponds, roughly, to a variation of 2°–5° in the exospheric temperature (larger at sunspot minimum than at maximum). Variations directly attributable to variable solar XUV radiation can be as large as 900 K. Assuming that we have a model that can correctly represent these variations and at the same time accurately take into account all non XUV-induced variations, we would, ideally, need solar-activity parameters consistent to within 0.002–0.005 of their ranges. This nominal accuracy is, roughly, found in the 10.7-cm solar flux; but, can the same be said of XUV intensities? If we consider photon counts within predetermined spectral regions and limit ourselves to a single instrument, the answer should be yes. The trouble with XUV experiments, however, is that in the past they have been short-lived – at least compared to the 11-year solar cycle – and that for them there is no convenient natural calibration standard such as satellite drag for atmospheric densities. And, unfortunately, the systematic errors of the individual experiments have been large – easily of the order of 10% and possibly larger, up to 30–40%. The situation has much improved during the last few years with the XUV monitoring by instruments on the Atmospheric-Explorer satellites, which has covered the rise in solar activity from the last minimum to the present maximum. It is to be hoped that also in the future the XUV monitoring of the sun will be done on a continuous basis, or at least that the experiments will overlap long enough to allow cross-calibration. There will still be some worry about whether the instrumental calibration holds constant over a long interval of time.

Next comes the question of what to pick out in the XUV spectrum and how to correlate it with the atmosphere. Out of the unmanageable wealth of data that a satellite can send to

earth we must make a judicious selection of a few representative features that have or might have relevance for thermospheric variations. We could, first, divide the spectral features into a few categories, such as:

1. Continuum at various wavelengths.
 2. Lower-excitation lines that contribute substantially to the disk component of the radiation.
 3. Higher-excitation lines that appear mainly in normally active areas.
 4. Very high excitation lines that appear only in exceptionally active areas or in flares.
- One or two representative features could be selected from each category. If the output is in the form of intensity integrated over fixed frequency intervals, it will be a matter of strategically selecting a few intervals in which the radiation comes predominantly from one of each category.

Let I_k be the intensity of a feature in category k ($= 1, 2, \dots, n$). At any time the exospheric temperature could, presumably, be expressed as

$$T_\infty = \sum_{k=1}^n w_k I_k + \text{terms not dependent on } I_k . \quad (1)$$

The coefficients w_k could be considered as constants in a first approximation and would have to be determined empirically. The linear relation between T_∞ and the I_k 's may actually not hold over a large range of temperatures, in which case equation (1) must be modified by the addition of nonlinear terms or by the introduction of a suitable nonlinear function. To each I_k there corresponds an effective absorption height that varies with T_∞ , so we must expect the shape of the temperature profiles to vary somewhat as a function of T_∞ .

SHORT- AND LONG-TERM CHANGES IN COMPOSITION; DIURNAL, ANNUAL, AND "GEOMAGNETIC" VARIATIONS

Since no feedback on T_∞ can be expected from the other thermospheric variations, we can model the solar-activity effect using XUV data as input and use the resulting T_∞ as one of the input data for the other types of variation. The solar-activity effect is the only variation in which we can ignore differences of temperature between different points on the globe, which through the phenomena of diffusion and circulation cause changes in atmospheric composition. Strictly speaking, even in the solar-activity effect there are such differences. According to Jacchia et al. [1] and Paul et al. [2] the lag between the variations of the exospheric temperature and those of the decimetric solar flux is larger at night than in daytime. It is obvious, however, that the dynamical effects of such a difference must be quite small.

The modeling of the geographic changes of composition are simplest in the seasonal-latitude variation, where the effect is only zonal, independent of longitude (the winter helium bulge is the most conspicuous feature of this type of variation). The situation would be similar in the semiannual variation, were it not for its poor degree of repeatability, which makes its analysis more difficult. Both the annual and the semiannual variations are suspected of being affected by the level of solar activity (as they logically should), but how much is still unclear.

By contrast, complex changes in composition, dependent on longitude, latitude, and height, are observed in both the diurnal and the geomagnetic variations. Theoretical modeling [3] has achieved considerable success in explaining and representing the observed phenomena in both variations. The purely empirical models [4, 5, 6] approximate the observed variations with considerably less labor than the theoretical models, which require the integration of partial differential equations, but even so are complex enough. A closer approximation to reality along their lines would require even greater complexity. In search for a good solution, one might be guided by the theoretical approach and try to find suitable

analytical expressions that approximate the solutions of the differential equations. The numerical coefficients of these expressions can then be evaluated to fit the actual observed data. I used a somewhat similar approach recently [7] trying to avoid the necessity of using numerical integration to compute densities in the thermosphere when the shape of the temperature profiles is distorted by geomagnetic perturbations.

The theoretical approach to the changes in composition is possible only if we have a good model of the energy input and dissipation. In this respect the diurnal variation can be handled much more confidently than the geomagnetic variation, in spite of the many problems that have to be solved for it, too. The diurnal variation is inextricably enmeshed with the annual, or seasonal-latitudinal variation. As the declination of the sun varies in the course of the year, the amplitude and phase of the diurnal variation changes at any given latitude, and so does the mean temperature, giving rise to an annual variation. Although the maximum daily temperature at the time of solstices occurs at midlatitudes, the daily mean temperature at the same time continues to increase with latitude right to the summer pole, engendering a pole-to-pole annual variation in composition. There is still no consensus on the latitude at which the maximum daily temperature occurs at the solstices. The main difficulty here is the strong "geomagnetic" heating in the polar regions. Even a very moderate level of geomagnetic activity, corresponding to a K_p between 1 and 2, is sufficient to displace the global temperature maximum from midlatitudes to the area of the geomagnetic pole. There are those who think that there is some polar heating even during ideally quiet conditions ($K_p = 0$).

Another area that requires more research is that of the harmonics in the diurnal variation. What are the amplitudes and the phases of the semidiurnal and the terdiurnal components at different heights, especially in the lower thermosphere? Concerning the semidiurnal component, one difficulty seems to be that to isolate it, it is generally assumed that the fundamental variation is sinusoidal, whereas that is definitely not the case - and the deviations from a sinusoidal first harmonic contribute to the amplitude of a second harmonic. In other words, the semidiurnal term in a Fourier series fitted to the observed daily temperature variation may not represent a true tidal oscillation. Higher harmonics are progressively less affected by the shape of the fundamental oscillation.

The energy model of the geomagnetic variation is much more complex and wanting, although we have begun to make some sense of the temperature variations with geomagnetic latitude [8] and with local magnetic time [9]. A feature of the geomagnetic variation that is often neglected in modeling, but must be taken into account, is the "equatorial wave" [10, 8, 6], in which the density of all atmospheric constituents varies with the same amplitude and phase. In spite of the complexity of the phenomenon, it is remarkable how closely empirical models can predict the atmospheric variations that accompany geomagnetic disturbances.

REFERENCES

1. L.G. Jacchia, J.W. Slowey, and I.G. Campbell, Planetary Space Science **21**, 1835 (1973).
2. G. Paul, H. Volland, and M. Roemer, Space Research XIV, 189 (1974).
3. H. Volland and H.G. Mayr, Journal of Atmospheric Terrestrial Physics **34**, 1745 (1972).
4. A.E. Hedin, J.E. Salah, J.V. Evans, C.A. Reber, G.P. Newton, N.W. Spencer, D.C. Kayser, D. Alcayde, P. Bauer, L. Cogger, and J.P. McClure, Journal of Geophysical Research **82**, 2139 (1977).
5. A.E. Hedin, C.A. Reber, G.P. Newton, N.W. Spencer, H.C. Brinton, and H.G. Mayr, Journal of Geophysical Research **82**, 2148 (1977).
6. L.G. Jacchia, Smithsonian Astrophysical Observatory Special Report No. 375, 1977.
7. L.G. Jacchia, Space Research XIX, 179 (1979).
8. L.G. Jacchia, J.W. Slowey, and U. von Zahn, Journal of Geophysical Research **82**, 684 (1977).

9. J.W. Slowey, Presented at the XXIII COSPAR Meeting, 1980.
10. L.G. Jacchia, J.W. Slowey, and U. von Zahn, Journal of Geophysical Research 81, 36 (1976).

ENERGY SOURCES FOR THE IONOSPHERE—A SURVEY

K. Rawer

University of Freiburg, Freiburg, FRG

ABSTRACT

An outline is given of early aeronomical ideas about the formation of the ionosphere by solar wave radiation, and its development under the impetus of increasing basic knowledge. In particular, the development concerning solar radiation in the far ultraviolet and X-ray ranges is discussed (Sect. 1). General considerations on the relation with observable ionospheric parameters are given in Sect. 2, while the individual layers are discussed in Sect. 3. It is found that older investigations, with wrong assumptions came to the right densities while their estimates of production rates were far too low. Since two years only satellite and laboratory data allow satisfying estimates.

INTRODUCTION

In the following considerations emphasis is laid on the historical development rather than discussion of today's problems. Only the main source of diurnal ionization i.e. solar shortwave radiations, is taken into consideration. A fuller treatment of the subject should, of course, take also account of other energy sources which are of importance in certain regions and, in particular, during disturbed conditions.

1. SOLAR RADIATION IN THE U.V. AND X-RAY RANGES

The idea that ionization is produced in the terrestrial atmosphere by solar wave radiation at ultraviolet (u.v.) and shorter wavelengths is older than the very discovery of ionospheric layers. At that time, astronomers used a 'black body' model of between 5000 and 6000 K to describe approximately, the (unabsorbed) spectrum of solar radiation in the then accessible range between near infrared and near u.v. To my knowledge, Elias [1] was first to compute, in an isothermal atmosphere, the shape of the ion production and ionization equilibrium profiles. However, he did not discuss absolute values thus avoiding the difficult question after the total energy needed to produce and maintain such layers.

Since ionization can only be produced by quanta from the far u.v. which range could not directly be measured one tried to make an estimate of u.v. intensities from their effects, i.e. from the observed ionization. The black body model giving by far too low shortwave intensity the ratio of needed to black body radiation was introduced as an 'ultra violet excess factor'. Lind [4] and Kiepenheuer [5] estimated its order to be as large as 10⁶.

However, when the first rocket observations in the u.v. became available [4] it appeared that below 500 nm the intensity was not greater but even smaller than deduced from a black body at 6000 K. When describing the u.v. spectrum in terms of an 'effective temperature' this latter was found to be only 3000 K at 250 nm and as low as 4000 K at 100 nm. Only in the 117 to 134 nm range first measurements with gas-filled photocells [5] gave intensities agreeable to about 6000 K. There was, however, no doubt that this had to be interpreted as a strong line emission namely the hydrogen resonance line L-alpha at 121.6 nm. Its intensity was estimated to 0.1 mW m⁻². It is now known to be up to 50 times greater than that.

Meanwhile, refined methods for computing the radiation output of a hot sun's atmosphere had been developed by astrophysicists [6].

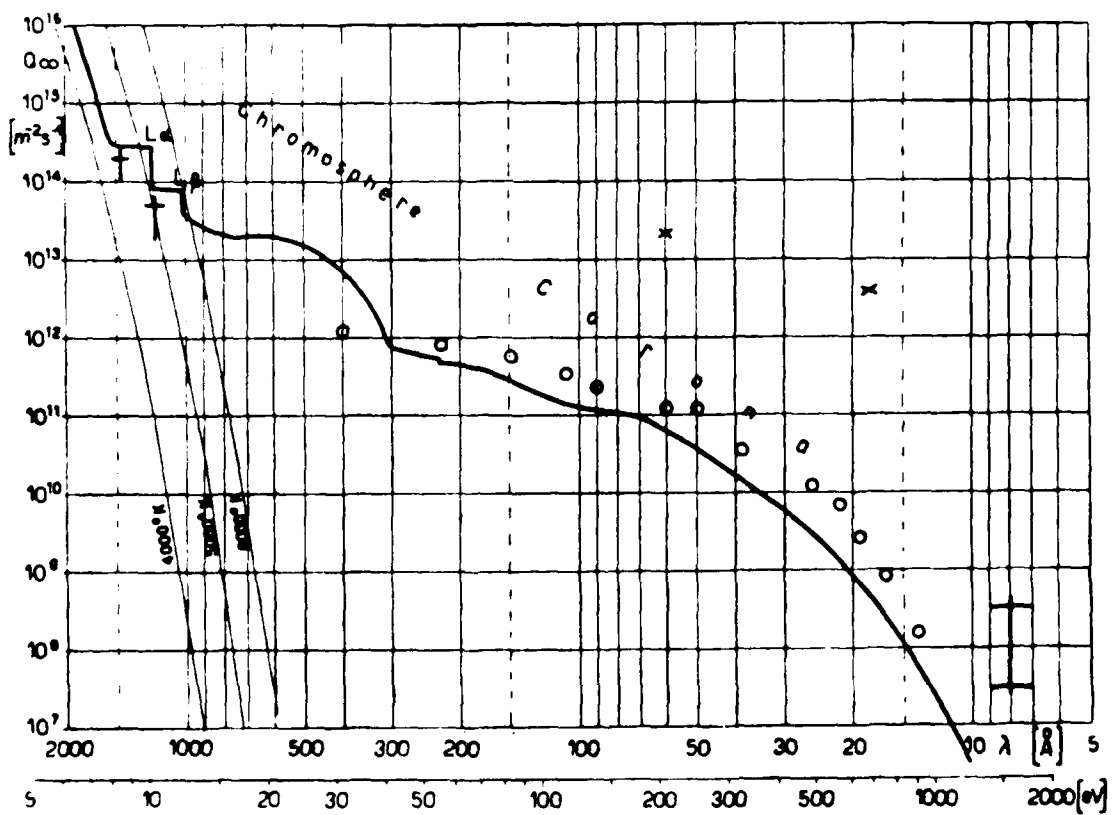


Fig.1 Integrated quantum flux in the solar XUV spectrum presented in [6] after Nicolet's 1951 estimate [7].

Nicolet [7] in 1951 presented results of theoretical reasonings about the solar radiation below 100 nm distinguishing between the chromospheric radiation above 40 nm and that from the corona below. Fig. 1 shows his results presented as an integrated spectrum of photon flux (i.e. to a given wavelength the total flux of quanta with energy greater than that corresponding to the given wavelength) [8]. It appears that in the far u.v. the decrease with increasing wave number is small and variable compared with black body models (shown in fig. 1) such that it is no more reasonable to define a hypothetic solar spectral temperature rather than to evaluate the contributions according to their origin in different layers of the solar atmosphere.

While Nicolet's aim was a solar radiation model applicable to aeronomical computations Elwert, a disciple of Unsöld, began in 1952 to carry out a thorough computation using Unsöld's [6] methods. Similar to Kiepenheuer [3] he felt that free-free transitions and recombination should prevail. So he computed the different continua which he expected to be emitted in the corona. For this latter he assumed a temperature of either $5.7 \cdot 10^6$ or 10^6 K [9]. His results for the latter coronal temperature were compared with Nicolet's and showed reasonable agreement [10] in the wavelength range mainly attributed to the corona (which had alone been considered by Elwert). In spite of this agreement further theoretical work ended up with considerably greater estimates of coronal emission intensity. First, different from his earlier estimate, when going through more detailed computations, Elwert realized that the contribution from line emissions was more important than that of the continua [11]. Thus maximum spectral density of the emissions is now found at 6 to 8 nm instead of below 5 nm in his previous work. This resulted from Elwert's very laborious detail computations. The emitted energy was so increased by a factor of almost 3 coming now well above Nicolet's earlier estimate. The integrated energy fluxes given by the three models are presented in Fig. 2. (The slopes are less steep in this energy presentation than for integrated photon fluxes as given in Fig. 1).

Meanwhile more wavelength ranges had become accessible due to the filter cell techniques developed by Friedman and his co-workers at NRL [5, 12, 13]. Observations with this technique have low spectral resolution but give quite reliable absolute energy fluxes in certain spectral ranges. Of the few experiments flown by NRL before 1954 [14] only one had covered the most interesting range 4.4 to 10 nm giving $.05 \text{ mW m}^{-2}$ which is almost in agreement with Elwert 1954. However, at shorter wavelengths, in particular for .8 to 2 nm, the measured intensities were much greater (from $.02 \text{ up to } .6 \text{ mW m}^{-2}$) than predicted by then existing theories ($.0001$ and $.0006 \text{ mW m}^{-2}$ for Nicolet 1951 and Elwert 1954, respectively). Thus some additional intensity had to be found in that range. Solar eclipse observations in 1948 [15] had shown strongly emitting bright areas (of about 0.4% of the disk area) with a mean brightness temperature of $5 \cdot 10^6$ K. The phenomenon was explained as a 'coronal condensation' with about twenty-fold increased electron density [16]. Since the relation between emission intensity and plasma temperature and density is non-linear and, in particular, the short wave limit is very sensitive, a small hot area would give a large contribution at the short wavelength end.

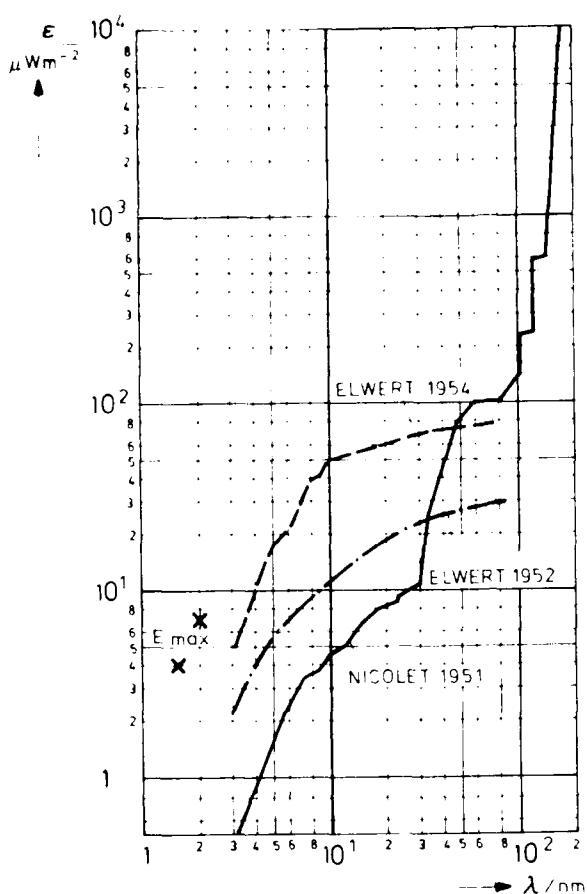


Fig. 2 Integrated energy flux spectrum of the Sun after theoretical estimates prior to 1960 [7, 9, 11, 17].

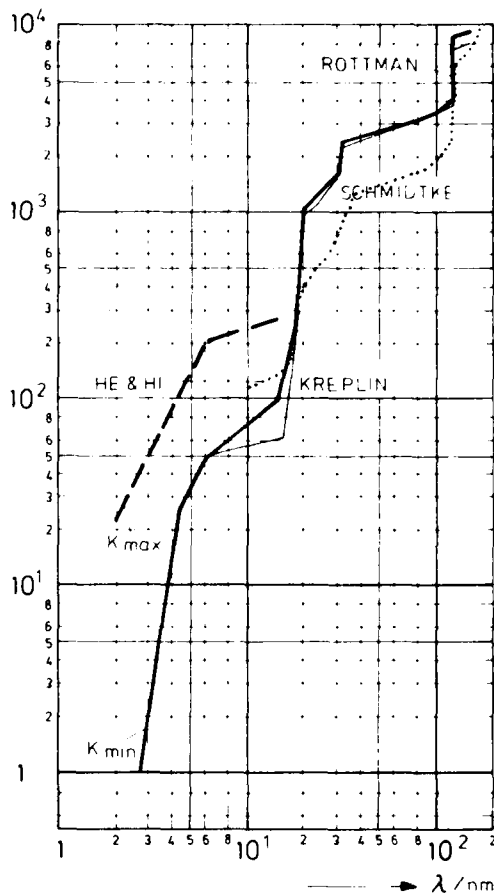


Fig. 3 Integrated energy flux spectrum of the Sun after recent space measurements [19, 22, 23].

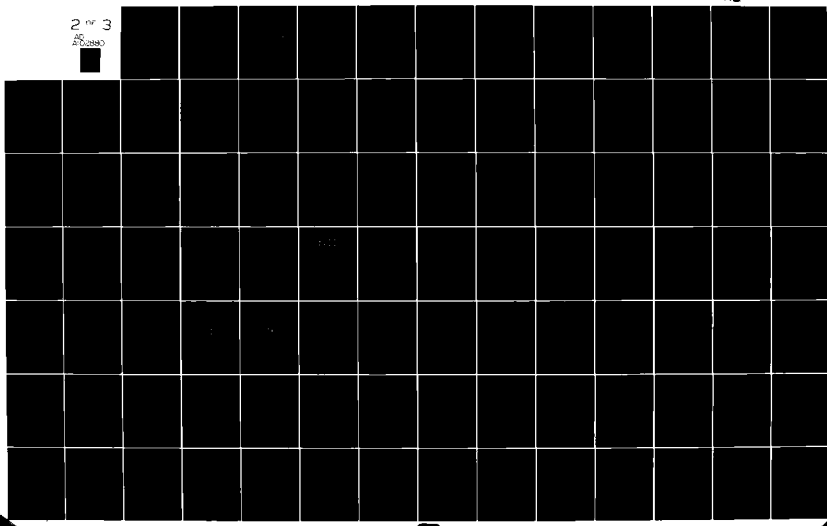
In 1956 paper Elwert [17] took account of just one such area at $6 \cdot 10^6$ K. Fig. 4 shows the relevant emission lines occurring below 2 nm (20 Å). Summing up these intensities we came to the crosses labelled E_{\max} in Fig. 2. For comparison with these predictions Fig. 3 shows an integrated energy spectrum, comparable to Fig. 2 but derived from modern measured data. In the X-ray range data from the long series of NRL's SOLRAD satellites were used as input [18, 19]. The curves labelled K_{\max} and K_{\min} give rough average values for high and low solar activity periods. The bold curve is for conditions of 1973, before the 1974 solar minimum. Some uncertainty reigns in the 'transitional' range between 6 and 15 nm where the experimental basis is scarce. In this range, the bold curve is probably a better estimate than the thinner curve below corresponding to a low energy estimate for that range. The upper values agree besides with the measurement reported in [14].

AD-A102 880 AIR FORCE GEOPHYSICS LAB HANSCOM AFB MA
THE MESOSPHERE AND THERMOSPHERE; (U)
1981 K S CHAMPION, G SCHMIDTKE
UNCLASSIFIED AFGL-TR-81-0210

F/G 4/1

NL

2 or 3
552040



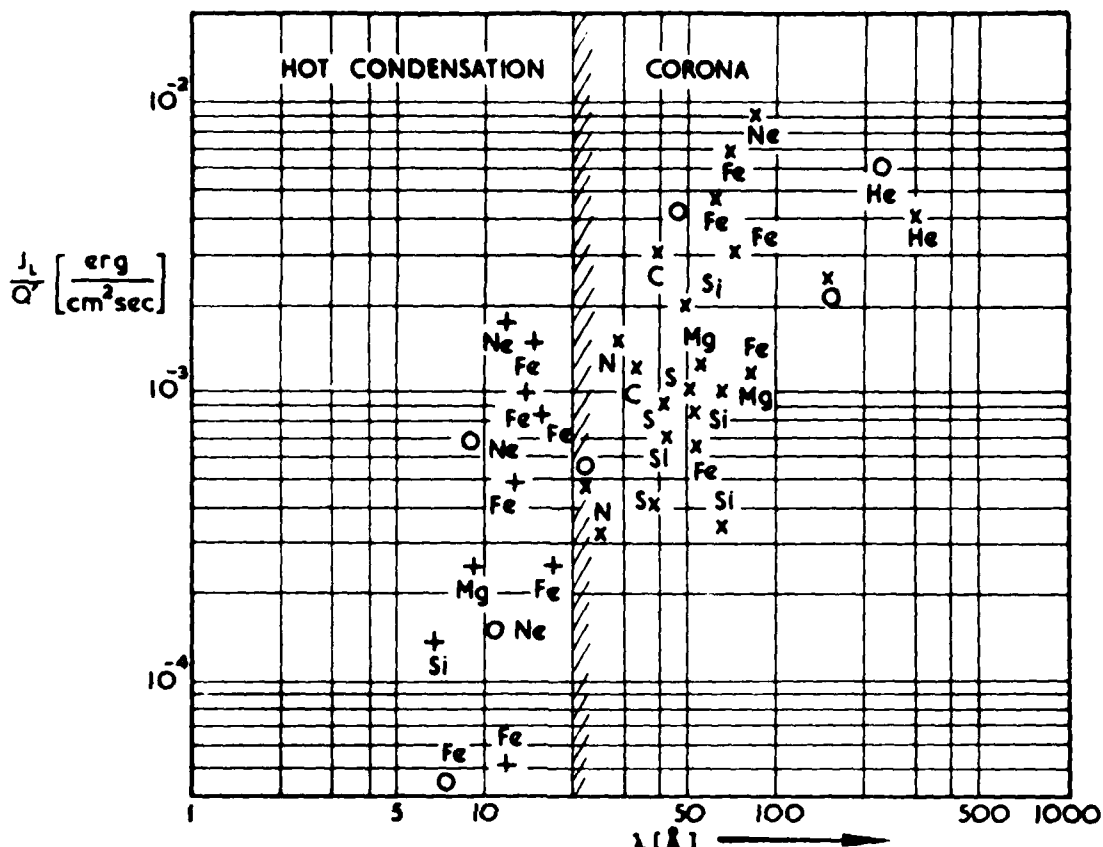


Fig. 4. Energy flux due to strong coronal emission lines after Elwert's 1956 computation [17]. Emissions left of the shaded line stem from an assumed hot coronal condensation of $6 \cdot 10^6$ K over .4% of the solar disk.

At wavelengths above 16 nm there is now Schmidtke's series of measurements aboard the AERCS-A satellite [20], obtained with the first in-flight calibrated instrument [21] and thus reliable. For Fig. 3 I used data of the typical day with Covington index 95 which is reproduced in [22]. Around 10 nm, between his and Kreplin's [19] data remains a gap where no measurements are available (see above). The uncertainty of integrated flux, due to this transitional range decreases of course with increasing flux values. As for the very strong Lyman alpha emission line I used maximum and minimum values of Rottman's as tabulated in [22]. For comparison, the 1974 (true solar minimum) spectrum of Heroux and Hinteregger [23] is also shown.

Recently, Hinteregger's instruments aboard the Atmospheric Explorer satellites AE-C and AE-E have procured a wealth of new data. Taking account of solar activity these are in good agreement with Schmidtke's which I used in Fig. 3 (for moderate solar activity).

We have shown above that astrophysical estimates had a general trend towards greater intensities. Now comparing Figs. 2 and 3 one realizes that this change was needed indeed. As described above, in 1956 Elwert by admitting density fluctuations in the corona and,

at times, coronal condensations [17] was able to lift his own 1954 estimate (broken curve in Fig. 2) quite considerably. Starting with his maximum estimate (crosses at 1.5 and 2 nm in Fig. 2) the lifted curve lies now in the range of Kreplin's measurements, i.e. between curves K_{\min} and K_{\max} . This is at least so below, say, 5 nm. Above 10 nm, however, the theoretical estimates are too low by a factor of more than 10.

For the range above 20 nm we find rather similar shape of the spectra given by Schmidtke [20] for 1973 and by AFCRL for 1967 [24] and 1974 [23]. Absolute values compare well for 1973 and 1967 but this should not be taken as agreement because in 1967 the solar radio flux was much greater: 144 against 95 Covington index. The intensities measured by AFCRL in 1974, however, are lower and match well with Schmidtke's from 1973 if the decrease of solar activity is taken into account.

For solar cycles previous to number 21, the solar cycle variation of the absolute intensities is still not well known [25]. It can, however, be taken for certain that the energy flux available in the 20 to 100 nm range is a few mW m^{-2} (Fig. 3), thus much larger than gave earlier theoretical estimates (Fig. 2). We are still waiting for a detailed astrophysical theory explaining such large intensities.

2. SOLAR RADIATION AND THE FORMATION OF IONOSPHERIC LAYERS

Ground-based observations of the ionosphere are carried out since several decades now. From the large thesaurus of data so obtained we have rather good information about the ionization existing in the terrestrial atmosphere. We know not only the peak values of electron density in the main layers but know also layer height and thickness. When aeronomical considerations about the formation of ionospheric layers were first undertaken there was a tendency to identify each layer with the ionization of a specific atmospheric constituent supposed to be ionized in a rather limited wavelength range. (A survey is found in [8, 10].) It was later found that there is considerable overlap between various ionization processes and radiations. So the atmospheric effects due to the different wavelength ranges must be summed up in order to obtain realistic profiles of ionization production.

It is important to note that the height range where production occurs is independent of the radiation intensity. This is a consequence of the fact that in the terrestrial atmosphere the ionized population remains always a minor constituent. The maximum of production is usually found in that altitude where the atmospheric absorption is strongest for a given radiation; the shape of the production profile depends exclusively on two basic data: the effective cross section and the density profile of each neutral constituent that is ionized. Since for a long time information about both was scarce rather wide-spread assumptions were acceptable. In particular though ionization potentials were quite well known the relevant cross sections were not well known and could be chosen almost arbitrarily.

Thus, when the first u.v. measurements were made in rockets the absorption profile was an important feature to be determined [5]. Combining with cross section determinations the atmospheric densi-

ty models could be checked by such observations. Fig. 5 [26] summarizes conclusions drawn from NRL measurements in the X-ray ranges.

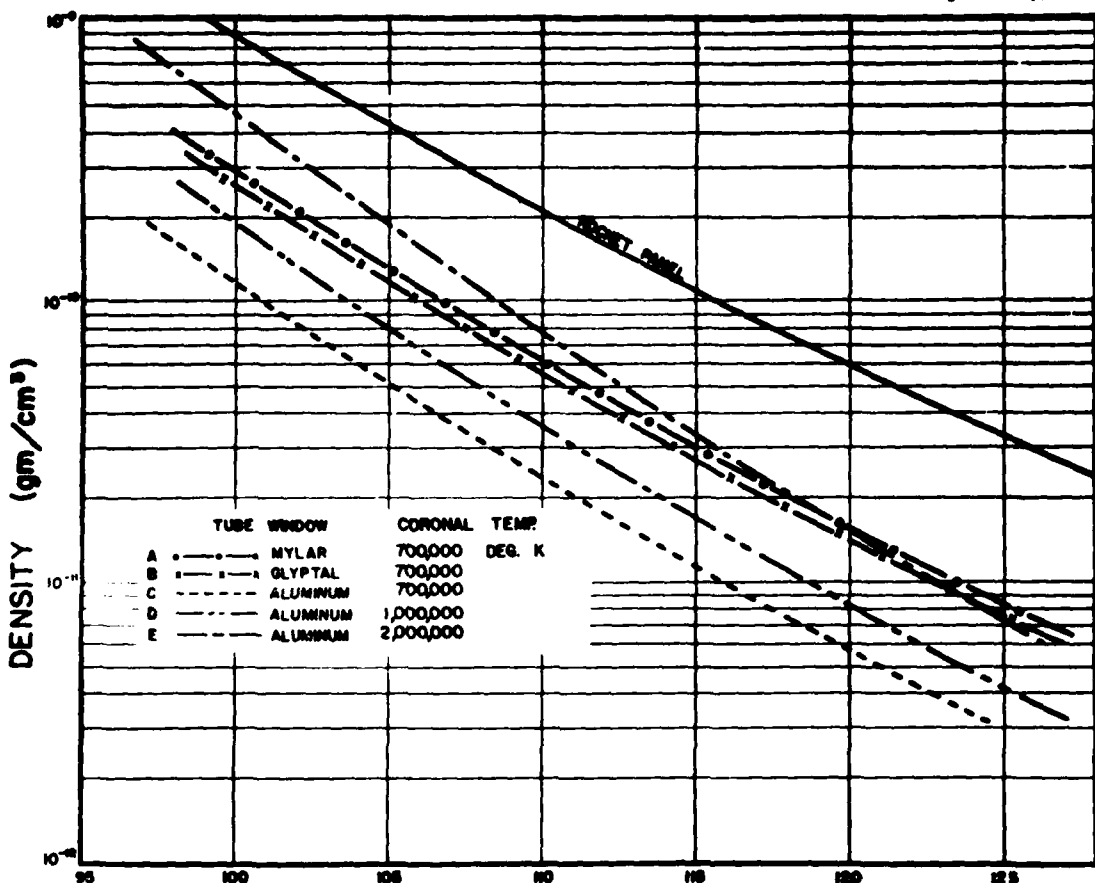


Fig. 5 Air densities computed from X-ray measurements with counters behind different windows. (The saw-tooth shape of the absorption spectrum makes that the results depend on the assumed coronal temperature.) The full line on top is the 1952 estimate of the USA rocket panel. [26].

Penetration curves from the same source are presented in Fig. 6 covering wavelengths between .1 and 10 nm (next page). Penetration curves for 30 to 130 nm were first presented in 1962 by the AFCRL team [27], see Fig. 7. It is important to note that the level of maximum absorption is not a monotoneous function of the wavelength. Minimum penetration occurs around 30...60 nm in the e.u.v. range while longer and shorter wavelengths penetrate deeper. Thus the uppermost ionospheric region F is mainly due to the e.u.v. spectral range while at lower altitudes X-rays and u.v. radiation must both be considered.

Figs. 6 and 7 are, of course, reproduced as examples of the historical development. They can no more be considered as valid. Tabulations of modern reaction rates and cross sections can be found in [28, 29].

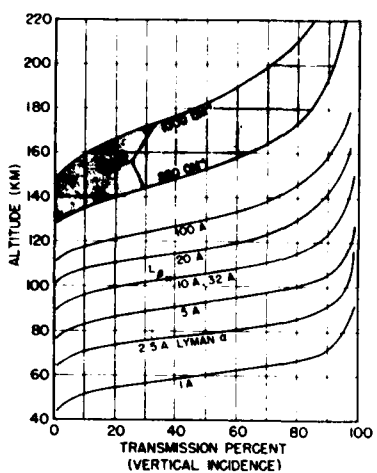
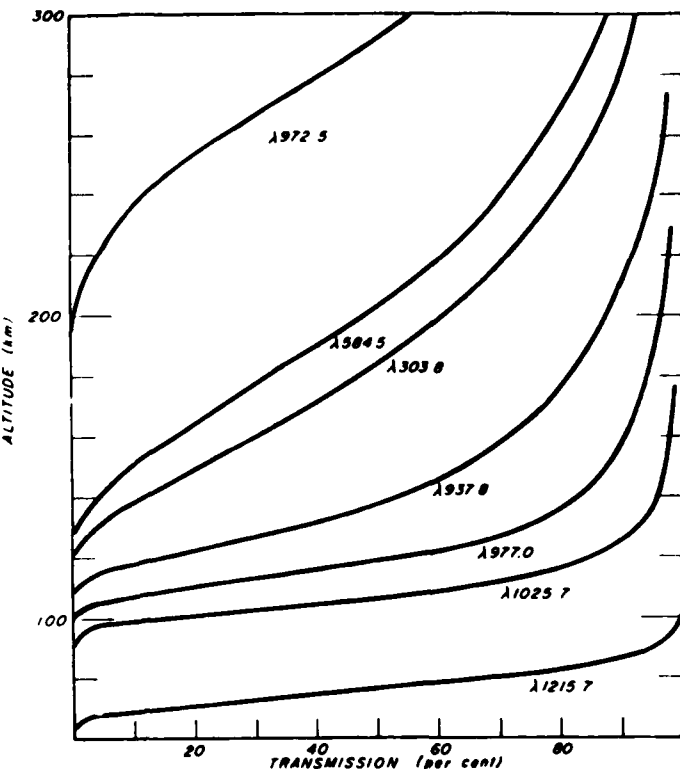


Fig. 6 NRL: XUV range atmospheric transmission curves published 1960 [26].

Fig. 7 AFCRL: EUV range atmospheric transmission curves published 1962 [27].



The primary ion/electron production rate can be computed from the following inputs: density profiles of the atmospheric constituents, -cross sections of the different reactions of photo-ionization, -absolute intensities in the solar X/u.v. spectrum. While these are nowadays rather accurately at hand, the situation was largely open in the past. As stated above, corpuscular ionization is neglected here, an assumption which is justified under quiet day conditions, except for high latitudes and night [30]. Even if the primary production rate is calculated, this is not directly a measurable quantity. Ground-based observations end up with electron density profiles which are obtained from ionosonde stations since several decades, now also from incoherent scatter techniques. These latter and in-situ measurements as well provide also electron and ion temperatures and some information about ion composition. Unfortunately, the step from the production rate to the measurable electron density is not easy since ion chemistry and transport phenomena are engaged and can be quite involved. Thus, some aeronomic considerations and - often - assumptions are contained in the process of deducing electron densities from the incident solar radiation.

3. DETAILED DISCUSSION OF THE MAIN IONOSPHERIC LAYERS

The longest series of reliable measurements is due to ionosondes. From the ionograms all stations deduce at least peak values for the E- and F-region which are very reliable [31]. Thus, during day at least, height and density of the two peaks are experimentally well established parameters for comparison with theory. Further, from other radio techniques, there exists some information about the lower ionosphere (lower E- and D-region) [32, 33, 34]. The International Refe-

rence Ionosphere (IRI) may be used as a summary of present knowledge for such purposes [35]. When now considering the three regions separately we shall meet rather different conditions.

3.1 The D-Region

The electron densities given in IRI are mainly based upon in-situ measurements with probes [33]. There seems still to exist some discrepancy between these and radio wave absorption measurements [36]; these are not yet resolved. The aeronomics situation is very involved below about 70 km due to the presence of negative cluster ions; positive clusters as found below 90 km are of some influence in the ion chemistry [29]. Therefore, it is probably too early to formulate a reliable picture of the recombination processes in D. On the other hand ion production in the D-region is also particular. Most of the spectrum is absorbed above the 70...90 km range. Apart from X-rays below 1 nm -emitted only under flare conditions- there is the strong Lyman-alpha resonance emission at 121.6 nm which is very strong, viz. 3...5 mW m⁻². So, there is no problem from the energy side. However, the Lyman-alpha quantum being below the ionization energy of most atmospheric gases, only the molecule NO could be ionized [37]. Thus, the question is reduced to the chemistry of this minor constituent. In the computations one assumes a certain height profile of NO which is of crucial importance for the radiation estimate.

The constants are short in the D- and E-regions so that equilibrium is rapidly obtained. Adopting a recombination type loss term with height-dependent recombination coefficient, one has to equate this with the production function obtained as triple product of ionization cross section, local density of NO, and L-alpha photon flux. The latter is obtained from the unabsorbed solar spectral intensity reduced by the absorption suffered above the level considered. Non-ionizing absorption in O₂ must be considered, too.

Along these lines Houston [34] in 1957 computed equilibrium electron densities in the D-region. A flat peak occurs in the 80...90 km height range with an electron density of 1...1.4·10⁹ m⁻³. This is in agreement with the rocket data gathered in [33] but the dependence on the solar zenith angle modelled in [33] (data of different sources is stronger. The parameters adopted by Houston (first line) are compared in Table 1 with recent data (in the second line).

TABLE 1 D-Region

Recombination	Cross section	El. density	Flux				
a(80)	a(90)	S(NO)	S(O ₂)	n(80)	n(90)	Q	Ref.
m ³ s ⁻¹ 3·10 ⁻¹³	m ³ s ⁻¹ 10 ⁻¹³	m ² 2.5·10 ⁻²²	m ² 10 ⁻²⁴	m ⁻³ 6.5·10 ¹³	m ⁻³ 1.2·10 ¹³	mWm ⁻² 0.2	[34]
10 ⁻¹²		2·10 ⁻²²	10 ⁻²⁴	2·10 ¹³	2.5·10 ¹³	4.2	[29]

Agreement between both lines is quite good, except for the first and last column. In fact, the solar radiation intensity was largely underestimated in [34] but the same was true for the recombination coefficient. So we have compensation of two errors. Of course, the ion pro-

duction is much greater after [29] than after [34] ($5 \cdot 10^6 \text{ m}^{-3} \text{s}^{-1}$ compared with $2 \cdot 10^5$, at 85 km).

We realize that estimates of radiation intensity by 'inverse' aeronomic considerations are rather dangerous since so many parameters interfere. Error compensation may produce apparent agreement with quite wrong radiation intensities.

3.2 The E-Region

Normal E is the most regular layer of the ionosphere. The peak electron density follows the solar zenith angle very accurately and the observed (monthly) spread of absolute values is only $\pm 10\%$. The time constant for recombination is a few min so that the assumption of equilibrium is fully justified. Unfortunately, in the altitude range between 100 and 130 km radiation from both ends of the X/uv spectrum is absorbed so that the first question was after the wavelength range to be considered.

The first aeronomic explanations of the normal E-layer were published quite early. Bhar as well as Schröer [39, 40] attributed the layer to photo-ionization of molecular oxygen in its second ionization potential. Laboratory measurements had shown that the ionization cross section was much greater at the second (16.1 eV) than at the first (12.1 eV) limit; intensities were not identified. With the neutral density data of that time penetration could be expected. Later when rocket measurements had shown the densities to be higher, Nicolet's (earlier) idea [37] of a two step process (preionization) around 90...100 nm was taken up. This process was shown [41] to cover Lyman-

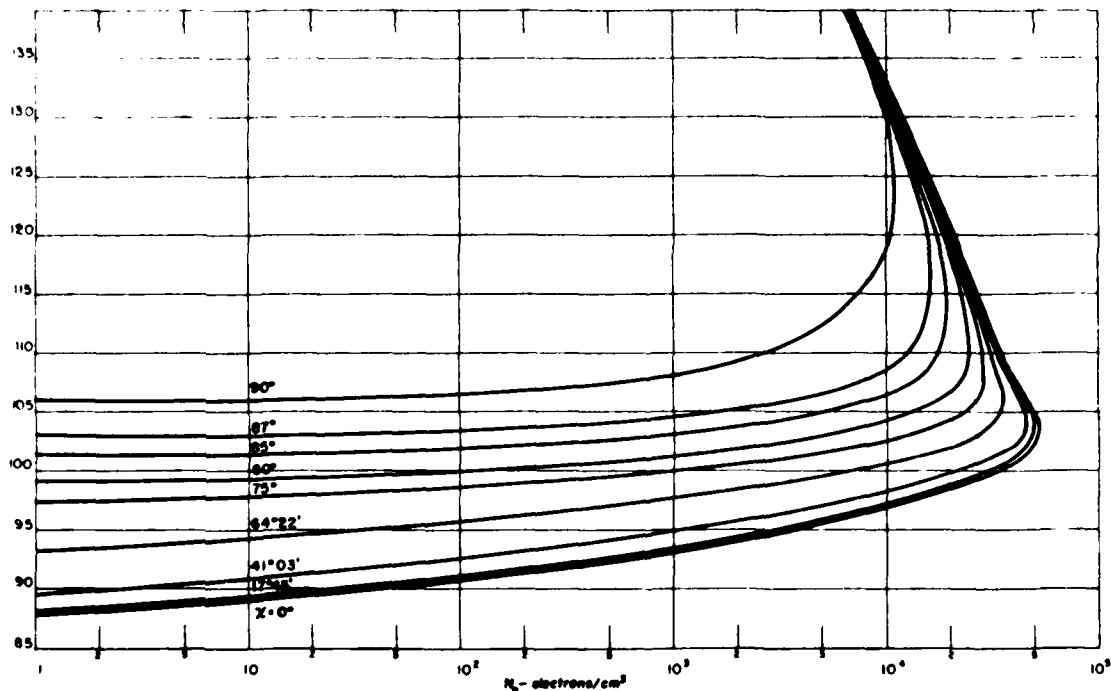


Fig. 8 Computed electron densities in the E-region for different solar incidence angles. Lyman-beta is assumed to be the only source of ionization [34].

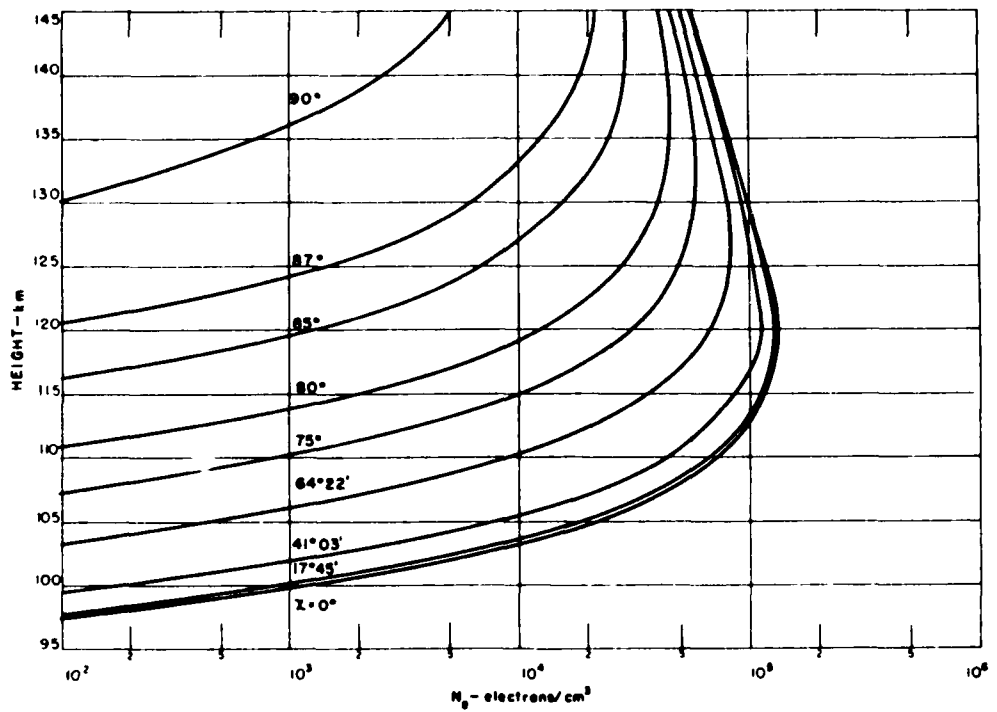


Fig. 9 Computed electron densities in the E-region for different solar incidence angles. Solar X-rays are assumed to be the only source of ionization [34].

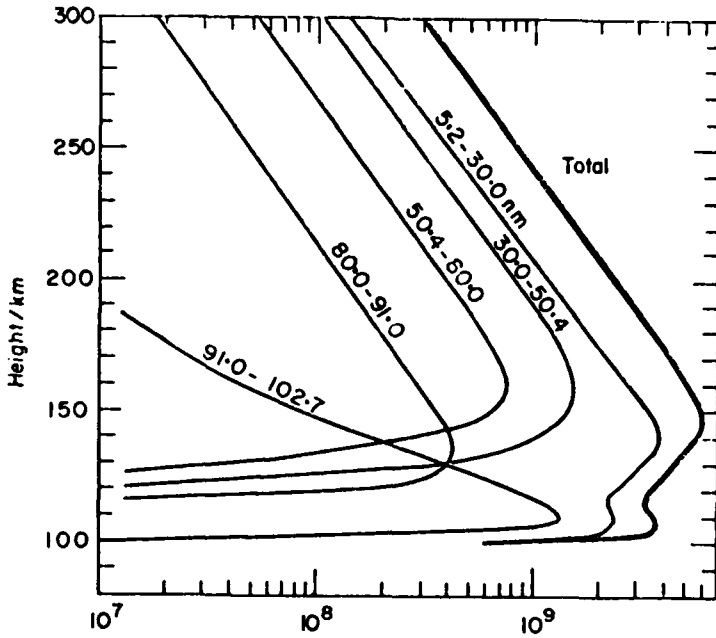


Fig. 10 Ion pair production rate/ $\text{m}^{-3} \text{s}^{-1}$ from measured solar emission intensities in the whole X_{nv} -range. After Heroux et al [42], reproduced in [29].

beta, too, from which ray a quite important contribution was expected. With a cross section of $1.54 \cdot 10^{-22} \text{ m}^2$ and a flux of only 0.007 mW m^{-2} Houston [34] obtained an electron density up to $4 \cdot 10^{10}$ at 103 km (Fig. 8). Present values [29] are 10^{21} and 0.1...0.2, resp. so that, again, the earlier estimate of electron density was not too bad in its result but obtained by compensation of two errors. The production, of course, had been underestimated in [34] : 10^8 instead of $10^9 \text{ m}^{-3} \text{s}^{-1}$ [42] near 105 km.

Since the electron density deduced from the longer wavelengths was too small, and after greater X-ray intensities had become probable [9] an earlier suggestion of ionization by X-rays [43] was taken up by Argence and Rawer [44, 45]. With the data available in 1951 they found maximum contribution from the 10...23 nm range which, together with shorter waves gave a production peak of $2.2 \cdot 10^8 \text{ m}^{-3} \text{s}^{-1}$ at 115 km. Later Elwert [46] critically analyzed the absorption conditions in this range and found 8...10 nm more important; he took also account of secondary ionization by photo-electrons ending up with $3.3 \cdot 10^8 \text{ m}^{-3} \text{s}^{-1}$ at 118 km. With improved basic data Houston [34] then produced the curves of Fig. 9 peaking at 120 km with about 10^{11} m^{-3} . While this is correct, the ion production rate was found too small: $2 \cdot 10^8 \text{ m}^{-3} \text{s}^{-1}$ instead of 10^9 [42]. For the incident X-rays he did not specify the wavelength range, just admitting a photon flux of $5 \cdot 10^{12} \text{ m}^{-2} \text{s}^{-1}$ and an average cross section of 10^{-22} m^{-2} . Recent production computations [42] show the whole 5...30 nm range must be taken into account giving a maximum production of $2.3 \cdot 10^9 \text{ m}^{-3} \text{s}^{-1}$ at 110 km (see Fig. 10).

3.3 The F-Region

As early as 1937 Mohler [47] became aware that the height of the F2-layer is too great to be coincident with a maximum of ion/electron pair production. He felt that the F2-layer, in spite of its large electron density, is a by-product of a production process peaking at the F1 level. The fact that the recombination decreases quicker with increasing altitude than the production rate decreases is the reason why an F2-layer is formed.

This said it is at once clear that the relation between electron density and ionizing radiation is too much involved to be helpful for estimating solar radiation intensities. Further, since the time constants are great, plasma transport by diffusion, winds and electric fields, plays a most important role. For the same reason the energy needed to produce this most important ionospheric region is smaller than needed for the E- and D-region (see the modern production rates of Fig. 10) [29].

4. CONCLUSIONS

The earlier idea that solar XUV radiation intensities might, at least roughly, be estimated from its observed effects in the terrestrial atmosphere was - historically seen - misleading. While the direct photo-chemical reactions are straight forward and so rather easily understood this is not so with the inverse processes of recombination which are chemical in nature. At lower heights the ion chemistry is too involved, at greater heights - where it is simpler - transport phenomena influence and disturb the chemical game.

Earlier numerical estimates often went wrong by a compensation of errors, i.e. the well-known equilibrium density was reached with a wrong production term. Now-a-days reaction cross-sections of the main photo-chemical effects are quite well known from laboratory measurements. Only recently the solar spectral intensities have been quantitatively determined by rocket and satellite techniques. Also, atmospheric density and composition were derived from satellite data. So the primary production profile can now be computed with satisfying accuracy (Fig. 10).

Thus, wherever we have approximate equilibrium between production and recombination, from the analytical accessibility of the production term follows a global accessibility of the recombination term, too. With other words, in the lower layers - where transport is also negligible - and under day conditions, we know now the effective recombination profile quite well, and this quantitatively. Only we do not yet know well by which processes this result is brought about in detail. Apparently, the E-region is the most appropriate field for further work along these lines. The goal should be to measure the individual densities of all the different intermediate species which are of importance in the game of ion chemistry, and so reach a better understanding of its main features.

5. REFERENCES

1. G.J. Elias, Tydschr. Nederl. Radio Gen. 2, 1 (1923).
2. N. Saha, Proc. Roy. Soc. A 160, 155 (1937).
3. K.O. Kiepenheuer, Ann. d'Astrophys. 8, 210 (1945).
4. N. Best, R. Havens and H. Lagow, Phys. Rev. 71, 915 (1947).
5. H. Friedman, S.W. Lichtman and E.T. Byram, Phys. Rev. 83, 1025 (1951).
6. A. Unsöld, Physik der Sternatmosphären, Springer, Berlin, 1. ed. 1938, 2nd ed. 1955.
7. M. Nicolet, Document of the Oslo 1948 meeting of the Int. Ass. Terr. Magnetism, Doc. T58 (1951).
8. K. Rawer, Die Ionosphäre, Noordhoff, Groningen, 1953.
9. G. Elwert, Ztschr. Naturforschung 7a, 202 (1952).
10. K. Rawer, The Ionosphere, Frederick Ungar, New York (1957).
11. G. Elwert, Ztschr. Naturforschung 9a, 637 (1954).
12. E.T. Byram, T. Chubb and H. Friedman and N. Gailar, Phys. Rev. 91, 1278 (1953).
13. E.T. Byram, T. Chubb and H. Friedmann, in: Rocket Exploration, Pergamon, London, 1954, p. 274.
14. O.E. Hulbert, Advances in the Physics of the Upper Air since 1950, Report 4600, Naval Research Laboratory, Washington, 1954.
15. W.N. Christiansen, D.E. Yabsley and B.Y. Mills, Austr. J. Phys. 6, 190, 262 (1953).
16. M. Waldmeier and H. Müller, Ztschr. Astrophysik 27, 58 (1950).
17. G. Elwert, J. Atmosph. Terr. Phys., Spec. Suppl. to 6, 167 (1956).
18. B.N. Gregory and R.W. Kreplin, J. Geophys. Res. 72, 4815, 1967.
19. Regular publication under 'Solar X-rays' in: Solar Geophysical Data, N.O.A.A., Boulder/Colo, U.S.A.
20. G. Schmidtke, Daily Solar EUV Intensities obtained during the AEROS-A Mission, Report W.B. 3, Inst. für physikalische Weltraumforschung, Freiburg, 1978.
21. G. Schmidtke, J. Geomag. Geoelectr., Suppl. to 31, S81, (1979).
22. J.P. Delaboudinière, R.F. Donnelly, H.E. Hinteregger, G. Schmidtke and P.C. Simon, Intercomparison compilation of relevant solar

- Flux Data related to Aeronomy, COSPAR Technique Manual No. 7,
COSPAR, Paris, 1978.
23. L. Heroux and H.E. Hinteregger, J. Geophys. Res. 83, 5305 (1978).
 24. H.E. Hinteregger, Annls. Géophys. 26, 547 (1970).
 25. G. Schmidtke, Planet. Space Sci. 26, 347 (1978).
 26. H. Friedman, in: J.A. Ratcliffe (ed.), Physics of the Upper Atmosphere, Academic Press, New York, 1960, p. 133.
 27. K. Watanabe and H.E. Hinteregger, J. Geophys. Res. 67, 999 (1962).
 28. K.G. Roble, A.I. Stewart, M.R. Torr, D.W. Rusch and R.H. Wand, J. Atmosph. Terr. Phys. 40, 21 (1978).
 29. L. Thomas, The Neutral and Ion Chemistry of the upper Atmosphere, in: K. Rawer (ed.), Handbuch der Physik 49/6 (in print).
 30. G.S. Ivanov-Kholodny, Annls. Géophys. 26, 575 (1970).
 31. W.R. Piggott and K. Rawer, URSI Handbook of Ionogram Interpretation and Reduction, 1st ed: Elsevier, Amsterdam, 1961; 2nd ed: Report UAG-23, World Data Center A for Solar-Terrestrial Physics, Boulder/Colo. U.S.A., 1972 (several translations).
 32. K. Rawer (ed.), Manual on Ionospheric Absorption Measurements, Report UAG-57, World Data Center A for Solar-Terrestrial Physics, Boulder/Colo. U.S.A., 1976.
 33. E.A. Mechtly and D. Bilitza, Models of D-Region Electron Concentrations, Report W.B. 1, Inst. für physikalische Weltraumforschung, Freiburg, 1974.
 34. R.E. Houston jr., The effect of certain solar radiations in the lower Ionosphere, Scient. Rep. 95, The Pennsylvania State University, Ionospheric Res. Lab. U.S.A., 1957.
 35. K. Rawer, S. Ramakrishnan and D. Bilitza, URSI-COSPAR Internationale (U.R.S.I.), Bruxelles, 1978. (An edition '1979' including many tables and figures is under way at World Data Center A für Solar-Terrestrial Physics. Boulder/Colo. U.S.A.).
 36. W. Singer, J. Taubenheim and J. Bremer, J. Atmosph. Terr. Phys., 1980.
 37. M. Nicolet, Mém. Inst. Roy. Mét. Belgique 19, 1 (1945).
 38. L.G. Meira, J. Geophys. Res. 76, 202 (1971).
 39. J.N. Bhar, Ind. J. Phys. 12, 363 (1938).
 40. E. Schröer, Ztschr. Meteorologie 1, 110 (1947) - posthumous.
 41. K. Watanabe, F. Marmo and J. Pressman, J. Geophys. Res. 60, 513 (1955).
 42. L. Heroux, M. Cohen and J.E. Higgins, J. Geophys. Res. 79, 5237 (1974).
 43. D.R. Bates and F. Hoyle, Terr. Mag. 53, 51 (1948).
 44. E. Argence and K. Rawer, C.R. Acad. Sci. (Paris) 233, 1280 (1951).
 45. K. Rawer and E. Argence, Phys. Rev. 94, 253 (1954).
 46. G. Elwert, J. Atmosph. Terr. Phys. 4, 68 (1953).
 47. F. Mohler, Bur. Stand. J. Res. 19, 447, 559 (1937), 25, 507 (1940).

COMPREHENSIVE INVESTIGATION OF THE BASIC PARAMETERS OF THE UPPER ATMOSPHERE AT THE TIME OF THE FLIGHT OF THE GEOPHYSICAL ROCKET “VERTICAL-6”

I. Apáthy,¹ I. Szemerey,¹ P. Bencze,² K. Kovács,²
V. Afonin,³ V. Bezrukih,³ K. Gringauz³
and N. Shutte³

¹ Central Institute for Physics; ²Geodetical and Geophysical
Research Institute, Hungarian Academy of Sciences, Hungary

³ Institute for Space Research, Academy of Sciences of
the USSR, Moscow, USSR

ABSTRACT

Ion temperature and total ion concentration measured on 25th October 1977 during the flight of the geophysical rocket "Vertical-6" are analyzed. The solar EUV fluxes determined in five wave-length bands with a photoelectron analyzer are also given. The observed anomalous variation of ion temperature between 700 and 900 km and the measured ion concentration can be explained, if the charge exchange reactions $H^+ \rightleftharpoons O^+$ and diffusion are taken into account.

INTRODUCTION

The geophysical rocket "Vertical-6" was launched on 25th October 1977, 15 15 MVT from the midlatitude area of the European part of the USSR for a comprehensive investigation of the upper atmosphere in the framework of the Intercosmos program. The rocket reached an altitude of 1500 km and its trajectory was very close to the vertical, the deviation being not greater than about 3° . The rocket was three-axis stabilized with an accuracy of $\pm 3^\circ$. The measurements, the results of which are analyzed here, were carried out by means of five planar retarding potential analyzers (RPA) looking into different directions of space and by a photoelectron analyzer, which allowed the determination of the solar EUV flux in five different wave-length bands [1]. The ion temperature and total ion concentration have been determined from the characteristic curves of the RPA looking vertically upwards, using a multi-parameter curve fitting [2, 3, 4], as well as from the results of one of the analyzers looking horizontally. In addition, electron temperature and the concentration of different ions measured on "Vertical-6" [5] are also used.

"Vertical-6" was launched during a geomagnetically very quiet period. The relative sunspot number was 28, the solar radio flux, measured at 10,7 cm, and the three-hourly geomagnetic index K_p were 88, ($10^{-22} \text{ cm}^2 \text{ Hz}^{-1}$), and 0, respectively. The launch time was preceded and followed by a period of low solar activity.

Since rocket experiments reaching altitudes above 500 km and especially those, by which the ion temperature is determined, too, are rare, the results of such measurements are useful both from the point of view of aeronomical studies and the checking of models.

RESULTS AND ANALYSIS

For the determination of energy input by the solar EUV radiation into the upper atmosphere, the fluxes in five different ranges of the spectrum have been determined by means of the photoclectron analyzer. Above the absorbing region of the atmosphere the values given in Table 1 were obtained. Because of the known limited resolving power of the method comparison of these values with the results of more direct EUV measurements [6, 7] shows that the fluxes given by us for the wave-length bands 60-90, 90-110 and 110-135 nm are in this order 1.4, 2.4 and 0.76 times of the values published in [7]. These data indicate that the input of energy by solar EUV radiation was similar to that found during the flights of Vertical-1 and 2, when the solar radio fluxes at 10,7 cm were 89 and 82 ($10^{-22} \text{ cm}^{-2} \text{ Hz}^{-1}$) respectively. Thus, the agreement noted above proves that during the flight of "Vertical-6" quiet conditions prevailed in the upper atmosphere. At the same time it justifies the use of atmospheric models [8].

In Fig. 1 the variation of total ion concentration with height is shown. For comparison the total ion concentrations obtained with an ion trap on the rocket [5] are also plotted. The maximum of the F2 layer was located at an altitude of about 230 km.

In Fig. 2 the ion temperature profile is shown. In addition, the electron temperature profile taken from [5] is also plotted. The ion temperature shows values equal to the neutral temperature to an unusually high altitude of about 550 km. It begins to differ from the neutral temperature only above this height, where a relatively steep increase in ion temperature is observed. Then at 700 km an isothermal region follows, above which at about 800 km a minimum occurs and the ion temperature shows a steep increase again. Thus, the isothermal region at 700 km may also be interpreted as a local maximum. A less steep height gradient of the ion temperature is reached at about 900 km.

DISCUSSION

The variation of electron temperature with height is affected by the electron (ion) density profile to a height of about 500 km. The decrease of electron (ion) density above the maximum of the F2 layer is reflected by the electron temperature in Fig. 2, as a steep increase at the same altitude, indicating that due to the decrease of electron (ion) density the cooling of the electron gas decreases considerably. A region of almost constant electron temperature is formed [9], as the ion temperature begins to increase at a height of 550 km due to the heating by the ambient

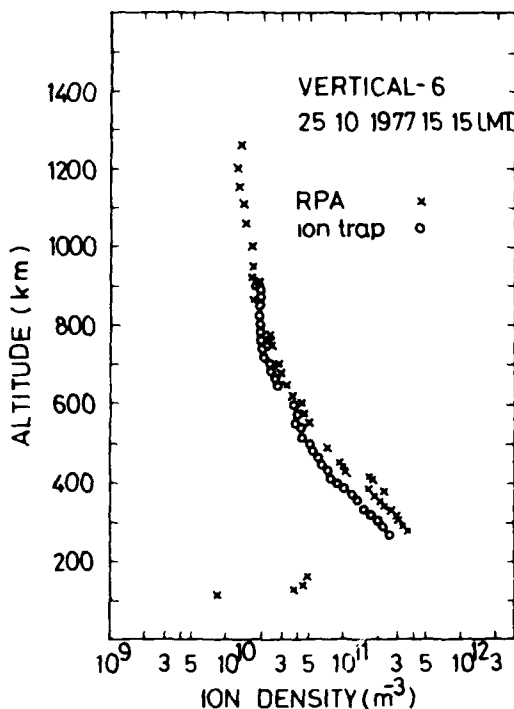


Fig. 1
Total ion density profile,
measured by planar retarding
potential analyzers and ion
densities, obtained with an
ion trap and taken from [5].

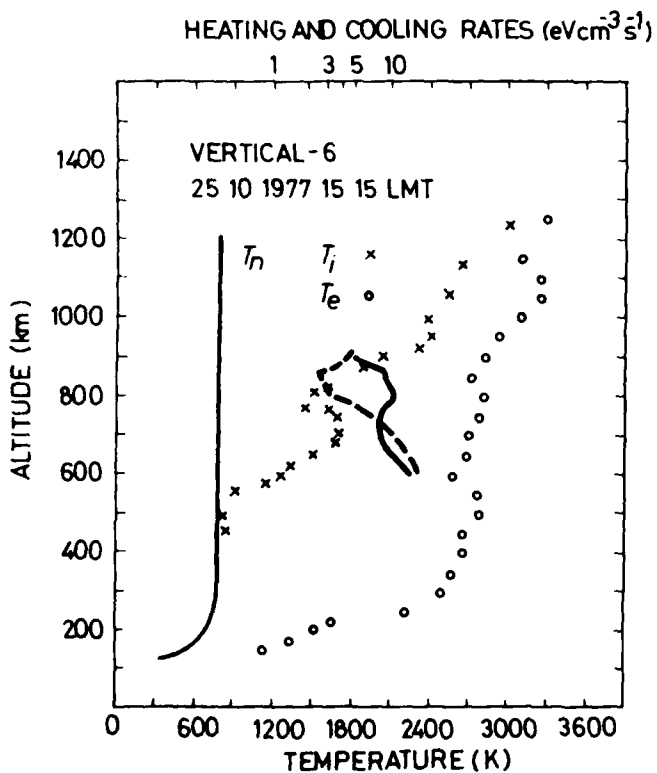


Fig. 2
Variation of ion tempera-
ture with altitude, de-
termined by means of a
planar retarding potential
analyzer (x) and the
electron temperature pro-
file, taken from [5] (o).
The heating rate (—)
and cooling rate (---)
of the ion gas are also
shown.

electrons. This process holds, till the steep increase in ion temperature does not cease. Above this region, at an altitude of about 800 km a small maximum occurs in the electron temperature profile. This small maximum of electron temperature coincides with a minimum in the ion temperature, above which an ion temperature gradually approaching the electron temperature may be observed with smaller fluctuations superposed on both profiles.

Since the ion temperature shows especially anomalous variations between the altitudes of 700 and 1000 km, this region will be discussed in more detail. This region lies just above the critical height [10], below which chemical processes are dominant and above which diffusion begins to control the distribution of plasma. The ion composition is yet largely determined by the charge exchange reactions $H^+ + O \rightarrow O^+ + H$, and $O^+ + H \rightarrow H^+ + O$ respectively. These reactions can affect the ion temperature, too. It is known

[11] that the heating rate of hydrogen ions due to the ambient electrons is sixteen times larger than that of the oxygen ions. At the same time the cooling rate of the oxygen ions, attributed to elastic collisions with neutrals and moving in this height region practically in their parent gas, is about two to three times larger than that of the hydrogen ions [12]. Thus, the heating and cooling of the ion gas also depends on the ratio of the concentration of hydrogen ions to the concentration of oxygen ions. Therefore, in the upper part of the height region considered, where $O^+ + H \rightarrow H^+ + O$ is the dominant charge exchange reaction, the heating of the ion gas may be more effective, consequently the cooling less intense (see steep increase of the ion temperature in Fig. 2), than in the lower part of this region, where in a small height interval the reverse reaction is prevailing [13] (see ion temperature minimum in Fig. 2). The altitude of transition between the dominant charge exchange reactions may change due to the counterstreaming of O^+ and H^+ ions [13, 14, 15]. It should be noted that in this case the ion composition does not reliably indicate the variation of ion temperature, since the rate coefficient for the reaction $O^+ + O \rightarrow O + O^+$ is comparable to that of the charge transfer $H^+ + O \rightarrow O^+ + H$ [16]. In Fig. 2 the heating and cooling rates, computed according to [11, 12] with the observed total ion density, ion composition, electron and ion temperatures, as well as taking the neutral number density and neutral temperature from CIRA 1972, are also plotted. The data show that between 700 and 900 km increased heating and somewhat decreased cooling take place. This shows that the height region mentioned is a region of non-steady conditions like a transitional zone. (Quasi-adiabatic heating due to plasma compression [17, 18] can also not be excluded, as the RPA measurements indicate strong downward flow of plasma.) Further investigations are needed to clarify the observed features of the ion temperature profile.

REFERENCES

1. N.M. Shutte, in: Proc. Int. Symp. on Physics of the Earth's Ionosphere and Magnetosphere and of the Solar Wind, Inst. Space Res. Acad. Sci. USSR, Geophys. Inst. Slovac. Acad. Sci., Hurbanovo, 1977, p. 263.
2. W. C. Knudsen, J. Geophys. Res. **71**, 4669 (1966).
3. S. J. Moss and E. Hyman, J. Geophys. Res. **73**, 4315 (1968).
4. W. B. Hanson, S. Sanatani, D. Zuccaro and T. W. Flowerday, J. Geophys. Res. **75**, 5483 (1970).

5. K. Serafimov, I. Kutiev, S. Chapkunov, D. Teodosiev, L. Bankov, Tz. Dachev, G. Gdalevich, V. Gubskii, W. Istomin, V. Krshova and J. Smilauer, Space Research XIX, 291 (1979).
6. G. Schmidtke, Geophys. Res. Letters, 3, 573 (1976).
7. L. Heroux and H. E. Hinteregger, J. Geophys. Res. 83, 5305 (1978).
8. CIRA 1972, COSPAR International Reference Atmosphere 1972, Akademie Verlag, Berlin, 1972.
9. G. L. Gdalevich, N.M. Shutte, Space Research XI, 1117 (1971).
10. W. B. Hanson and I. B. Ortenburger, J. Geophys. Res., 66, 1425 (1961).
11. A. Dalgarno, M. B. McElroy, M.H. Rees and J.G.G. Walker, Planet. Space Sci., 16, 1371 (1968).
12. P. M. Banks, Ann. de Geophys., 22, 577 (1966).
13. E. R. Young, D. G. Torr and P. G. Richards, Geophys. Res. Letters, 6, 925 (1979).
14. J. F. Vickrey, W. E. Schwartz and D. T. Farley, J. Geophys. Res., 84, 7307 (1979).
15. G. J. Bailey, R. J. Moffett and J. A. Murphy, Planet. Space Sci., 25, 967 (1977).
16. H. C. Carlson and R. M. Harper, J. Geophys. Res., 82, 1144 (1977).
17. W. B. Hanson, A. J. Nagy and R. J. Moffett, J. Geophys. Res., 78, 751 (1973).
18. H. Rishbeth, T. E. Van Zandt and W. B. Hanson, Planet. Space Sci., 25, 629 (1977).

TABLE 1 Solar EUV Fluxes

wave-length (nm)	< 60	60-90	90-110	110-135	>135
flux (10^{12} photons $m^{-2}s^{-1}$)	53	190	710	4110	3830

EXPERIMENTAL TESTING OF “CORPUSCULAR” HYPOTHESIS OF NIGHT-TIME MID-LATITUDE IONOSPHERE—RESULTS OF SIMULTANEOUS ROCKET- SATELLITE INVESTIGATIONS

S.I. Avdyushin, L.L. Bukusova, V.M. Feigin,
G.S. Ivanov-Kholodny, T.V. Kazachevskaya,
M.A. Savylyev and V.F. Tulinov

*The USSR State Committee for Hydrometeorology and
Control of Natural Environment, Moscow, USSR*

ABSTRACT

In June of 1978 a joint Soviet-American experiment (JASPIIC) was carried out; its objective was to investigate nighttime corpuscular fluxes in the mid-latitude ionosphere. Simultaneous satellite measurements are in a good agreement with rocket results.

INTRODUCTION

One of the basic problems of the mid-latitude ionosphere is the problem of the nighttime source of ionization. As far back as in 1961 there was set up a hypothesis [1] about the corpuscular origin of the nighttime sources of ionization in the mid-latitude ionosphere. Since then a great number of experiments has been carried out [2] and [3]. The existence of nighttime corpuscular fluxes is beyond doubt now, but the intensity of these fluxes and, therefore, their role in the nighttime mid-latitude ionosphere is still being discussed.

To maintain the ionospheric nighttime E-region the precipitating electron fluxes below $10^{-4} \text{ mW m}^{-2} \text{ sec}^{-1} \text{ sr}$ are practically of no importance. At the same time electron flux values, measured by different authors at middle latitudes at solar zenith angles $Z \geq 86^\circ$ are within the range of $10^{-4} - 10^{-7} \text{ mW m}^{-2} \text{ sec}^{-1} \text{ sr}$ [2, 3]. Such a great discrepancy between the measurement results, even taking into account different geophysical conditions under which experiments were carried out, naturally gives rise to questions about methodological homogeneity of the compared experimental data.

In June of 1978 a joint Soviet-American experiment was carried out; its objectives were to intercalibrate instruments and to correlate methods used both by Soviet [4-6] and American [3, 7] scientists for measuring precipitating corpuscular fluxes. Besides, one more objective of the experiment was to measure nighttime precipitating electron fluxes under disturbed geomagnetic conditions.

During the experiment several simultaneous launchings of the Soviet

MR-12 and US Nike Tomahawk and Nike Apache rockets were conducted. The US rockets were fired from the NASA Wallops Flight Center ($\varphi=38^\circ\text{N}$, $\lambda=75^\circ\text{W}$); the MR-12 were fired from the research ship "Professor Vize" which was in the Atlantic Ocean several kilometers off the WFC.

Results. To measure precipitating electron fluxes, MR-12 were equipped with instruments of three types: "Phosphor" [5], two-channel spectrometer "CKP-2M" and Geiger detector unit "Electron" [6]. Table 1 gives dates and time (UT) of MR-12 firings, solar zenith angles (Z), three-hour values of geomagnetic planetary K_p index and local index (Fredericksburg), solar radio emission $F_{10.7}$ (Ottawa). The table gives parameters of precipitating electron fluxes detected at heights above 150 km: integral energy flux $\text{mW m}^{-2}\text{sec}^{-1}\text{sr}^{-1}$ for electrons with energy $\geq 7\text{keV}$ and $\geq 1\text{keV}, N(>40\text{keV})$ = integral intensity of electrons with energies above 40 keV.

Data on electron fluxes obtained by different instruments are in a satisfactory agreement and complement each other.

Table

No.	Date	UT	Z	K_p	$F_{10.7}$	"Phosphor"	"CKP-2M"	"Electron"
						$E \geq 7\text{keV}$	$E \geq 1\text{keV}$	$N(>40\text{keV})$
						$\text{mW m}^{-2}\text{sec}^{-1}\text{sr}^{-1}$	$\text{cm}^{-2}\text{sec}^{-1}$	sr^{-1}
1.	11.06.78	06.27	116°	5-4	110	7×10^{-5}	3×10^{-3}	1.6×10^1
2.	20.06.78	04.10	118°	3-3	169	3×10^{-5}	$\leq 3 \times 10^{-4}$	0.5×10^1
3.	24.06.78	02.13	107°	5-5	189	-	$\leq 4 \times 10^{-5}$	0.6×10^1
4.	26.06.78	01.78	102°	4-4	178	5×10^{-5}	$(0.8-8) \times 10^{-4}$	-

As it is evident from the Table reliable records of electron fluxes were obtained in firing No.1, for firings No.2 and 3 one can point out only upper estimates of fluxes. The experiment confirmed once again that night corpuscular flux intensities affecting the mid-latitude ionosphere are subjected to significant variations. Earlier we mentioned [7,8] that the precipitating electron intensity depends on geomagnetic activity.

Electron fluxes ($E=0.1-20\text{ keV}$) were also measured on board the satellite "Meteor-28" [9] (near circular orbit, $H \approx 650\text{ km}$). We use for the analysis the channels of the satellite spectrometer for the electron fluxes with pitch angles less than 65° within the invariant latitudes 50°N-50°S. Therefore, one can assume that precipitating electron fluxes were detected in the given channel for the nightside satellite orbits (local time in subsatellite points is 19-05 hr), averaged over 10-degree intervals of invariant latitude. These results show, that in equatorial and mid-latitudes the precipitating electron flux (averaged for June 1978) is about $(2-3) \times 10^{-3} \text{ mW m}^{-2}\text{sec}^{-1}\text{sr}^{-1}$, which approximately correspond to the sensitivity threshold of the satellite spectrometer. Rather reli-

able records of precipitating electron fluxes in the middle latitudes were very rare.

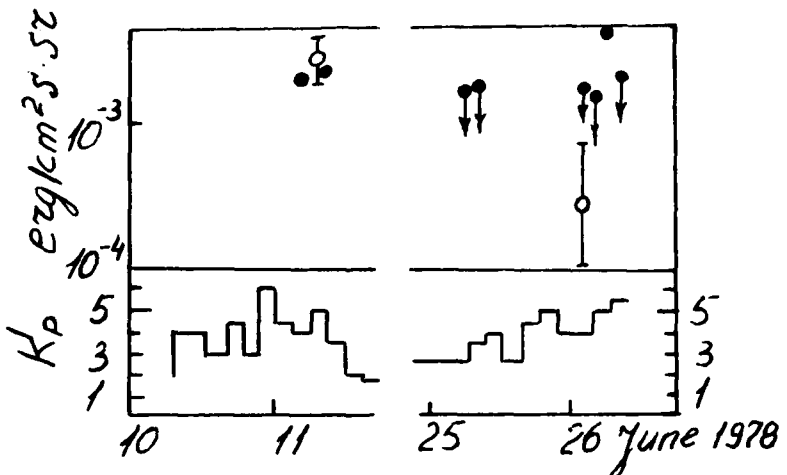


Fig. 1

Fig. 1 gives the results of rocket (circles with error flags) and practically simultaneous satellite measurements (points) and estimates (arrows) of precipitating electron fluxes. Downward arrows show that electron intensity did not exceed the instrument sensitivity threshold. It should be taken into account, that satellite measurements were carried out rather far from the area of MR-12 launchings. Nevertheless, one can point out that it was on the 11th and 26th of June that the satellite spectrometer readings exceeded background values. Data on energy fluxes, obtained in the experiment, are in agreement with the results of the analogous measurements made earlier [8, 10-12], as well as with the data on the nighttime glow when there is no low-latitude polar aurora [13, 14].

Conclusion. From simultaneous rocket and satellite measurements it follows:

During moderate geomagnetic disturbances in the nighttime mid-latitude ionosphere the precipitating electron fluxes with energies $E \geq 1$ keV may reach $(2-4) \times 10^{-3}$ mW m⁻² sec⁻¹ sr⁻¹; under undisturbed conditions electron fluxes decrease by 1-2 order of the magnitude. Precipitating electron fluxes may be an important ionization source of the ionospheric nighttime E-region during geomagnetic disturbances.

REFERENCES

1. L. A. Antonova, G. S. Ivanov-Kholodny, Geomagnetism and Aeronomy, 1, 164, (1961).
2. G. S. Ivanov-Kholodny, G. M. Nikolsky, Sun and Ionosphere, Science, Moscow, 1969.

3. F.A. Morse, C.Y. Rice, J.Geophys. Res., 18, 2795, (1976).
4. G. S. Ivanov-Kholodny, T.V. Kazachevskaya, V. V. Savelyev, Solar-Atmospheric Relations, Gidrometeoizdat, Moscow, 47, 1974.
5. T. V. Kazachevskaya, in: Planetary and Space Science, 12, 2, (1964).
6. J. F. Tulinov, in: Kosmicheskie issledovaniya, XIII, (1975).
7. L. G. Smith, in: J. Atmospher. Terrestr. Phys., 36, 1601, (1974).
8. V. F. Tulinov, in: Kosmicheskie issledovaniya, XII, (1974).
9. V.F. Tulinov, in: KAPG Symposium on Solar-Terrestrial Physics, Science, Ashhabad, 1979.
10. V.F. Tulinov, in: Kosmicheskie issledovaniya, XIII, (1975).
11. T. V. Kazachevskaya, A. I. Koryagin Kosmicheskie issledovaniya, VII, 6, (1969).
12. V. F. Tulinov, in: Geomagnetism and Aeronomy, 17, 491, (1977).
13. Yu. I. Galperin, News of the Academy of Sciences, Geophysical Series, 2, 252, (1962).
14. A.Dalgarno, Ann. Geophys., 20, 1, 65, (1964).

PART II
ISC C Session 3—Models of the Terrestrial
Mesosphere and Thermosphere

SECTION 1
Stratosphere—Mesosphere

MODELS OF THE HIGH LATITUDE STRATOSPHERE AND MESOSPHERE

G.A. Kokin, D.A. Tarasenko and L.A. Ryazanova

State Committee of the USSR for Hydrometeorology and Control of Natural Environment, Moscow, USSR

ABSTRACT

Methods of calculation of interhemispheric and longitudinal differences are discussed. It is noted that in models one should take into account the solar activity influence. Network rocket sounding accuracy, devices and technique compatibility are analysed.

INTRODUCTION

The paper deals mainly with high latitude temperature models. The reasons for this are as follows. First, temperature is one of the two principal parameters measured directly in the world rocket sounding station network. Pressure and density are derivative values calculated by means of the hydrostatic equation. Second, temperature data are applied for calculation of regression relations used in processing of satellite radiometric measurements. Third, horizontal temperature gradients are initial data for calculations of the thermal winds often used in models.

The CIRA 1972 model describes adequately major features of the stratosphere and mesosphere [1]. However, in CIRA 1972 there are no models for latitudes exceeding 70° and no models for the southern hemisphere. Besides, the CIRA 1972 model takes into account only in part longitudinal differences between the eastern (65°E) and western (80°W) hemispheres. It does not include interannual variations for the high latitude winter. Long-period temperature and wind trends in the stratosphere and mesosphere are not taken into account. In particular, there is no relationship of thermodynamic parameters with the 11-year solar activity cycle.

We have available the following information (in addition to other data) to develop high latitude models:

- in the northern hemisphere: rocket data from Heiss Island ($80^{\circ}37'N$ $58^{\circ}03'E$) for the period 1960-1980 (1000 observations),
- in the southern hemisphere: rocket data from Molodezhnaya station ($67^{\circ}40'S$ $45^{\circ}51'E$) for the period from August 1969 to 1980 (500 observations).

TEMPERATURE DATA

Before the discussion of characteristic temperature profiles one should examine problems connected with rocket sounding accuracy and compatibility of instrumentation and methods. A large amount of laboratory investigations and technical designing was completed in the USSR during recent years concerning improvement of the sounding accuracy of the M-100B rocket. Great attention has been paid to laboratory experiments concerning aerodynamic coefficients of rocket thermistors, to increase the accuracy of radiometric and remote measurements, to decrease the fall velocity of rocketsondes and increase the movement stability of rocketsondes.

In particular, it was found that due to the aerodynamical effect thermistors of the former design [2] lowered the measured mesospheric temperature. In this connection, a modified design of resistance thermistor was developed [3].

In 41 pairs of simultaneous temperature measurements by the two types of resistance thermistor the difference was equal to 2°C at 45-50 km altitudes, 7°C at 55 km, 12-15°C at 60-65 km and 9°C at 70 km. Instrument calibration errors and shortcomings of the mathematical processing program also influenced the measured results. The total error in temperature measurements by resistance thermistors depends on contributed errors of the radiometric and radar systems, on errors in determination of experimental values in the fundamental equation of thermistors, as well as on processing methods.

The standard error was found both theoretically and experimentally taking into account all these factors. It changes from 2 K at an altitude of 50 km to 6 K at 80 km.

Temperature measurement systematic differences were determined by comparative launchings of different types of rockets [2]. The results of comparisons of Soviet (M-100B) and American (Super-Loki-datasonde) rocket systems are given in Fig.1.

The differences given in Fig.1 should not be considered as the systematic errors of the Soviet resistance thermistor, because systems being compared have their own non-accounted measurement systematic errors. In the Soviet Union for synoptic studies the MM-R-06 rocket system is used. Some weather ships of the State Committee of the USSR for Hydrometeorology and Control of Natural Environment are supplied with this rocket system. Microresistance is used to measure air temperature. Descent velocities of MM-R-06 rockets are less than the velocities of M-100B rockets. The results of comparison of MM-R-06 and M-100B rockets are given in Fig.2. They show slight systematic differences of the sounding systems up to 55 km altitude.

Differences in data obtained by means of grenades, Pitot [4] and rocket thermistors of modified design on M-100B rockets require further comparisons and careful analysis of instrument systematic errors. Causes of summer temperature differences of 9°C at the 65 km altitude are not yet clear (Fig.3).

From [5] it is seen that the grenade method is rather representative. In this connection, for temperature analysis at altitudes above

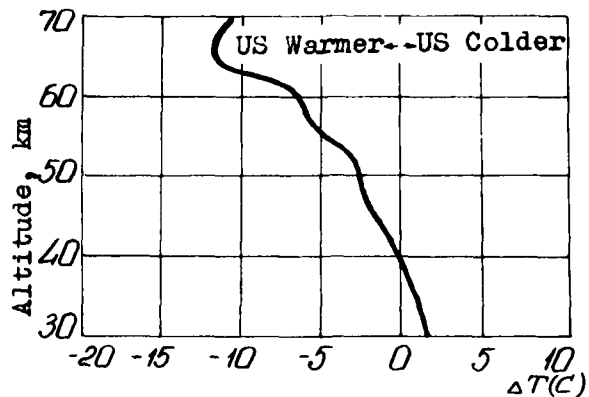


Fig.1. Temperature discrepancies (T) between the Soviet (M-100B) and American (Super-Loki-Datasonde) rocket systems obtained during the intercomparison test (wallops Island, 1977)

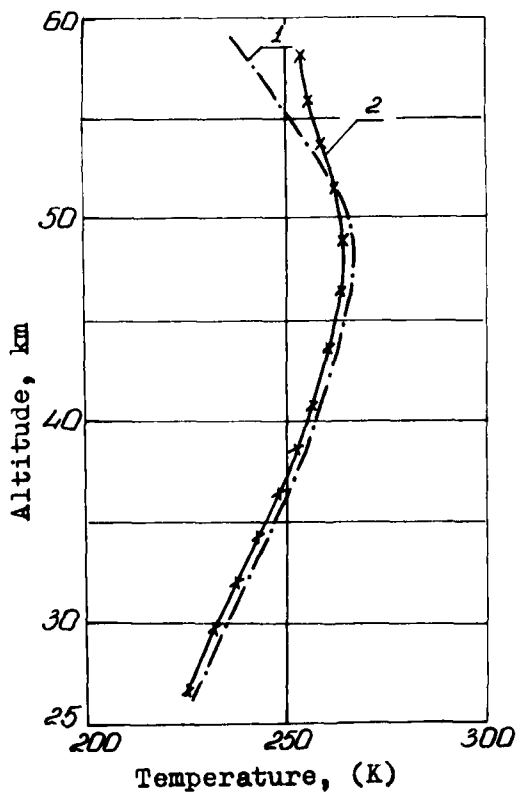


Fig.2. Results of M-100B (1) and M.R.-06 (2) rocket systems comparisons, May 1979, Indian ocean, near the equator, mean values of 7 pairs of simultaneous measurements.

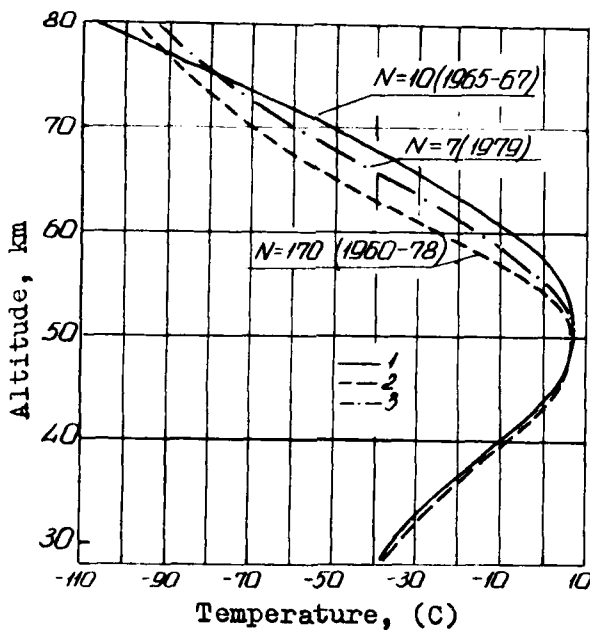


Fig.3. Temperature profiles obtained by means of grenades and Pitot (1) at Point Barrow, M-100 rocket (2) and M-100B rocket (with thermistors of modified design) (3) at Heiss Island, summer.

50 km we used grenade data as basic values. Adjustments were introduced into Soviet rocket sounding data [9]. Mean annual variations of wind and temperature over Heiss Is. and Molodezhnaya st. were presented earlier in [10, 11]. Warm season models represent completely characteristic features of the summer atmosphere, which can not be said about winter distributions which are very variable due to the development of strato-mesospheric warmings and related circulation reversals. The method of presentation of warm and cold models of the winter stratosphere for polar latitudes is examined in [7].

Longitudinal variations of mean temperature and wind in the upper stratosphere and mesosphere can be revealed in mean charts of distribution of these meteorological parameters. Global mean 2, 0.4 and 0.1 mbar contour charts and the northern hemisphere 0.001 mbar charts [12, 13] are compiled, which exhibit both temperature and wind longitudinal variations. As an example the wind data for different longitudes [14] are given in Table 1.

Interhemispheric as well as longitudinal differences are especially large in winter seasons of the both hemispheres. Usually the Antarctic polar cyclone in the lower and middle stratosphere is much colder than the Arctic one (by 10-20°C). At the same time the summer stratosphere of the southern hemisphere is warmer than that of the

TABLE I

Wind Velocity Zonal Component for High Latitudes of the Northern Hemisphere at 80 km Altitude (in m/s)

Longitude	0	90°E	180°	90°W				
Months	I	VII	I	VII	I	IV	I	VII
Latitude								
60°N	42	10	54	8	0	7	35	15
70°N	21	8	26	7	-6	-12	14	8
80°N	-11	-23	0	-24	-12	-7	-6	-8

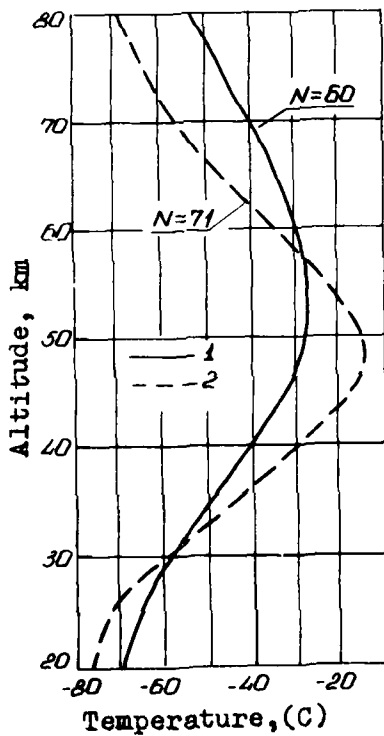


Fig.4. Temperature profiles over Heiss Is. in maximum (1) and minimum (2) solar activity years, winter.

Northern Hemisphere. In winter seasons at high latitudes temperature differences in the upper stratosphere between the northern and southern hemispheres are absent. However, according to Molodezhnaya station data the upper stratosphere of the Antarctic in late winter is warmer on the average than that of the Arctic [1]. This is explained by the fact that Molodezhnaya station is situated in the warm sector of the Antarctic. Longitudinal differences in the winter stratosphere and mesosphere of the Antarctic are important. Temperature values in the winter mesosphere over the Antarctic are also somewhat higher than over the Arctic. Similar results are obtained in [11, 16, 17]. Observational models of thermodynamic parameters and zonal wind velocity distributions in the upper stratosphere and mesosphere of the southern hemisphere are presented in [11]. The data kindly presented by the Prof. G. Doughton's group from Oxford were used for analysis of the spatial distribution of temperature and other parameters.

Finally, let us consider the solar activity influence during an 11-year cycle on the temperature in the stratosphere and mesosphere of the polar region in winter. For the present, data considered are of an illustrative character and indicate the necessity of taking into account solar activity in development of stratospheric and mesospheric models.

In polar winter regions solar radiations direct influence in the electromagnetic band is a minimum. Therefore, effects connected with the disturbed Sun must appear more distinctly. Hence, polar electrojet dynamics and corpuscular fluxes in the winter season of the polar region and their contribution to the energy budget should be more marked. Taking into account these circumstances, let us consider temperature variation in an 11-year solar activity cycle in the polar region.

As a measure of solar activity the exospheric minimum temperature was used, this is affected both by solar flux at 10.7 cm ($F_{10.7}$) and by geomagnetic activity (k_p index). Validity of this parameter and of the method of calculation is described in [18].

In winter mean values of T_e (December-January-February) for the period from 1966 to 1976 two maxima are seen: the first one, the main, was in 1968 equal to 1330 K and the second, in 1970 equal to 1230 K. The least value was observed in 1976, with $T_e = 900$ K. So, in this period of observations the maximum amplitude of the winter mean values of T_e was equal to 400 K.

To compare T_e with temperature values in the stratosphere and mesosphere all data were grouped into two main periods - maximum (1968-1971) and minimum (1974-1976) solar activity. As an example, winter mean values of T_e and mean temperatures at the altitudes of 45 km (the stratosphere) and 70 km (the mesosphere) over Heiss Is. are given in Table 2. It is seen from Table 2 data that atmospheric temperature in the polar region is different in years of maximum and minimum solar activity. Note that these temperature differences are significant in all layers.

In Figs. 4-5 temperature vertical profiles over Heiss Is., Molodezhnaya st., Point Barrow, Fort Churchill for periods of maximum

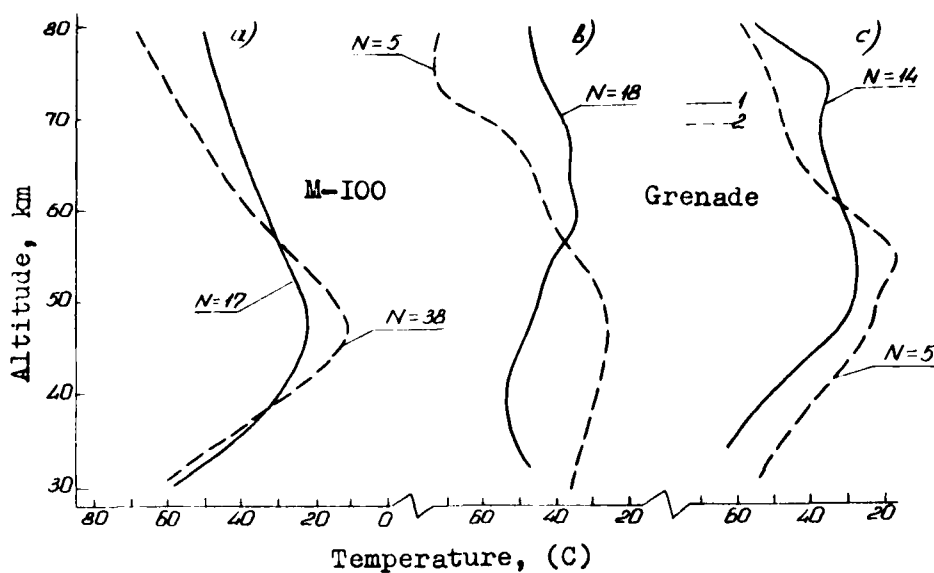


Fig. 5. Temperature profiles over Molodezhnaya st. (a), Point Barrow (b) and Fort Churchill (c) in maximum (1) and minimum (2) solar activity years. Winter

TABLE 2

Winter Mean Values of T_e and Temperature T (C) over Heiss Is. in Years of Maximum and Minimum Solar Activity at Altitudes of 45 and 70 km

H km	Winter mean tem- perature K in 1968-1971	Winter mean tem- perature K in 1974-1976	Temperature diffe- rences over the pe- riods mentioned, K
T_e	1233	996	237
T-70	217	202	15
T-45	233	263	-30

and minimum solar activity are given. For high latitude stations in the western hemisphere grenade data were used. Temperature profiles for minimum solar activity are obtained on the basis of the XXI solar cycle data.

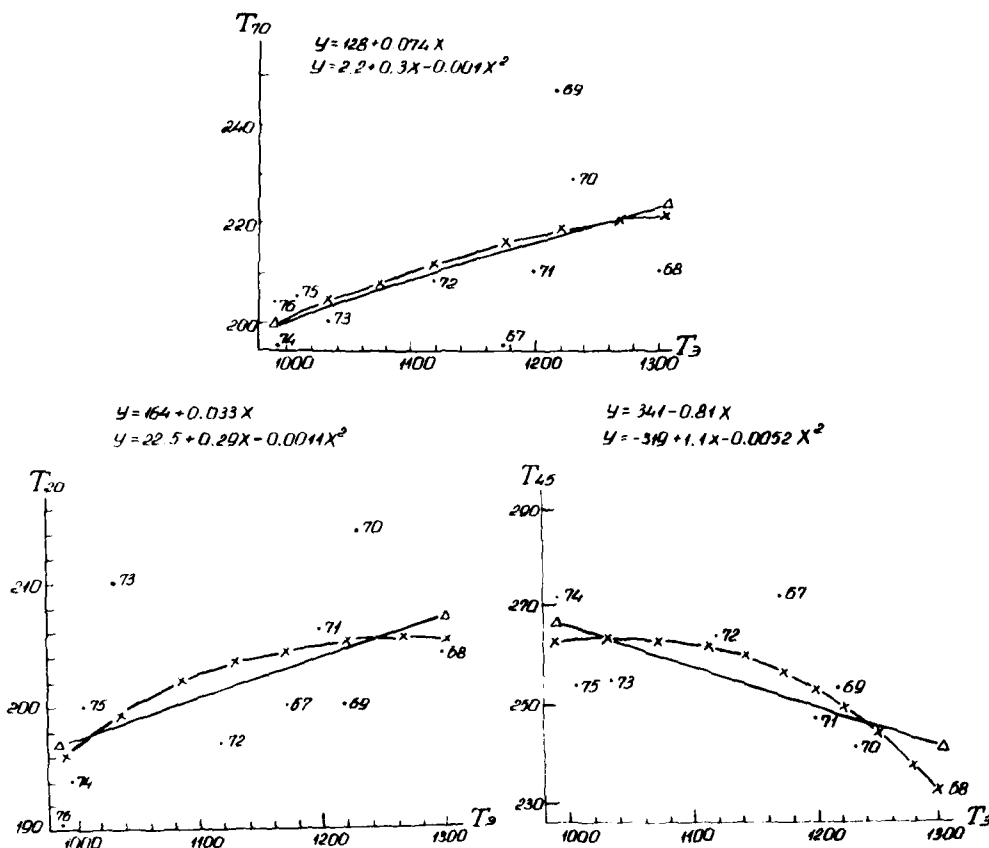


Fig.6. Regression dependences between exospheric minimum temperature (T_e) and temperature over Heiss Is. (T) at 70, 45 and 20 km altitudes.

The connection between solar activity and temperature of different atmospheric layers can be seen from Fig.6, which represents linear and quadratic regression relations for Heiss Is. Numbers near points indicate years for which temperature mean values are obtained. At the 70 km altitude the large deviation of the 1969 point may be explained by a major mesospheric warming observed at this period.

In our opinion, dependence of the thermal regime on solar activity is seen from the variability of a lot of factors, for example, long planetary waves, turbulent heat conduction, vertical currents, the polar electrojet, as well as radiative cooling connected with atmospheric air content variation.

Solar activity influence on temperature of the stratosphere and mesosphere was considered in papers [18-20], and the conclusion about the necessity of taking into account solar activity influence in development of models is in agreement with results obtained by other authors [17].

REFERENCES

1. COSPAR International Reference Atmosphere 1972, CIRA 1972 , Akademie Verlag, Berlin, 1972.
2. E.A. Besyadovsky et al., Trudy CAO, 82, 3 (1969).
3. A.I. Ivanovsky et al., Space Research XXI, 127 (1979).
4. J.S. Theon et al., The Mean Observed Meteorological Structure and Circulation of the Atmosphere, NASA TR R-375, Washington, D.C. 1972.
5. J.L. Schmidlin, Preliminary Results of the US-USSR Meteorological Rocketsonde Intercomparison Held at Wallops Island, Va., August 1977, Presented at COSPAR XXI Innsbruck, 1978.
6. GOST 4401-73. Standard Atmosphere. Parameters. Izdatelstvo Standartov, 1974.
7. ISO/TC-20/SC-6 (USA-10) 102.E, April 1977.
8. S.S. Gaigerov et al., Meteorologia i Gidrologia, 3, 106 (1978).
9. M.E. Gelman et al., J. Atmosph. Sci., 32, 9, 1705 (1975).
10. D.A. Tarasenko, Space Research XIX, 135 (1979).
11. Yu.P. Koshelkov, Circulacia i Stroenie Stratosferi i Mesosferi Yujnogo Polusharia, Gidrometizdat, Leningrad, 1980.
12. S.S. Gaigerov et al., Space Research XI, 799 (1971).
13. S.S. Gaigerov et al., Space Research XX, (1980).
14. ISO/TC-20/SC-6, 1978.
15. S.S. Gaigerov and Yu.P. Koshelkov, Space Research XIII, 173 (1973).
16. Knittel, J. Meteor. Abhandlungen, Ser.A, 2/1-1, 1 (1976).
17. K. Labitzke, Phil. Trans. R. Soc. Lond., A296 (1980).
18. G.A. Kokin et al., Meteorologia i Gidrologia 7, 10 (1977).
19. J.K. Angell and J. Korshover, J. Atmos. Sci., 35, 1758 (1978).
20. R.S. Quiroz, J. Geoph. Res., 84, 2415 (1979).

MESOSPHERIC STRUCTURE AND THE D-REGION WINTER ANOMALY

D. Offermann,¹ H.G. Brückelmann,¹ K.M. Torkar²
and H. Widdel³

¹ University of Wuppertal, Wuppertal, FRG

² University of Graz, Graz, Austria

³ Max-Planck-Institut, Lindau, FRG

ABSTRACT

Model mechanisms to explain the D-region winter anomaly have so far not really been successful, considering the many different aspects of this atmospheric/ionospheric phenomenon. A new model is therefore proposed relating the winter anomaly essentially to atmospheric temperature and wind variations. The new mechanism is checked by a set of data obtained during the Western European Winter Anomaly Campaign 1975/76, and additionally by a second set of data taken in earlier years.

INTRODUCTION

The ionospheric D-region in winter exhibits erratic and strong enhancements of radio wave absorption ("winter anomaly") (for a recent review see Offermann [1]). It is widely accepted today that these enhancements are due to increases of electron density in the D-region. The question is what makes the electron density rise so steeply, and afterwards decay again. Temperature variations affect the chemistry of neutral atmosphere minor constituents as well as the ion chemistry. They have, therefore, been discussed for some time in the literature as a possible cause. It was shown by Offermann et al. [2], however, that they can give only one half of the picture: a co-factor is needed to act together with the temperature changes to explain the full variability of the electron density. Enhanced nitric oxide density in the D-region has long since been suspected as a reason of the winter anomaly because of resulting increases in electron production. Thus horizontal or vertical transport of NO might act as the co-factor needed. Enhanced NO-densities were found indeed during all winter anomaly events when in-situ NO measurements were performed (for the respective literature see Offermann [1]).

Horizontal transport of NO from the auroral zone to medium latitudes has repeatedly been discussed in the literature as a source of such D-region NO enhancements. It appears, however, that during the Western European Winter Anomaly Campaign 1975/76 in Spain, such advection was insufficient to explain the required NO variations (Offermann [3]). Downward transport of NO from the E-region by turbulence is another mechanism discussed in the literature. It has the difficulty, however, that it cannot fully explain the speed at which the winter anomaly varies. As was pointed out by Offermann [3] vertical transport can principally explain the short rise time of 1 day (or less) of the electron density by assuming a sudden increase

of turbulence. It fails, however, to explain the winter anomaly decay time, which is as fast as its rise time. Photodissociation of NO in the D-region is much too slow (Nicolet and Cieslik [4]). The problem remains unsolved so far how to remove the NO from the region once it has been taken there by turbulence.

DATA ANALYSIS AND RESULTS

The advanced data evaluation of the Western European Winter Anomaly Campaign 75/76 shows that turbulence was strong in the D-region during that time. The Richardson numbers measured indicate an association of increased turbulence and winter anomaly (Brückelmann [5]). Mass spectrometer composition measurements on a winter anomalous day of that campaign also indicate increased turbulence (Offermann et al. [6]). During a winter anomaly campaign performed at Wallops Island simultaneously with the European one, decreased turbulence on a non winter anomalous day was observed (Philbrick et al. [7]). Hence these data make it possible to assume that turbulence is a build-up mechanism for winter anomaly.

The decay mechanism, however, has to be something different. When looking for a measured parameter varying fast enough the horizontal wind speed was considered. It is indeed found to be a suitable NO removal mechanism, as it could just blow away a cloud of increased NO density. Combined action of vertical transport, modulated horizontal wind speed, and horizontally inhomogeneous NO density in the E-layer could, therefore, explain the fast winter anomaly variations, as far as NO is concerned. This "model 1" has, however, to assume a suitable horizontal structure of NO density in the E-region. There appear to be no satellite data available for the time of the campaign discussed here to check on this structure, and hence model 1 contains an annoying free parameter.

This free parameter is not required in "model 2", which is sketched in Fig. 1: In an upper atmospheric layer NO is produced, and its density is assumed to be horizontally uniform. In this layer the horizontal wind speed is assumed to be zero, whereas in the atmospheric layer below there are horizontal winds of varying speed. (This lower layer may be roughly identified with the D-region) This may be a somewhat idealized picture. The model proposed is, however, always valid if only the winds in the upper layer are different from those in the lower layer. Furthermore the CIRA 1972 tables show a node in the prevailing winds above the D-region in winter at medium latitudes. The essential part of the model is its assumption of a boundary in the atmosphere in the effective vertical transport velocity w : In Fig. 1 w is low in the left hand side of the picture, and high in the right hand side. This vertical transport may be turbulent transport, i.e. the model assumes a cell of enhanced convection in the right side of Fig. 1. The low downward velocity w_1 represents the normal state of the atmosphere. It must therefore be small enough (a few cm/s) to allow photodissociation to produce the deep valley in D-region NO density which is observed under quiet conditions, and which is indicated by the inserts in Fig. 1 (see Baker et al. [8], Offermann [3]). If switched on, the increased downward velocity w_2 on the right side easily fills that valley (by even moderate eddy coefficients, see Baker et al. [8]), as is indicated by the inserts in Fig. 1. The action of the varying horizontal wind speed is now to sweep the boundary between low and high NO density in the D-layer across the atmospheric regime which is probed by radio wave absorption methods. Hence the observing station "sees" increased NO density and therefore a winter anomaly event in case of low horizontal wind speed v_1 , and no winter anomaly at high wind speed v_h . This "inverted chimney model" easily explains the NO density variations of about a factor 4 (or more) observed during winter anomaly activity in the D-region.

The model uses only two atmospheric parameters: increased turbulence to switch on the winter anomaly, and increased horizontal wind speed to switch it off again.

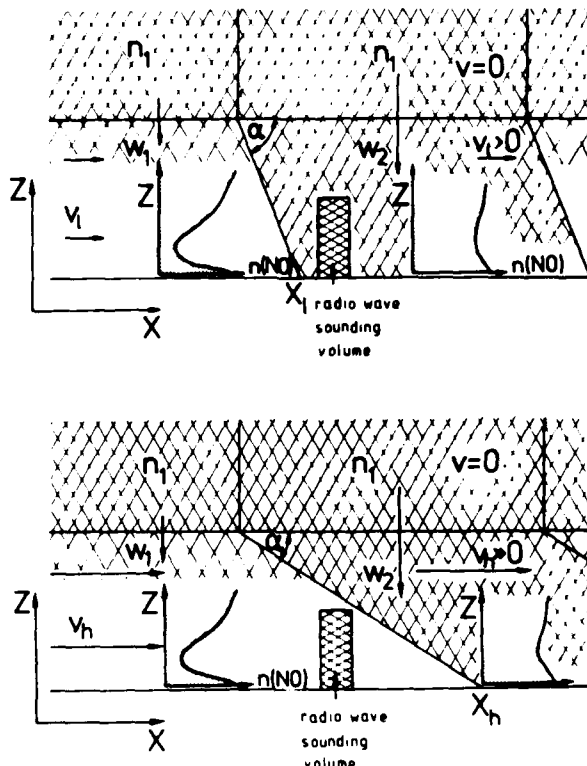


Fig. 1 A model to explain D-region $n(\text{NO})$ density variations by the combined action of varying vertical transport velocity w and varying horizontal wind speed v (upper part: low horizontal wind speed v_1 ; lower part: high horizontal wind speed v_h ; $\tan \alpha = w_2/v_{1,h}$)

Either process undoubtedly is fast enough to act with a time constant of about 1 day. The model suggests that the winter anomaly is associated with increased turbulence, as is indicated by the data discussed above. It furthermore requires that winter anomaly activity be anti-correlated with horizontal wind speed in the altitude layer involved. This anticorrelation refers to the absolute values of the wind speed.

During the Western European Winter Anomaly Campaign 1975/76 a number of wind measurements by means of chaff clouds were performed (Rees et al. [9]). Fig. 2 shows the results of a correlation analysis of the wind speeds obtained and the A3 radio wave absorption measurements around the time of the rocket flights. The expected anti-correlation is clearly seen in the D-region. As the number of rocket flights was limited (13) the significance of the correlation coefficients r is limited. The vertical bars in Fig. 2 indicate altitude regimes where the significance is better than 95%. (The reversal of the correlation at lower altitudes may be due to the strong oscillations present in the atmosphere during that campaign, see Offermann et al. [2]).

To improve the statistics a set of earlier measurements of wind speed and radio wave absorption (at the same place in Spain) was analyzed. About 30 rockets measurements were performed during winter anomaly periods ("patches") in the years 1968-1975. Preliminary results of the correlation analysis are also shown in Fig. 2. They are very similar to those of the 1975/76 campaign. It is therefore

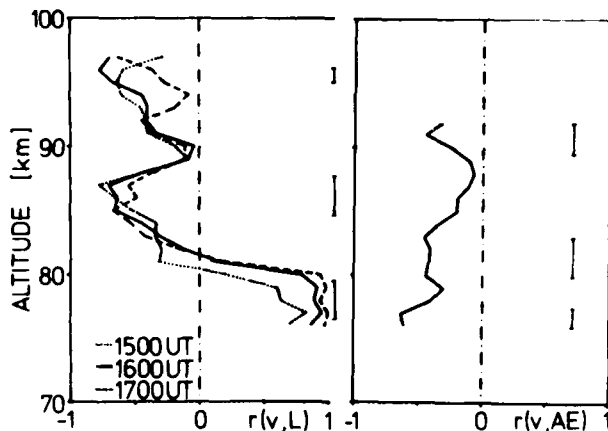


Fig. 2 Correlation coefficient r of horizontal wind speed v (absolute values) and radio wave absorption L . The left picture shows the results of the Western European Winter Anomaly Campaign 1975/76. L values were taken around the launch times of the rockets. The right picture shows respective results from earlier measurements in 1968 to 1975 (noon measurements).

felt that the "inverted chimney model" together with mesospheric temperature variations bears some significance for the explanation of the winter anomaly. It should be noted that this model predicts a reversed correlation if the location of the radio wave sounding volume is shifted from the upwind boundary of the region of enhanced NO density (Fig. 1) to its downwind boundary. Respective data are presently analyzed.

References

1. D. Offermann, J. Atmos. Terr. Phys. 41, 735 (1979).
2. D. Offermann, P. Curtis, J.M. Cisneros, J. Satrustegui, H. Lauche, G. Rose, and K. Petzoldt, J. Atmos. Terr. Phys. 41, 1051 (1979).
3. D. Offermann, Phil. Trans. R. Soc. Lond. A 296, 261 (1980).
4. M. Nicolet and S. Cieslik, Planet Space Sci. 28, 105 (1980).
5. H.G. Brückelmann, Diplomarbeit, Univ. Wuppertal, Physics Dept. (1981).
6. D. Offermann, V. Friedrich, P. Ross and U. von Zahn, submitted to Planet. Space Sci. (1980).
7. C.R. Philbrick, G. Faucher and P. Bench, Space Res. XVIII, 139 (1978).
8. K.D. Baker, A.F. Nagy, R.O. Olsen, E.S. Oran, J. Randhawa, D.F. Strobel and T. Tohmatsu, J. Geophys. Res. 82, 3281 (1977).
9. D. Rees, A.F.D. Scott, J.M. Cisneros, J.M. Satrustegui, H. Widdel and G. Rose, J. Atmos. Terr. Phys. 41, 1063 (1979).

DISSIPATION OF TEMPERATURE PERTURBATIONS IN THE MIDDLE ATMOSPHERE

G.E. Thomas

*Laboratory for Atmospheric and Space Physics and
Department of Astro-Geophysics, University of Colorado,
Boulder, CO, USA*

ABSTRACT

It is often observed that the stratospheric and mesospheric temperature structure undergoes transient disturbances from its averaged steady-state behavior. The causes may be traceable to gravity waves, planetary waves, solar proton and relativistic electron precipitation, etc. We examine the theoretical time behavior of the atmospheric temperature following the cessation of such heating phenomena as it relaxes toward its quiescent steady-state value. We also study the time-dependent response during a model stratospheric-warming/mesospheric-cooling event. In particular, we investigate the roles of eddy heat conduction, non-LTE cooling in the $15\mu\text{m}$ CO_2 band, and an ambient vertical wind, and their relative importance as they depend upon altitude and time, in modifying temperature changes in this region.

INTRODUCTION

In the height region 50-100 km, the mean temperature structure is controlled by UV heating, wave heating, eddy cooling and long-wave cooling in the $15\mu\text{m}$ CO_2 band.

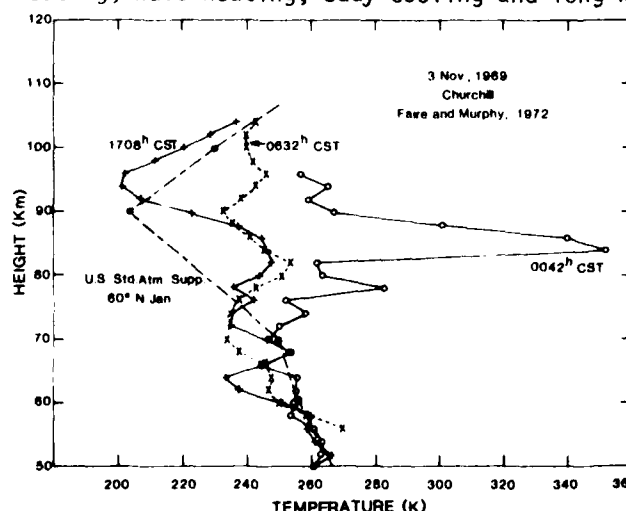


Fig. 1. A strongly perturbed atmosphere during a solar proton event [8].

However, the standard mean temperature is often strongly perturbed by transient heating, which is commonly attributed to increased wave activity. Other sporadic heating mechanisms may be important at high latitudes, such as deposition of solar protons (Fig. 1) and joule heating (Banks, [1]). The present interest is not so much in these heating processes, but in the dissipative processes restoring the disturbed temperature to its mean state.

These dissipative processes are eddy conduction and long-wave radiative transfer. Both these influences are important in the mesosphere. Radiative processes dominate below about 40 km, and eddy conduction dominates

above about 60 km, at least according to the profile of the eddy conductivity K_H of Park and London [2]. This value of K_H is quite uncertain, and may vary from season to season. Indeed, there are good reasons for doubting the validity of the entire concept of the mixing-length theory as applied to the mesosphere; however, as discussed later, the present results may be useful in evaluating its usefulness.

In contrast, the radiative processes are fairly well understood, at least in the region below ~75 km, the height of vibrational relaxation of the $15\mu\text{m}$ CO_2 band. Above this altitude it is necessary to take into account non-LTE effects of the thermal emission properties of the atmosphere. We have adopted the method of Kupetov [3] for calculating the non-LTE heating rate in the region above 75 km. This provides greater accuracy than the cooling-to-space, or Newtonian cooling method, which is in wide use in numerical modelling.

FORMULATION

To study time-dependent changes in temperature T , it is necessary to consider the thermodynamic equation. It may be shown that this takes the form (e.g., Gay and Thomas, [4])

$$\frac{\partial}{\partial t}(\rho c_p T) = \rho c_p(q_r + q_d) + wgp - \nabla \cdot \vec{F}_h - \frac{\partial F_z}{\partial z} \quad (1)$$

where

$$\vec{F}_h = \rho c_p \vec{V}_h T \quad \text{and} \quad F_z = -\rho c_p K_H (\partial T / \partial z + g/c_p) + \rho c_p wT$$

t = time, ρ = density, c_p = specific heat at constant pressure, q_r and q_d are the diurnal averages of the net radiative heating and dynamical heating rates per unit mass, w and \vec{V}_h are the diurnal averages of the vertical and horizontal wind components, and K_H is the eddy conductivity. \vec{F}_h and $\rho c_p wT$ are the advective enthalpy fluxes in the horizontal and vertical directions, and $-\rho c_p K_H (\partial T / \partial z + g/c_p)$ is the eddy flux. A daily average is required in order to suppress changes such as 24-hour changes in solar insolation, tidal and gravity wave heating. We assume that the mean diurnally-averaged temperature is in a steady-state

$$\frac{\partial}{\partial t}(\rho c_p T) = \rho c_p(\bar{q}_r + \bar{q}_d) + \bar{w}gp - \nabla \cdot \vec{F}_{\text{tot}} = 0 \quad (2)$$

The bars ($\bar{\cdot}$) denote the values of the various quantities in the steady-state. Introducing a perturbation heat source q' , it is easily shown that the perturbed temperature, given by $T(z,t) = \bar{T}(z) + \theta(z,t)$, is described by

$$\frac{\partial}{\partial t}(\rho c_p \theta) = \rho c_p(q'_r + q_p) + \frac{\partial}{\partial z}[\rho c_p K_H \frac{\partial \theta}{\partial z}] - \frac{\partial}{\partial z}[\rho c_p \bar{w}\theta] \quad (3)$$

where we have assumed that q_p and hence θ depend upon height and time only, and are not functions of the horizontal coordinate. We have suppressed any consequent changes in the vertical wind field, due to the increased heating, since this may be lumped into the heat source q'_r . q'_r is the change in the net heating rate, due to the different temperature. We will assume that the UV heating term is unaffected and that q'_r describes only the long-wave IR radiative heating/cooling.

SIMULATIONS

Two model situations are studied: 1) an initial-value problem of the relaxation of an initial temperature 'spike' (actually a thin sheet), and 2) a model stratospheric warming event. We first consider the relaxation of an initial 10K temperature perturbation centered at 90 km. Equation (3) was integrated numerically, assuming $\partial p / \partial t$, q'_r and q_p are all zero and with the boundary conditions $\partial \theta / \partial z(120 \text{ km}) = \theta(50 \text{ km}) = 0$. The results are shown in Figure 2 for a total

period of 10 days, revealing the expected broadening of the initial spike and the decrease of the maximum temperature. After an initial period of rapid cooling (~ 2 days) due to eddy conduction, the profile has broadened to the point where eddy cooling gives way to a slower radiative cooling with a time constant of ~ 5 days. Note also the drift upwards of the position of the maximum temperature. This is due to the term $\partial/\partial z(p_c K_H)\partial\theta/\partial z$ which acts like an (upward) advection term, where the effective vertical velocity is $W_{eff} = (pc_p)^{-1}\partial/\partial z(p_c K_H)$.

Figure 3 shows the influence of a typical mid-latitude solstice-condition vertical velocity ($+1 \text{ cm s}^{-1}$ in summer, -1 cm s^{-1} in winter). During the summer, eddy conduction bolsters the overall advective velocity to $\sim 1.9 \text{ cm s}^{-1}$, and during the winter, diminishes the velocity to $\sim 0.4 \text{ cm s}^{-1}$. Similar results were found for an initial peak centered at 70 km.

We now consider the dissipative effects of eddy conduction and radiative transfer on a stratospheric warming event propagating upwards into the mesosphere. Geisler [5] has presented calculations of the perturbed winds and temperatures in the mesosphere during such an event, but has included only a constant Newtonian-cooling coefficient. In lieu of solving the full set of dynamical and thermodynamical equations, we have used the results of Geisler for the heating rate $q_p(z,t)$, due to both adiabatic cooling and horizontal advection. However, we include the damping mechanism of eddy conduction and consider a more accurate treatment of the radiative

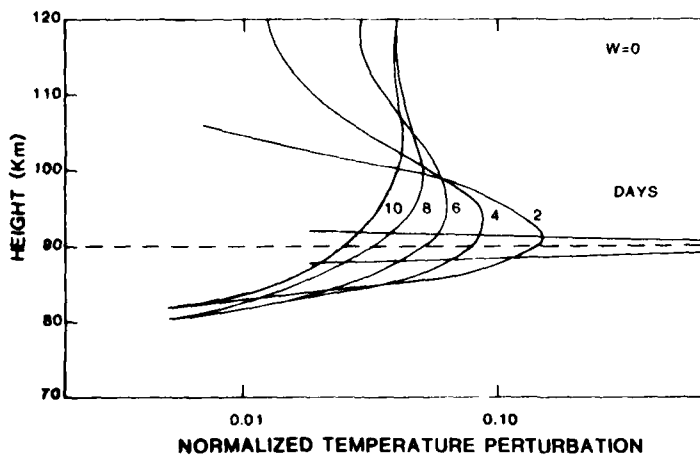


Fig.2 Relaxation of a 'thin-sheet' temperature perturbation.

ence of a typical mid-latitude solstice-condition vertical velocity ($+1 \text{ cm s}^{-1}$ in summer, -1 cm s^{-1} in winter). During the summer, eddy conduction bolsters the overall advective velocity to $\sim 1.9 \text{ cm s}^{-1}$, and during the winter, diminishes the velocity to $\sim 0.4 \text{ cm s}^{-1}$. Similar results were found for an initial peak centered at 70 km.

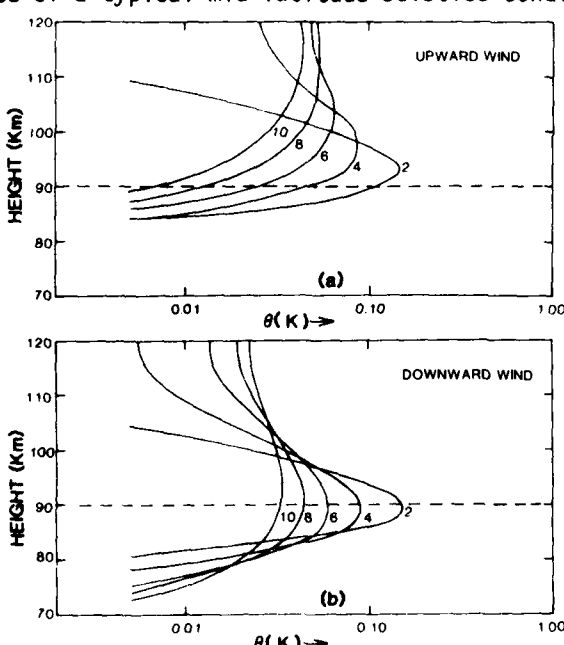


Fig.3 (a) Same as Fig.2 but for an upward wind W of $+1 \text{ cm s}^{-1}$. (b) for a downward wind W of -1 cm s^{-1} .

transfer, including the non-LTE effects. Geisler's results show that the effect of horizontal advective heating dominates q_p in the lower mesosphere and stratosphere, but that adiabatic cooling, due to the vertical wind, is dominant in the upper mesosphere. This out-of-phase relationship is in agreement with observations (e.g., Labitzke, [6]).

The effects of the upward propagating planetary wave are shown in Figure 4. To illustrate the dramatic damping effects of eddy conduction and radiative transfer,

we compare the model predictions with those using only the simple Newtonian cooling. This shows how the temperature evolves with time at fixed height levels. The 'wave' of cooling in the upper mesosphere is followed by a compensating warming as the air subsides. However the presence of eddy dissipation drastically reduces the temperature amplitude, by more than a factor of two in the mesopause (80-90 km) region. The spatial redistribution of the heat also causes the phase of the disturbance to be advanced by as much as 4 days.

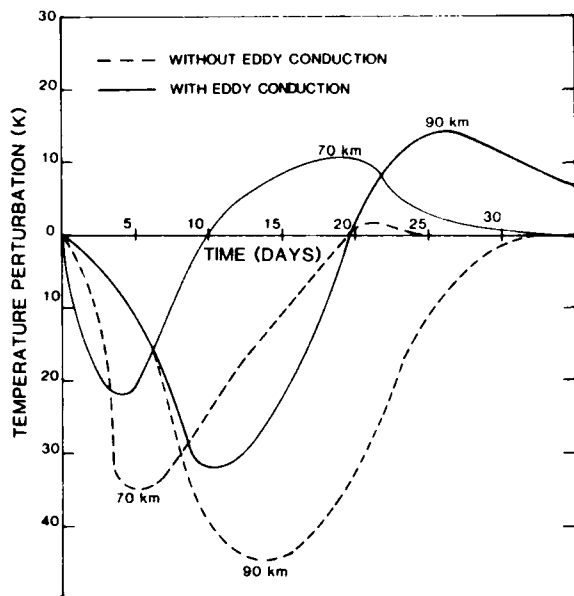


Fig. 4 Time evolution of the model stratospheric-warming/mesospheric cooling at fixed heights. Dashed curves - results for Geisler's model including only Newtonian cooling. Solid lines - present results, including eddy heat conduction.

cooling and eddy conduction must be taken into account in calculating the temperature damping in any realistic numerical models of the upper mesosphere. With the availability of satellite measurements, it should now be possible to submit the often-abused concept of eddy heat conduction to a critical test. We suggest that a good way to do this is to examine the transient behavior during disturbed periods.

This work has been supported by the Atmospheric Sciences Section of the National Science Foundation.

REFERENCES

1. D. M. Banks, *Geophys. Res. Lett.* **84**, 6709 (1979).
2. J. H. Park and J. London, *J. Atmos. Sci.* **29**, 1395 (1974).
3. A. A. Kuteпов, *Izvest. Atmos. Ocean. Phys.* **14**, 154 (1978).
4. C. Gay and G. E. Thomas, *J.Q.R.S.T.*, in press (1980).
5. J. E. Geisler, *J. Atmos. Sci.* **33**, 4989 (1974).
6. K. Labitzke, *J. Atmos. Sci.* **29**, 1395 (1972).
7. G. Hernandez, *J. Geophys. Res.* **82**, 2127 (1977).
8. A. C. Faire and E. A. Murphy, in: *AFCRL-72-0474*, J.C. Ulwick (Ed.), August 1972, P. 445.

SECTION 2
Thermosphere—Exosphere

PROPERTIES OF THE MESOSPHERE AND LOWER THERMOSPHERE

K. S. W. Champion

Air Force Geophysics Laboratory, Hanscom AFB, MA, USA

ABSTRACT

The variability and systematic variations of the properties of the upper mesosphere and lower thermosphere are probably the least well known aspects of the terrestrial atmosphere. Satellite measurements of this region are very limited and rocket and remote sounding techniques do not provide comprehensive coverage. Progress is being made in theoretical studies of this region, primarily with regard to tidal effects, and some progress is being made in analyzing the relatively sparse experimental data that are available. Turbulence dynamics of the region has been studied by analyzing structure measurements at Kwajalein, wind data from Natal and systematic variations of the turbopause altitude determined from measurements of the diffusive separation of argon. One question that is being raised at this time, and it is appropriate at a time near solar maximum, is the extent of solar activity control of the properties of this region of the atmosphere. The occurrence rates and magnitudes of the turbulent diffusivity in the 70 to 90 km altitude region appear to correlate with solar activity with a time lag, as do also the incidence of aurora and the atomic oxygen green line intensity. Solar cycle dependence has been identified in mean zonal wind speeds in the 65 to 110 km altitude region above Saskatoon and in lower thermosphere temperatures measured at Heiss Island and at St. Santin. Millstone Hill data show that the mean meridional wind changes during a solar cycle. Solar cycle variations have also been detected in the stratosphere and troposphere.

TIDES IN THE MESOSPHERE AND THERMOSPHERE

Forbes and Marcos [1] have determined the diurnal and semidiurnal tidal variations in the lower thermosphere (150-250 km) from analysis of total mass density data from the miniature electrostatic accelerometer (MESA) on the Atmosphere Explorer-E (AE-E) satellite. Comparisons have been made with other experimental data and theoretical predictions. Because of the low orbital inclination of the satellite the data are limited to latitudes less than 20°. The amplitude of the diurnal tide in mass density for solar minimum is shown in Figure 1. Plotted are curves from the MSIS 1977 [2] and Jacchia 1971 [3] models, Forbes [4] theory, and MESA and NACE experimental data. It can be seen that the diurnal amplitude of the Jacchia 1971 is too large below 250 km altitude. Figure 2 is the corresponding plot of the phase of the diurnal tide. Big differences between the data and the MSIS model occur in the lower thermosphere. Theoretical amplitudes for the diurnal and semidiurnal tidal components of mass density at solar minimum are

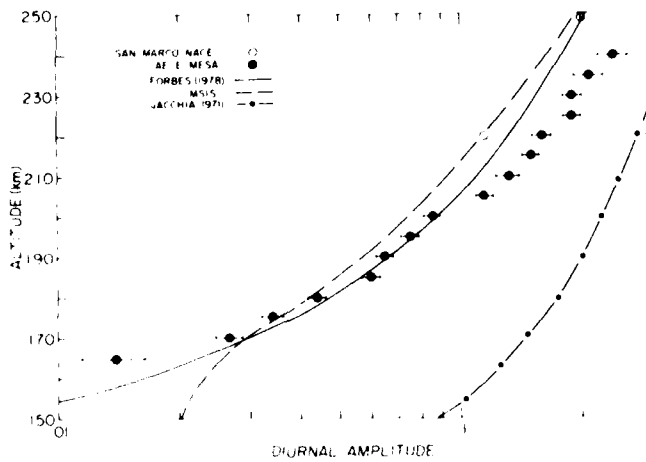


Fig.1 Diurnal amplitude of total mass density versus height for the AE-E MESA data (solid circles), San Marco 3 NACE (open circles), Forbes 1978 (solid curve), MSIS (dashed curve), and Jacchia 1971 (dash-dot curve) for equatorial latitudes at sunspot minimum.

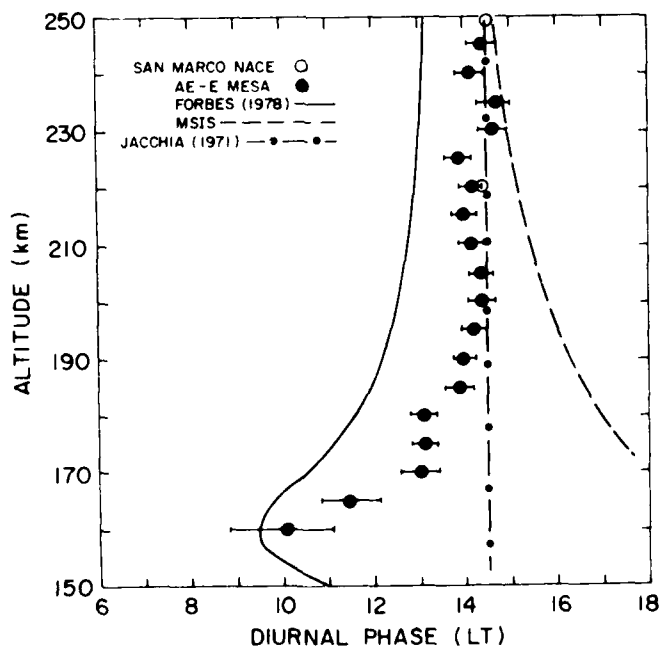


Fig. 2 Same as Figure 1 except for phase of diurnal component.

shown in Figure 3 for the equator and 40°N. The predominant tide changes from semidiurnal below approximately 180 km to diurnal above this transition altitude. The semidiurnal tide has an important latitude dependence.

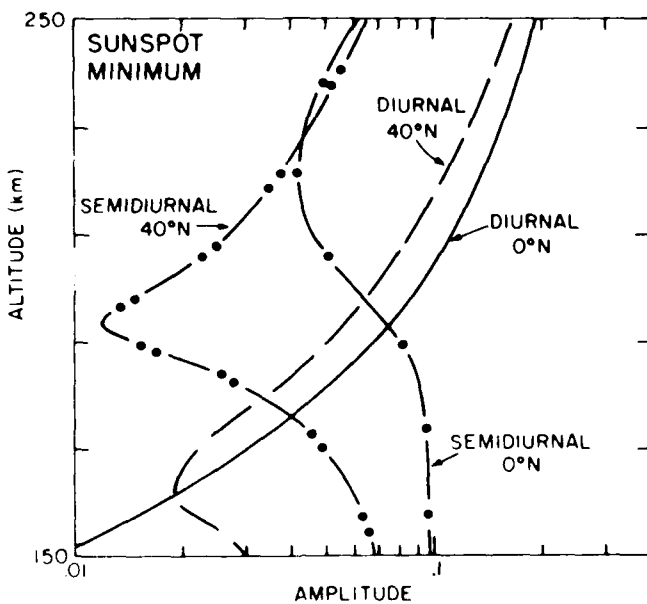


Fig. 3 Theoretical calculations for amplitude of diurnal and semidiurnal components of total mass density at 0°N and 40°N under equinox conditions at sunspot minimum, using the Forbes 1978 model with tidal winds and temperatures from Garrett and Forbes 1978 as input.

Forbes and Marcos [5] have extended the diurnal tide portion of the previous study from considering only total density to include also O and N₂, from considering only solar minimum to also solar maximum, and to a large range of latitudes. Theory indicates that oxygen variations are strongly influenced by seasonal differences in the winds, whereas N₂ responds primarily to temperature, which has a different seasonal dependence than the winds. The tidal variation of total density is primarily determined by the sum of that of O and N₂ and thus is rather complicated. Figure 4 shows the theoretical amplitudes and phases of the O, N₂, and total density diurnal tide during solar minimum compared with AE-E composition [6] and density [1] data. The O data and theory agree well, but the N₂ and total density values are essentially interchanged. Refinements in the theory may result in changes, but it is expected that the total density curves will be some weighted average of those for O and N₂ in this altitude region. Forbes [7] has obtained an updated least-squares fit to the 1970-1975 Millstone Hill exospheric temperatures in a 12 term expression similar to that in the MSIS model. A number of the coefficients have values significantly different from those in the MSIS model. The differences between Forbes' results and the MSIS values are largely due to the use by Forbes of the more accurate two-pulse data, whereas the MSIS model is based on the less accurate and uncorrected one-pulse data. In addition, the solar cycle coverages of the two studies are different.

Forbes plans to extend his study to 1979 using Millstone Hill data and back to 1966 using Arecibo data.

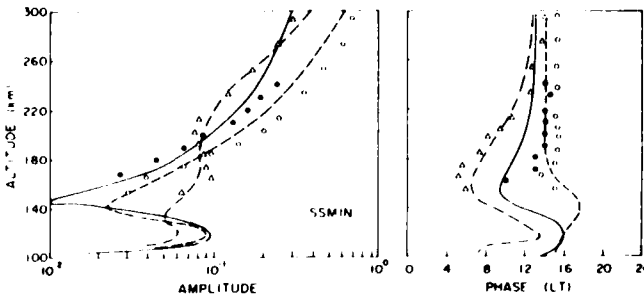


Fig. 4 Theoretical diurnal amplitudes and phases at SSMIN for O (---), N_2 (- - -) and total mass density (—) under equinox conditions at the equator. Data for oxygen (triangles), nitrogen (solid circles) and total mass density (open circles).

In further theoretical tidal calculations Forbes [7] has used improved representations of ion drag, molecular viscosity and conductivity, EUV heating, and background temperature. He now finds that the diurnal exospheric temperature maximum is at 15.1 hours at the equator, which is in much better agreement with satellite and incoherent scatter measurements. The amplitude of the semidiurnal exospheric temperature variation associated with the (2,2) mode propagating into the thermosphere is found to have a much smaller solar cycle dependence. The amplitude of the thermospheric semidiurnal temperature variation generated by in-situ UV and EUV absorption is determined to be twice as large as was found in previous calculations. Further improvements in the theory will include the addition of background winds, latitude variations of background temperature and composition, and mutual diffusion between O and N_2 .

Hedin et al [6] analyzed neutral composition and temperature data from the Neutral Atmosphere Composition Experiment (NACE) and Neutral Atmosphere Temperature Experiment (NATE) on the Atmosphere Explorer-E (AE-E) satellite for magnetically quiet periods between December 1975 and September 1976. The diurnal tidal amplitudes and phases for N_2 , O, He, Ar, and temperature were derived. They are applicable to low latitudes ($\pm 20^\circ$). Figure 5 shows the diurnal amplitudes and phases for N_2 and O, plus the MSIS model and Mayr and Harris [8] model profiles. The amplitudes of O, He and Ar near 150 km are significantly larger than the amplitude of N_2 . The circulation model predicts these effects, being the result of wind-induced molecular diffusion that is mainly effective between 120 and 200 km, as can be seen by the sharp amplitude drop below 150 km. N_2 is least affected because it is most nearly in diffusive equilibrium. The temperature tidal amplitudes deduced from the N_2 , O and He density profiles are in good agreement with those measured by NATE, except for the He amplitude below 200 km where transport causes important departures from diffusive equilibrium.

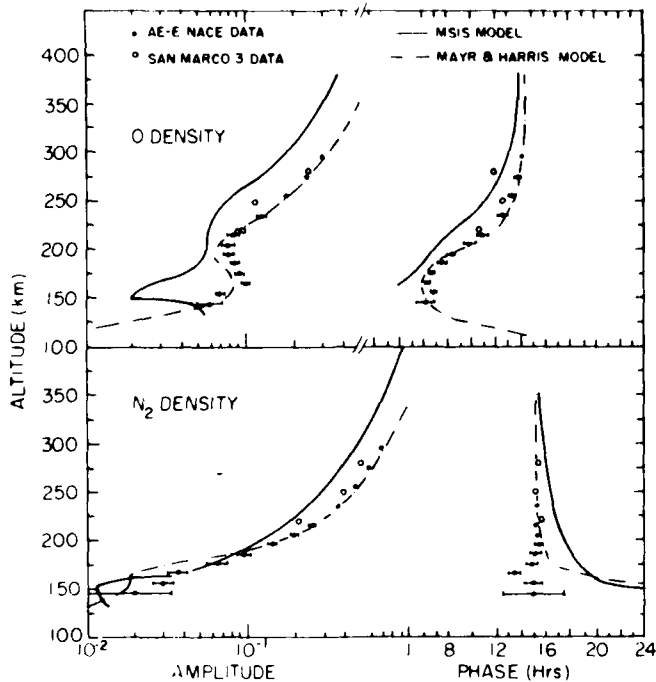


Fig. 5 Diurnal amplitude (logarithmic) and phase versus altitude for N_2 and O. Shown are data from AE-E and San Marco 3 as well as the MSIS empirical model and the Mayr and Harris theoretical model.

In a further study Hedin et al [9] derived the amplitudes and phases of the semidiurnal and terdiurnal tides in the equatorial thermosphere from NACE and NATE measurements on the AE-E satellites for the same time period for which they derived the properties of the diurnal tide. Figure 6 shows the semidiurnal amplitude and phase for O from the NACE data, plus some San Marco 3 data and curves for diffusive equilibrium, MSIS, Forbes and Mayr models. The agreement between experiment and theory is reasonably good. For N_2 , diffusive equilibrium and the MSIS model agree better with the experimental data than do the Forbes and Mayr models. This again supports the conclusion that N_2 is very nearly in diffusive equilibrium. The amplitude of the semidiurnal tide near 150 km is roughly the same for all atmospheric species and increases with decreasing altitude. This suggests an origin in the lower thermosphere or below for the observed semidiurnal tide. Figure 7 shows the terdiurnal amplitude and phase for O from NACE, plus curves for the MSIS and Mayr models. The Mayr model agrees well with the data but the MSIS model considerably underestimates the amplitude. Mayr et al [10] have suggested that the terdiurnal tide arises from a nonlinear interaction between the semidiurnal and diurnal tides.

Tidal data have been obtained in the altitude range 90 to 100 km by determining winds using LF drift measurements [11]. The exact height of the measurement is determined by the reflection height and this varies with time. Measurements are

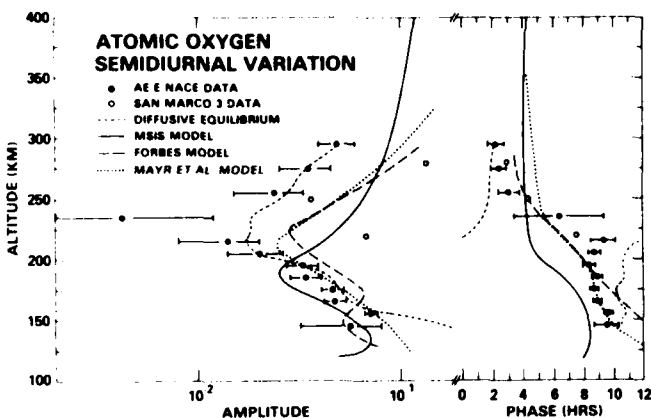


Fig. 6 The semidiurnal variation of atomic oxygen density from AE-E NACE and San Marco 3 plus four theoretical curves.

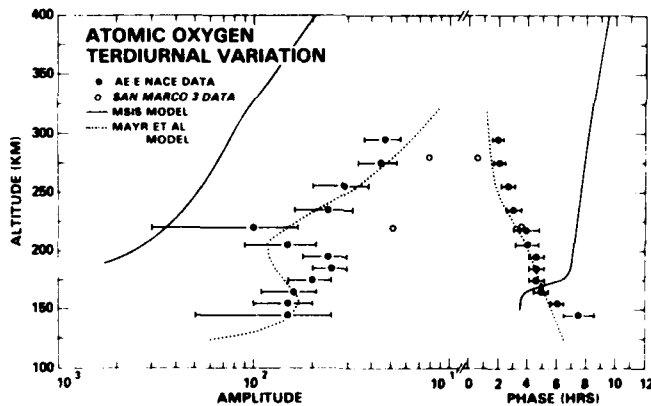


Fig. 7 The terdiurnal variation of atomic oxygen density from AE-E NACE and San Marco 3 data plus two curves from models.

normally restricted to the period between sunset and sunrise due to the high daytime ionospheric absorption of LF waves. Both zonal and meridional wind components have been measured at the Collm Geophysical Observatory, GDR since 1959. The semidiurnal tide dominates both wind components, but the prevailing wind can also be determined. Particular attention has been given to seasonal variations of the wind and changes during stratospheric warmings and geomagnetic storms. For example, every autumn rapid phase movements occur between 10 and 30 October and they can be very different from one year to another. In addition, a reversal has been observed in the zonal prevailing wind direction between 20 September and 20 October. In general, wind field disturbances accompanying

stratospheric warmings extend to the 90 to 100 km altitude region, but there are a few cases, mostly early winter events, where stratospheric warming has no effect at all in this altitude region. The measured winds show short-period velocity fluctuations, presumably caused by internal gravity waves.

TURBULENCE DYNAMICS

Zimmerman, Philbrick and colleagues have studied turbulence dynamics in the mesosphere and lower thermosphere. In one study [12] they analyzed data from several sets of measurements of atmospheric density, temperature and winds in the mesosphere obtained at Kwajalein Atoll during 1976-1978. The measurements were made with passive inflatable spheres and accelerometer instrumented rigid spheres. Richardson numbers were calculated from the wind and temperature data and were used to indicate the regions where turbulence would be expected. Figure 8 shows the density profiles plotted relative to the Cole and Kantor [13] tropical atmosphere. In addition, the Richardson numbers calculated from the temperature

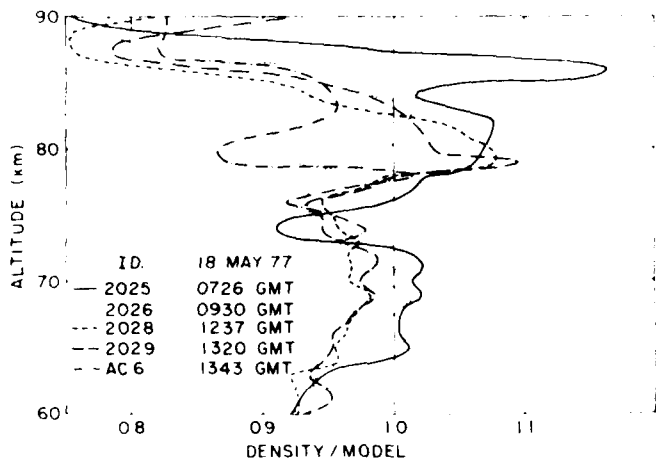


Fig. 8 Density measurements and Richardson numbers for falling sphere flights at Kwajalein Atoll on 18 May 1977. (a) the density measurements are shown as a ratio to the Cole and Kantor tropical atmosphere for four Robin Sphere flights and one accelerometer instrumented sphere.

and wind data are plotted for the range of values ($0 \leq R_i \leq 1$). Negative values are plotted at $R_i=0$, and the values less than 0.25 are indicated by solid shading. Values less than 0.25 are accepted as an indication of the presence of turbulence. The regions that exhibit a large variability between successive density profiles taken several hours apart correspond to the regions predicted by the stability calculations to be turbulent. These data also indicate that the vertical thickness and persistence of the turbulent layers in the mesosphere tend to increase with increasing altitude.

The deviations from the mean of observed meridional wind amplitudes at Natal for the altitude region 35 to 85 km [14] are shown in Figure 9. Here can be seen an exponential increase of the amplitude with altitude, somewhat indicative of the conservation of energy density $1/2 \rho v^2$ where ρ is the mass density. The large shears generated at the upper altitudes by the increasing wind amplitude and a relatively constant wavelength, cause the upper altitude regions to tend towards instability, as indicated by decreasing values of the Richardson number. This was seen in the Kwajalein data in Figure 8. Comparison of turbulence occurrence rate data for Wallops Island (in Figure 10) with the equatorial data shows a more marked instability occurrence in the midlatitude lower mesosphere than at the equator.

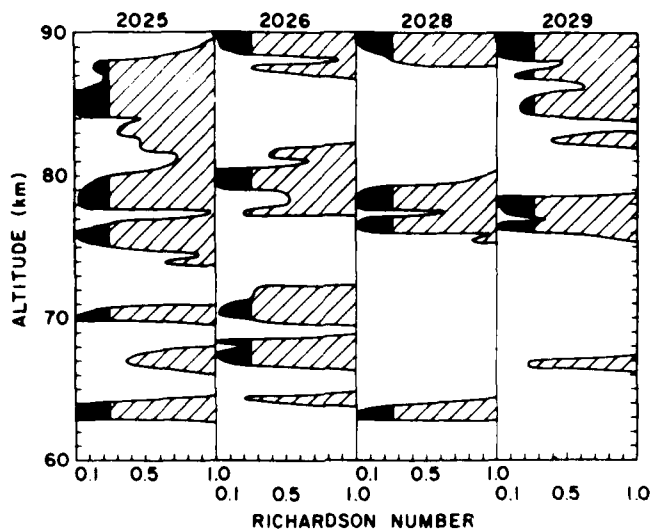


Fig. 8(b) The Richardson numbers calculated from the temperature and wind measurements are shown for the range of values $0 < R_i < 1$ with the negative values ($R_i < 0$) indicated at $R_i + 0$.

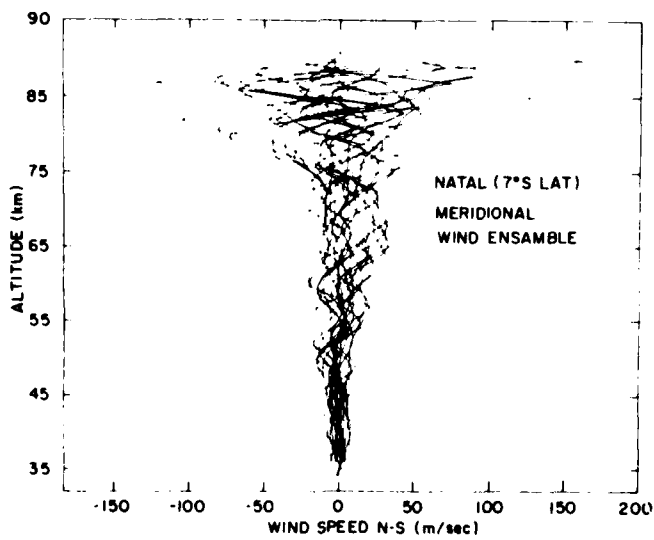


Fig. 9 Deviations from the mean of meridional wind speeds at Natal in the 35 to 85 km altitude region.

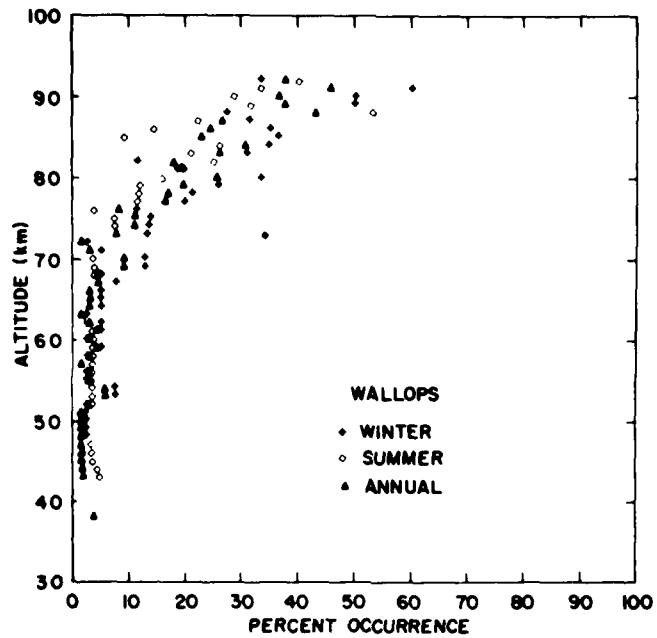


Fig. 10 Turbulence occurrence rate as a function of altitude at Wallops Island, VA (38°N) for the years 1961-1967.

The dynamics of the upper mesosphere and lower thermosphere have been studied using rocketborne chemical releases, radio meteor analysis and diffusive separation of Ar and N₂ from mass spectrometer measurements. In particular, the turbopause altitude was derived from the Ar/N₂ ratio by Danilov et al [15,16]. The diurnal variation of the turbopause altitude was determined for both winter and summer. Figure 11 shows the mid (30°N) and high (80°N) latitude winter average diurnal variation of the turbopause altitude [14]. Figures 12 and 13 show the relationships between the equatorial turbopause variability and a_p and T_{120} , respectively. The turbopause-temperature 120 km relation implies that turbulent heat transfer is the dominant mechanism controlling the local energy flux. Thus, as the turbopause altitude increases enhanced heat transfer occurs just below the turbopause, with a reduction of the temperature which, because of continuity of transfer across the turbopause, is felt at 120 km.

SOLAR CYCLE DEPENDENCE

There is probably some solar cycle dependence of the properties of all regions of the atmosphere. To date the only region for which this dependence is accurately quantified and well understood is the upper thermosphere. There are two reasons for this. The first is that in some ways the physics and dynamics of this region is simpler than that of the lower regions of the atmosphere and the second (and the prime reason for the first) is that the ratio of the input solar radiation energy to the thermal and dynamic energy stored in the atmosphere is larger and thus the solar cycle dependence is larger. Nevertheless, solar cycle dependence in other regions of the atmosphere must be looked for and identified. Some

research in this area is reviewed in this section. It must be realized that some of the results are preliminary and not necessarily conclusive and that, at this time, we do not have a conclusive picture of the solar cycle dependence of these portions of the atmosphere.

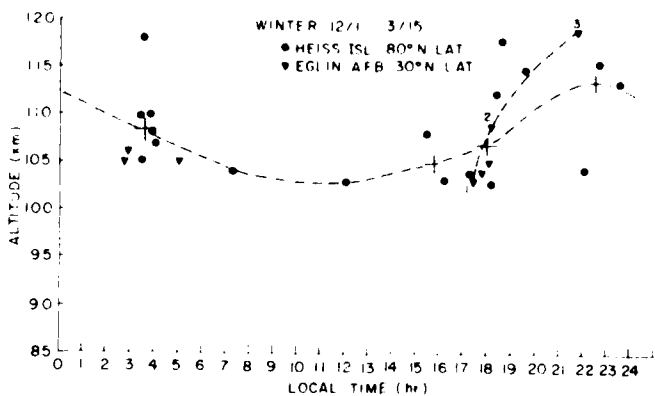


Fig. 11 The turbopause altitude as a function of local time at midlatitude (30°N) and at high-latitude (80°N).

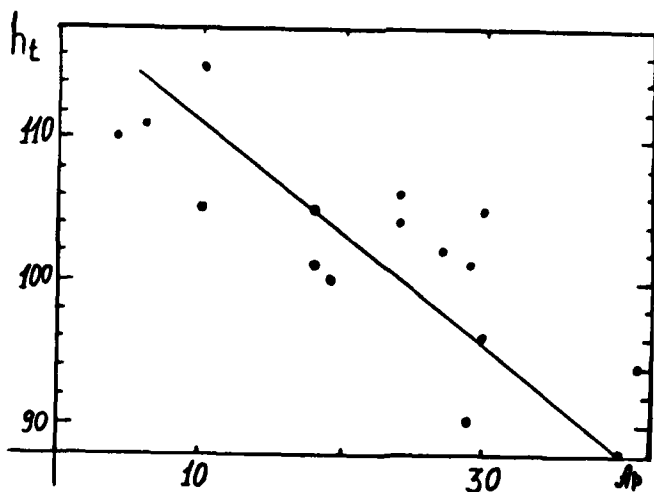


Fig. 12 Equatorial turbopause height (h_t) as a function of a_p .

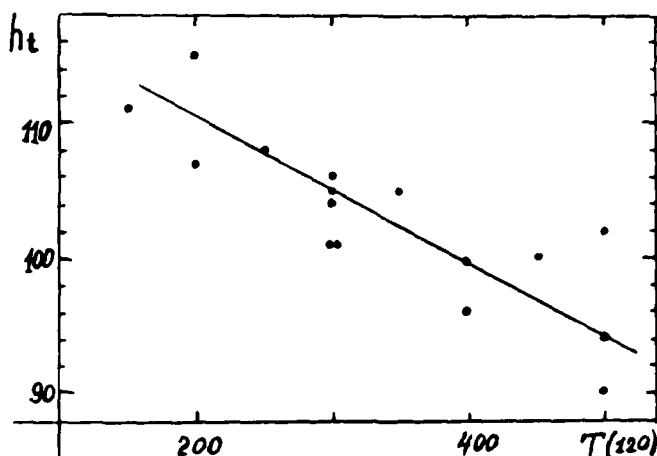


Fig. 13 Equatorial turbopause height (h_t) as a function of the temperature at 120 km.

Zimmerman and Murphy [17] plotted yearly averaged occurrence rates of turbulence and turbulent diffusivity summed over the altitude region 75 to 90 km for Wallops Island (Figure 14) and compared them with sunspot numbers and the 10.7 cm solar flux for the period 1961-67. These data suggest a correlation with a two year time lag. Zimmerman [14] comments that it is fairly apparent that the turbulence occurrence is wave induced and that one should look into the lower atmosphere for the source mechanism of these waves to understand more properly the solar relationship. Silverman [18] found that the incidence of aurora and the atomic oxygen green line intensity correlate with the sunspot number with a time lag of about one year (Figure 15). These phenomena occur at higher altitudes than those of the Zimmerman study and probably also involve different processes.

Gregory and his colleagues [19] have measured winds at Saskatoon in the altitude region 65 to 110 km since 1969 using the partial reflection radio wave technique. The data for the period 1969-1975 have been analyzed for long period waves. Waves with periods of 3-months, semi-annual and annual were found, in addition to a quasi-biennial oscillation [20]. Recently, Gregory [21] has found in the monthly mean zonal wind speeds a marked solar cycle dependence, with a 6 to 1 ratio of wind speed values, for the half solar cycle (1969-1975). We will eagerly await analysis of more recent data (to complete one solar cycle) and a determination of the physical cause of the phenomenon. Gregory states that similar effects have been observed at Christchurch, N.Z. and in Germany.

Results of neutral temperature measurements of the polar lower thermosphere using artificial sodium clouds at Heiss Island (80°N) during the period 1968 to 1976 show a large variation as a function of the solar cycle [22]. The measurements were made at twilight during spring or autumn. Primarily data obtained under relatively quiet conditions were analyzed for this study. Figure 16 shows the observed lower thermosphere temperatures. The values at 90 km were obtained with a ground-based LIDAR interacting with the natural atmospheric sodium layer. Figure 17 shows a plot of the temperature at 165 km compared with the sunspot numbers for the same time period. The data suggest an inversion between 120 and 170 km with the temperature becoming less when solar activity increases. This may be a genuine effect at high latitudes. The data are not consistent with many

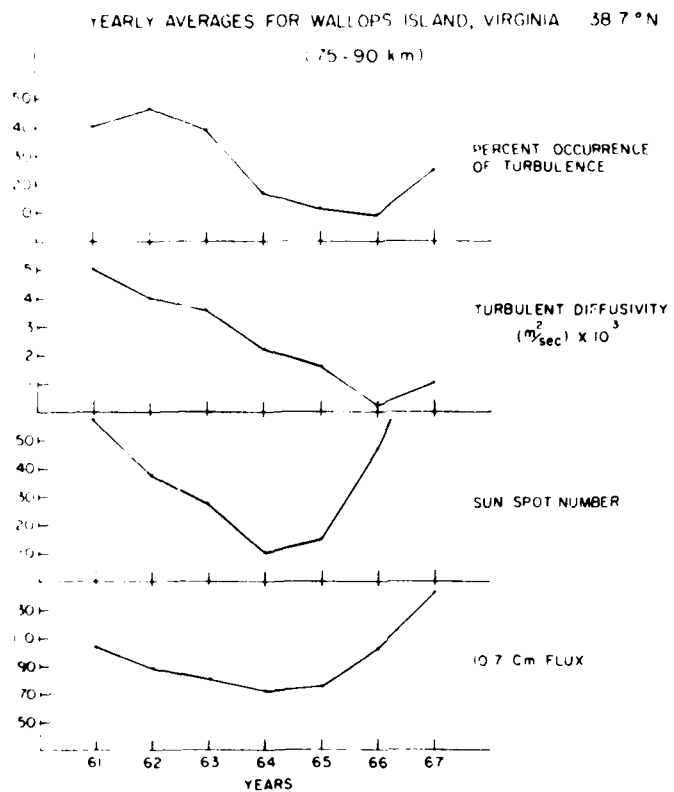


Fig. 14 The Wallops Island yearly averaged occurrence rate and turbulent diffusivity summed over the altitude region 75 to 90 km compared to the 10.7 cm flux and sunspot number.

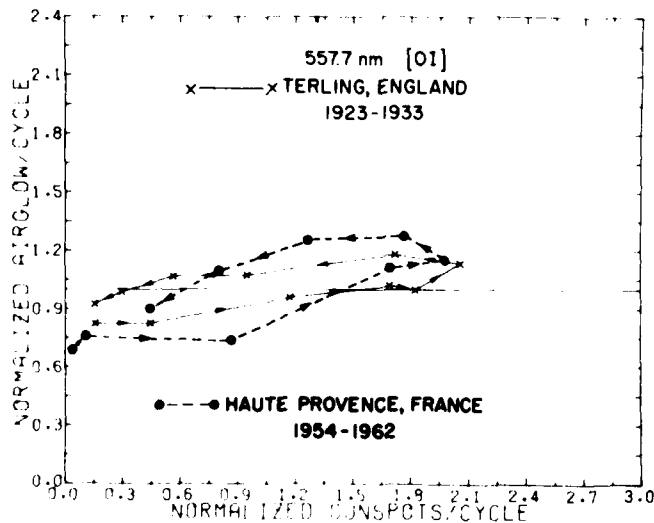


Fig. 15 Atomic oxygen (557.7 nm) airglow intensity normalized per solar cycle as a function of the sunspot number also normalized per cycle.

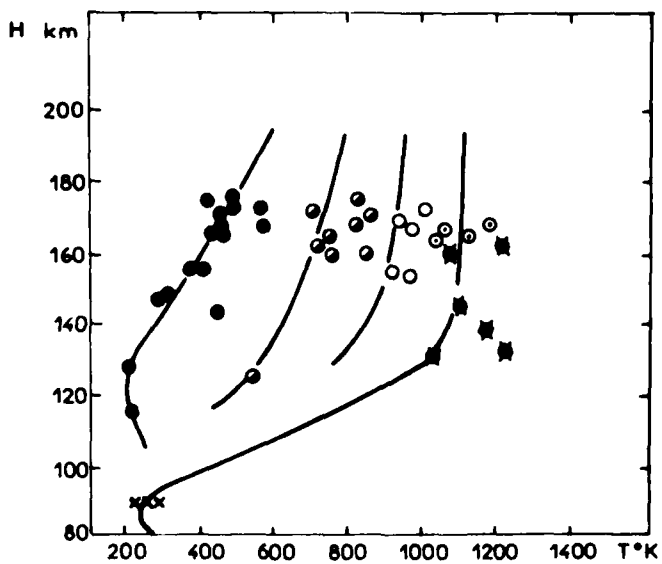


Fig. 16 Neutral temperatures measured with artificial sodium clouds, 1968-1970 (solid circles), 1970-1972 (half-solid circles), spring 1974 (open circles), autumn 1974 (encircled dots) and 1976 (crossed solid circles). The temperatures at 90 km were obtained by Lidar sounding.

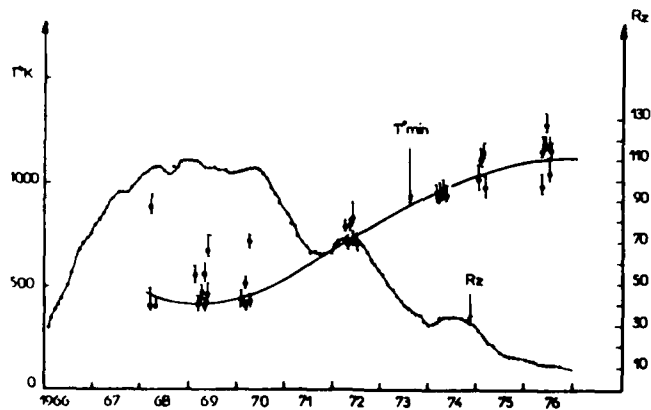


Fig. 17 Temperatures measured at 165 km (circles with error bars) plotted as a function of time between 1968 and 1976. The sunspot numbers for this period are also plotted.

atmospheric models. For example, the Jacchia 1971 model gives an exospheric temperature of 840K for the conditions pertaining when the 1976 data were obtained. This is considerably less than the observed temperature of approximately 1100K near 150 km. On the other hand, temperatures measured by chemical releases (tri-methyl aluminum--TMA) at Churchill (59°N) in 1968 [23] were much higher than those from Heiss Island at about the same time as can be seen in the Table .

<u>Location</u>	<u>Date</u>	<u>Temperature</u>
Heiss Island	Spring 1968	420K
Churchill	Jan 1968	650K
Churchill	Aug 1968	700-800K

Table. Measured temperatures at 165 km

Golomb et al comment with regard to the August data. The highest temperatures at Churchill (800K) were observed 24 hours after a relatively "cold" dawn. There was no evidence of strong auroral activity when the temperatures were high. However strong activity was observed during a subsequent measurement when the temperatures were the lowest of the August series. The results can be seen in Figure 18. These results suggest that particle heating (presumably enhanced during

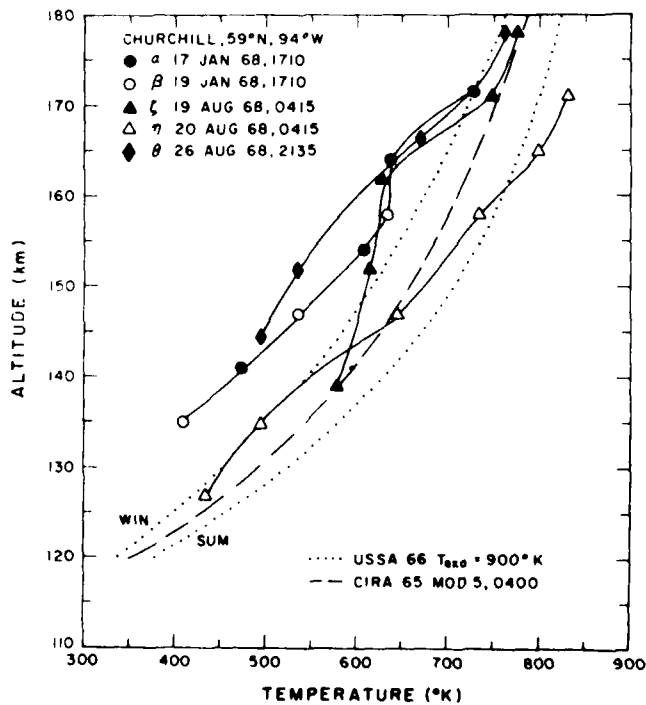


Fig. 18 Neutral atmospheric temperatures at Churchill determined by measuring the rotational temperatures of AlO produced by the release of TMA in the upper atmosphere.

solar maximum) can result in reduced temperatures in the lower thermosphere but also that the temperatures tend to return towards higher values at altitudes of 170 km and above. The reduced temperatures in the lower thermosphere during enhanced activity could be caused by an increased production of nitric oxide with a resulting increased rate of radiation cooling by emission of the 5.3 μm funda-

mental band [24]. Kockarts finds that at 120 km altitude the temperature gradient decreases from about 20K/km with no nitric oxide to 6K/km with the NO concentration of Trinks et al [25]. These are consistent with the Chanin and Tulinov values of 7K/km for this gradient under high solar activity to 21K/km under minimum activity, implying that the major cause of the change is due to a major change in the NO concentration, the NO concentration being considerably enhanced during periods of high solar activity. Measurements should be made to attempt to verify this hypothesis.

Oliver [26] has made an extensive analysis of data collected by the bistatic incoherent scatter radar at St. Santin (45° N). We will consider in this review only the solar cycle dependence of lower thermosphere properties. The data are only for daylight hours and primarily near noon. Bates formula for the neutral temperature profile above 120 km is

$$T(z) = T_{\infty} - (T_{\infty} - T_0) \exp[-s(z - z_0)]$$

where $T(z)$ is the temperature at altitude z , T_{∞} is the exospheric temperature, T_0 is the temperature at the reference altitude z_0 (often taken to be 120 km) and s is the temperature profile shape factor indicating how rapidly the temperature rises from the reference altitude. Figure 19 shows the solar-cycle and solar-rotation variation of s . The solar-cycle variation clearly demonstrates the

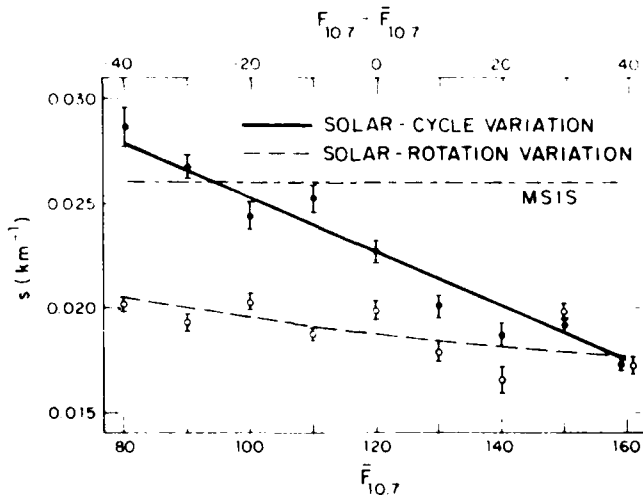


Fig. 19 Variation of s with solar-cycle and solar-radiation.

inverse variation of s with scale height (or temperature) gradient since, at low- and mid-latitudes, the upper thermosphere temperatures increase with solar activity. The solar-rotation variation of s is also shown in Figure 19. This variation is less by a factor of 3 or 4 than the solar-cycle variation, indicating a more marked atmospheric response to variations in the total solar UV disk component than in its active area component. The seasonal variation of s for high and low solar activity is shown in Figure 20. The variation is very solar cycle

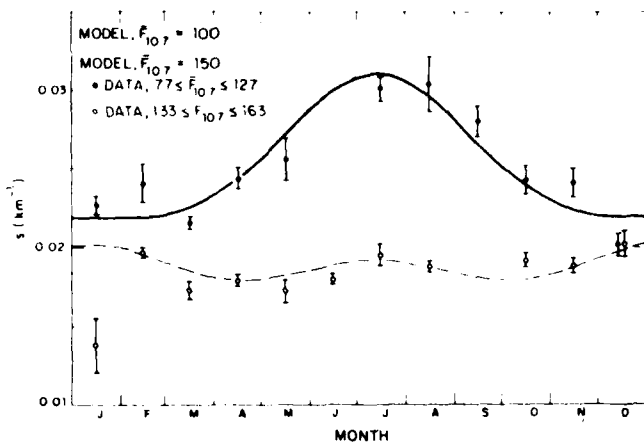


Fig. 20 Variation of s with season for high and low solar activity.

dependent and becomes quite small at high activity. The value of s might be expected to decrease in the summer due to higher temperatures, but preferential transport of lighter constituents away from the summer hemisphere tends to increase the mean mass and hence the value of s , and this increase dominates at low activity but the effects approximately cancel at high activity.

Babcock and Evans [27] analyzed thermospheric winds derived from incoherent scatter measurements at Millstone Hill (42°N). Data for geomagnetically quiet days from 1970 (near solar maximum) to 1975 (near minimum) were analyzed in this study. The meridional and zonal winds showed a marked seasonal variation. The amplitude of this oscillation did not appear to change with solar activity. However, the annual mean meridional wind was found to decrease from 25 m/s equatorward to about 0 m/s over the 6-year period. It is believed that this is due to a much larger reduction in the high-latitude (particle) heating between maximum and minimum than in the magnitude of the solar UV heating over the same period. For the same reason, the meridional winds near equinox shifted from being generally equatorward at maximum to being poleward at minimum and the winds in winter became more strongly poleward at minimum. No solar cycle dependence was found for the diurnally averaged zonal winds, which are generally eastward in winter and westward in summer.

Although this review is not concerned with the stratosphere and troposphere some work on identifying possible solar cycle variations in these regions will be briefly discussed because they could determine the variations in the mesosphere and above.

Quiroz [28] has analyzed temperature data from arcasondes and datasondes for 35 and 50 km (near the stratopause) altitudes taken during solar cycle 20. The yearly departures as well as 3-year moving averages (with 1-2-1 weighting) were compared to the mean annual sunspot number, both for the individual stations and for all seven stations. The smoothed temperature departures for the combined data show a correlation of +0.89 with sunspot numbers at both altitudes, but with a greater temperature range (4.5K) at 35 km. The data from the individual stations also show high correlation except at Poker Flat and Ascension Island at 50 km. With the exception of these two stations, the temperatures at 35 and 50 km show a reduction of 3 to 6K between solar maximum (1968-69) and solar minimum (1976). The

data at 35 km tend to follow the mean annual sunspot numbers closely, but the data at 50 km do not follow as closely. The smoothed combined data give more than a 4K temperature reduction at 35 km, but only a 3K reduction at 50 km.

Quiroz [29] has also found that the period and amplitude of the stratospheric tropical quasi-biennial oscillation (QBO) in zonal wind are inversely related to solar activity. The correlation for the period relationship is stronger than for the amplitude. Data in the altitude region 25 to 35 km were analyzed for the time period 1951-1978. The highest negative correlation coefficient in this altitude region was obtained with a time lag of about 21 months, with an inferred in-phase relation near 50 km altitude. Periods in the range 27-34 months were associated with low solar activity and periods of 22-26 months with high solar activity. The QBO may be caused by absorption of solar UV by ozone and the period due to the interaction of the 11-year cycle and seasonal variations. The 11-year cycle of solar flux is not a simple sine wave and contains components of higher harmonics. A frequency five times that of the fundamental corresponds to a period between 26 and 27 months. Sakurai [30] has reported a quasibiennial variation of the solar neutrino flux and solar activity.

Nastrom and Belmont [31] report that the amplitudes of the harmonics of the annual cycle in stratospheric zonal wind speed vary with the solar activity. The annual wave's amplitude increases from solar maximum to minimum by as much as 20%, while the amplitude of the semiannual wave varies in the opposite direction, decreasing up to 50% from solar maximum to minimum. The apparent solar cycle modulation is present, with varying magnitude, at all latitudes and is generally largest near the stratopause. Minjushink [32] has extended the work of Quiroz and has investigated the possible influence of the 11-year solar cycle on stratospheric circulation. He predicts that near and following a solar minimum subtropical high pressure systems strengthen, high latitude low pressure cyclones deepen and summer anticyclones weaken. Conversely, near and after a solar maximum the tropical high pressure system weakens, high latitude cyclones become less intense and summer anticyclones are more developed. Nastrom and Belmont [33] have extended their stratospheric studies down to the troposphere and have determined the amplitudes and phases of the 11-year solar cycle component in wind speed and temperature at radiosonde levels. The largest amplitudes are near the tropopause in winter where, in several regions, over 40% of the interannual variance of the wind speeds is explained by the solar cycle dependence.

REFERENCES

1. J. M. Forbes and F. A. Marcos, J. Geophys. Res. 84, 31 (1979).
2. A. E. Hedin, J. E. Salah, J. V. Evans, C. A. Reber, G. P. Newton, N. W. Spencer, D. C. Kayser, D. Alcayde, P. Bauer, L. Cogger and J. P. McClure, J. Geophys. Res. 82, 2139 (1977).
3. L. G. Jacchia, SAO Spec. Report 332 (1971).
4. J. M. Forbes, J. Geophys. Res. 83, 3691 (1978).
5. J. M. Forbes and F. A. Marcos, J. Geophys. Res. 85, 3489 (1980).
6. A. E. Hedin, N. W. Spencer, H. G. Mayr, I. Harris and H. S. Porter, J. Geophys. Res. 83, 3355 (1978).
7. J. M. Forbes, private communication (1980).
8. H. G. Mayr and I. Harris, J. Geophys. Res. 82, 2628 (1977).

9. A. E. Hedin, N. W. Spencer and H. G. Mayr, J. Geophys. Res. 85, 1787 (1980).
10. H. G. Mayr, I. Harris, N. W. Spencer, A. E. Hedin, L. E. Wharton, H. S. Porter, J.C.G. Walker and H. C. Carlson, Geophys. Res. Lett. 6, 447 (1979).
11. R. Schminder and D. Kürschner, J. Geophys. Res. 84, 7353 (1979).
12. C. R. Philbrick, E. A. Murphy, S. P. Zimmerman, E. T. Fletcher and R.O. Olsen, Space Research XX, in press, (1980).
13. A. E. Cole and A. J. Kantor, Tropical Atmospheres, 0 to 90 km, AFGL-TR-75-0527, Air Force Geophysics Laboratory, (1975).
14. S. P. Zimmerman, presented at Workshop on the Equatorial Ionosphere at Cornell University, 22 Oct 1979.
15. A. D. Danilov, U. A. Kalgin and A. A. Pokhuskov, Space Research XIX, 173(1979).
16. A. D. Danilov, U. A. Kalgin and A. A. Pokhuskov, presented at XXII COSPAR Meeting, Bangalore, India, June, 1979.
17. S. P. Zimmerman and E. A. Murphy, in: NATO Advanced Study Institute Series "C", D. Reidel, Dordrecht, 1977, p.35.
18. S. M. Silverman, presented at Yosemite Solar Terrestrial Coupling Conference, Feb., 1978.
19. A. H. Manson, J. B. Gregory, C. E. Meek and D. G. Stephenson, J. Atmos. Sci. 35, 592 (1978).
20. A. D. Belmont and G. D. Nastrom, J. Geomag. Geoelectr. 31, 165 (1979).
21. J. B. Gregory, private communication (1980).
22. M. L. Chanin and G. F. Tulinov, J. Geophys. Res. 84, 406 (1979).
23. D. Golomb, D. F. Kitrosser and R. H. Johnson, Space Research XII, 733 (1972).
24. G. Kockarts, Geophys. Res. Lett. 7, 137 (1980).
25. H. Trinks, U. von Zahn, C. A. Barth and K. K. Kelly, J. Geophys. Res. 83, 203 (1978).
26. W. L. Oliver, Ann. Geophys. 35, 121 (1979).
27. R. R. Babcock and J. V. Evans, J. Geophys. Res. 84, 7348 (1979).
28. R. S. Quiroz, J. Geophys. Res. 84, 2415 (1979).
29. R. S. Quiroz, private communication (1979).
30. K. Sakurai, Nature, 278, 146 (1979).
31. G. Nastrom and A. Belmont, Geophys. Res. Lett. 7, 457 (1980).
32. L. S. Minjushink, presented at XXII COSPAR meeting, Bangalore, India (1979).
33. G. Nastrom and A. Belmont, J. Geophys. Res. 85, 443 (1980).

DEVELOPMENT OF WIND OBSERVATIONAL MODELS FOR THE UPPER ATMOSPHERE OF THE EARTH BASED ON THE JOINT ANALYSIS OF DIRECT AND INDIRECT SOUNDING DATA

S.S. Gaigerov, D.A. Tarasenko, V.V. Fedorov,
V.G. Kidiyarova, Yu.P. Koshelkov, M.Ya. Kalikhman,
R.A. Britvina and L.V. Scherbakova

*State Committee of the USSR for Hydrometeorology and
Control of Natural Environment, Moscow, USSR*

ABSTRACT

Earlier latitudinal distribution models of zonal winds were developed mainly along the 80°W meridian [1, 2]. In this paper an attempt is made to take into account longitudinal differences in zonal and meridional wind distributions. These are considerable in winter periods.

INTRODUCTION

Wind models for the northern hemisphere stratosphere and mesosphere are based on charts of mean values of zonal and meridional wind components and their standard deviations for the 20–80 km altitudes with height intervals of 5 km. Rocket sounding station network data (1969–1977) and USSR scientific research ship rocket data (1962–1977) were used for compilation of the charts.

As rocket sounding data do not provide necessary spatial resolution, satellite radiometer sounding data transmitted from the USA as scientific exchange information were used for compilation of the charts. Earlier 5, 2 and 0.4 mbar contour charts were compiled for geostrophic wind calculations. For the 1972–1973 period the charts were taken from [3]. Beginning from 1975 similar charts have been compiled in the Central Aerological Observatory. Geostrophic wind values were calculated in 48 points of the hemisphere (with 20° latitudinal and 50° longitudinal intervals).

WIND MODELS

Monthly mean values of geostrophic wind components and rocket sounding data were plotted on charts and analysed. An example of these charts for the 40 km level in January is given in Fig.1.

On the basis of the charts analysed vertical cross sections of monthly mean values of zonal and meridional wind components and their standard deviations along four meridians (0°, 90°E, 180°,

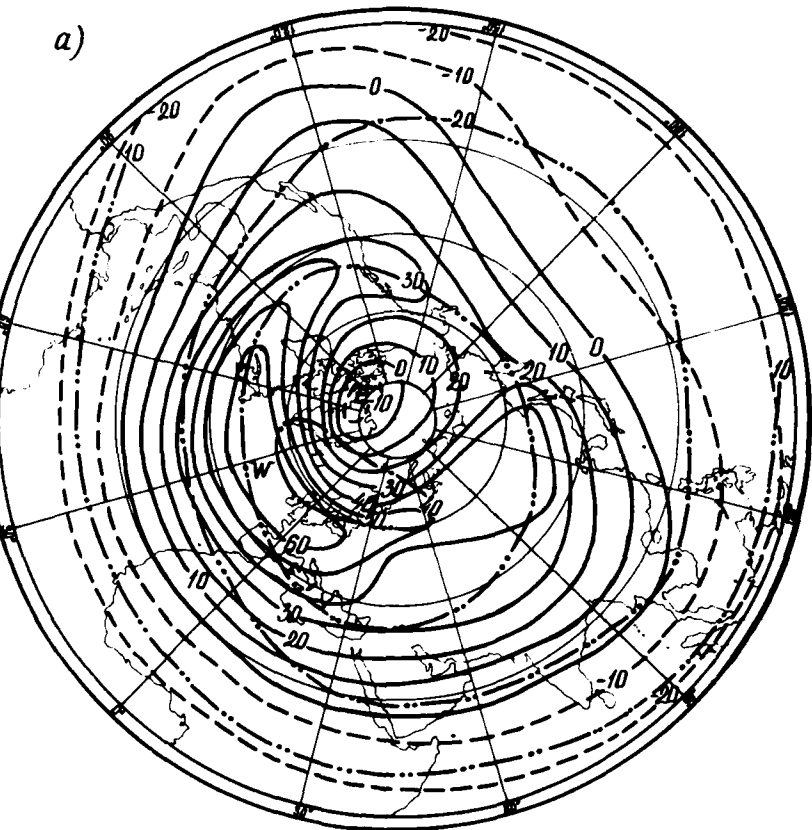


Fig.1. a) Chart of zonal wind mean monthly values and their standard deviations. January, 40 km level. Solid lines represent western wind component, dashed lines - eastern wind component, dash-dotted lines - standard deviations

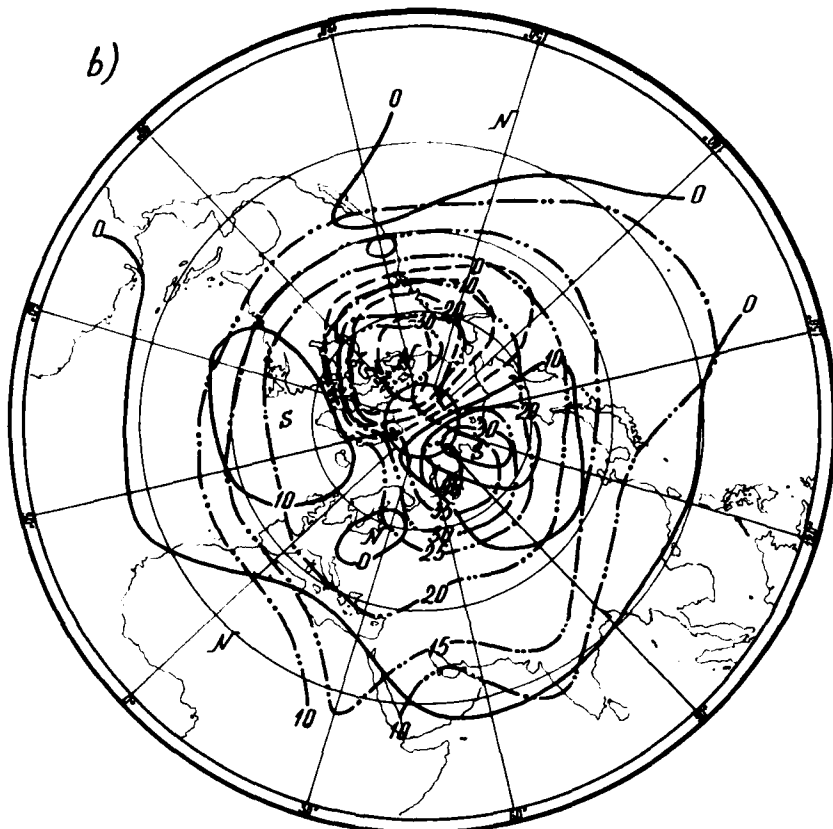


Fig.1. b) Chart of meridional wind mean monthly values and their standard deviations. January, 40 km level. Solid lines represent southern wind component, dashed lines - northern wind component, dash-dotted lines - standard deviations

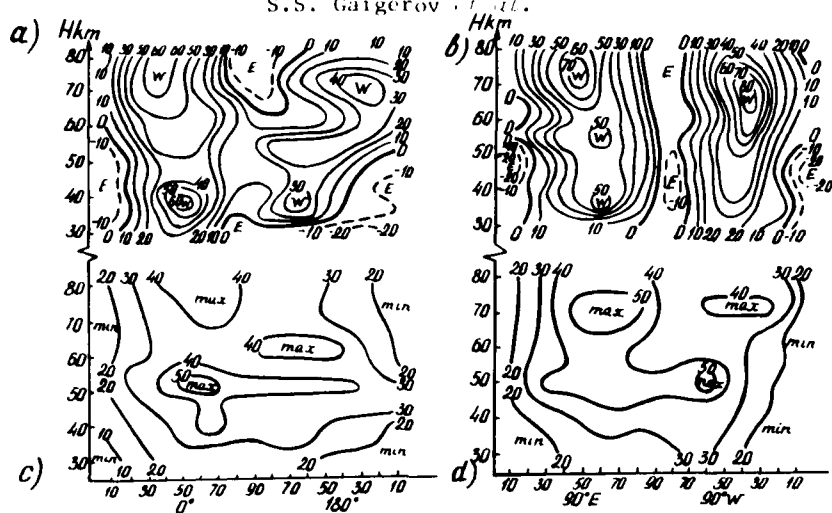


Fig.2. Vertical cross sections of zonal wind mean values along meridians 0° - 180° (a) and 90°E - 90°W (b) and their standard deviations along meridians 0° - 180° (c) and 90°E - 90°W (d). January

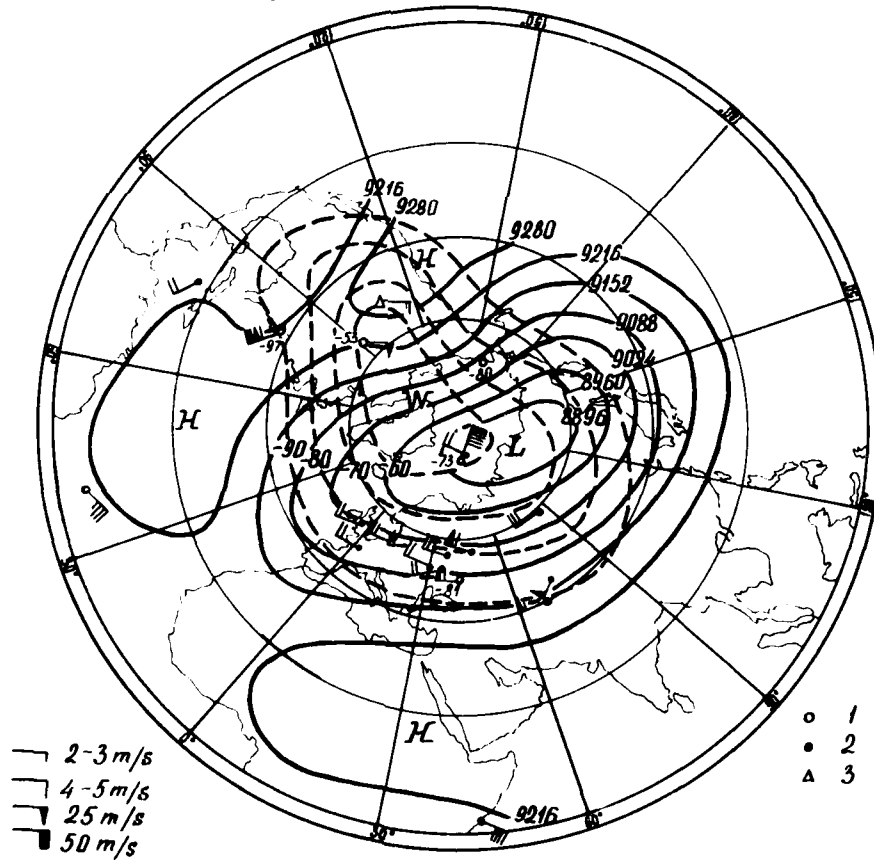


Fig.3. Mean 0.001 mbar constant pressure chart for January: 1 - rocket data; 2 - radiometer data; 3 - ionospheric data; solid lines - contours (dm); dashed lines - isotherms ($^{\circ}\text{C}$)

90° E..) from 10° W to 80° N were obtained. The choice of meridians was determined by the following reasons. The 0° - 180° cross section gives latitudinal wind distribution over the northern hemisphere oceans and the 90° E - 90° W cross section gives wind distribution over the continents. An example of similar cross sections is given in Fig.2.

These latitudinal and longitudinal wind distribution models characterize mean circulation conditions of many years in the stratosphere and mesosphere of the northern hemisphere.

The charts for rather high levels (Fig.3) will provide the material for further development of more valid, detailed models of the upper mesosphere and thermosphere.

References

1. COSPAR International Reference Atmosphere 1972, CIRA 1972, Akademie-Verlag, Berlin, 1972.
2. A.D.Belmont, D.G.Patt, G.D.Nastrom, Journ. Appl. Meteorology 14, 585 (1975).
3. Staff, Upper Air Branch NOAA, National Meteorological Center, Synoptic Analyses, 5-, 2- and 0.4-millibar surfaces for January 1972 through June 1973, NOAA SP-3091, Washington, D.C., 1975.

EDDY DIFFUSION COEFFICIENT AND ATMOSPHERIC MODELS

K.G.H. Schuchardt and P.W. Blum

*Institut für Astrophysik und Extraterrestrische Forschung,
Universität Bonn, 5300 Bonn, FRG*

ABSTRACT

Since the importance of the coupling mechanisms between the mesosphere and the thermosphere has increasingly been recognized, the structure and variation of turbulence has become one of the subjects of extended investigations and discussions. In spite of the fundamental role of turbulence, theoretical difficulties and lack of observational information restrict its applicability to atmospheric modeling. In the following paper the basic ideas of the parameterization of turbulence and the most important observational techniques and results are reviewed. The comparison of observations with theoretical model calculations shows the difficulties which underly current investigations and indicates the trends of future research.

INTRODUCTION

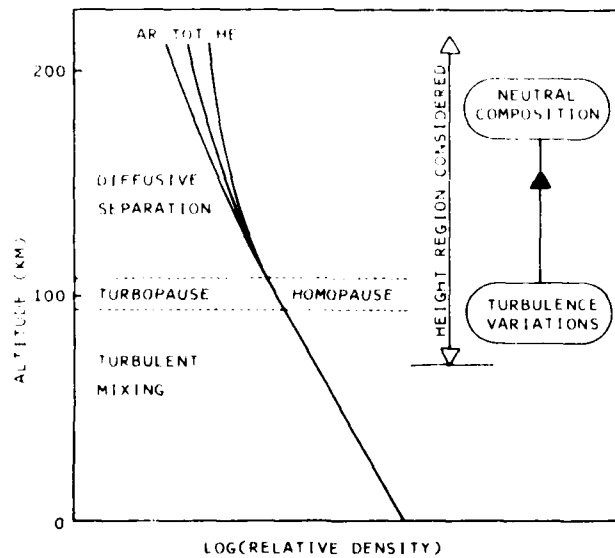


Fig. 1 Overview on the subjects covered in this paper.

This review is primarily intended to give information on turbulence and its role in upper atmospheric modeling to those who are not experts on this subject. Therefore complicating details will be avoided, and emphasis will be placed on the presentation of the basic concepts of the theory and observations of turbulence, especially with regard to thermospheric modeling. A synopsis of the subjects covered in this paper is given by Figure 1. Below about 100 km the atmosphere is mixed by turbulent processes, and all major species show a similar height variation. At the turbopause level turbulence ceases, and at higher altitudes the atmospheric constituents are diffusively separated. Light constituents, such as helium, have larger scale heights than heavy constituents such as argon. Thus the turbopause region corresponds to the homopause region where the homogeneous mixing ends. We shall mainly discuss the altitude region above the mesopause and the effect of turbulence variations on the neutral composition of the thermosphere.

BASIC THEORETICAL CONCEPTS OF TURBULENCE

Turbulence is the most complicated fluid motion we know. Even in the simplest cases, no analytical solutions of the hydrodynamic equations are known. But nature itself offers a way out of this dilemma: turbulence is a stochastic process, and therefore it can be appropriately described by statistical methods.

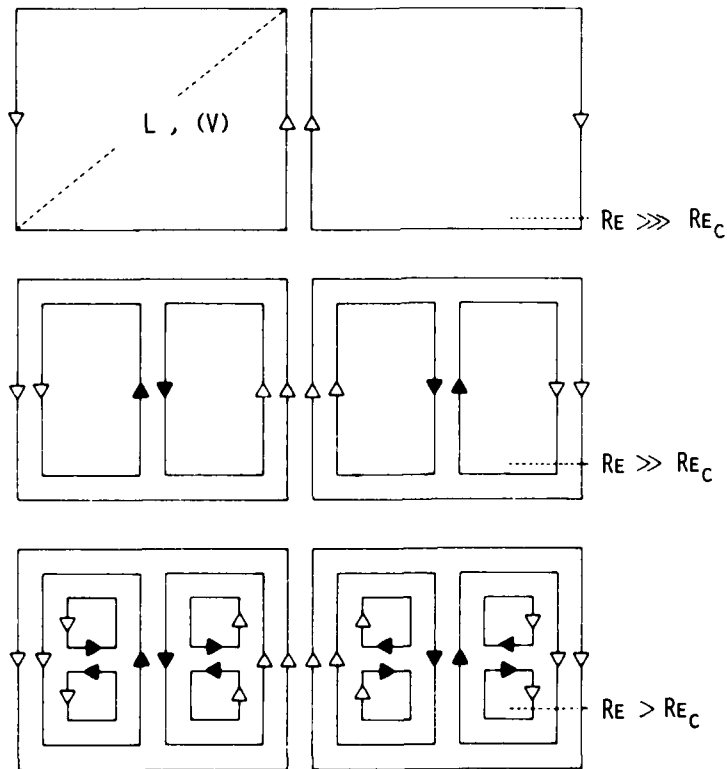


Fig. 2 Schematic representation of turbulent motion.

In the schematic illustration of Figure 2 turbulent motion is described as the superposition of large-scale eddies of characteristic dimensions L and velocity fluctuations (V). The velocity fluctuation (V) is the statistical parameter underlying most of the observational results. The dimensionless Reynolds number Re is associated with the eddies according to

$$Re = \frac{L(V)}{v} = \rho \frac{L(V)}{\eta} \quad (1)$$

where v and η are the kinematic and dynamic viscosities and ρ is the density. Re can also be considered as the ratio of inertial to viscous forces. For small values of Re effects of viscosity exceed the effects of inertia: the flow is non turbulent or laminar. For values of Re larger than a critical Reynolds number Re_c , the inertial forces dominate over the viscous forces and the fluid motion becomes turbulent. As also can be seen from Figure 2, the large eddies must have very high Reynolds numbers due to the high values of L and (V) . Viscous dissipation is then of minor importance. The large eddies therefore transfer their kinetic energy to smaller eddies. The Reynolds number becomes smaller for smaller eddies, and thus the importance of dissipative processes increases. Finally, the smallest eddies have Reynolds numbers of the order of Re_c , or even smaller. Here the energy is dissipated by viscous damping.

This simple illustration of turbulent motion shows that the kinetic energies of the eddies depend on their characteristic scales. The interdependence of both these parameters - kinetic energy and characteristic scale L - is called an energy spectrum. The typical functional form of a turbulent energy spectrum is shown in Figure 3. Starting at very high values of L , the energy is first fed into the largest eddies and turbulent motion is built up. Then the energy is coupled to eddies of decreasing size: viscosity is not yet of importance, and thus this region is called the 'Inviscid Range'. Finally - in the 'Viscid Range' - effects of viscosity become dominant and the turbulent motion is destroyed by viscous dissipation of energy. The range of energy input is called 'Non-Universal' because it depends on the type of force. In spite of this, the inviscid and viscous ranges are called 'Universal': they are independent of the forces and are described exclusively by the parameters L , (V) and v , which are characteristic for the medium and the geometry under consideration.

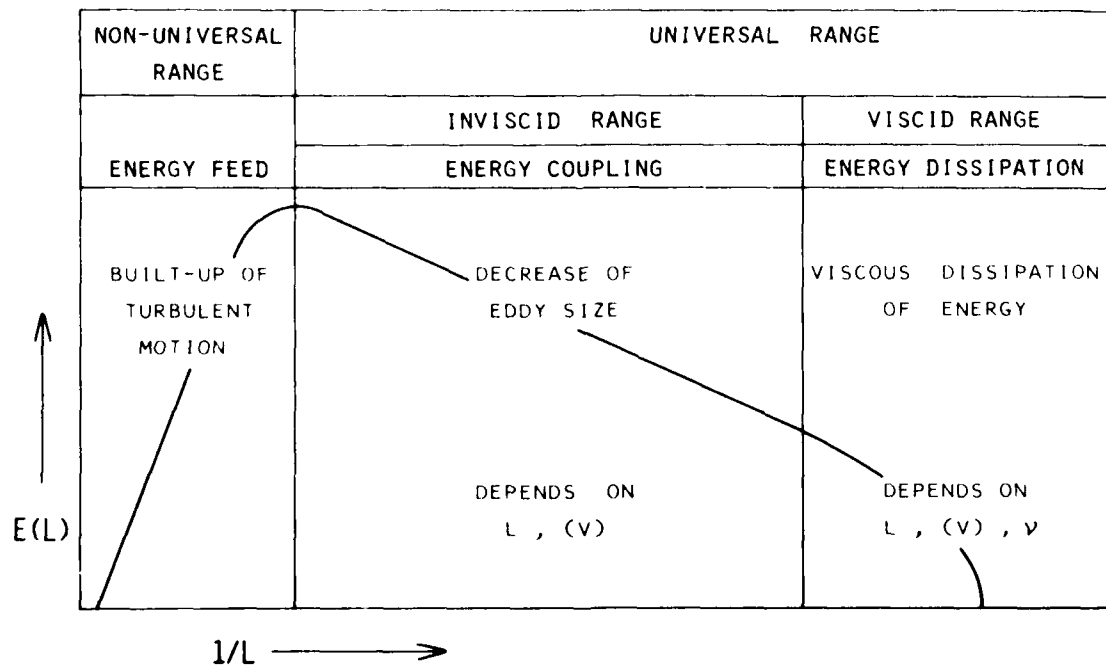


Fig. 3 The turbulent energy spectrum.

Obviously, a very important turbulence parameter is the energy dissipation rate, which describes the energy transfer in the inviscid range. It can be expressed as a function of L and (V) , and the theoretical expression may easily be derived from a simple dimensional analysis. The energy dissipation rate ϵ per unit mass has the dimension m^2/s^3 . The only combination of L and (V) which results in this dimension is given by

$$\epsilon \propto \frac{(V)^3}{L} \quad (2)$$

Importance is also ascribed in atmospheric dynamics to the Richardson number Ri , which is the ratio of the buoyancy forces to the inertial forces. It is given by

$$Ri = \frac{g \frac{\partial T}{\partial z} + \Gamma}{T \left(\frac{\partial V}{\partial z} \right)^2} \quad (3)$$

Here g is the acceleration of gravity, $\partial T/\partial z$ the vertical temperature gradient, Γ the adiabatic lapse rate and $\partial V/\partial z$ the vertical gradient of the horizontal wind.

Thus we have obtained three important parameters characteristic for turbulent processes: the Reynolds number, the energy dissipation rate and the Richardson number. In atmospheric dynamics the Richardson number is of greater importance than the Reynolds number because buoyancy forces are generally more significant than viscous forces. Observational evidence has shown that fluid motion becomes turbulent for

$$Ri > 0.25 \quad (4)$$

In upper atmospheric modeling an even simpler description of turbulence has proven to be successful: it is the concept of the eddy diffusion coefficient K . Analogous to the molecular diffusion coefficient D , which is given approximately by the product of the mean thermal velocity \bar{V}_{th} and the mean free path λ of the particles according to

$$D \sim \bar{V}_{th} \lambda \quad (5)$$

K is defined as the product of the velocity fluctuation (V) and the characteristic eddy scale L :

$$K = (V) L \quad (6)$$

But, whereas the molecular diffusion coefficient D can be derived from elementary principles of gas dynamics, K must at the present be considered as a purely phenomenological quantity, in spite of the fact that a theory for K must somehow be hidden in the fundamental Navier-Stokes equations of fluid motion.

Although according to equation (6) the eddy diffusion coefficient depends on the eddy scale sizes, only an average value of K is used in atmospheric modeling. An interpretation of D and K used in atmospheric modeling is shown in Figure 4. The left of the upper diagram shows characteristic altitude profiles of the coefficients of molecular diffusion D and eddy diffusion K [1,2]. The region of the turbopause is indicated by the dashed stripe. On the right of the upper diagram corresponding altitude profiles of the relative atmospheric densities of light and heavy constituents are given. Diffusive separation starts at the homopause, which is approximated by the point where K is equal to D . D describes the tendency of a gas mixture towards diffusive separation, whereas K describes its mixing tendency. It is important to note that the effects of eddy diffusion on

thermospheric composition can also be represented by simpler profiles of K , such as the one indicated by the dotted vertical line, without a serious loss of accuracy [3]. The lower diagram of Figure 4 shows the effect of changes of the eddy diffusion coefficient on atmospheric composition. An increase of eddy diffusion in the way shown in this figure is equivalent to an increase in the homopause height. In the height range above the homopause this leads to an increase in the density ratio of heavy to light constituents.

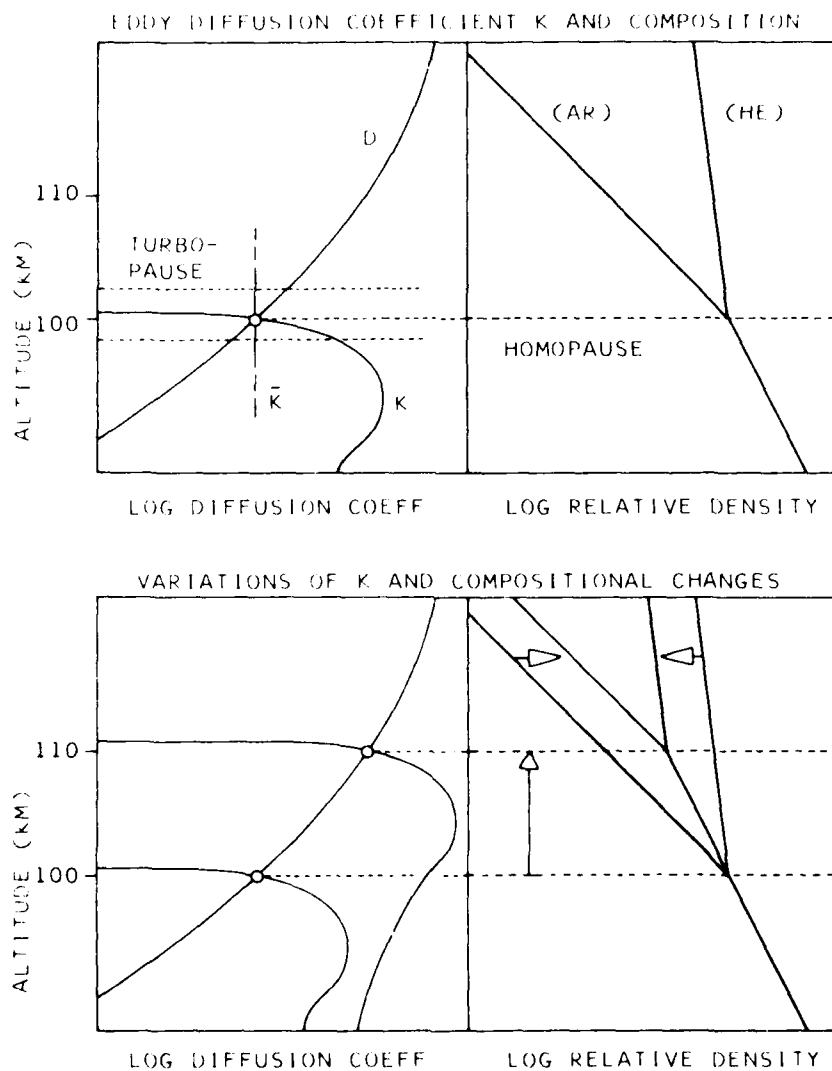


Fig. 4 The eddy diffusion coefficient and its effect on neutral composition.

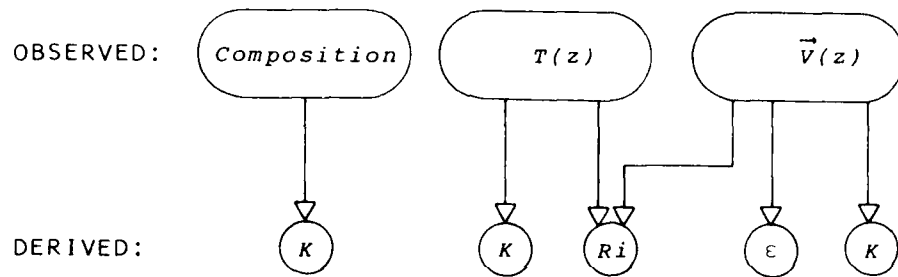
From Figure 4 two important conclusions can be drawn:

1. Most important with respect to thermospheric composition is the altitude variation of turbulence between about 90 and 110 km.
2. A mass-spectrometric determination of the atmospheric composition around 100 km offers a method to determine the homopause height and thus yields an estimate of the eddy diffusion coefficient at this altitude [3-5].

OBSERVATIONAL METHODS OF TURBULENCE PARAMETERS

In the upper part of Figure 5 some results of our foregoing discussion are presented, with special attention given to observational techniques. Observable atmospheric quantities and the turbulence parameters which can be derived from them are shown.

1. Composition measurements lead to an estimate of K at the homopause altitude.
2. Wind observations lead to the determination of K and ϵ .
3. In addition, temperature profiles are required for the determination of the Richardson Number Ri .
4. Finally, although not yet mentioned, consideration of the turbulent heat conduction and vertical temperature profiles allows a determination of the height dependence of K to be made [6,7].



METHOD	PARAMETER	HEIGHT REGION (KM)					
		70	80	90	100	110	120
FALLING SPHERES	Ri, ϵ, K						
GRENADE EXPLOSIONS	Ri, ϵ, K						
CLOUD RELEASES	ϵ, K						
RADIO METEOR DATA	ϵ, K						
PARTIAL REFLECTION	ϵ, K						
INCOHERENT SCATTER	K						
COMPOSITION	K						

Fig. 5 Important observational techniques of turbulence parameters.

In the lower part of Figure 5 the altitude ranges and the turbulence parameters which can be determined by seven important observational techniques are presented:

1. The observation of falling spheres in the mesosphere and lower thermosphere yields all three important turbulence parameters [38].
2. The method of grenade explosions consists of an acoustic ray tracing of rocket-borne explosions and also leads to the determination of the three turbulence parameters R_i , ϵ and K . It is limited to an upper altitude of 90 km [8,9].
3. Rocket-borne cloud releases [10-16] and
4. radio-meteor data are analogous methods. Optical scattering and scattering of radio waves from meteor trails are observed in the first and second cases, respectively. Both of these techniques yield ϵ and K and cover the altitude region around 100 km [17-21].
5. The partial reflection method was originally developed for D-region observations of electron densities. It also yields ϵ and K , but it is limited to the mesosphere and lower thermosphere [22].
6. Radar-deduced information on turbulence can be extended to higher altitudes by incoherent scatter observations of the lower thermospheric temperature profile, from which K can be derived [7].
7. Finally, composition measurements allow estimates of the homopause height and thus of K [4,23].

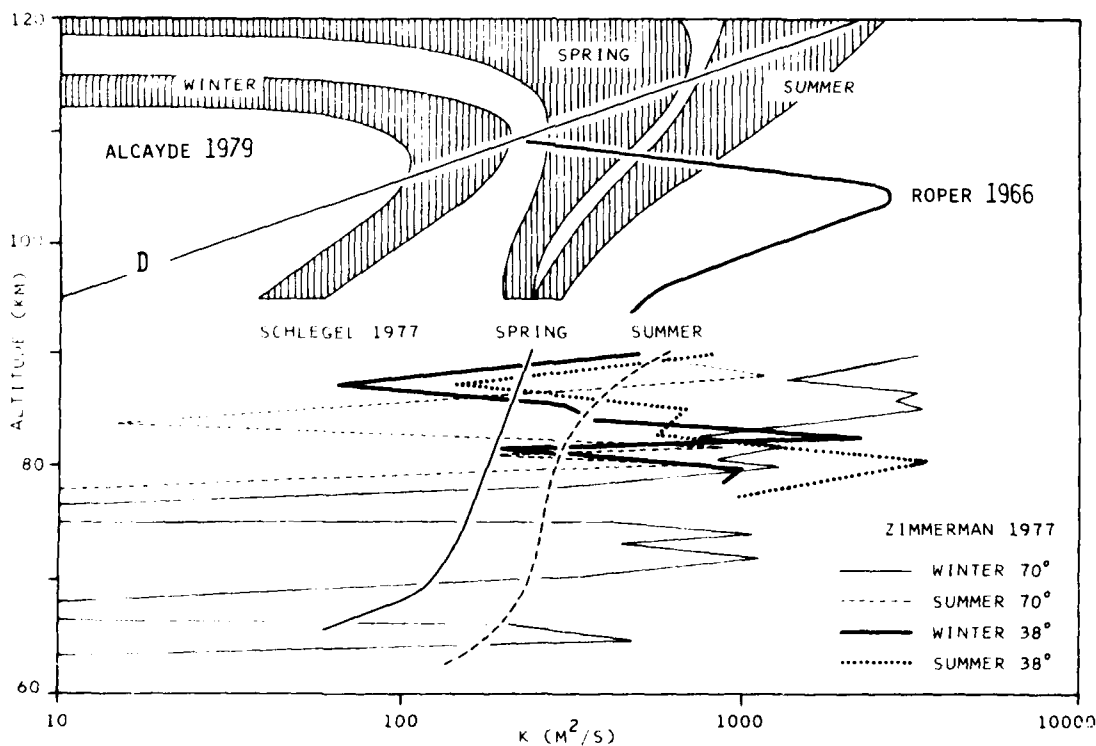


Fig. 6 Profiles of the eddy diffusion coefficient obtained by different methods: altitudinal and seasonal dependence.

Figure 6 shows the altitude dependence of the eddy diffusion coefficient as derived from four different methods. All observations refer to mean and high latitudes. Roper [18] derived his profile from cloud observations, Zimmerman et al. [9] from grenade explosions at 70° and 38° , respectively, Schlegel et al. [22] from the partial reflection method at 70° and, finally, Alcayde et al. [7] estimated their profiles from incoherent scatter temperature profiles at 45° . Most of the profiles do not cover the turbopause region. Moreover, a comparison with the molecular diffusion coefficient D shows that - with the exception of the profiles derived by Roper [18] and Alcayde et al. [7] - they do not allow conclusions to be made on the homopause height. Thus these observations do not permit an estimate of the influence of turbulence on neutral composition. However - even less satisfactory - different methods yield different, if not contradictory results. These discrepancies do not refer to absolute values only, but even to the qualitative seasonal behaviour of turbulence. Thus the grenade data [9] show high winter and low summer turbulence at high latitudes in the mesosphere, while the partial reflection method [22] indicates an increase of turbulence from spring to summer. The partial reflection data exhibit the same tendency as the profiles derived from incoherent scatter temperatures [7], which also show a high summer and a low winter turbulence. They obviously disagree with the high latitude mesospheric observations of Zimmerman et al. [9], while they are in better accordance with Zimmerman's mean latitude results.

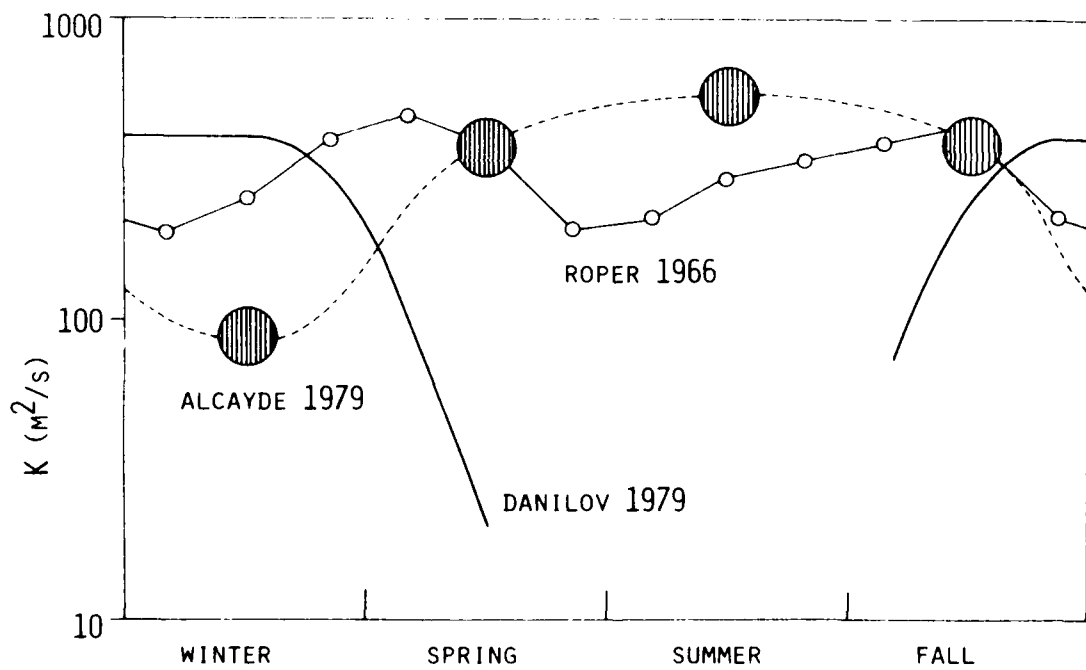


Fig. 7 Seasonal variations of the eddy diffusion coefficient at 100 km obtained by different methods.

In order to obtain better information on the seasonal variation of turbulence with respect to neutral composition changes, we will now restrict our considerations to observations in the homopause region around 100 km. Three techniques yield suitable results: the incoherent scatter data derived by Alcayde et al. [7], composition measurements and radio meteor data. The latter two methods were not included in Figure 6.

Figure 7 shows the seasonal changes of turbulence deduced from these three methods. The diagram presents the variation of the eddy diffusion coefficient versus season for an altitude of about 100 km. The dashed curve represents the data derived from incoherent scatter [7], the fully drawn curve indicates composition measurements by Danilov et al. [23] and the dotted curve shows radio-meteor data by Roper [21]. Whereas [7] and [23] refer to the northern hemisphere, [21] refers to the southern hemisphere. Obviously, there is a strong seasonal variation of turbulence. But it is not possible to combine all results in order to obtain at least an unambiguous trend. Therefore it is impossible at the present to rely on conclusive observations of seasonal changes of turbulence in modeling the upper atmosphere.

TURBULENCE AND ATMOSPHERIC MODELING

Due to the lack of observational information on the details of turbulent behaviour, no final determination of the role of turbulence in upper atmospheric models is presently possible. Thus we shall discuss in the third section of our paper the following question: what phase and amplitude must the seasonal variation of turbulence possess in order to explain the observed thermospheric variations of neutral composition?

Figure 8 shows the seasonal variation of the relative densities of He and Ar at 250 km at high northern latitudes. The observations are derived from the MSIS-model [24] and are given by the fully drawn lines. The dashed lines result from seasonal temperature variations alone. Thus a considerable part of the seasonal changes - indicated by the hatched areas - is possibly due to seasonal variations of turbulence. Recalling the effects of turbulence variations on neutral composition as sketched in Figure 4, we expect low winter turbulence due to the winter He bulge [25] and high summer turbulence due to the summer Ar bulge.

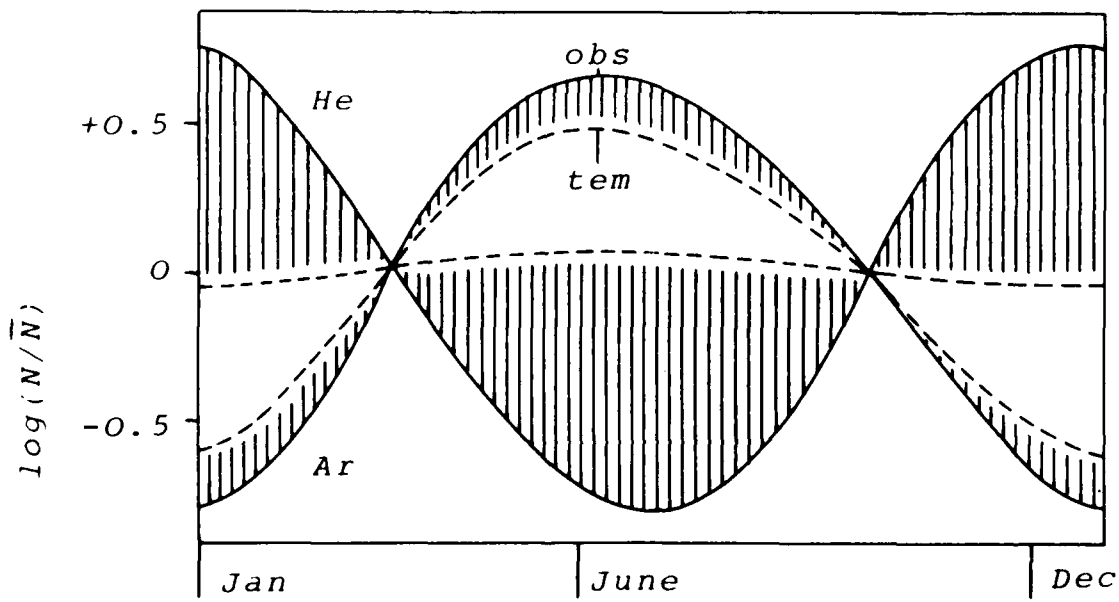


Fig. 8 Observed seasonal variations of helium and argon in the upper thermosphere at 250 km and high northern latitudes derived from the MSIS model. The dashed curve indicates density variations caused solely by changes of the exospheric temperature.

This assumption is indeed confirmed by model calculations [26-28] as shown in Figure 9. The horizontal axis gives the season, and the vertical axis gives the turbopause height. The diagram refers to mean and high latitudes. The dashed line represents the results of the model calculations by Blum et al. [27] which are compared to turbopause height determinations derived from mass spectrometer and incoherent scatter data. Obviously the model contradicts the observations of Danilov et al. [23] but it is qualitatively in agreement with the observations of Alcayde et al. [7]. It is important to note that the absolute values of the model depend on the boundary conditions. Therefore the quantitative difference between the incoherent scatter derived data and the model poses no serious problems.

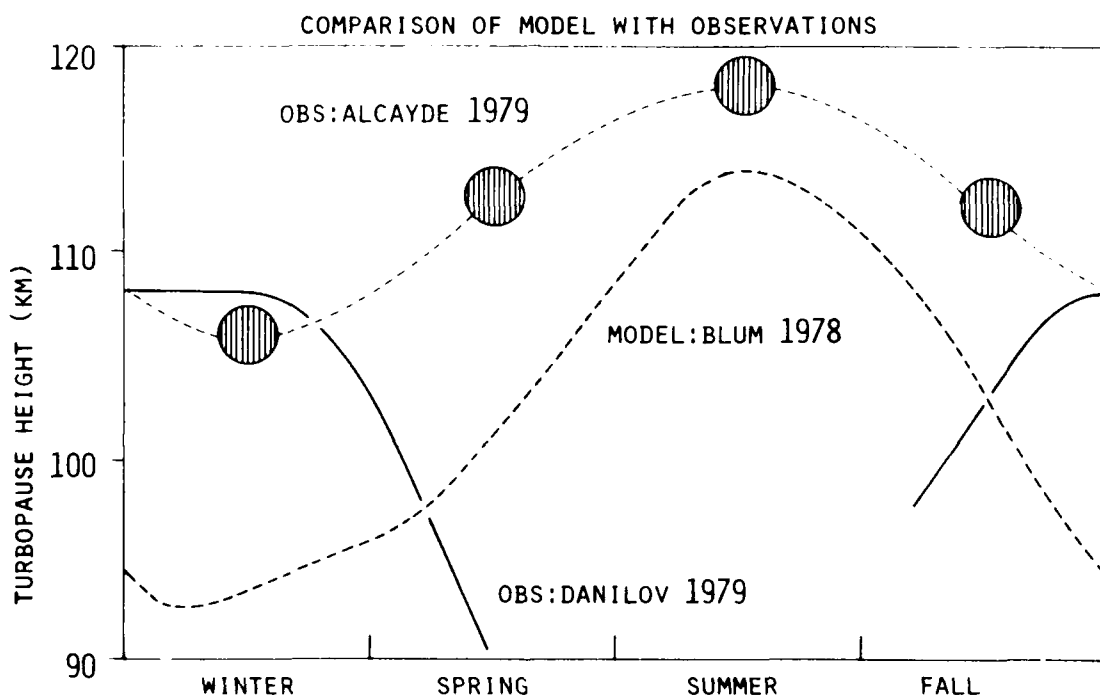


Fig. 9 Comparison of calculated seasonal variations of turbopause height with variations derived from observations of turbulence parameters.

It should be pointed out that turbulence variations are not necessarily required to explain the seasonal variation of composition. A different, but also successful explanation is offered by the process of redistribution of thermospheric constituents due to global seasonal winds [29-32]. But as this is not the subject of this paper, we will not enter into the details here. In another paper in this volume [30] these problems are discussed more extensively.

Unfortunately, no compelling theoretical arguments can be given for either one of the seasonal variations of turbulence shown in Figure 9. Thus, at least at the present, the discrepancies between some observations and model calculations and - even more confusing - between observations obtained from different techniques cannot be resolved.

Finally, another phenomenon will be considered, which has been suggested by various investigators to be possibly caused by variations of turbulence: the change of upper atmospheric composition during geomagnetic disturbances [33,34]. The left side of Figure 10 shows the latitudinal changes of composition during the main phase of a geomagnetic storm. The vertical axis gives the ratio of the disturbed to the undisturbed densities. The data are derived from ESR 4 mass spectrometer observations [35]. These changes qualitatively resemble the seasonal changes from winter to summer conditions: the He-density is decreased, and the Ar-density is increased. This behaviour suggests an explanation similar to the explanation of seasonal density changes: a variation of the turbopause height with latitude. The right side of Figure 10 shows model calculations by Blum et al. [34] which relate the observed density distribution to an increase of the turbopause height with latitude. Combined with variations of the exospheric temperature, this mechanism is indeed able to explain the observations.

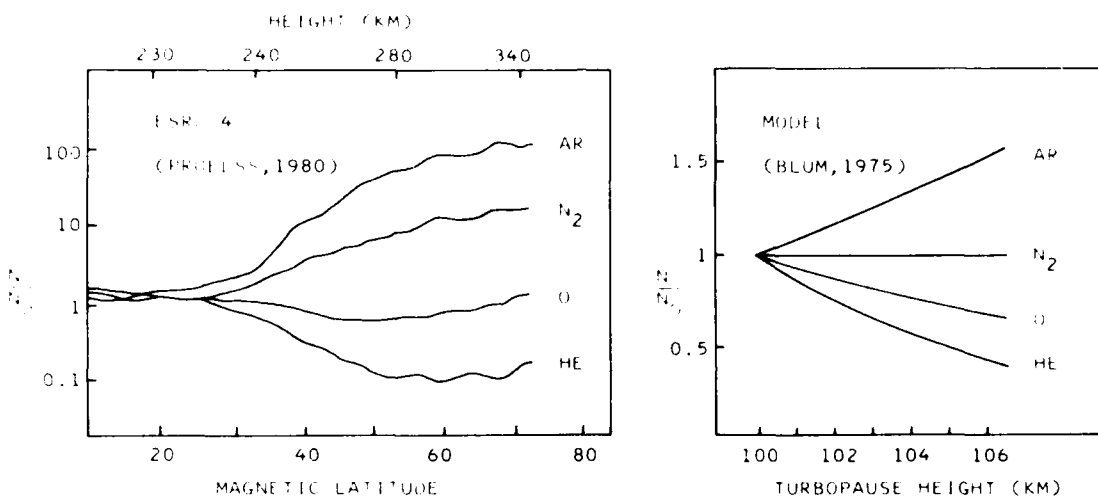


Fig. 10 Compositional changes during geomagnetic disturbances:
observations and model calculations.

Unfortunately, this explanation runs into theoretical difficulties, as the characteristic time τ for eddy diffusion processes is given by

$$\tau \approx \frac{H^2}{K} \quad (7)$$

where H is the atmospheric scale height. It is easily seen that τ is of the order of hours to days at the turbopause level. Therefore the characteristic reaction time of the atmosphere to turbulence changes is much longer than the characteristic time of the geomagnetic disturbance. On the other hand, the very simplicity of this explanation and the good fit of the observations seem to indicate that turbulence variations are very useful as a parameter even in cases where the physics behind the processes is not yet fully understood [36]. Those who strongly object to this application of turbulence variations should be reminded that the hydrodynamic equations give good results even under conditions where they should not theoretically be applicable.

Just as in the case of seasonal variations of composition, in the case of geomagnetic variations the mechanisms of global thermospheric wind fields also offer an alternative explanation of the observed compositional changes [37].

CONCLUSIONS

Before summarizing our conclusions, we would like to note that we have omitted a discussion of the mesospheric and lower thermospheric sources of turbulence, as this is a broad and complicated field of theoretical studies and investigations outside this review. In conclusion, the present results of the effects of turbulence on the neutral upper atmosphere can be summarized as follows:

1. Observations below 90 km do not allow conclusions on neutral composition.
2. Observations covering the turbopause altitude do not show consistent results.
3. Model calculations based on upper thermospheric composition suggest low winter and high summer turbulence.
4. During geomagnetic disturbances model calculations suggest an increase of turbulence.
5. The effects of winds tend to alter the calculated turbulence variations significantly.
6. No theoretical evidence is known for turbulence variations.
7. More observations of turbulence in the turbopause region are required.

ACKNOWLEDGEMENT

The authors wish to thank Dr. K. Champion for his helpful comments.

REFERENCES

1. T.J. Keneshea and S.P. Zimmerman, J. Atmos. Sci. 27, 831 (1970).
2. T. Shimazaki, J. Atmos. Terr. Phys. 33, 1383, (1971).
3. P.W. Blum, H.J. Beese and K.G.H. Schuchardt, in: Terrestrial Atmosphere, Contributed Papers presented at the Solar-Terrestrial Physics Symposium, Innsbruck, 1978.
4. U. von Zahn, J. Geophys. Res. 75, 5517 (1970).
5. U. von Zahn and T. Herwig, in: Dynamical and Chemical Coupling, Reidel, Dordrecht, 1977, p. 49.
6. F.S. Johnson and B. Gottlieb, Planet. Space Sci. 18, 1707 (1970).
7. D. Alcayde, J. Fontanari, G. Kockarts, P. Bauer and R. Bernard, Ann. Geophys. 35, 41 (1979).
8. S.P. Zimmerman, A.C. Faire and E. Murphy, Space Research XII, 615 (1972).
9. S.P. Zimmerman and E.A. Murphy, in: Dynamical and Chemical Coupling, Reidel, Dordrecht, 1977, p. 35.
10. J.E. Blamont and C. de Jager, Ann. Geophys. 17, 134, (1961).
11. J.E. Blamont, Planet. Space Sci. 10, 89 (1963).
12. S.P. Zimmerman and K.S.W. Champion, J. Geophys. Res. 68, 3049 (1963).
13. C.G. Justus, J. Atmos. Sci. 26, 1137 (1969).
14. K.H. Lloyd, C.H. Low, B.J. McAvaney, D. Rees and R.G. Roper, Planet. Space Sci. 20, 761 (1972).
15. S.P. Zimmerman and C.A. Trowbridge, Space Research XIII, 203 (1973).
16. H. Teitelbaum and J.E. Blamont, Planet. Space Sci. 25, 723 (1977).
17. R.G. Roper and W.G. Elford, Nature 197, 963 (1966).
18. R.G. Roper, J. Geophys. Res. 71, 5785 (1966).
19. S.P. Zimmerman, J. Geophys. Res. 78, 3927 (1973).
20. S.P. Zimmerman, J. Geophys. Res. 79, 1095 (1974).

21. R.G. Roper, in: Proc. Int. Conf. on Structure, Composition and General Circulation, Melbourne, Australia, 1974.
22. K. Schlegel, A. Brekke and A. Haug, in: Dynamical and Chemical Coupling, Reidel, Dordrecht, 1977, p. 253.
23. A.D. Danilov, U.A. Kalgin and A.A. Pokhunkov, Space Research XIX, 173 (1979).
24. A.E. Hedin, C.A. Reber, G.P. Newton, N.W. Spencer, H.C. Brinton and H.G. Mayr, J. Geophys. Res. 82, 2148 (1977).
25. G. Kockarts, J. Atmos. Terr. Phys. 34, 1729 (1972).
26. K.G.H. Schuchardt and P.W. Blum, Space Research XVII, 335 (1977).
27. P.W. Blum, K.G.H. Schuchardt and U. von Zahn, J. Atmos. Terr. Phys. 40, 1131 (1978).
28. P.W. Blum and K.G.H. Schuchardt, J. Atmos. Terr. Phys. 40, 1137 (1978).
29. K.G.H. Schuchardt and P.W. Blum, Space Research XX, 101 (1980).
30. K.G.H. Schuchardt and P.W. Blum, this volume.
31. H. Volland and H.G. Mayr, Rev. Geophys. Space Phys. 15, 203 (1977).
32. C.A. Reber and P.B. Hays, J. Geophys. Res. 78, 2977 (1973).
33. A.K. Sinha and S. Chandra, J. Atmos. Terr. Phys. 36, 2055 (1974).
34. P.W. Blum, C. Wulf-Mathies and H. Trinks, Space Research XV, 209 (1975).
35. G.W. Prölss, Rev. Geophys. Space Phys. 18, 153 (1980).
36. L.G. Jacchia, J.W. Showey and U. von Zahn, J. Geophys. Res. 81, 36 (1976).
37. H.G. Mayr and H. Volland, J. Geophys. Res. 78, 2251 (1973).
38. A.C. Faire and K.S.W. Champion, Space Research IX, 343 (1969).

EDDY MIXING AND COMPOSITION VARIATIONS OF EARTH'S UPPER ATMOSPHERE

L.A. Antonova and V.V. Katjushina

*Institute of Applied Geophysics, USSR State Committee for
Hydrometeorology, Moscow, USSR*

ABSTRACT

Solar radiation intensity variations lead to eddy diffusion coefficient variations and are closely connected with variations of both neutral atmosphere constituents in which only eddy mixing (helium) plays a determining part and those in which photochemical processes (atomic oxygen) are also significant. A possible mechanism of the semiannual density variation occurrence in the Earth's upper atmosphere is obtained.

K eddy Variations

The process of eddy diffusion determines to a great extent the neutral composition of Earth's upper atmosphere and its variations. However, the question of nature, intensity and variations of upper atmosphere mixing has not been definitely solved at present. A number of authors put forward atmospheric circulation as an alternative to eddy mixing.

Eddy mixing occurrence at heights ≤ 100 km is connected with atmosphere heating under molecular oxygen dissociation by solar radiation. (High latitude regions would not be considered here because of the existence of specific heating sources). Paper [1] suggests a calculation scheme for the eddy diffusion coefficient K based on thermosphere and mesosphere thermodynamic stability. Assuming full heat redistribution over the globe, the mean eddy diffusion coefficient was obtained in [1] and estimates were made of maximum rates of vertical movements and corresponding horizontal winds necessary for elimination of asymmetry in the energy input into the upper atmosphere. In the other extreme case - when a global wind system is not formed and heat redistribution over the globe does not occur - we get estimates of maximum K value variations. In [2] with conditions for different latitudes during solstice it is found that the value of K_m - the maximum eddy diffusion coefficient - varies little, being $\sim 10^5 \text{ cm}^2 \text{s}^{-1}$ in the summer hemisphere, and decreasing abruptly to $\sim 10^5 \text{ cm}^2 \text{s}^{-1}$ at $\psi = 60^\circ$ in the winter hemisphere. Similar values are obtained in [3] for mid-latitudes.

τ_{eddy} and τ_w

Let us estimate the characteristic time of heat transfer to the lower atmosphere by eddy heat conduction $\tau_{\text{eddy}} \sim H^2/K$. For $K = 10^7$, 10^6 , $10^5 \text{ cm}^2/\text{s}$ and $H = 6 \text{ km}$ we get respectively $\tau_{\text{eddy}} \approx 4(10^4, 10^5, 10^6) \text{ s}$. Comparing the value with the characteristic time necessary for gas transfer across half of the terrestrial hemisphere with horizontal wind rate for heights 100-110 km $V \sim 5 \text{ m s}^{-1}$ [1], $\tau_w \approx 2 \cdot 10^6 \text{ s} \approx 25 \text{ days}$, we see that τ_{eddy} and τ_w are comparable only for the winter hemisphere region where $K_m \approx 10^5 \text{ cm}^2/\text{s}$. This means that this is the only region where one can expect horizontal wind transfer (and hence corresponding vertical gas movements) to have a considerable influence on upper atmosphere composition. In all other regions eddy diffusion prevails, vertical movements playing only "corrective" or long term roles.

The eddy diffusion coefficient has its maximum and minimum coinciding with heat influx maximum and minimum, respectively. Similar conclusions were obtained in [2] where K_m was estimated from atmospheric composition variations in He and ^{16}O . However, in the intermediate region K_m values are lower, and thus the "corrective" role of the wind system takes place. Note that it also follows from the abovementioned estimates of τ that atmospheric midlatitude turbulence reacts relatively fast (several hours) to incoming energy variations in summer in comparison to winter (several days).

O/N_2 variations

Calculations of annual midlatitude variations of O/N_2 at a height of 130 km were performed on the basis of annual variations having a maximum in summer [4]. These values were obtained from known helium concentration variations and corresponding solar dissociating radiation variations. Dissociating radiation increase leads to an increase in the O density. Corresponding eddy mixing intensification increases the downward flow of atomic oxygen, that is decreasing the O density. The net effect of these actions results in O/N_2 maximums in equinoctial periods, that agree well with experimental data at 130 km (Fig.1). (See e.g. [4], [5]).

CONCLUSION

Thus, solar radiation intensity variations, caused by latitude or season changes lead to eddy diffusion coefficient variations and are closely connected with variations of both neutral atmosphere constituents in which only eddy mixing (helium) plays a determining part and those in which photochemical processes (atomic oxygen) are also significant. A possible mechanism of the semiannual density variations occurrence in the Earth's upper atmosphere is obtained that should be considered while modelling the neutral composition.

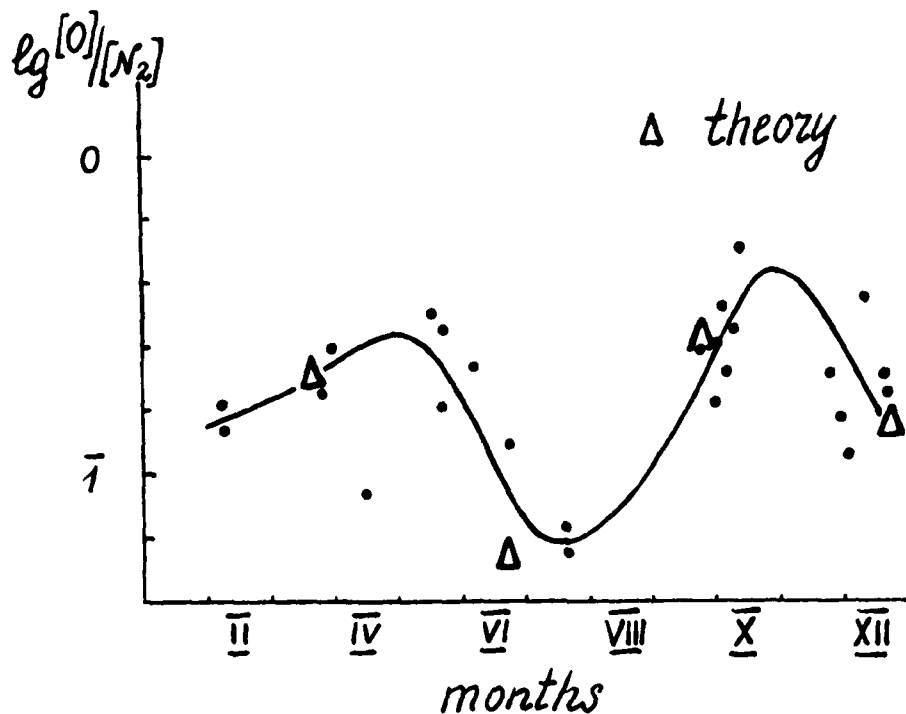


Fig. 1. Semiannual variations of O/N ratio at 130 km (— experimental data, —theory).

References

1. F.S. Johnson, B. Gottlieb, Planet. Space Sci., **18**, 1707 (1970).
2. L.A. Antonova, V.V. Katjushina, Geomagnetism and aeronomy, **20**, 67 (1980).
3. D. Aicayde et al., Ann. Geophys., **35**, 41 (1979).
4. L.A. Antonova, V.V. Katjushina, Geomagnetism and aeronomy, **16**, 311 (1976).
5. D. Offerman, J. Geophys. Res., **79**, 4281 (1974).

THERMOSPHERIC MODEL CALCULATIONS BASED ON TURBULENCE DATA

K.G.H. Schuchardt and P.W. Blum

*Institut für Astrophysik und Extraterrestrische Forschung,
Universität Bonn, 5300 Bonn, FRG*

ABSTRACT

Thermospheric model calculations are presented which explain the seasonal compositional changes of helium and argon by the combined effect of seasonal-latitudinal variations of turbulence and global seasonal winds. The observational base of the model calculations is given by empirical data of upper thermospheric densities and by estimates of the turbopause height derived from composition measurements and incoherent scatter temperatures in the lower thermosphere. The results are compared with observations of the seasonal variability of atomic oxygen in the turbopause region.

INTRODUCTION

Empirical models based on the satellite observations of the last two decades have led to significant progress in the phenomenological description of the upper thermosphere [1]. Our understanding of the dynamical processes required for the construction of theoretical atmospheric models is much less complete. The two mechanisms 'wind' and 'turbulence' are both considered to be major causes of seasonal variations in the thermosphere [2,3]. Between the cold winter and the hot summer hemisphere a pressure gradient develops, which induces a thermospheric meridional wind blowing from summer to winter. This results in upward winds in summer and downward winds in winter. Quantitative observations of the seasonal winds are difficult, although they have been verified qualitatively. In addition, seasonal variations of turbulence have been observed. The boundary layer between mixing and diffusive separation undergoes a seasonal variation of the order of 10 to 20 km [4,5]. These observations are still controversial with respect to quantitative values as well as to the qualitative seasonal behaviour of turbulence. Both mechanisms - winds as well as turbulence variations - significantly affect the neutral composition of the thermosphere. A winter decrease of the turbopause height as well as a summer-to-winter wind would produce the winter He bulge and the summer Ar bulge [6], in exact agreement with mass spectrometer observations [7].

MODEL CALCULATIONS AND RESULTS

In this paper model calculations are presented which interpret the seasonal density variations of helium and argon as a combined effect of global winds and seasonal-latitudinal variations of turbulence. The model is a three-component

model with a background gas and the two minor constituents He and Ar and refers to the altitude range between 80 and 300 km. Our model is based on simplified hydrodynamical equations in order to give more transparency to the calculations [8]. As we are dealing with long-time variations, the continuity equations apply to the stationary state. Only the momentum equations of the minor constituents, i.e. the diffusion equations, are considered. Finally, the energy equation is replaced by observed temperatures and by the parameterization of the meridional wind field and the eddy diffusion coefficient.

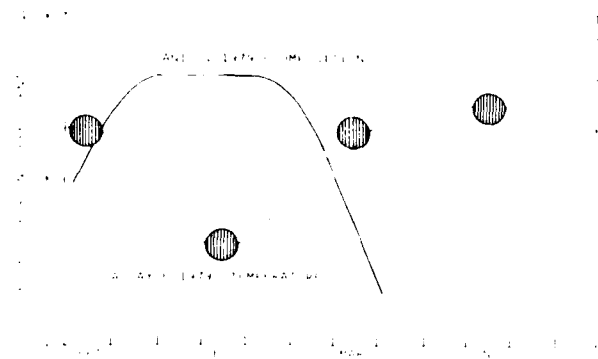


Fig. 1 Observed relative variations of turbulence in the northern hemisphere.

First results of the model [6] have already shown that for any given turbulence variation a well-determined wind field can be derived from the compositional changes of the wind constituents. However, from theory alone it cannot yet be decided which of the two mechanisms is more effective. Therefore observational data of either turbulence or winds are required. Figure 1 shows two different seasonal variations of the eddy diffusion coefficient in the northern hemisphere. The solid line is derived from lower thermospheric composition measurements by Danilov et al. [4]. The dots and the intuitively drawn connecting line are inferred from incoherent scatter temperatures by Alcayde et al. [5]. While in both cases the extremes occur at solstice, the amplitudes have different signs, clear evidence for the unreliability of available observations.

Helium and Argon

Thus two different annual variations of turbulence are derived from Figure 1 and are used as the basic observational information in our model calculations. These turbulence variations and the corresponding wind fields resulting from the model are given in Figure 2. In the upper diagram, the solid curve shows the turbulence variation derived from the incoherent scatter data by Alcayde [5]. The dashed curve is inferred from the homopause observations by Danilov [4]. Both these variations refer to the polar northern hemisphere. Therefore - due to their symmetry with respect to season - the south polar turbulence is given by the mirror images of these curves. The two lower diagrams represent the wind fields at 120 km, which are required in addition to the turbulence variations to result in observed seasonal changes of He and Ar in the upper thermosphere. In both cases the curves show the typical structure of the seasonal meridional wind cell: at winter solstice we obtain south-to-north horizontal winds and northern downward winds. The maximum velocities are 10 m/s in the horizontal and 0.2 m/s in the vertical direction. Thus the vertical velocity is generally smaller than the horizontal velocity by a factor of about 50. These large wind amplitudes are based on high winter turbulence (dashed curves). A low winter turbulence (fully drawn lines) results in meridional winds which are considerably smaller. It should be mentioned that this latter case is similar to the results derived in our turbulence models [3] and discussed in our preceding review paper [9].

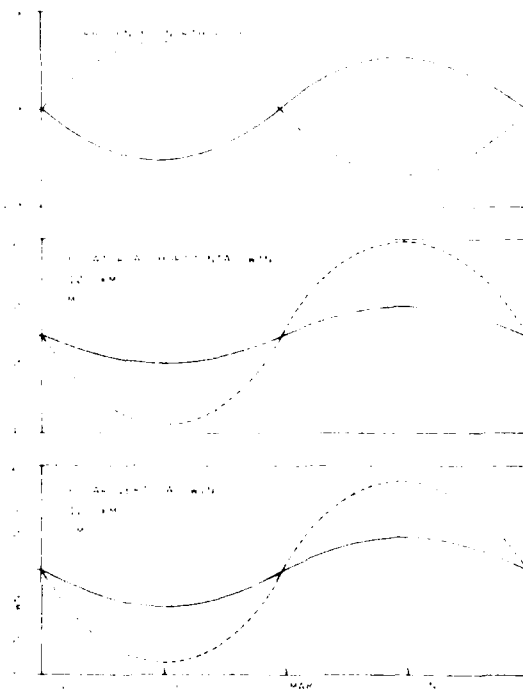


Fig. 2 Seasonal variations of turbulence and meridional winds. The turbulence variations are derived from the data shown in Figure 1, the winds result from model calculations based on these turbulence variations.

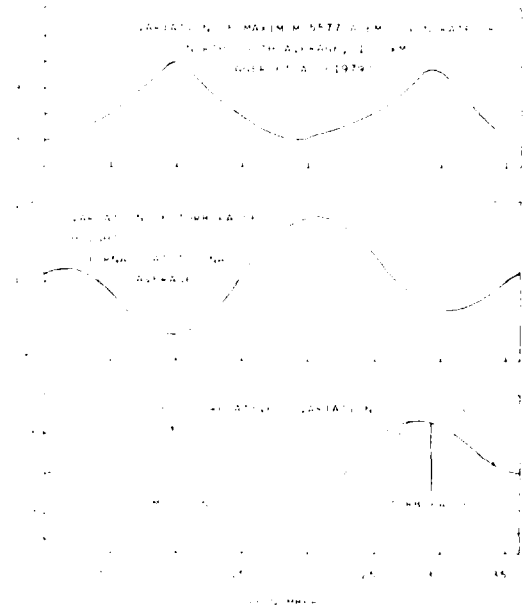


Fig. 3 Upper part: Seasonal variation of the airglow emission rate. Middle part: Seasonal variation of the globally averaged turbopause height derived from helium and argon. Lower part: Relative oxygen variation at 100 km deduced from turbopause height and airglow.

It would be most desirable now to compare the seasonal wind amplitudes obtained from the model calculation with observational wind data. Unfortunately, no observations of seasonal winds in the lower thermosphere are available, so that at the present a test of compatibility of our model results with a complete set of observations is not possible.

Atomic Oxygen

So far we have considered in our model calculations compositional changes of He and Ar only. But atomic oxygen is also a sensitive indicator of dynamic processes in the atmosphere. Indeed, observations reveal a strong seasonal variation of the atomic oxygen concentration even at very low thermospheric altitudes. The upper diagram of Figure 3 shows the seasonal variation of the midlatitude maximum of the oxygen airglow emission rate at 100 km derived by Cogger et al. [10] from satellite-borne photometer observations. The data are combined from both hemispheres, and thus they can be interpreted as to indicate the seasonal variation of the global mean value of the atomic oxygen density in the 100 km region [10]. Moreover, as the observations refer to the homopause region, they should directly reflect possible variations of turbulence.

It has been shown in the foregoing discussion that if the turbulence variations derived from the incoherent scatter data [5] are used in our model the resulting wind field was of minor importance. Thus, in this case, it can be neglected in a first approximation, and seasonal changes of composition are then mainly ascribed to turbulence variations. Consequently, the question arises whether the seasonal variation of the turbopause based on compositional changes of helium and argon is compatible with the observed oxygen variation. The second diagram in Figure 3 shows the global mean of the seasonal variation of the turbopause calculated from the seasonal variations of the diurnally and latitudinally averaged He and Ar densities. The relative variation of Θ resulting from these turbulence changes is shown in the lower diagram of Figure 3 by the solid curve. If, for comparison, the oxygen variation is estimated from the observed emission rate [10], one obtains the dashed curve. Not only the phase, but also the amplitudes of both the observed and the calculated variations are in good agreement. This last result provides additional evidence of the important role of turbulence variations for the explanation of thermospheric behaviour, although no doubt many additional observations are required in order to determine finally the role of turbulence in atmospheric dynamics.

ACKNOWLEDGEMENT

This work was supported in part by the Deutsche Forschungsgemeinschaft.

REFERENCES

1. G. Kockarts, this volume.
2. H.G. Mayr and H. Volland, *J. Geophys. Res.* **77**, 6774 (1972).
3. P.W. Blum, K.G.H. Schuchardt and U. von Zahn, *J. Atmos. Terr. Phys.* **40**, 1131 (1978).
4. A.D. Danilev, U.A. Kalgin and A.A. Pokhunkov, *Space Research XIX*, 173 (1979).
5. D. Alcayde, J. Fontanari, G. Kockarts, P. Bauer and R. Bernard, *Ann. Geophys.* **35**, 41 (1979).
6. K.G.H. Schuchardt and P.W. Blum, *Space Research XX*, 101 (1980).
7. A.E. Hedin, C.A. Reber, G.P. Newton, N.W. Spencer, H.C. Brinton and H.G. Mayr, *J. Geophys. Res.* **82**, 2148 (1977).
8. P.W. Blum and K.G.H. Schuchardt, *Space Research XX*, 97 (1980).
9. P.W. Blum and K.G.H. Schuchardt, this volume.
10. L.L. Cogger and R. Khaneja, *Can. J. Phys.* **57**, 926 (1979).

THE INFLUENCE OF RADIATIVE COOLING AND TURBULENCE ON THE HEAT BUDGET OF THE THERMOSPHERE

B.F. Gordiets,¹ Yu. N. Kulikov,² M. N. Markov¹
and M.Ya. Marov²

¹ Lebedev Physical Institute; ² Keldysh Institute of Applied
Mathematics, The Soviet Academy of Sciences,
Moscow, USSR

ABSTRACT

Numerical models of the thermal budget of the Earth's upper atmosphere in the height range of 90-500km are developed. The main sources and sinks of energy including infra-red radiative cooling by vibrational-rotational bands of NO, CO₂, OH and O₃ as well as heating and cooling arising from dissipation of turbulent energy and eddy heat transport are taken into account. The calculated temperature and density height profiles are in good agreement with the respective profiles from CIRA 72 and Jacchia 1977 models. It is shown for the models considered that IR-radiative cooling by CO₂ and NO in the 15 μ and 5.3 μ bands, not eddy turbulence provides the major loss of heat from 90 to 180km.

INTRODUCTION

In recent years considerable progress has been achieved in the development of theoretical models of thermospheric dynamics and the heat budget. Nevertheless, serious difficulties concerning the correct treatment of cooling mechanisms are not yet resolved. They are primarily connected with the relative importance of infra-red radiation and eddy turbulence, the latter being responsible for not just cooling but, also, heating of the gas due to viscous dissipation of the turbulent kinetic energy.

The difficulties of the correct description of turbulent heating and the necessity to find an effective heat sink in the lower thermosphere have apparently led to the fact that in some theoretical models [1,8] turbulent heating is utterly ignored. However, temperature height distributions calculated with these models are substantially different from the empirical ones corresponding to CIRA 72 [2] or Jacchia [9] thermospheric models. The disagreement between theory and experiment (both for the lower and upper thermospheres) is caused by a number of reasons. A considerable underestimation of IR-cooling in the thermospheric heat budget is perhaps one of them.

The theoretical analysis of IR-radiation at heights from 90 to 250

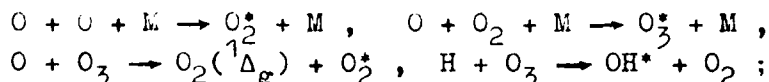
km [6] and the experimental results [11,15] indicate that for development of an adequate thermospheric model a correct treatment of IR-radiation in the $1.2-20\mu$ wavelength region, primarily in the 5.3μ and the 15μ bands of NO and CO_2 , is of critical importance. The aim of this study is to simulate the main heating and cooling mechanisms including eddy turbulence and IR-radiation and to evaluate their relative contribution to the heat budget of the Earth's thermosphere.

BASIC ASSUMPTIONS AND METHOD OF CALCULATION

For the analysis the number concentrations of the atmospheric constituents at the lower boundary (or in some vicinity of it) are assumed to be known. The concentrations of N_2 and O_2 are taken according to the CIRA 72 model atmosphere [2]. The atomic oxygen distribution from 90 to 120 km is taken according to measurements [4] and above 120 km is assumed to be in diffusive equilibrium. Apart from the major constituents N_2 , O_2 and O, some minor ones such as NO, CO_2 , O_3 and OH which give the major contributions to the thermospheric IR-radiation in the $2.8-17\mu$ wavelength region are also considered. The NO concentration height distribution is taken in accordance with recent measurements and calculations carried out by various authors. The distribution of CO_2 below 100 km is determined from the approximate solution of the stationary one-dimensional continuity equation with allowance for eddy mixing and photodissociation and above 100 km from the condition of diffusive equilibrium. The ozone concentration at all heights is derived from the assumption of photochemical equilibrium, with O_3 production by the reaction $\text{O} + \text{O}_2 + \text{M} \rightarrow \text{O}_3 + \text{M}$ and loss due to photodissociation and reactions with O and H_2O .

To determine the temperature and density distributions in the altitude range of 90-500 km the one-dimensional equations of continuity, hydrostatic and heat balance are solved, together with the equations of vibrational kinetics for the radiating molecules. In the heat balance equation the following heat sources and sinks are taken into account:

- heating arising from photodissociation of O_2 and O_3 ;
- heating available from N_2 , O_2 and O photoionization and ionization by precipitating electrons;
- chemical heating in the reactions with atomic oxygen and ozone:



- IR-cooling by the vibrational-rotational bands of CO_2 , NO, O_3 , OH, NO_2 , N_2O_5 and CO, in the 1.27μ O_2 band and in the 63μ atomic oxygen line;
- heating and cooling produced by diurnal contraction and expansion of the thermosphere;
- molecular heat conduction;
- turbulent heating and conduction.

The volume heating and cooling rates for the processes in question are discussed in detail in [7]. Here we only point out that the induction heating rate is calculated from the equation

$$q_{cc} = \frac{\partial}{\partial z} \left[\rho c_p K_h \left(\frac{\partial T}{\partial z} + \frac{g}{c_p} \right) \right] \quad (1)$$

where K_h - eddy thermal conductivity (assumed to be equal to the eddy diffusion coefficient); C_p - the specific heat at constant pressure; ρ - gas density and P_g - the acceleration due to gravity. The rate of turbulent heating is calculated from the equation

$$q_{eh} = K_h \frac{\rho g}{T} \left(\frac{\partial T}{\partial z} + \frac{g}{C_p} \right) \frac{1}{Rf_0} \quad (2)$$

where Rf_0 is the dynamic Richardson number for quasi-stationary turbulent motion. Eq.(2) implies that gas heating arises from both the viscous dissipation of turbulent energy and the work of turbulent pulsations against buoyancy forces. The height distribution of the dynamic Richardson number needed for the computation of q_{ec} and q_{eh} is derived from the measured wind shear height profiles [12] using the height average value of the inverse turbulent Prandtl number equal to 0.3 which has been deduced from experiments [10]. The square of the Brunt-Väisälä frequency $(\partial T/\partial z + g/C_p) g/T$ is derived from the mean temperature height distribution of the Jacchia 1977 model [9]. For the function $K_h(z)$ the analytic approximation suggested in [14] is adopted. The height z_m at which K_h attains its maximum value K_h^{\max} has been varied within the range 100-110km. K_h^{\max} in its turn has been varied from 10^6 to 10^7 cm²/s. Besides, the functional relation between K_h and Rf_0 derived from analysis of experimental data and physical considerations of the semi-empirical theory of turbulence is also used. This relation has the form

$$K_h = 3 \times 10^5 \frac{1 - Rf_0}{\sqrt{Rf_0}} \text{ cm}^2 \text{ s}^{-2} \quad (3)$$

To calculate the IR-radiative cooling in the 15μ band of CO₂ the escape-to-space approximation is adopted which takes into account reabsorption and transfer of radiation. The equations which describe the state of the thermosphere are solved numerically for the time of equinox at the equator. The flux of solar radiation is assumed to correspond to the middle level of solar activity for which, at zero solar zenith angle, the flux of ionizing UV-radiation ($\lambda < 1027\text{A}$) at the top of the thermosphere is about 3.7 ergs/cm²/s [3]. The brightness temperatures of the lower atmospheric radiation are supposed to be equal to their typical values, namely 210K for the 14μ band of O₃ and 240K for the 5.3μ and 9.6μ bands of NO and O₃. The collisional deactivation rate constants for the NO(v=1), CO₂(01⁰0), O₃(01⁰0) and O₃(00⁰1) vibrational levels are taken to be (in units of cm³/s)

$$\begin{aligned} k(\text{NO}-0) &= 3.6 \times 10^{-11} \\ k(\text{CO}_2-\text{O}_2) &= 3xk(\text{CO}_2-\text{N}_2) = 4.4 \times 10^{-15} T \exp(-41/T^{1/3}) \\ k(\text{O}_3(01^00)-0) &= k(\text{O}_3(00^01)-0) = 3.1 \times 10^{-12} \end{aligned} \quad (4)$$

The rate constant for the CO₂(01⁰0) relaxation in collisions with atomic oxygen has been derived from a numerical experiment. The rate constants for the other processes have been assumed to be the same as in [6,7].

RESULTS AND DISCUSSION

First let us consider the static thermospheric models which correspond to the steady state solutions of the hydrostatic and heat ba-

lance equations with the rates of heating by UV-radiation taken to be equal to their daily average values and the coefficient $K_b(z)$ such that $K_b^{\max} = 10^6 \text{ cm}^2/\text{s}$ at 105km. The value of the $\text{CO}_2(\text{O}^{\text{I}}\text{O})$ deactivation rate constant in collisions with atomic oxygen has been determined by means of adjusting the calculated temperature distribution to the experimental one. The agreement between the two has proved to be fairly satisfactory for

$$k(\text{CO}_2-\text{O}) = 3 \times 10^{-11} \exp(-800/T) \text{ cm}^3/\text{s} \quad (5)$$

The respective temperature height distributions are shown in Fig.1a. Throughout the whole height range considered there is a good agreement between the calculated (curve 1) and the empirical distributions. The calculated atmospheric density is also close to the experimental values at all heights.

TABLE 1 Daily Average Vertical Energy Fluxes for Radiative and Conductive Cooling and Turbulent Heating at 90 and 120km ($\psi = \delta = 0^\circ$, $F_{10.7} = 150$)

Emission, process	Flux ($\text{ergs/cm}^2/\text{s}$)	
	90km	120km
1. $1.27\mu \text{ O}_2$ (chemical)*	-0.08	0
2. $2.8\mu \text{ OH}^2$ (chemical)	-0.06	0
3. $9.6\mu \text{ O}_3$ (chemical)	-0.01	0
4. $14.4\mu \text{ O}_3$ (chemical and thermal)	-0.01	0
5. $4.3-5.3\mu \text{ CO}_2, \text{CO}, \text{NO}, \text{NO}^+$, $\text{N}^{14}\text{N}^{15}$ (chemical)	-0.12	-0.1
6. $5.3\mu \text{ NO}$ (thermal)	-0.17	-0.16
7. $15\mu \text{ CO}_2$ (thermal)	-1.81	-0.15
8. $63\mu \text{ O}$ (thermal)	-0.12	-0.1
9. Molecular conduction	0	-0.39
10. Eddy conduction	-0.95	0
11. Turbulent heating	+1.25	0
12. Total flux	-2.08	-0.9

*excitation mechanism

In order to compare the relative contributions of various cooling mechanisms to the thermospheric heat budget we have computed the daily average radiative vertical fluxes for the bands in question, as well as the fluxes due to the molecular and eddy heat conduction at 90 and 120km. The results are presented in Table 1. It has been found that at the height of 120km the thermospheric radiation in the 5.3μ and 15μ bands of NO and CO_2 is the main mechanism of energy loss, with the fluxes being greater by factors of 1.6 and 1.5, respectively, than that for the 63μ atomic oxygen line. Radiative cooling in these bands is determined by the thermal excitation of NO and CO_2 vibrations in collisions with oxygen atoms. In the height range of 90-120km radiation in the 15μ band of CO_2 appears to be the dominant mechanism of energy loss. The temperature height profiles shown in Fig.1a by the curves 2 and 3 are obtained on the assumption that no vibrational excitation takes place in collisions between NO and O (curve 2) and between CO_2 and O (curve

5). It can be easily seen from Fig. 1a that collisions between NO and CO₂ and atomic oxygen play an important role in the formation of the thermospheric temperature height distribution.

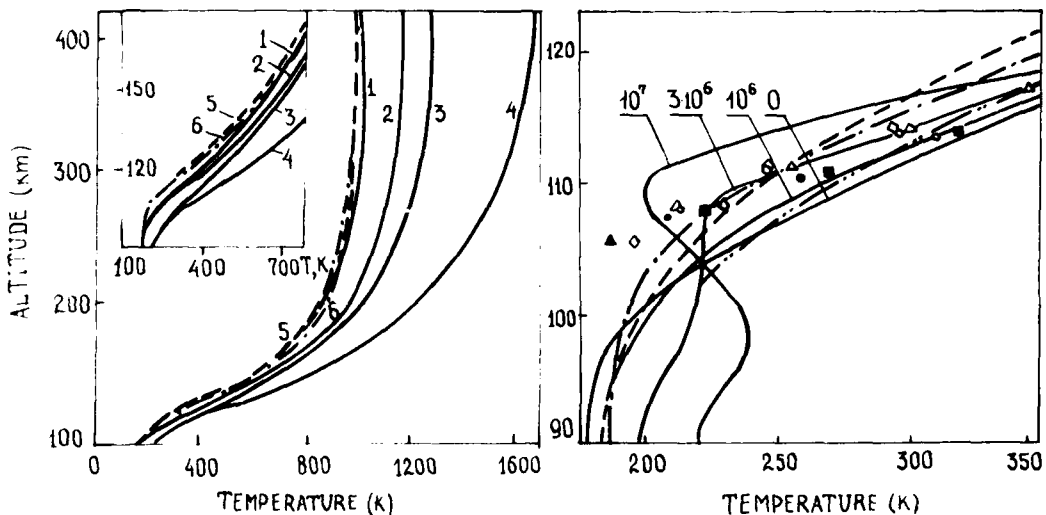


Fig. 1a(left) The altitude temperature distributions for the theoretical and empirical models. The calculations are carried out for the altitude profile of $K_h(z)$ characterized by $K_h^{\text{Max}} = 10^6 \text{ cm}^2/\text{s}$ and $z_m = 105 \text{ km}$. 1 - vibrational excitation of NO($v=1$) and CO₂(O1 Δ) in collisions NO-O and CO₂-O is taken into account; 2 - no excitation in collisions NO-O; 3 - no excitation in collisions CO₂-O; 4 - no excitation in collisions of O with both NO and CO₂; 5 - CIRA 72 model; 6 - Jacchia 1977 model. Fig. 1b(right) The altitude temperature profiles in the lower thermosphere for varying values of K_h^{Max} at $z = 105 \text{ km}$. Also shown are: CIRA 72 model (dashed line), Jacchia 1977 model (dot-dashed line), measurements [13] (double-dot-dashed line), measurements [5] (open and solid circles, triangles and squares).

In order to study the relative importance of turbulence and IR-radiation in the thermospheric heat budget we have carried out a number of computations using various values of the eddy thermal conductivity. The calculated temperature height distributions shown in Fig. 1b are in satisfactory agreement with the corresponding profiles of the CIRA 72 and Jacchia 1977 models and the experimental data [5, 13] if K_h^{Max} does not exceed the value of about $2 \times 10^6 \text{ cm}^2/\text{s}$. For larger values of K_h^{Max} the temperature profiles do not agree with the experimental data. Contrary to the results of [1] our calculations show that the value of K_h^{Max} does not have much effect on the exospheric temperature T_∞ and, therefore, there is no need to assume larger values for K_h^{Max} in order to get closer agreement between calculated and experimental values of T_∞ . It is not eddy turbulence but radiative cooling in the 5.3 μ and 15 μ bands of NO and CO₂ that affect the value of T_∞ . In [1, 8] this radiative heat sink was either ignored (for NO) or essentially underestimated (for CO₂).

In order to get additional information on the typical average value

of K_h in the lower thermosphere we have compared the calculated rates of turbulent energy dissipation ϵ_d with the experimental data. For $K_h^{\max} = (1-3) \times 10^6 \text{ cm}^2/\text{s}$ the agreement between calculated and experimental values of ϵ_d has turned out to be rather satisfactory. It should be noted that the adoption of the functional relation (3) (for which $K_h^{\max} \leq 10^6 \text{ cm}^2/\text{s}$) also results in T and ϵ_d distributions which are in close agreement with the experimental data.

Thus the results bring us to the conclusion that the maximum value of eddy thermal conductivity K_h^{\max} in the lower thermosphere for an average quasi-stationary thermospheric condition cannot exceed $2 \times 10^6 \text{ cm}^2/\text{s}$. The analysis has also shown that for altitudes $z > z_m$, where eddy heat conductivity is decreasing with height, the net effect of eddy turbulence is to cool the thermosphere. It results from the fact that at these altitudes a sharp decrease of $K_h(z)$ with height causes a rapid cessation of turbulent heating (Cf. (2)) while eddy conduction always cools the thermosphere at the heights where $K_h(z)$ is decreasing with z (Cf. (1)). In the region $z < z_m$ the effect of turbulence on the thermospheric heat budget is determined largely by the shape of the height profile of K_h . If $K_h(z)$ increases from a value of $(3-5) \times 10^7 \text{ cm}^2/\text{s}$ at the mesopause level to a value of $(1-3) \times 10^6 \text{ cm}^2/\text{s}$ at the height z_m , turbulence provides net gas heating in this height region. For K_h increasing with height more rapidly than $1/[\rho C_p (\partial T/\partial z + g/C_p)]$ the value of q_{ec} is positive, that is eddy conduction provides not cooling but heating, in addition to the heating arising from turbulent energy dissipation. If the value of K_h is constant from the mesopause level to the height z_m or increases only slightly, eddy conduction always cools this region of the thermosphere and the net result of eddy turbulence can be either heating or cooling. However, in any case when $K_h^{\max} \leq 10^6 \text{ cm}^2/\text{s}$ it is IR-radiation that provides the major loss of energy from the thermosphere.

In order to estimate the effect of the other possible energy sources in the lower thermosphere (tides, acoustic and internal gravity waves, etc.) on the temperature height distribution we have introduced into the energy equation an additional heat source with the volume heating rate decreasing exponentially with a scale height of 6km. It has turned out that this energy source does not change thermospheric temperatures significantly if the additional influx of heat at the mesopause level $z_m = 90\text{km}$ is not greater than about 2 erg/cm²/s. Almost all this energy is radiated away in the 15μ band of CO_2 .

Apart from the static thermospheric models the alternative dynamic models describing the diurnal variations of the basic thermospheric parameters have also been considered. Some results of the calculations are presented in Figs. 2a and 2b. It can be seen that at local noon infra-red radiation is the major mechanism of energy loss in the height range of 90-180km. Molecular conduction prevails as a cooling process only at heights above 180km. Among IR-radiation bands the 15μ band of CO_2 dominates in cooling over the others in the altitude range of 90-120km. The 5.3μ band of NO prevails from 120 to 250km. Radiative cooling in the 63μ line of atomic oxygen becomes dominant only above 250km. The results of the analysis show, however, that the diurnal variations of gas temperature and density at exospheric heights derived from the models are noticeably greater than those obtained from experiments. This departure may be

attributed to the fact that a number of processes are not properly taken into account in the dynamic models. First of all, perhaps, the advective energy transport due to thermospheric winds. In the static models, however, this process of horizontal heat advection is effectively averaged over a day. That is why the calculated thermospheric parameters, at least for low and middle latitudes, have proved to be in good accord with observational data.

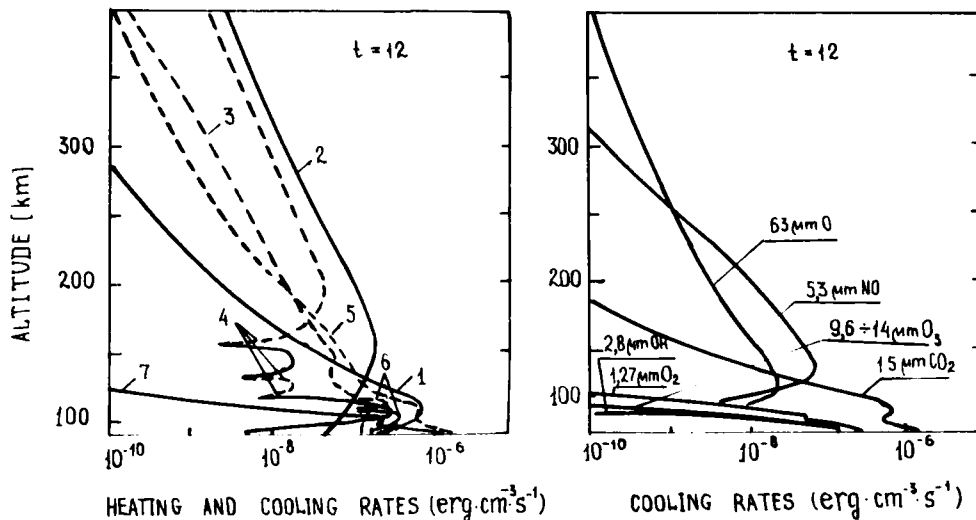


Fig.2a(left) Thermospheric cooling (dashed curves) and heating rates (solid curves) vs altitude at local noon ($\varphi = \delta = 0^\circ$, $F_{10.7} = 150$). 1 - heating arising from O_2 photodissociation; 2 - heating available from photoionization; 3 - cooling due to thermospheric expansion; 4 - cooling and heating due to molecular conduction; 5 - radiative cooling in the $1.27\text{-}63 \mu\text{m}$ wavelength region; 6 - turbulent heating and cooling; 7 - chemical heating. Fig.2b(right) Radiative cooling rates vs altitude at local noon.

SUMMARY

The main results of this study can be summarized as follows.

1. The static and dynamic theoretical models of the Earth's thermosphere which take into account eddy conduction and heating arising from turbulent energy dissipation and also IR-radiation in the $1.27\text{-}63 \mu\text{m}$ wavelength region, including vibrational-rotational bands of the minor atmospheric constituents (NO , CO_2 , OH , O_3), are considered. Throughout the whole altitude range (90-500 km)³ there is good agreement between the empirical and theoretical thermospheric temperature and density height distributions derived from the static model in which thermal excitation of molecular vibrations in collisions of CO_2 and NO with atomic oxygen is taken into account.
2. A parametric study of the role of eddy turbulence in the thermospheric heat budget in which the basic parameters are the eddy thermal conductivity K_h and the dynamic Richardson number R_f is carried out. An estimate of the maximum time average value of K_h^{\max} in the

lower thermosphere based on energy considerations and equal to $(1-2) \times 10^6 \text{ cm}^2/\text{s}$ is obtained. For such values of K_h^{max} there is fairly good agreement between the calculated and experimental height distributions of T and ϵ_d in the lower thermosphere.

3. At heights above the height z_m of the maximum eddy heat conductivity, the presence of turbulence results in gas cooling. Below this altitude, turbulence can either cool or heat the thermosphere depending on the shape of the height profile of $K_h(z)$. For the approximation usually adopted for $K_h(z)$ (an exponential growth of K_h with height for $z < z_m$) eddy turbulence heats the thermosphere in this region.

4. The major loss of energy in the altitude range of 90–180 km is provided by IR-radiation, primarily, in the 15μ band of CO₂ (90–120 km) and in the 5.3μ band of NO (120–180 km). The contribution of IR-radiation in the 63μ line of O and of molecular and eddy conduction to the thermospheric heat budget at these heights has proved to be less important than it was supposed to be in the earlier theoretical studies of thermospheric energetics.

References

1. S. Chandra and A. K. Sinha, J. Geophys. Res. 79, 1916 (1974).
2. COSPAR International Reference Atmosphere – 1972, Akad. Verl., Berlin, 1972.
3. J. P. Delaboudinière, R. F. Donelly, H. E. Hinteregger, G. Schmidtke and P. C. Simon, Intercomparison/Compilation of relevant solar flux data related to aeronomy (Solar Cycle 20), COSPAR Manual, No.7, Bruxelles, 1978.
4. P. Dickinson, R. Bolden and R. Young, Nature 252, 289 (1974).
5. J. V. Evans, W. L. Oliver Jr. and J. R. Salah, J. Atmos. Terr. Phys. 41, 259 (1979).
6. B. F. Gordiets, M. N. Markov and L. A. Shelepin, Planet. Space Sci. 26, 933 (1978).
7. B. F. Gordiets, Yu. N. Kulikov, M. N. Markov and M. Ya. Marov, Preprint No.112, Lebedev Phys. Inst., Sov. Ac. Sci., 1979.
8. G. V. Gridchin, E. A. Zhadin and A. I. Ivanovskii, Geomagn. Aeronom. 16, 143 (1976).
9. L. G. Jacchia, SAO Special Report No.375, Smithson. Inst. Astrophys. Obs., Cambridge, 1977.
10. C. G. Justus, J. Geophys. Res. 72, 1035 (1967).
11. M. N. Markov and V. S. Petrov, Trans. Lebedev Phys. Inst. 105, 72 (1978).
12. N. W. Rosenberg, J. Atmos. Terr. Phys. 30, 907 (1968).
13. J. Salah and R. H. Wand, J. Geophys. Res. 79, 4295 (1974).
14. T. Shimazaki, J. Atmos. Terr. Phys. 33, 1383 (1971).
15. A. Stair, J. Ulwick, D. Baker, C. Wyatt and K. Baker, Geophys. Res. Lett. 1, 117 (1974).

COMPARISON OF THE EMPIRICAL THERMOSPHERIC MODELS AND THE SELF-CONSISTENT MODEL OF THE IONOSPHERIC PLASMA

M.N. Vlasov¹ and A.G. Kolesnik²

¹ Institute of Applied Geophysics, The USSR State Committee
for Hydrometeorology, Moscow, USSR

² Tomsk University, The USSR Academy of Sciences, Moscow,
USSR

ABSTRACT

The comparison of the self-consistent theoretical model with empirical models and experimental data is presented. The cause of the discrepancies of these models is discussed.

INTRODUCTION

The availability of large data bases resulting from measurements of various thermospheric parameters has led to the development of empirical models of the upper atmosphere. At present the best models for general use are Jacchia-71 (1), MSIS (2) and DTM (3). Jacchia's 1971 model is based on satellite drag data and results of rocket measurements of the upper atmospheric composition below 200 km (4). In order to account for the variations of the individual constituents a number of additional corrections to a diffusive equilibrium model have been made in Jacchia's 77 model (5), in which a separate "pseudotemperature" profile has been introduced for each constituent. However, the great complexity of this model makes its use awkward. The main feature of the MSIS model is that it is based on measurements of atmospheric composition from mass spectrometers on five satellites (AE-B, OGO-6, San Marco 3, Aeros A and AE-C) and neutral temperature inferred from incoherent scatter measurements at four ground stations. The DTM model is based on a combination of satellite drag data and optical measurements of the width of the 630 nm line of atomic oxygen providing a global temperature model independent of any assumption related to the distribution of atmospheric constituents. From comparisons of these models it would be unfair to conclude (6,7) that any of the models is completely inadequate to represent the structure of the terrestrial thermosphere although there are marked discrepancies between these models.

On the other hand, the development of the ionospheric plasma theory makes it possible to solve the task of the self-consistent description of the charged and neutral constituent behaviour. The basis of this description is a system of hydrodynamic equations. The self-consistent theoretical model has been described in (8). The space-time variations of the neutral, charged and excited species may be

obtained from this model. The main purpose of this paper is the comparison of the temporal and spatial variations of the ionospheric plasma parameters calculated from the self-consistent model with the same parameters according to the empirical models J 71, MSIS, DTM and the determination of the reasons of the discrepancies.

RESULTS AND DISCUSSION

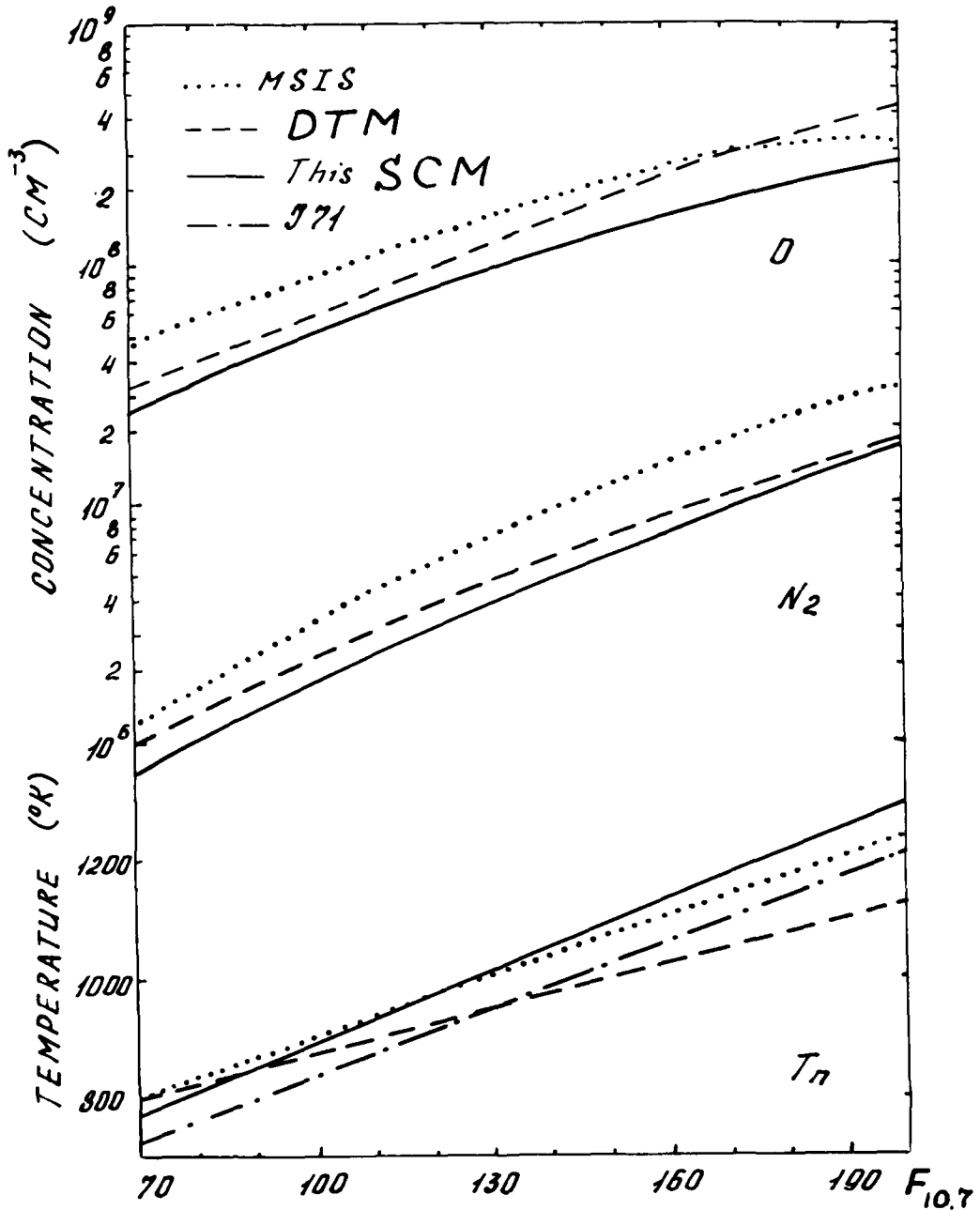


Fig. 1 Variations of the daily averaged neutral gas temperature, O and N₂ concentrations with solar activity at 400 km.

Fig.1 shows the variations of the daily averaged neutral gas temperature, the atomic oxygen and molecular nitrogen concentrations with solar activity at 400 km. The comparison between J 71, MSIS, DTM and self-consistent model (SCM) is presented for equinox conditions and $K_p = 2$. The comparison indicates that the neutral temperature is a linear function of the solar decimetric flux $F_{10.7}$. However, the rate of increase of the neutral temperature according to SCM is higher than these values according to J 71, MSIS and DTM. The best agreement between the models is obtained for mean solar decimetric fluxes ranging from approximately 100 to $130 \times 10^{-22} \text{ Wm}^{-2} \text{ Hz}^{-1}$. The largest discrepancies occur for high fluxes.

The molecular nitrogen and atomic oxygen concentrations deduced from the theoretical model are smaller than the concentrations determined from the empirical models. First of all, these differences are connected with the lower boundary conditions. The results of the O, O₂ and N₂ rocket measurements (9) were used for the determination of the lower boundary conditions in the self-consistent model. The O, O₂ and N₂ concentrations at the lower boundary in the DTM and MSIS models significantly differ from the concentrations measured by rockets (9). For example, the O concentration at 120 km in MSIS is higher by a factor of 2 than the results of the rocket measurements (9, 10) and the N₂ concentration at 120 km is higher by a factor of 1.3 than this value according to (9, 10).

Fig.2 compares the annual variation of the diurnally averaged neutral temperature, atomic oxygen and molecular nitrogen concentrations and total density at 400 km for 45° latitude, geomagnetic index $K_p = 2$ and solar decimetric flux $F_{10.7} = 150$. A good agreement of the neutral temperature calculated from SCM with the MSIS, DTM and J 71 neutral temperature is evident from Fig.2. However, the SCM model neutral temperature is about 10% above that of the J 71, MSIS and DTM models.

The theoretical total density is smaller than the empirical model total densities. The seasonal variation of the theoretical N₂ concentration agrees with this variation from the MSIS and DTM empirical models.

The theoretical neutral temperature diurnal variation is presented in Fig.3. This variation is compared with the MSIS model, the OGO-6 measurements (11) and incoherent scatter data (12, 13). The best agreement occurs for the comparison with the incoherent scatter measurements at St. Sartin in (13). The theoretical neutral temperature in summer is higher than the empirical temperatures at 16 - 24 hr due to a shift in the time of the temperature maximum. This shift may be caused by the one-dimensional description of the ionospheric plasma in the SCM model.

The theoretical T_n in November is smaller than the empirical T_n. In winter the shift of the diurnal variation maximum is smaller in comparison with this shift in summer. In total, the comparison between the models indicates that the theoretical self-consistent model describes the main features of the upper atmosphere as well as the empirical models.

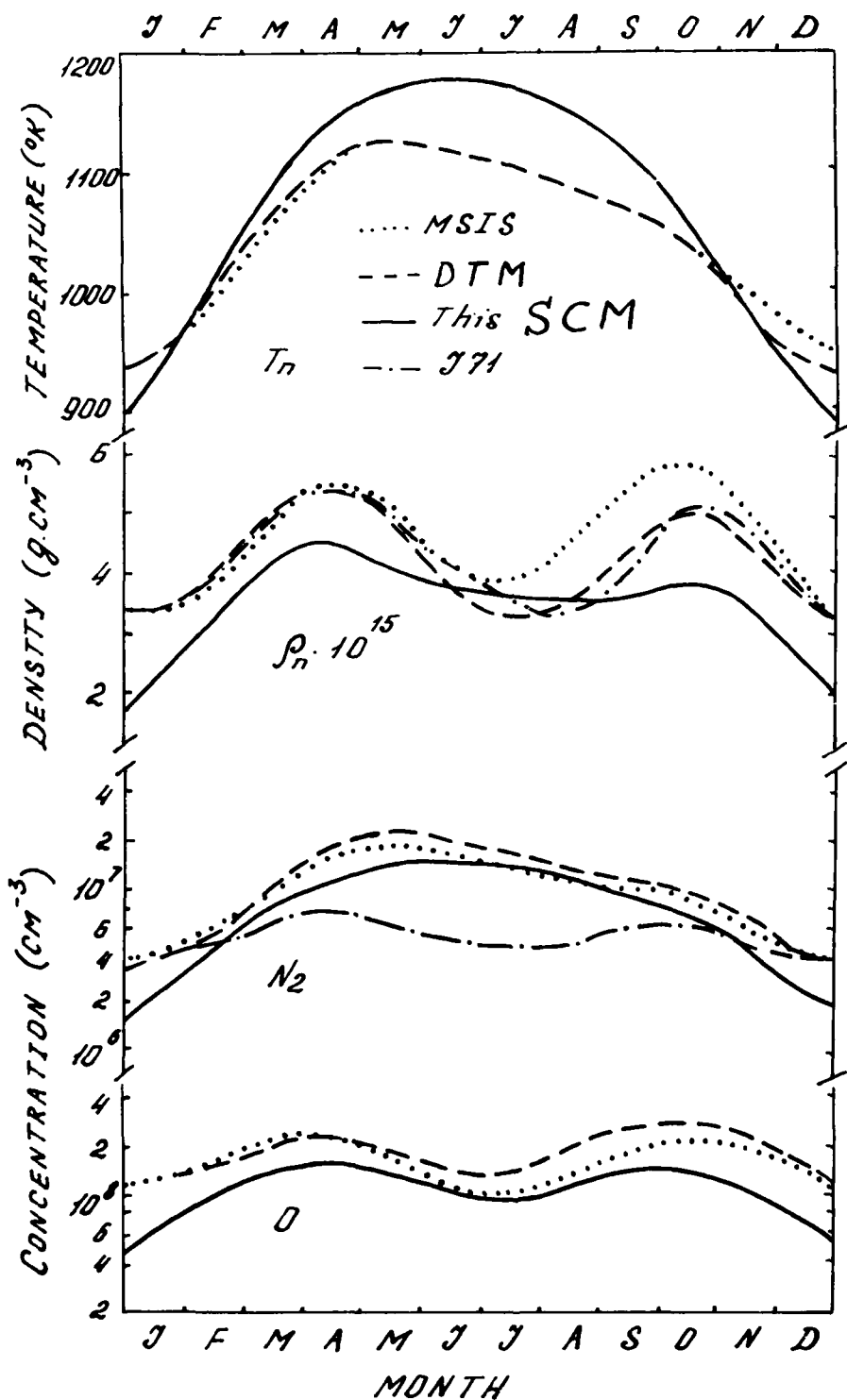


Fig. 2 Annual variation of the neutral temperature, total density, O and N_2 concentrations.

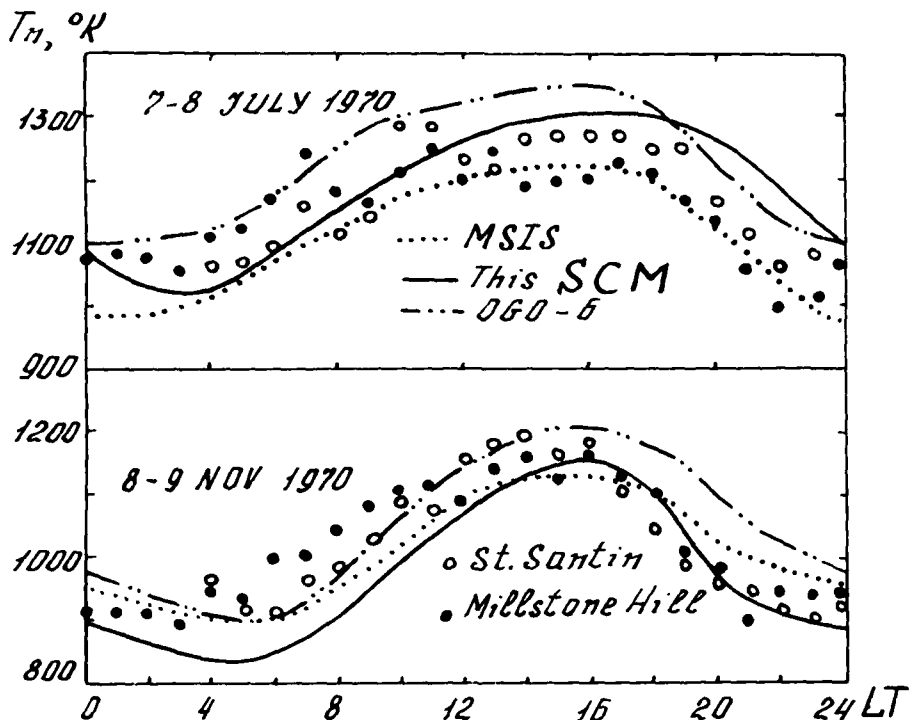


Fig.3 Diurnal variation of the neutral temperature.

The main feature of the self-consistent model is the description of the charge constituents behaviour simultaneously with the behaviour of the neutral constituents. This makes it possible to estimate the reliability of this model by comparison of the theoretical ionospheric parameters with the experimental data.

Fig.4 shows height profiles of the ion and electron temperatures for low solar activity ($F_{10.7} = 70$) according to (8) and values of these parameters measured by the incoherent scatter method (13). It is evident that good agreement occurs for summer and winter. Thus the electron and ion temperatures calculated from the SCM model are reliable for different but not all ionospheric conditions.

Comparisons between the plasma frequency variation deduced from the SCM model (8) and vertical incidence sounder data of ionospheric stations are presented in Fig.5. The comparison of the theoretical model with experimental data indicates that the self-consistent model reflects the main features of the ionospheric behaviour.

A system of hydrodynamic equations makes it possible to construct a theoretical model of the ionospheric plasma without including empirical parameters. In this model the simultaneous behaviour of the neutral and charged constituents is described. The comparison of the theoretical model with empirical models and experimental

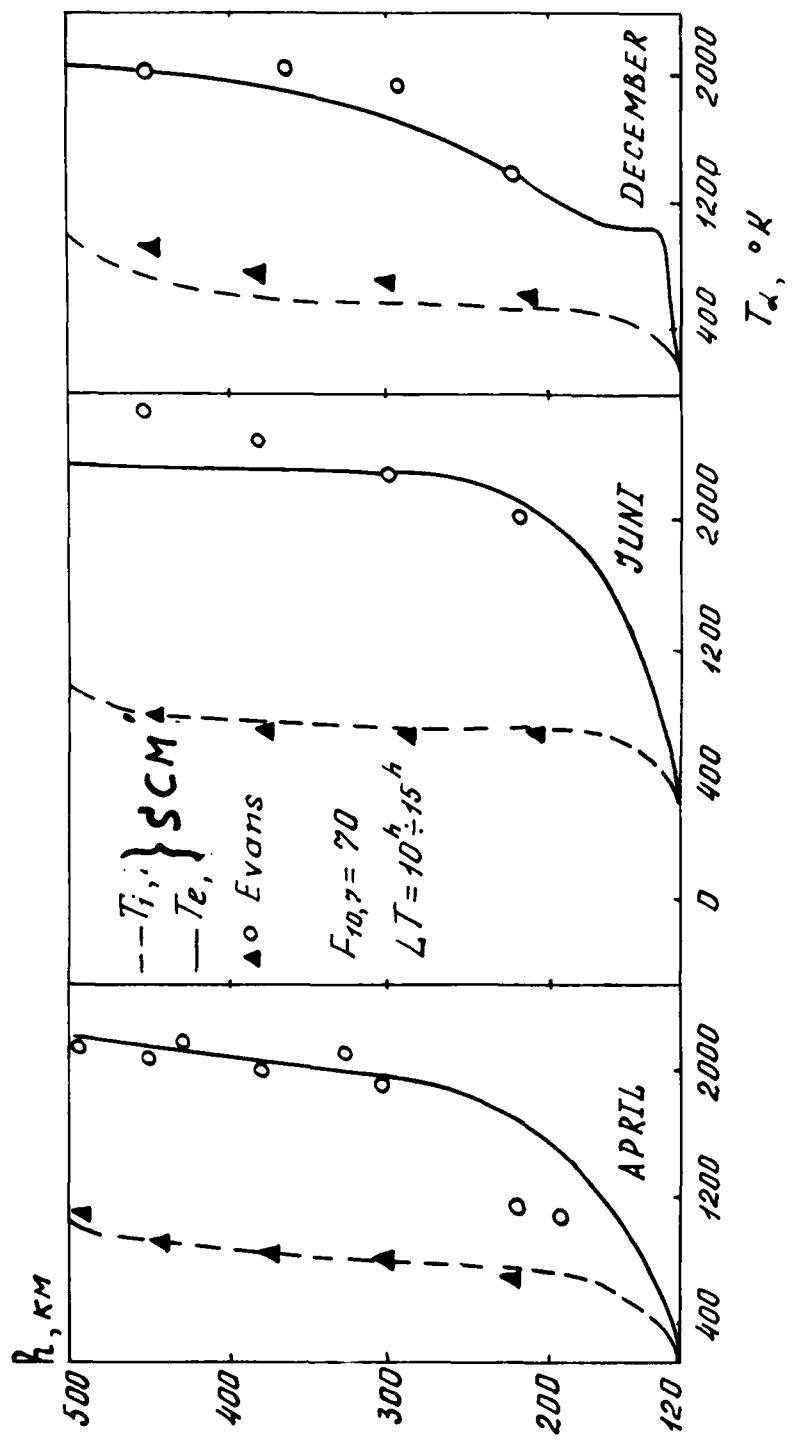


Fig.4 Height profiles of the ion and electron temperature for low solar activity ($F_{10,7} = 70$).

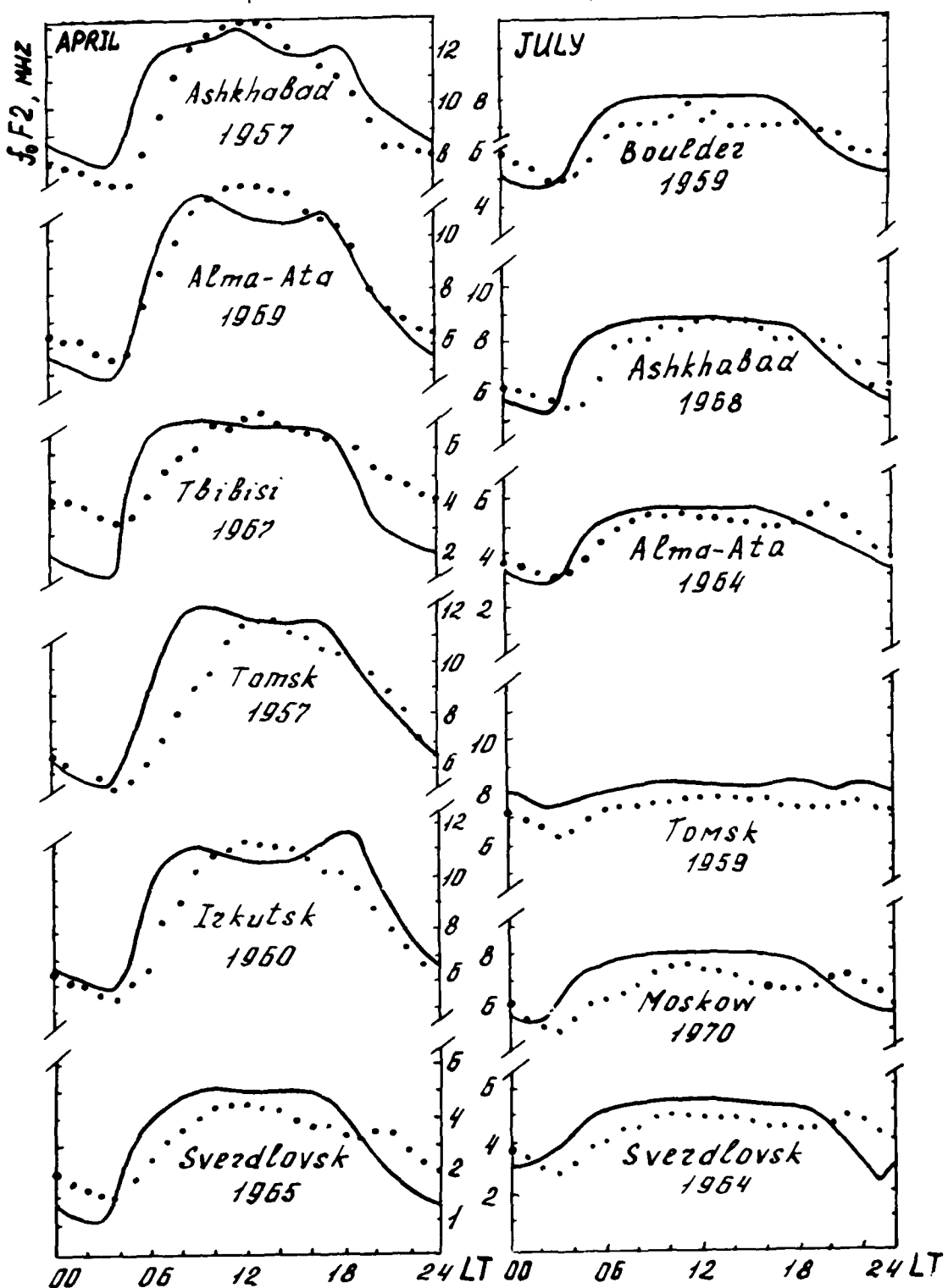


Fig. 5 Diurnal variations of the plasma frequency.

AD-A102 880 AIR FORCE GEOPHYSICS LAB HANSCOM AFB MA
THE MESOSPHERE AND THERMOSPHERE, (U)
1981 K S CHAMPION, G SCHMIOTKE
UNCLASSIFIED AFGL-TR-81-0210

F/G 4/1

NL

3rd 3
40-5640

END
DATE
9 81
DTIC

data shows good agreement. However, there are differences between the theoretical and empirical models and it is necessary to develop a three-dimensional theoretical model. This is very important from the point of view of the reliable description of the neutral temperature distribution.

References

1. L. G. Jacchia, in: CIRA 1972, Akademie-Verlag, Berlin, 1972, p. 277.
2. A. E. Hedin et al, J. Geophys. Res. 82, 2139 (1977).
3. F. Barlier et al, Ann. Geophys. 34, 9 (1978).
4. U. von Zahn, J. Geophys. Res. 75, 5517 (1970).
5. L. G. Jacchia, Paper presented at 21st Meeting of COSPAR, Innsbruck (1978).
6. F. Barlier et al, J. Atmos. Terr. Phys. 41, 527 (1979).
7. J. M. Strauss and D. R. Hickman, Paper presented at the Solar-Terrestrial Predictions Workshop, Boulder (1979).
8. M. N. Vlasov and A. G. Kolesnik, Solar-Terrestrial Proceedings, vol. IV, U. S. Department of Commerce, Boulder, 205 (1979).
9. A. G. Kolesnik, Geomagnetism and Aeronomie 15, No. 2 (1975).
10. D. Offerman, J. Geophys. Res. 79, 4281 (1974).
11. A. E. Hedin et al, J. Geophys. Res. 79, 215 (1974).
12. J. E. Salah and J. V. Evans, Ann. Geophys. 32, 257 (1976).
13. J. V. Evans, Planet. Space Sci. 18, 1225 (1970).
14. R. W. Schunk and D. S. Watkins, Planet. Space Sci. 27, 433 (1979).

SECTION 3
Mesosphere—Thermosphere

SOME RECENT ADVANCES IN THERMOSPHERIC MODELS

G. Kockarts

*Institut d'Aéronomie Spatiale, 3 Avenue Circulaire,
B -1180 Bruxelles, Belgium*

ABSTRACT

Since the publication of the last COSPAR International Reference Atmosphere (CIRA 1972) valuable progress has been achieved in improving our understanding of the terrestrial thermosphere. As a result, several empirical models are now available for numerous applications. The reliability of these models is discussed within the framework of known physical phenomena. The most recent published advances deal with longitudinal and universal time effects. Some general shortcomings are pointed out in order to stimulate farther progress.

INTRODUCTION

Over a period of three years (1977-1979) five semi-empirical models of the terrestrial upper atmosphere were published in such a way that any potential user could easily compute total densities and temperatures without making use of the COSPAR International Reference Atmosphere [1]. Such a quantitative progress, which also involves a better representation of physical phenomena, implies the necessity for a revision of CIRA 1972. These new semi-empirical models, however, do not necessarily agree with each other for all existing geophysical conditions. This fact will not facilitate the construction and the adoption of a new CIRA, since all available models claim to reproduce observed quantities. The five recent semi-empirical models are designated by the following acronyms : MSIS [2,3], ESR04 [4], J77 [5], DTM [6] and AEROS [7]. Except for J77, all models are based on spherical harmonic expansions introduced by Hedin et al. [8] in thermospheric modelling.

A systematic comparison between the most recent semi-empirical models will not be undertaken, since such an analysis has been presented by Barlier et al. [9] for MSIS, ESR04, J77 and DTM and by Jacchia [10]. The thermospheric part of CIRA 1972, which was developed by Jacchia [11] has been compared to DTM and MSIS by Barlier et al. [6]. Nevertheless, some specific discrepancies between the recent models, not shown previously, are pointed out here and a comparison is made for a permanently minor constituent, i.e. atomic nitrogen which is given by Engebretson et al. [12] and by Köhnlein et al. [7]. Finally, the most recent developments dealing with longitudinal effects introduced in MSIS by Hedin et al. [13] and in ESR04 by Laux and von Zahn [14] are briefly compared.

COMPARISONS BETWEEN MODELS

A perfect model should be able to represent all physical conditions in the past, in the present and in the future. All semi-empirical models are, however, based on a limited set of data. Fig. 1 shows the monthly mean of the 10.7 cm solar flux used as an index under different forms in the models. The period shown covers two solar cycles and it appears immediately that the solar maximum in 1958 was much more intense than the last maximum in 1969. Horizontal lines in Fig. 1 indicate the periods during which different satellites gathered data used in various models. Only drag data leading to total densities are available since the

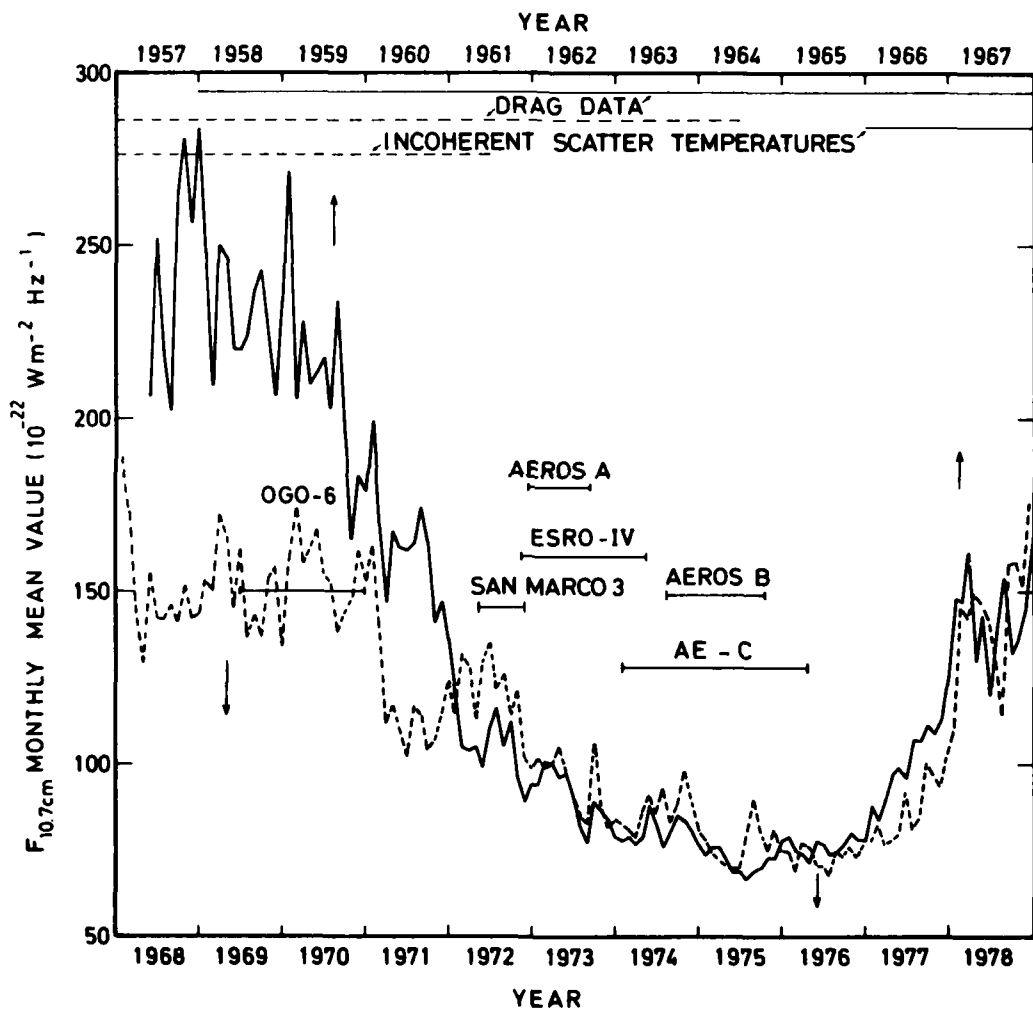


Fig. 1 Monthly mean of the solar decimetric flux as a function of time between 1957 and 1978. Horizontal lines indicate the periods covered by in situ satellite measurements (lower scale) as well as the period during which drag data and incoherent scatter data (upper and lower scale) were used for modeling purposes.

beginning of space age. This type of data is essentially used in two models, i.e. J77 and DTM. All other models are based on much more limited observational periods. This implies that when a spherical harmonic analysis is made, such models lead to extrapolated results when they are applied for geophysical conditions never encountered during the observational periods. It is, therefore, not surprising that a comparison between various models may lead to extreme differences of a factor of two, even in the total densities [9]. Furthermore, even the models J77 and DTM, with the largest data base, covering almost two solar cycles, have difficulties in representing appropriately short term phenomena. All models show different amplitudes in the diurnal variations of the individual components and the phases agree only above 200 km altitude. Incoherent scatter data provided considerable help in improving this situation [15], particularly with respect to the diurnal temperature maximum.

Since the AEROS model [7] was not available at the time when a systematic comparison between various models was made by Barlier et al. [9], Fig. 2 shows the annual variation of atomic oxygen concentrations at the geographic poles and at the equator obtained for AEROS, J77 and DTM. Results are given at 300 km

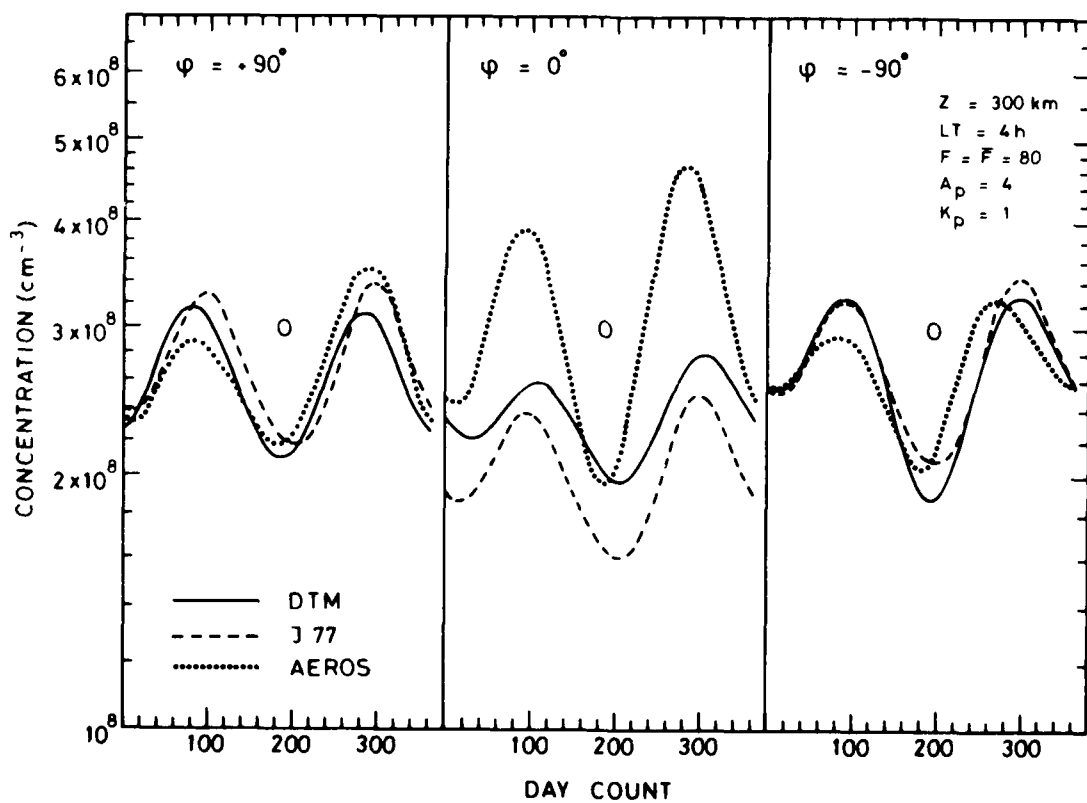


Fig. 2 Annual variation of atomic oxygen at 300 km computed at 4 hours LT with DTM, J77 and AEROS. Three latitudes are represented, i.e. north and south poles and equator. The daily solar decimetric flux F and the mean flux \bar{F} correspond to the average conditions covered by AEROS. Geomagnetic indices are $A_p = 4$ or $K_p = 1$.

altitude for a daily and mean solar decimetric flux $F = \bar{F} = 80 \times 10^{-22} \text{ Wm}^{-2} \text{ Hz}^{-1}$ which corresponds to average solar flux conditions during the mass spectrometric measurements used in the construction of AEROS. Quiet geomagnetic conditions ($K_p = 1$ or $A_p = 4$) are adopted and the computations are made for 4 hours local solar time since AEROS data were essentially obtained at 4 hours and 16 hours LT. For this reason, only a cosine term is used in the AEROS model [7] to represent the diurnal variation and this model is probably not appropriate to correctly model the diurnal variation. Köhnlein et al. [7] conclude that the AEROS model is in satisfactory agreement with MSIS and ESRO4. Although such a conclusion is also valid for J77 and DTM, it appears, however, in Fig. 2 that significant differences are present in the annual variation of atomic oxygen at the equator. Since atomic oxygen is a major constituent at 300 km altitude, Fig. 2 indicates that for equinox conditions AEROS leads to an equatorial total density which is almost a factor of two higher than in J77 or in DTM. Such a discrepancy cannot be attributed to a systematic difference between drag data and mass spectrometric measurements.

Since the amplitude of the winter helium bulge is not yet well known [9, 16], Fig. 3 shows the annual variation of helium concentrations at 300 km altitude for the same geophysical conditions as in Fig. 2. The amplitude of the bulge is similar in AEROS and in J77, but it is smaller in DTM where only drag data were used.

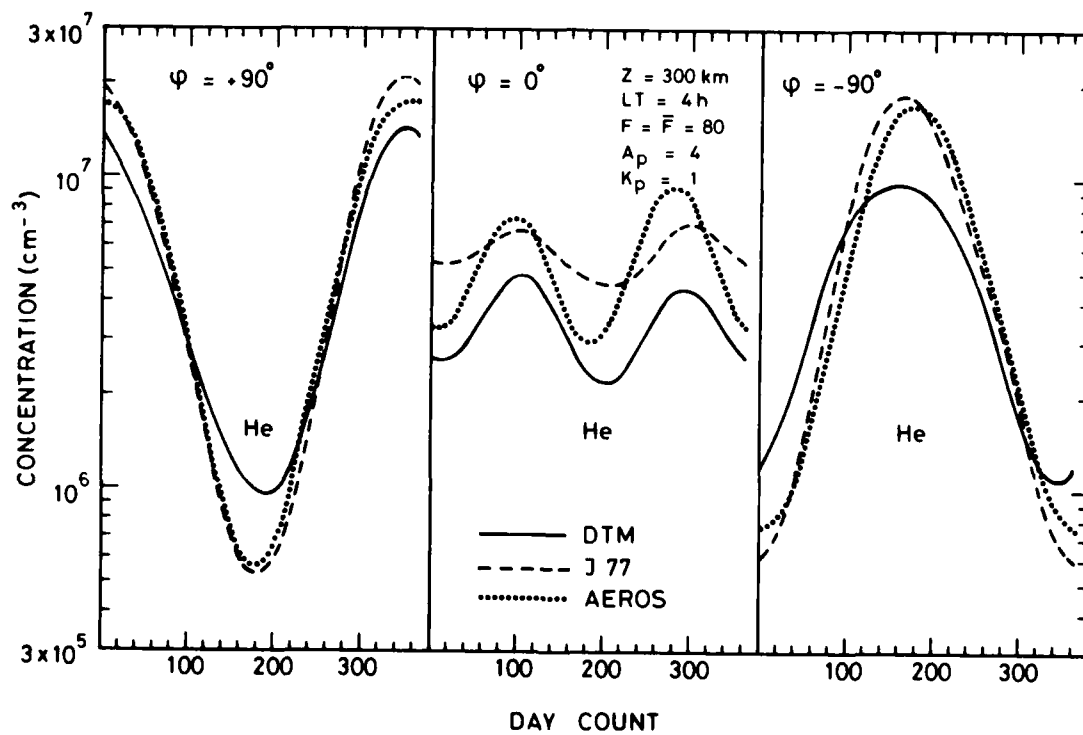


Fig. 3 Annual variation of helium at 300 km for the same geophysical conditions as in Fig. 2.

This remains an open question, although Anderson et al. [17] have shown in an analysis of He 58.4 nm dayglow emissions that both DTM and MSIS in general predict higher helium concentrations than the airglow-determined values. At the equator, the equinoctial maxima for helium are again larger in AEROS than in DTM or in J77, i.e. a situation similar to the atomic oxygen variation shown in Fig. 2. Examples shown in Figs. 2 and 3 indicate that significant differences still exist between the most recent semi-empirical models. When loose expressions like "satisfactory, reasonable or global agreement" are used in model comparisons, great care must be taken in specific applications of semi-empirical models. Even when a model agrees perfectly with a particular observation, it does not imply that the whole model is perfect for other conditions. This is a consequence of the fact that the mathematical formalisms presently used are not necessarily appropriate to represent all physical phenomena in the terrestrial thermosphere. It is even surprising that the use of two indices (solar decimetric flux and geomagnetic index) is sufficient to represent the atmospheric structure with a "reasonable" accuracy. Standard deviations given for a specific model usually represent an internal test for the consistency between the mathematical representation and the limited set of data used for the construction of the model. However, such deviations give no indication of the ability to represent external data not involved in the construction of the model.

EXTERNAL TESTS

Any comparisons between model results and observations not involved in the construction of the model is always a valuable test for the reliability of the model. When such an exercise is made for the diurnal variation of atomic oxygen as deduced by Alcayd^e and Bauer [18] from incoherent scatter data, it appears [9] that the amplitude of the diurnal variation is often larger in incoherent scatter data than in any model. This is particularly true for spring conditions at 45°N when the diurnal amplitude in the incoherent scatter data is of the order of a factor of three at 400 km altitude, whereas the largest amplitude in three dimensional empirical models is given by DTM and reaches only a factor of two. Nevertheless, all semi-empirical models are able to reproduce diurnal maxima occurring at different local times for different species. Amplitudes and phases of these maxima should probably be modified if new observational data become available, particularly below 200 km altitude.

Except for J77, all semi-empirical models are characterized by variable lower boundary conditions at 120 km altitude. The J77 model [5] starts at 90 km with constant boundary conditions, but empirical corrections are introduced between 90 km and 120 km to simulate departures from diffusive equilibrium. As a consequence, the concentrations in J77 are also variable at 120 km altitude. Spherical harmonics given at this height in the other semi-empirical models are, however, obtained from data gathered at greater altitudes and model values at 120 km may not necessarily represent real physical conditions, particularly for atomic oxygen which is influenced by photochemical reactions and by transport processes. Recently, Dickinson et al. [19] made a detailed analysis of several rocket flights during which atomic oxygen was measured between 60 km and 140 km using an optical resonance technique at 130 nm. Table I gives the measured atomic oxygen concentrations at 120 km for six rocket flights at South Uist (57.4°N, 7.4°W). Data are arranged in seasonal sequence.

TABLE I : Atomic Oxygen in (10^{11} cm^{-3}) at 120 km Altitude.

Date	7 Feb 77	11 Feb 77	1 Apr 74	8 Sep 75	29 Nov 74	28 Nov 75
Time (UT)	2309	1359	2237	2355	1153	1256
Dickinson et al. [19]	2.0	2.12	1.67	1.04	0.88	1.26
DTM	0.52	0.66	0.45	0.58	0.81	0.83
J77	0.64	0.72	0.53	0.78	0.84	1.06
MSIS	0.83	0.77	0.73	0.77	0.92	0.87
ESRO4	0.58	0.77	0.41	0.59	0.90	0.93
AEROS	0.68	0.79	0.53	0.72	1.12	1.15

Values obtained from the five semi-empirical models are also indicated and large discrepancies appear between all model values and the measurements. If such a comparison had been made only for the daytime flight on 29 November 1974, we could have stated that a "satisfactory agreement" exists between all models and the measurements. This is actually not the case and our semi-empirical representation of the lower thermosphere is far from being complete.

Since the measurements of Dickinson et al. [19] extend up to 140 km in some cases, Fig. 4 shows relative atomic oxygen concentrations obtained from measurements and from models. For the daytime flight on 11 Feb 1977 all models decrease faster than the observed values, whereas for the nighttime flight on 7 Feb 1977, only J77 is a little outside of the error bar. Dickinson et al. [19] made a similar analysis using CIRA 1972 [1] and concluded that in all cases the discrepancy between model values and the measurements is a consequence of transport phenomena. Above 120 km altitude MSIS is the only model which involves a correction to the usual assumption of diffusive equilibrium. Such a correction never exceeds 13% in Fig. 4 and it is insufficient to bring the daytime MSIS values (almost identical to DTM values) in agreement with the measurements. Model temperatures at 120 km and 150 km are also given in Fig. 4. At 150 km altitudes all models give almost identical temperatures but at 120 km altitude the J77 temperature is always 40 K to 50 K lower than in DTM or MSIS. Furthermore, the discrepancy between measurements and models is always larger for J77. It is therefore possible that the discrepancies shown in Fig. 4 are not due to transport but are an indication that the model temperatures are too low at 120 km altitude. Incoherent scatter temperatures at 120 km above Saint-Saintin are actually of the order of 408 K [20] with an amplitude of 15 K for the annual variation and a small negative dependence on solar decimetric flux.

MINOR CONSTITUENTS

Thermospheric minor constituents can be divided in two categories : those which are permanently minor at all heights and those which can become major constituents over certain height ranges as a consequence of diffusive separation in the gravitational field. The first category including argon, carbon dioxide, atomic nitrogen, nitric oxide never influence satellite drag data and they cannot be deduced from such data. The second category deals mainly with atomic oxygen, helium and atomic hydrogen which become successively the major thermospheric component as height increases. Permanently minor constituents are only accessible through selective measuring techniques, such as optical detection or mass spectrometric sampling. A good knowledge of any minor constituent is, however, of paramount importance since fundamental information can be gathered from trace constituents. As an example, mass spectrometric measurements of argon and/or helium

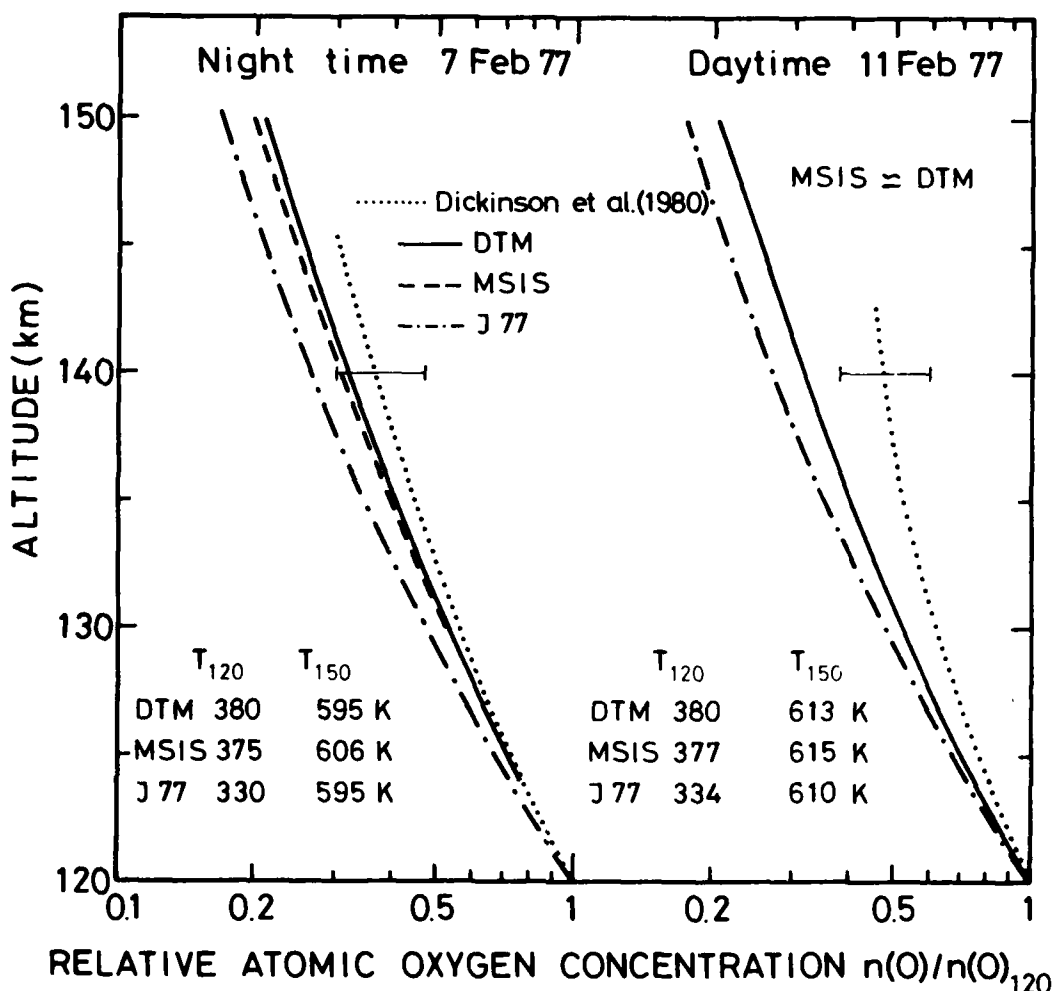


Fig. 4 Vertical distribution of relative atomic oxygen concentrations. Comparison between measured values by Dickinson et al. [19] and model values from DTM [6], MSIS [2,3] and J77 [5].

provide an excellent tool to investigate the transition from turbulent mixing to diffusive separation in the 100 km altitude region [21], although other techniques such as sodium clouds ejections [22] and rocket grenade data [23] also contribute significantly to the knowledge of this transition region. Unfortunately, no global coverage is yet available since direct in situ measurements can only be performed by rockets in this height range. Remote sensing from a satellite is probably the only way to solve this question if an appropriate optical technique is developed.

Among the permanently minor constituents, atomic nitrogen is the sole component given by two global models [7, 12]. The first model by Engebretson et al. [12] is based on a spherical harmonic expansion at 375 km altitude using mass spectrometer data from Atmosphere Explorer C during 1974 and part of 1975. Since atomic nitrogen is involved in numerous chemical reactions [24], its vertical distributions is not necessarily in diffusive equilibrium. It has been shown experimen-

tally [25], however, that atomic nitrogen is in diffusive equilibrium at least above 200 km altitude. Using the Atmosphere Explorer C model at 375 km, it is, therefore, possible to compute atomic nitrogen concentrations at any height above 200 km altitude by adopting a vertical temperature profile. The second atomic nitrogen model is included in AEROS, where the spherical harmonic expansion refers to 120 km altitude for reasons of uniformity with the other constituents. This does not mean that the model can be used at altitudes below 120 km [7]. Figs. 5 and 6 show the annual latitudinal variations of atomic nitrogen at 375 km as given by AEROS [7] and Atmosphere Explorer C [12] for 4 hours and 16 hours local solar times, respectively. These local times have been chosen since they correspond to the local times for which AEROS is the most reliable. Figs. 5 and 6 indicate that the general pattern of the annual variation is similar in both models. However, at 16 hours LT (Fig. 6) the concentrations given by the Atmosphere Explorer C model are approximately a factor of two higher than the values given by AEROS. Even with such differences atomic nitrogen models should be used as upper boundary conditions in a three-dimensional computation of odd nitrogen distributions below 200 km altitude. This could be of some importance for the energy budget of the thermosphere, since it has been shown [26] that nitric oxide is a major cooling agent below 200 km. There is actually a need for the introduction of permanently minor constituents in semi-empirical models in order to improve our knowledge all the physical mechanisms which influence the thermospheric structure.

LONGITUDINAL EFFECTS

The spherical harmonic expansion used in semi-empirical models depends on two angular variables, i.e. geographic latitude and local solar time. The last variable is a consequence of the assumed equivalence between longitude and local time. This implies that the diurnal variation should be exactly identical at any point of a latitudinal circle. However, the geomagnetic effect in J77 is expressed in terms of magnetic latitude and, as a consequence, a longitudinal effect is introduced, since the temperature increase associated with the K_p index is not symmetric with respect to the geographic north-south axis. It is, therefore, necessary to specify, in J77, the geographic longitude when comparisons are made with other models. In Figs. 2 and 3 the longitude is 0° for J77, whereas Fig. 4 is constructed for the longitude of South Uist (7.4° W). Thuillier et al. [27] have also introduced the geomagnetic latitude in their temperature model in order to obtain a better representation of the geomagnetic effect at high latitudes.

Hedin et al. [13] have reanalyzed the data used in the construction of MSIS. Spherical harmonic terms dependent on geographic latitude, longitude and universal time (UT) have been added to the previous expansion [2,3] which has not been modified. In such a way, a combined longitudinal/UT effect is introduced for the neutral temperature and composition. Longitudinal terms indicate a temperature enhancement of the order of 30 K near the magnetic poles. The universal time variation leads to an enhancement of the order of 30 K near 2130 UT in the northern hemisphere and nearly 70K around 0930 UT in the southern hemisphere. The combined longitude/UT effects lead to a rather complex pattern. As an example, Figs. 7 and 8 show the geographic distribution of ratios of the total density at 500 km between the modified model [13] and the initial model 2,3 for 3, -2, 15b and 21h UT respectively. Computations are made for $F = \bar{F} = 150 \times 10^{-22}$ Wm $^{-2}$ Hz $^{-1}$ and $A = 4$ under equinox conditions. The position of the sun is indicated on the equator by a small circle. It is clear that the universal time evolution of the longitudinal effect is a complex phenomenon which certainly needs further studies.

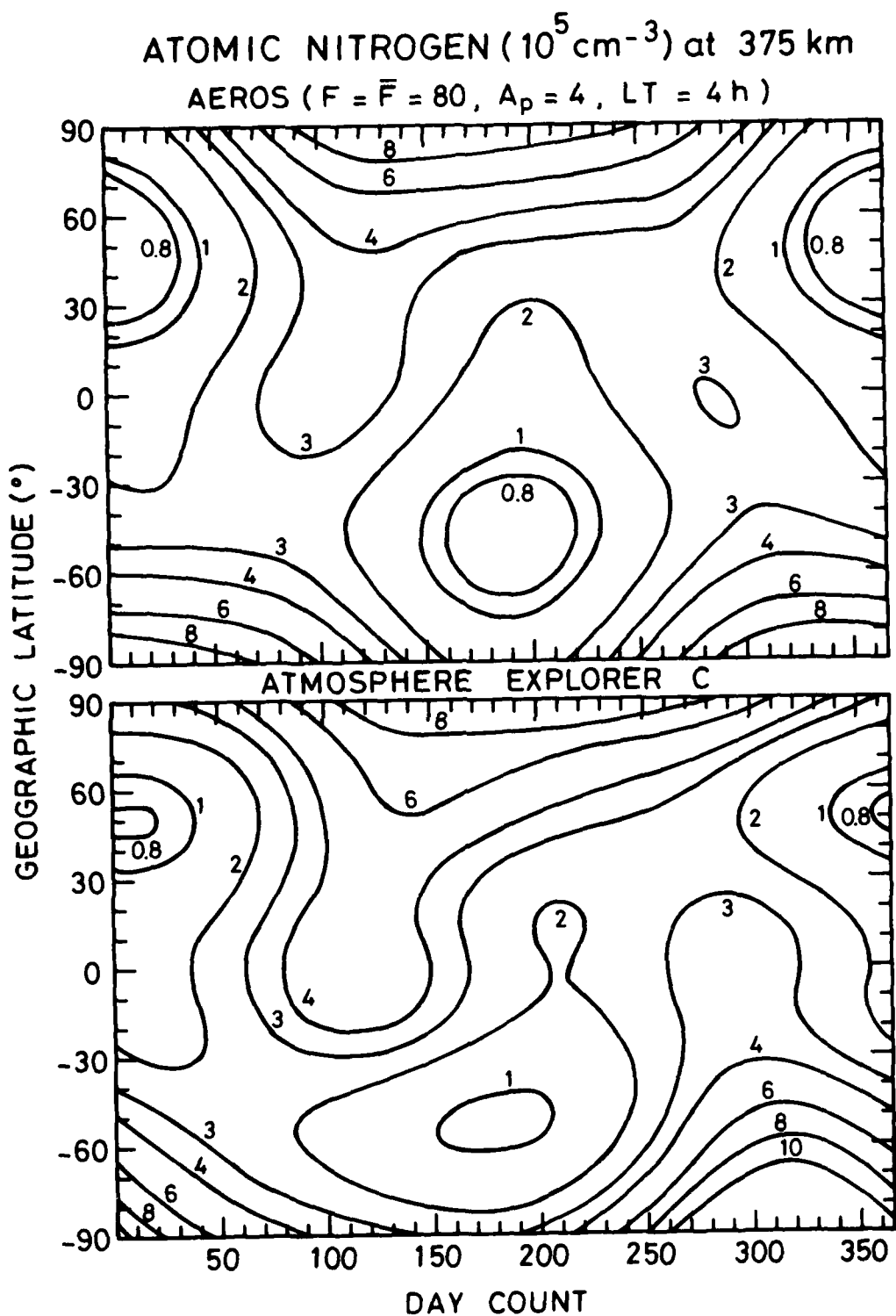


Fig. 5 Annual variation of atomic nitrogen at 375 km obtained at 4 hours LT for $F = \bar{F} = 80 \times 10^{-22} \text{ Wm}^{-2} \text{ Hz}^{-1}$ and $A_p = 4$. Isopleths are in units of 10^5 cm^{-3} .

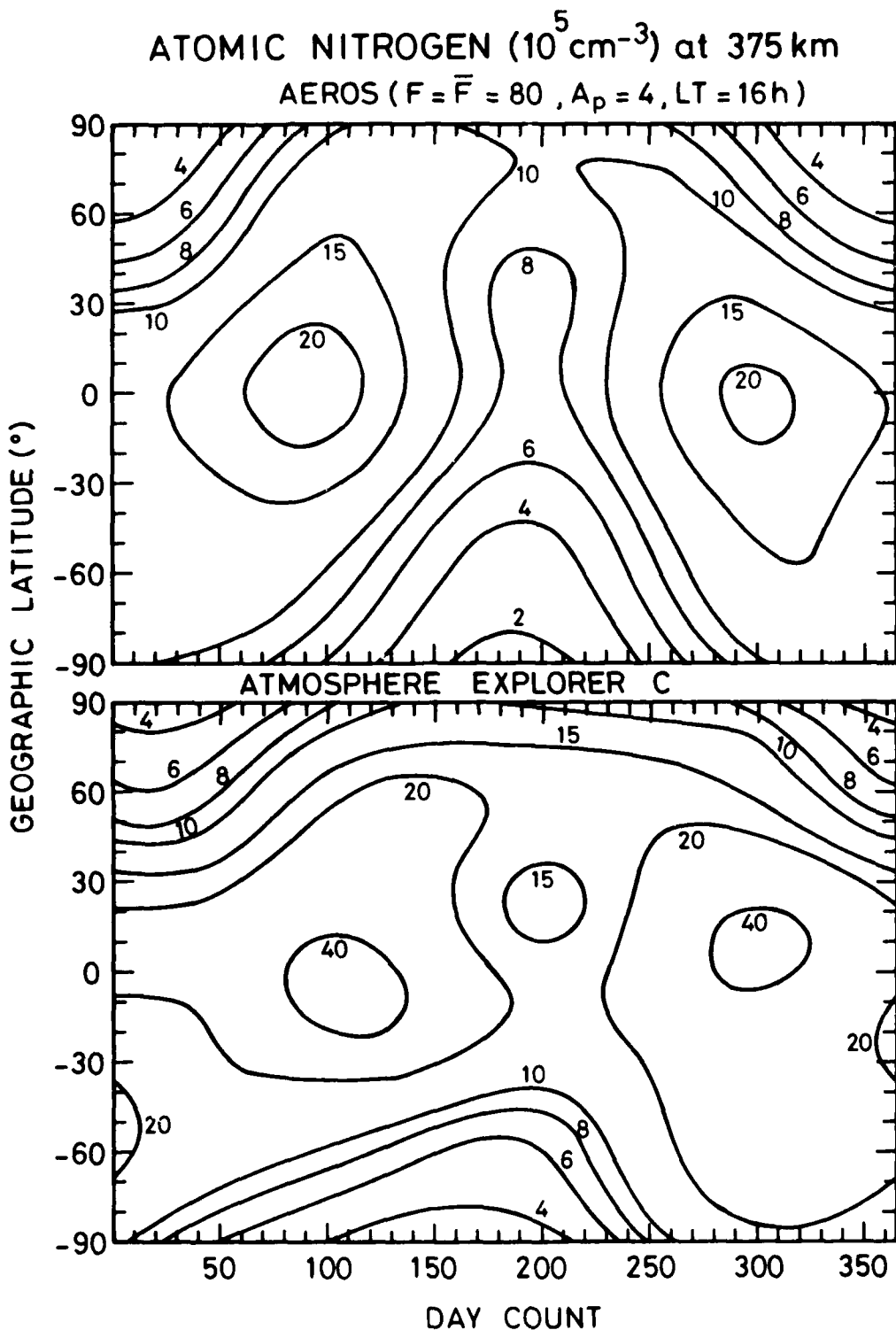


Fig. 6 Annual variation of atomic nitrogen at 16 hours LT for the same conditions as in Fig. 5.

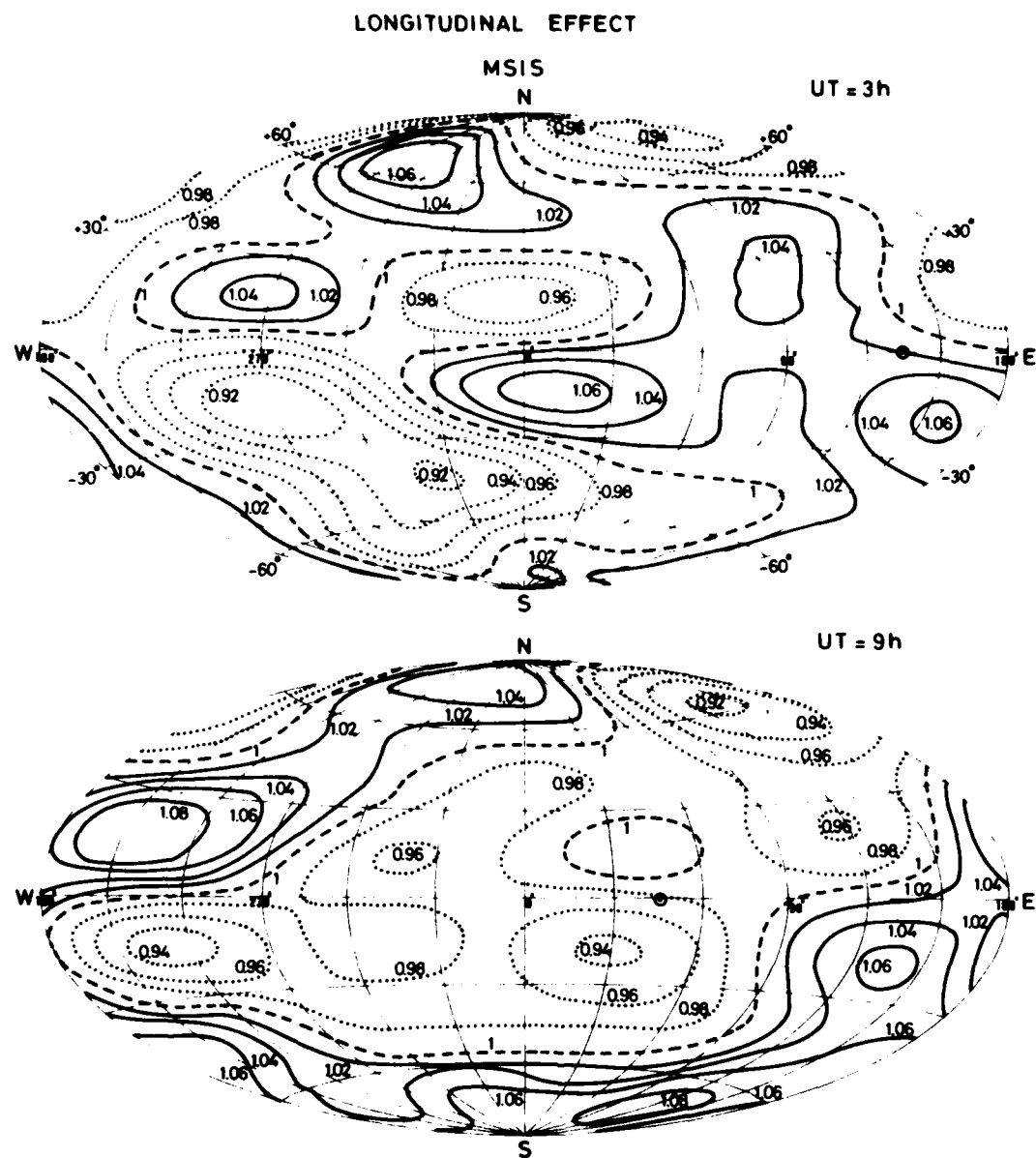


Fig. 7 Geographic distribution of the ratio between total densities at 500 km computed at equinox with and without longitudinal/UT effects in MSIS. Dotted isopleths correspond to ratios less than one and full isopleths to ratios greater than one. $F = F' = 150 \times 10^{-22} \text{ Wm}^{-2} \text{ Hz}^{-1}$ and $A_p = 4$. Upper part for 3 hours UT and lower part for 9 hours UT.

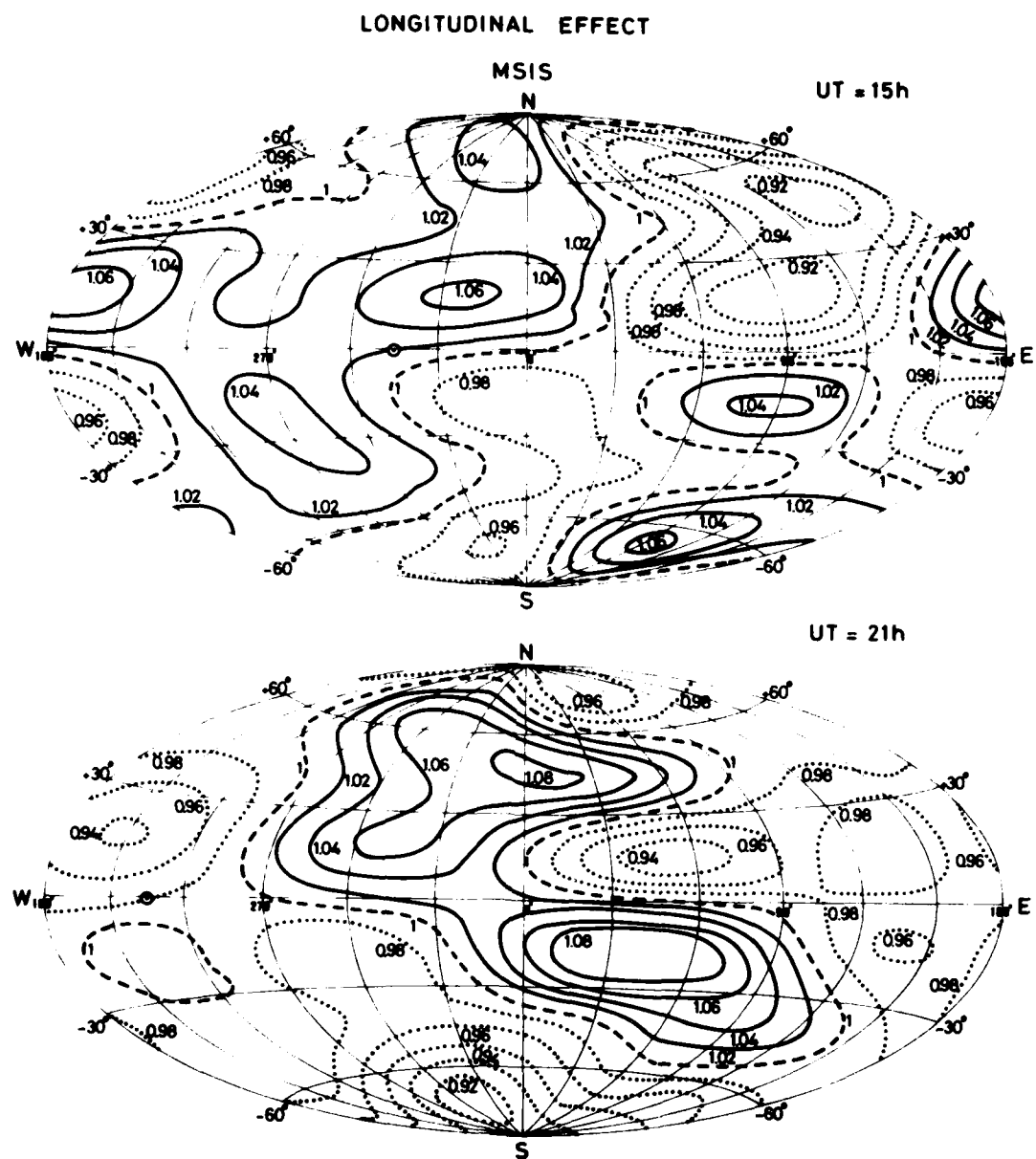


Fig. 8 Geographic distribution of longitudinal/UT effects for 15 hours and 21 hours UT. Same conditions as in Fig. 7.

A simpler approach has been undertaken by Laux and von Zahn [14] who introduced an empirical function for each atmospheric constituent of the ESRO 4 model [4]. These correction functions only depend on the geographic latitude and longitude. Possible universal time effects are, therefore, ignored and the temperature is not modified. Fig. 9 gives the longitudinal effect at 500 km on the total density in ESRO4 for the same solar and geomagnetic activities as in Figs 7 and 8. It should

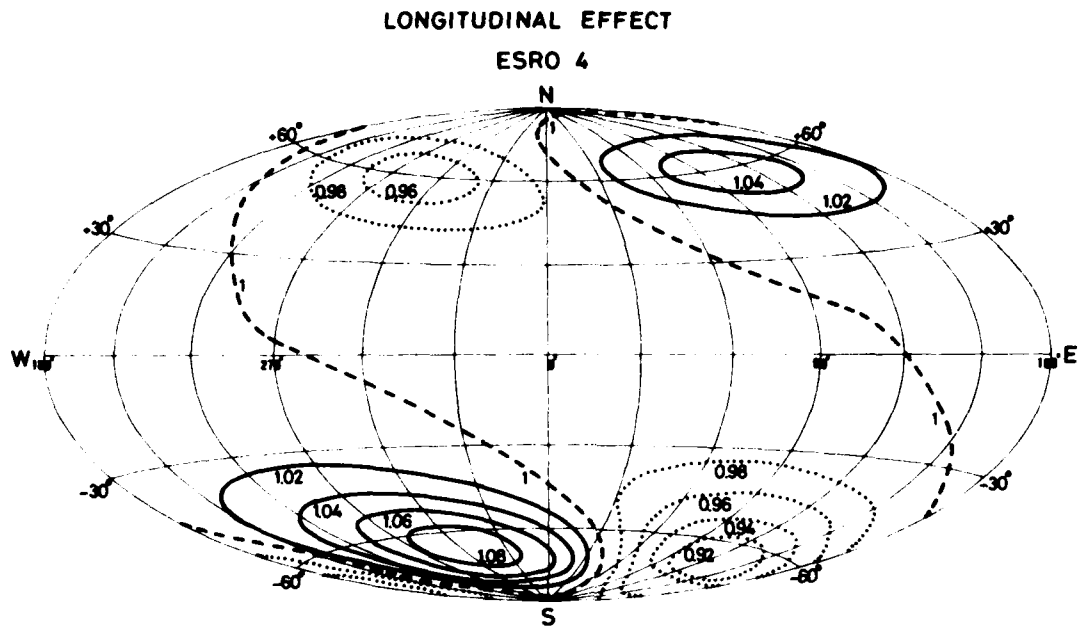


Fig. 9 Geographic distribution of longitudinal effects on the total density at 500 km in ESRO 4. $F = \bar{F} = 150 \text{ Wm}^{-2} \text{ Hz}^{-1}$, $A_p = 4$. Compare with Figs. 7 and 8.

be noted that the coefficient, C_7 for N_2 , should be read 2.118×10^2 instead of 2.118 in Table I given by Laux and von Zahn [14]. Furthermore, the so-called "covariant latitude" is actually the colatitude which varies from 0° at the North pole to 180° at the South pole. The longitudinal effect for ESRO4 (Fig. 9) is completely different from the results given by MSIS (Figs 7 and 8). This is clearly shown in Fig. 10 where the total density ratio at 500 km is given as a function of longitude at $\pm 65^\circ$ latitude for ESRO4 and for several universal times in MSIS. The maximum amplitude is of the order of $\pm 10\%$ in both models but the phases never agree. ESRO4 can predict a density increase when MSIS leads to a Fig. 10 Total density density decrease. It is difficult to reconcile these two pictures unless the differences are entirely attributed to universal time effects not included in ESRO4. Although longitudinal variations are correlated to the configuration of the geomagnetic field, it appears that a consistent global representation is not yet entirely available. One should, however, realize that longitudinal/UT variations imply modifications of the order of a few percent, whereas it has been shown that differences of the order of a factor of two can still exist between total densities deduced from various models.

The various topics discussed in the present paper should not give the impression

of a poor knowledge of the thermospheric structure. In 1975, Jacchia 28 wrote : "the variations in the uppermost parts of the terrestrial atmosphere can be much better accounted for than can the weather in the atmospheric region in which we live !". Such a statement essentially refers to the total density and the recent semi-empirical models significantly contribute to the way this total

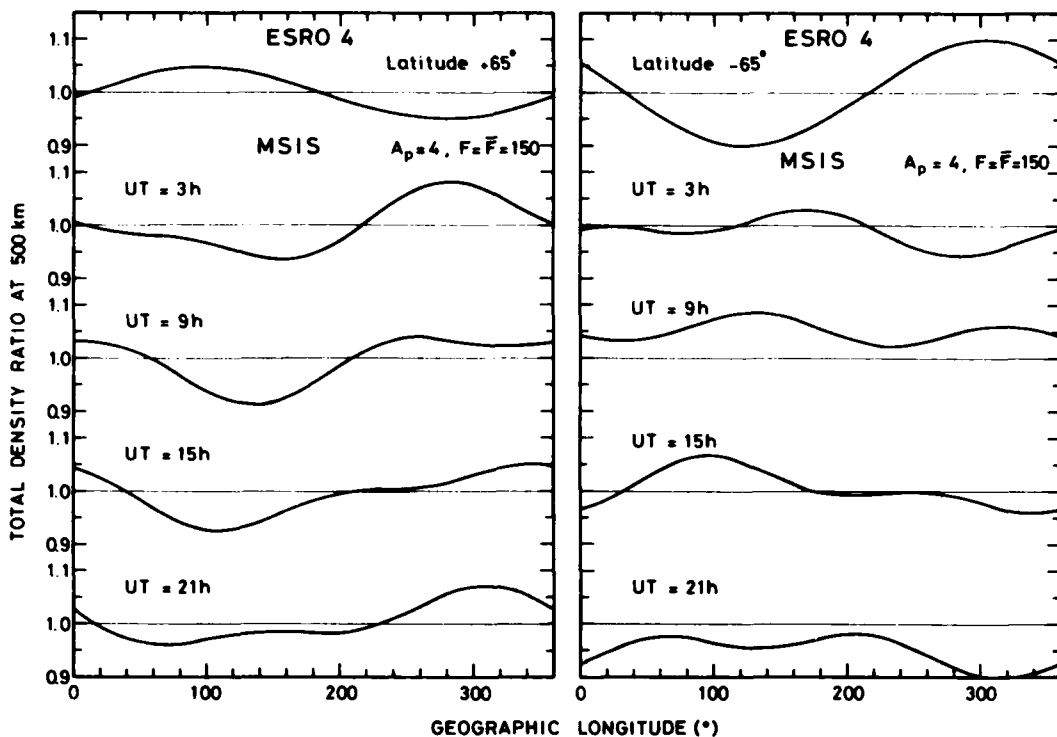


Fig. 10 Total density ratio at 500 km between models with and without longitudinal/UT effects at $\pm 65^\circ$ geographic latitude. MSIS ratios are given for the same universal times as in Figs. 7 and 8.

density is built up. Important discrepancies still exist and it would be unwise to declare that experimental and theoretical research in the terrestrial upper atmosphere has reached a stage of development in which no fundamental discovery can be made.

References

1. CIRA 1972, Cospar International Reference Atmosphere, Akademie Verlag, Berlin, 1972.
2. A.E. Hedin, J.E. Salah, J.V. Evans, C.A. Reber, G.P. Newton, N.W. Spencer, D.E. Kayser, D. Alcaydé, P. Bauer, L. Cogger and J.P. McClure, J. Geophys. Res. 82, 2139 (1977).
3. A.E. Hedin, C.A. Reber, G.P. Newton, N.W. Spencer, H.C. Brinton and H.G. Mayr, J. Geophys. Res. 82, 2148 (1977).

4. U. von Zahn, W. Kohnlein, K.H. Fricke, U. Laux, H. Trinks and H. Volland, Geophys. Res. Lett. 4, 33 (1977).
5. L.G. Jacchia, Smithson. Astrophys. Obs. Spec. Rep. 375 (1977).
6. F. Barlier, C. Berger, J.L. Falin, G. Kockarts and G. Thuillier, Annls Géophys. 34, 9 (1978).
7. W. Kohnlein, D. Krankowsky, P. Lämmerzahl, W. Joos and H. Volland, J. Geophys. Res. 84, 4355 (1979).
8. A.E. Hedin, H.G. Mayr, C.A. Reber, N.W. Spencer and G.R. Carignan, J. Geophys. Res. 79, 215 (1974).
9. F. Barlier, C. Berger, J.L. Falin, G. Kockarts and G. Thuillier, J. Atmos. Terr. Phys. 41, 527 (1979).
10. L.G. Jacchia, Space Research XIX, 179 (1979).
11. L.G. Jacchia, Smithson. Astrophys. Obs. Spec. Rep. 332 (1971).
12. M.J. Engebretson, K. Mauersberger, D.C. Kayser, W.E. Potter and A.O. Nier, J. Geophys. Res. 82, 461 (1977).
13. A.E. Hedin, C.A. Reber, N.W. Spencer, H.C. Brinton and D.C. Kayser, J. Geophys. Res. 84, 1 (1979).
14. U. Laux and U. von Zahn, J. Geophys. Res. 84, 1942 (1979).
15. D. Alcaydé, Space Research XIX, 211 (1979).
16. H. Trinks, U. von Zahn, C.A. Reber, A.E. Hedin, N.W. Spencer, D. Krankowsky, P. Lämmerzahl, D.C. Kayser and A.O. Nier, J. Geophys. Res. 82, 1261 (1977).
17. D.E. Anderson, Jr., R.R. Meier and C.S. Weller, J. Geophys. Res. 84, 1914 (1979).
18. D. Alcaydé and P. Bauer, Annls Géophys. 33, 305 (1977).
19. P.H.G. Dickinson, W.C. Bain, L. Thomas, E.R. Williams, D.B. Jenkins and N.D. Twiddy, Proc. Roy. Soc. Lond. A369, 379 (1980).
20. D. Alcaydé, J. Fontanari, G. Kockarts, P. Bauer and R. Bernard, Annls Géophys. 35, 41 (1979).
21. A.D. Danilov, U.A. Kalgin and A.A. Pokhunkov, Space Research XIX, 173 (1979).
22. H. Teitelbaum and J.E. Blamont, Planet. Space Sci. 25, 723 (1977).
23. S.P. Zimmerman and F.A. Murphy, in : Dynamical and Chemical Coupling between Neutral and Ionized Atmosphere (Grandal, B. and J.A. Holtet, eds), Reidel, Dordrecht, 1977, p. 35.
24. E.S. Oran, P.S. Julianne and D.F. Strobel, J. Geophys. Res. 80, 3068 (1975).
25. M.J. Engebretson, K. Mauersberger and W.E. Potter, J. Geophys. Res. 82, 3291 (1977).
26. G. Kockarts, Geophys. Res. Lett. 7, 137 (1980).
27. G. Thuillier, J.L. Falin and F. Barlier, J. Atmos. Terr. Phys. 42, to be published (1980).
28. L.G. Jacchia, Sky and Telescope 49, 294 (1975).

MODELS OF THE GEOMAGNETIC EFFECT IN THE EARTH'S THERMOSPHERE

J.W. Slowey

*Harvard College Observatory and Smithsonian Astrophysical
Observatory, Cambridge, Massachusetts, USA*

ABSTRACT

A study was made of the variations in exospheric temperature in the disturbed thermosphere as a function of geomagnetic latitude and local time and of the level of disturbance. Temperatures were derived from the N₂ densities measured by the gas analyzer aboard the polar-orbiting satellite ESRO 4. Results indicated two maxima in the temperature response in high geomagnetic latitudes that are probably associated with particle precipitation. These maxima occur near the poleward limit of the auroral belts, at about 9 and 0 hours of local magnetic time. There is also evidence of the effect of Joule heating due to the auroral electrojets in the morning and evening auroral belts. Enhancement of the temperature response in middle latitudes is observed throughout the night side and in a region centered in the late afternoon.

INTRODUCTION

Two earlier papers (Jacchia et al [1,2]) introduced a working model of the changes in temperature, density, and composition that occur in the disturbed thermosphere. It was based on densities of Ar, N₂, O, and He measured at a height of 280 km by the gas analyzer on the ESRO 4 satellite. It assumed the increase in the local exospheric temperature, ΔGT , to be a longitudinally symmetric function of the magnetic latitude with a maximum at the magnetic poles and to be accompanied by a virtual increase in the height of the homopause. An "equatorial wave", in which the composition remains undisturbed, was introduced to fit the density variations observed at low latitudes. Subsequently, a perturbation was added to the temperature profiles in the lower thermosphere (Jacchia [3]) in order to match densities observed at 160 km by Philbrick et al [4].

That relatively simple model has since been compared with constituent densities from a number of other gas analyzer experiments and has stood up remarkably well. However, the assumption that the thermospheric disturbance is longitudinally symmetric in magnetic coordinates is an obvious limitation to both the predictive capability of the model and to the insight it might provide regarding the physical processes involved. The principal energy sources in the disturbed thermosphere are thought to be particle precipitation and Joule heating by ionospheric current systems. Both are expected to act at a distance from the magnetic poles and to show a strong dependence on magnetic local time. Thus, we have set out to investi-

gate the local time dependence of the thermospheric response with the eventual objective of improving the existing model. Some of the preliminary results of this investigation are given here.

DATA ANALYSIS

We have again utilized the 280 km data from ESRO 4. These data cover the interval from December 1972 to April 1974 with only very minor interruptions and, since ESRO 4 was in a nearly polar orbit, provide ample coverage in high latitudes. They also have a distinct advantage over other data available to us in that a "quiet time" model has been specifically fitted to them (von Zahn et al [5]). It thus becomes a relatively simple matter to separate the geomagnetic variation from the various other thermospheric variations.

As we did in our earlier studies, the observed N_2 densities were used to derive values of the exospheric temperature. This was done in this case by inverse interpolation in the 1977 Jacchia model (Jacchia [3]) after first subtracting out the contribution of the "equatorial wave" to the N_2 density. The increase $\Delta G T$ in exospheric temperature due to a geomagnetic disturbance was then obtained by subtracting the interpolated temperature corresponding to the N_2 density for $K_p' = 0$ as given by the quiet time model of von Zahn et al [5].

In our existing model of the geomagnetic variation, $\Delta G T$ is given by

$$\Delta G T = A \sin^4 \phi$$

where ϕ is the geomagnetic latitude and the amplitude A is given by

$$A = 57.5 K_p' [1 + 0.027 \exp(0.4 K_p')] .$$

Here K_p' is the value of the K_p geomagnetic index for a time $t' = t - \tau$, where the time lag τ is given by

$$\tau = 0.1 + 0.2 \cos^2 \phi \text{ (days)} .$$

As in our earlier studies, we have used the invariant geomagnetic latitude throughout as it was included with the ESRO 4 data and seems to give the best results.

To study the form of the global increase in exospheric temperature, the values of $\Delta G T$ determined from the observed N_2 densities were normalized by dividing by the corresponding value of A computed from the equation above. The normalized values were then sorted into bins according to invariant latitude, local magnetic time (LMT), and the "lagged" geomagnetic index K_p' . The dimensions of the bins that were used were 10° in invariant latitude, 3h in LMT, and 1 unit in K_p' . Means were formed in each bin and values that departed from their respective mean by more than 3 times the RMS deviation were rejected and the means were then recomputed. The data points that were rejected amounted to only about 1% of the total. As could be expected, the RMS deviations were fairly large - typically about 0.2. The total number of data points corresponding to a given range of K_p' did, of course, decrease markedly with increasing K_p' . There were a total of almost 3000 data points in the range 3-4, but only about 500 data points in the range 5-6. Data for which K_p' exceeded 6 were too few in number to be of use in this study. All of the data were grouped together, regardless of hemisphere or season.

RESULTS

Examination of the means reveals the form of the global temperature increase to be rotationally asymmetric with respect to local time, but not to the extent that might have been expected. It is true that the maximum increase does not occur at the magnetic poles. Instead, there are, at least on the average, two maxima located near the poleward limit of the auroral oval. The largest of these is centered at about 9^h LMT and the other is centered at about 0^h LMT. They would seem to be related to heating resulting from particle precipitation. Their placement at such high latitudes and at nearly opposite local times produces latitudinal profiles that depart far less from our existing model than might have been expected.

These two high-latitude maxima can be seen in Figure 1. Here we have plotted the mean values of the normalized temperature increase as a function of LMT for the bins with invariant latitude centered at 75°. The values for two separate ranges of K_p' , 3-4 and 4-5, are plotted, primarily to show the consistency of the data with respect to these features.

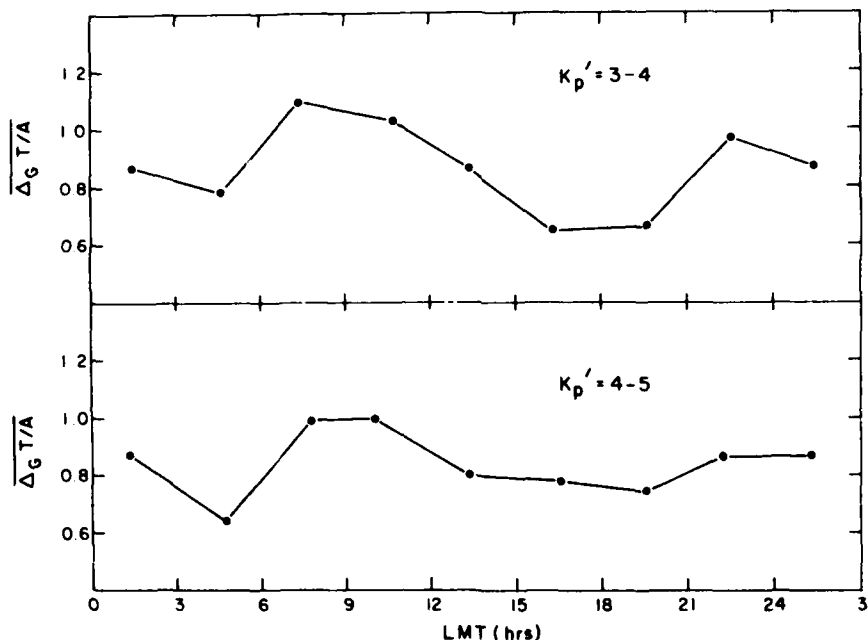


Fig. 1 $\Delta G T/A$ for the 10 degree latitude bins centered at 75° invariant latitude plotted as a function of LMT for two ranges of the K_p' index.

The two maxima are quite clearly seen when the means are plotted as a function of latitude for different values of the local time. This we have done in Figure 2, where latitudinal profiles are plotted for each of two perpendicular meridional planes for K_p' in the range 3-4. The two planes were chosen so as to pass close to the two high-latitude maxima on the one hand and to the two minima on the other.

No variation in the local times of the two maxima with K_p' could be discerned from the available data. There is, however, an indication that both maxima move toward somewhat lower latitudes within the auroral oval as K_p' increases. As a result, the temperature profiles seem to be significantly broadened in form in high latitudes as K_p' increases. For K_p' in the range 3-4, as can be seen in

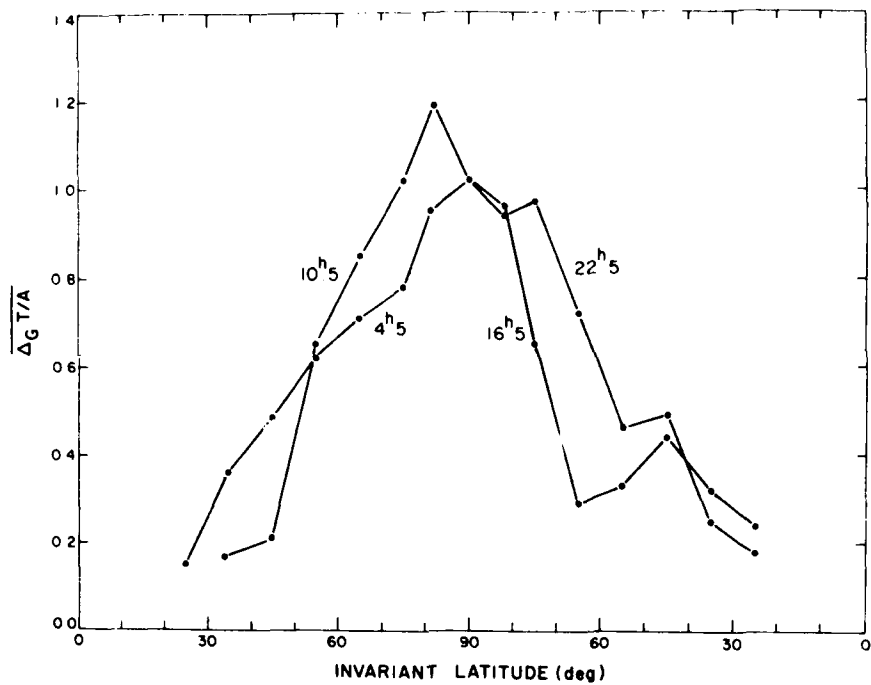


Fig. 2 Latitudinal profiles of $\Delta GT/A$ in the $10^h 5/22^h 5$ and $4^h 5/16^h 5$ meridional planes for K_p' in the range 3-4.

Figure 2, the maximum near 9^h LMT occurs at a latitude of about 80° , while that near 0^h LMT occurs at a latitude of about 75° . These latitudes correspond almost exactly to the poleward limits of the auroral oval (Bond and Akasofu [6]) at their respective local times. In Figure 3, we have replotted the profiles in the $10^h 5/22^h 5$ meridional plane from Figure 2 and have added those in the same plane

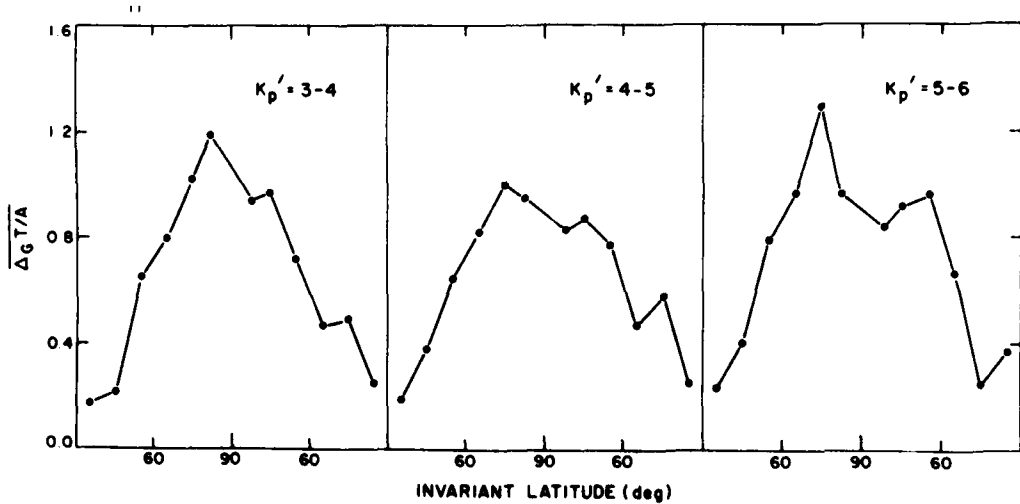


Fig. 3 Latitudinal profiles of $\Delta GT/A$ in the $10.5/22.5$ meridional plane for three different ranges of K_p' .

derived for K_p' in the range 4-5 and in the range 5-6. As can be seen, both high-latitude maxima appear to shift towards lower latitudes by 5 degrees or more in going from the lowest to the highest range of K_p' .

Some other important features of the global temperature increase have been revealed by this study. Returning to Figure 2, attention is called to the very remarkable decrease in the slope of the latitudinal profile for 4 h 5 LMT equatorward of 75° latitude. An appreciable temperature enhancement apparently occurs in the region of the auroral oval. Similar enhancements, though not so large, occur in the profiles for 7 h 5 and 19 h 5 LMT. This can be seen in Figure 4, where

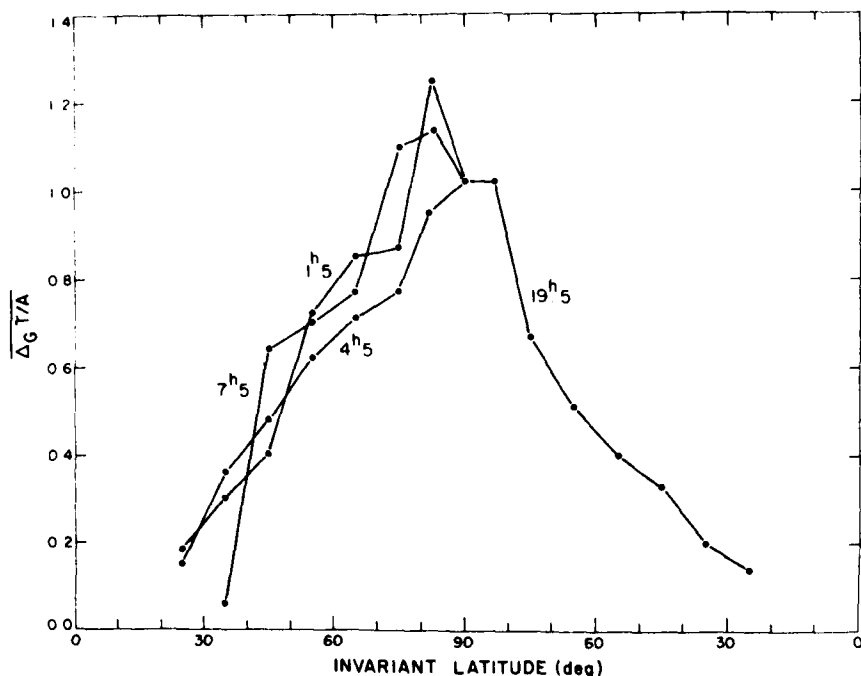


Fig. 4. Latitudinal profiles of $\Delta G T/A$ at 1 h 5, 4 h 5, 7 h 5, and 19 h 5 LMT for K_p' in the range 3-4.

we have plotted these three profiles for K_p' in the range 3-4, together with the only other profile that shows such an enhancement, that for 19 h 5 LMT. These enhancements most likely occur as a result of Joule heating, primarily by the westward auroral electrojet. The westward electrojet is the more intense of the two auroral electrojets and has two peaks, one in the evening sector and the other in the night (early morning) sector (see, for example; Kamide and Matsushita [7]).

The mid-latitude "wings" seen on many of the derived profiles are consistent features in the N_2 data. At first, we thought that these might simply be the result of imperfections in one or more terms of the diurnal variation as given by the ESRO 4 "quite time" model. The fact that these features appear with about the same relative intensity regardless of the level of disturbance argues strongly against this interpretation, however. What seems to be indicated is a persistent enhancement of the N_2 density throughout the night side and in a region centered in the late afternoon.

Figure 5 shows relative isotherms drawn to fit the means of $\Delta G T/A$ derived from the N_2 densities for K_p' in the range 3-4. The plot uses magnetic latitude and local

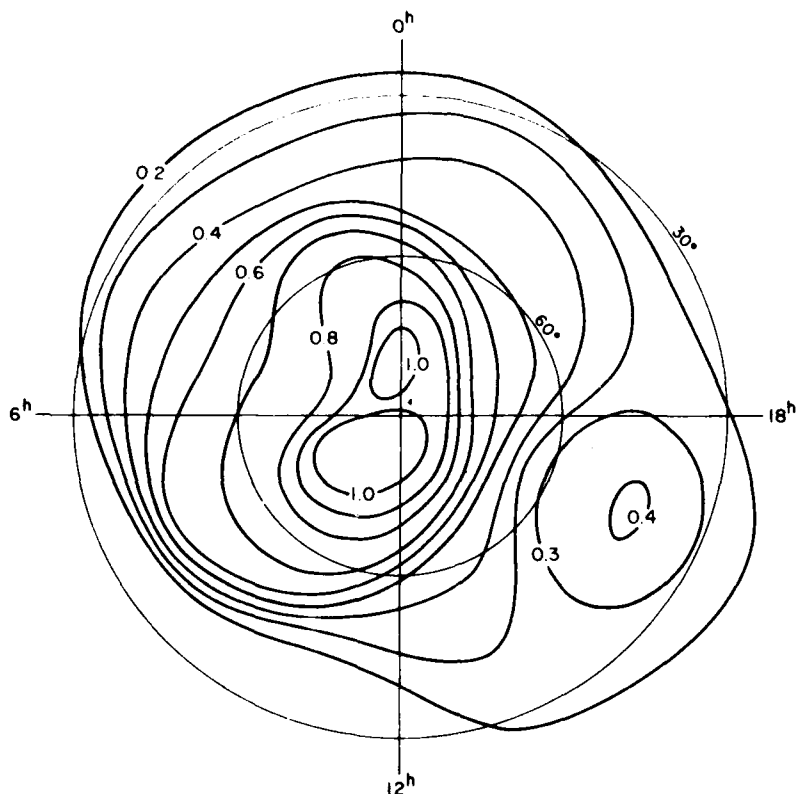


Fig. 5 Isotherms of the mean normalized temperature increase derived from N_2 densities for K_p' in the range 3-4.

time as co-ordinates and covers the region poleward of about 30° latitude. It illustrates all of the features that have been mentioned. As can be seen, the response at high latitudes is generally much greater in the night and late-morning sectors than it is elsewhere. This agrees with earlier results (Taeusch [8], Pröllss and von Zahn [9]) though both the intensity and latitudinal extent of the disturbance in the late-morning sector are somewhat surprising. The strong maximum in this sector is probably the same day side heating zone detected by earlier analyses of the ESRO4 data (Fricke et al [10], Raitt et al [11]) and shown to move towards lower latitudes as the level of disturbance increases. It would appear to be associated with the magnetospheric cleft region. In middle latitudes, there is little enhancement in the late-morning sector. As mentioned above, however, there is considerable enhancement throughout the night side and in a region centered at about 45° in the late afternoon. Specific instances of mid-latitude enhancement of N_2 on the night side have been previously reported by Raitt et al [11] and shown to be closely correlated with zones of high-energy electron flux. To our knowledge, the mid-latitude feature in the late afternoon has not been identified previously.

Studies of the global variations of the other constituents measured by the ESRO 4 gas analyzer, similar to that presented here for N_2 , are in progress. These will be of considerable help in developing a clearer picture of the disturbed thermosphere, especially in those aspects that may be related to dynamics.

ACKNOWLEDGMENTS

The author thanks U. von Zahn for providing the results of the ESRO 4 gas-analyzer experiment and for his helpful suggestions. This work was supported in part by contract F19628-78-C-0126 with the U.S. Air Force.

REFERENCES

1. L. G. Jacchia, J. W. Slowey, and U. von Zahn, J. Geophys. Res. 81, 36 (1976).
2. L. G. Jacchia, J. W. Slowey, and U. von Zahn, J. Geophys. Res. 82, 684 (1977).
3. L. G. Jacchia, Smithsonian Astrophys. Obs. Spec. Rpt. No. 375, (1977).
4. C. R. Philbrick, J. P. McIsaac, and G. A. Faucher, Space Research XVII, 349 (1977).
5. U. von Zahn, W. Köhnlein, K. H. Fricke, U. Laux, H. Trinks, and H. Volland, Geophys. Res. Lett. 4, 33 (1977).
6. F. R. Bond and S.-I. Akasofu, Planet. Space Sci. 27, 541 (1979).
7. Y. Kamide and S. Matsushita, J. Geophys. Res. 84, 4099 (1979).
8. D. R. Taeusch, J. Geophys. Res. 82, 455 (1977).
9. G. W. Prölss and U. von Zahn, Space Research XVIII, 159 (1978).
10. K. H. Fricke, H. Trinks, and U. von Zahn, EOS Trans. AGU 55, 370 (1974) (abstract).
11. W. J. Raitt, U. von Zahn, and P. Christopherson, J. Geophys. Res. 80, 2277 (1975).

DENSITIES FROM THE CACTUS ACCELEROMETER AS AN EXTERNAL TEST OF THE VALIDITY OF THE THERMOSPHERIC MODELS

J. L. Falin,¹ G. Kockarts² and F. Barlier¹

¹*Centre d'Etudes et de Recherches Géodynamiques et
Astronomiques, Grasse, France*

²*Institut d'Aéronomie Spatiale de Belgique, Bruxelles, Belgium*

ABSTRACT

Total density data were obtained from the accelerometer CACTUS on board of CASTOR-DSB 1975-39A. Numerous and precise data were obtained between 250km and 600km altitude in the equatorial region ($\pm 30^\circ$ latitude) for a period extending from May 1975 (minimum of solar activity) to February 1979 (already important solar activity). Since CACTUS data have not yet been used for the construction of empirical thermospheric models, a significant part of the data file is compared with several thermospheric models in order to provide an external test of the reliability of such models. Standard deviations of the order of 20% are apparent. The most significant differences extend over a few weeks and cannot be represented by the geophysical indices as they are presently used in the empirical models. Such an experimental fact suggests that the mathematical and physical aspects of the empirical models should be refined in order to achieve a better representation of physical reality.

INTRODUCTION

Several three dimensional thermospheric models have been recently developed by using satellite drag data, mass spectrometer measurements, optical data and incoherent scatter results [1-6]. Although these empirical models represent significant progress in the representation of the terrestrial thermosphere, a systematic comparison [7] has shown that important differences are present, particularly for extreme geophysical conditions.

The total density data obtained with the CACTUS accelerometer on board the CASTOR-DSB satellite provide an excellent means to test the validity of specific models and to stress the most important deviations. Data are obtained between 250 and 600km altitude with an accuracy of a few percent. The time resolution is 2.8s and the presently available data cover a period of 2.5 years. The present analysis deals with systematic variations covering periods of the order of a few weeks. Very short fluctuations of the order of a few seconds have already been analyzed [8] as well as problems related to geomagnetic activity [9].

DATA ANALYSIS AND GLOBAL COMPARISON

For each observed density $\rho(\text{CACTUS})$ and each model density $\rho(\text{MODEL})$ it is possible to compute a correction factor $f = \rho(\text{CACTUS})/\rho(\text{MODEL})$. Using 130,000 points unifor-

mly distributed over the period 06/30/75 to 12/30/77 one obtains an histogram of the decimal logarithm of f as shown in Fig.1 for three models, i.e. DTM [5] (adjusted model in order to take into account the under-estimation of high geomagnetic activity effects [7]), MSIS [2-3] and J71 [10], the last model being chosen since it has been widely used and since it takes much less computer time than the most recent one J77 [1]. Although CACTUS data have not been used in the construction of the empirical models, Fig.1 indicates a global agreement between the observed total densities and the model values with a standard deviation of the order of 20%. Such an external test is satisfactory but it gives no insight into any particular phenomenon which is not represented by any available model. Therefore, we have taken advantage of the fact that the CACTUS accelerometer data provide total densities between perigee at 250km and 600km altitude along each ascending and descending part of every orbit. Between 600km altitude and apogee height (1200km) radiation pressure effects become more and more predominant. Moreover, density determinations at 450km correspond to a local time difference of 7 to 8 hours and to a latitudinal change of 10° to 20° between the ascending and the descending parts of a specific orbit.

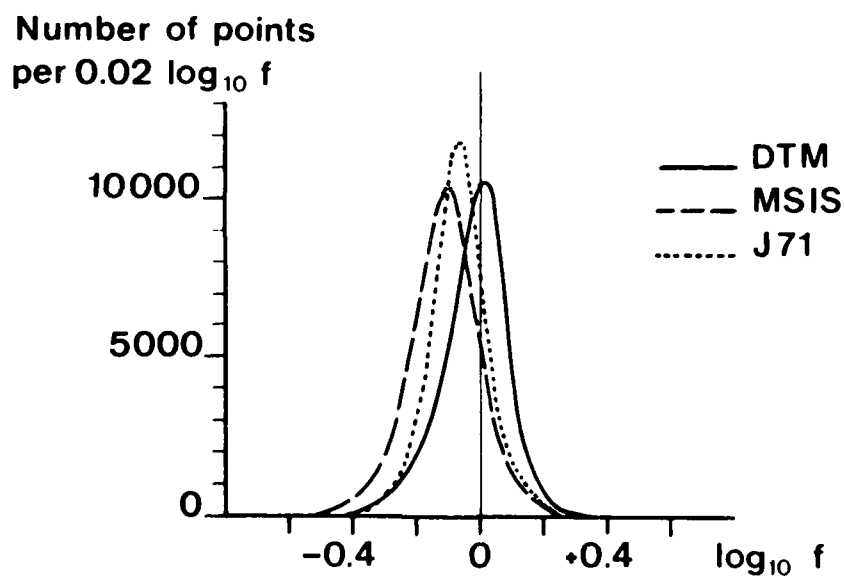


Fig. 1 - Histogram of $f = \rho(\text{CACTUS})/\rho(\text{MODEL})$ for three models. DTM(solid line), MSIS (dashed line), J71 (dotted line)

As a consequence, common phenomena observed at different heights during one orbit cannot be attributed to local time variations or to latitudinal variations. The present analysis is made for three standard altitudes, i.e. 270km, 350km and 450km. Observed densities along each orbit are reduced to a standard altitude by using a vertical model successively near perigee and in the height ranges 300km to 400km and 400km to 500km. Fig.2 shows observed total densities and model densities DTM [5] (for the perigee height) as well as the correction factor $f = \rho(\text{CACTUS})/\rho(\text{DTM})$ as a function of time from MJD 42820 to 42970 (February to July 1976), i.e. a period of 150 days. The geomagnetic index K_p and the solar decimetric flux F in $10^{-2} \text{ Wm}^{-2} \text{ Hz}^{-1}$ are also indicated as well as the latitude and

the local time at perigee. For the altitudes 350km and 450km only the correction factor f is shown. However a distinction is made between ascending (upleg) and descending (downleg) parts of each orbit in order to analyse their common features. Since the orbital period of CACTUS-D5B is of the order of 100 min a specific altitude can be sampled 14 times per day for upleg and downleg crossing. It appears that the correction factor is almost constant during a whole day. This implies that any departure of f from unity in Fig.2 is neither a universal time nor a longitudinal effect.

DETAILED COMPARISON

Although the histogram of the correction factors f , Fig.1, resembles a gaussian curve, these factors do not vary randomly on a time scale of a few weeks. They are characterized by apparent oscillations with a recurrence of the order of 20 to 30 days corresponding to the times of low solar activity, Fig.2. The minima appear in phase with the minima of the solar flux F and the differences of the factors f are greatest for the solar flux minima. This general aspect is found when other empirical models are used, such as J71 and MSIS. The amplitude of the oscillations increases with height and this fact could be interpreted as a temperature effect. Minima values of the correction factors correspond to an observed total density decrease of the order of 50% with respect to the model value at 450km altitude and could be interpreted in terms of a thermospheric temperature decrease of about 50K. In the model, the thermospheric temperature variation $\Delta T(K)$ related to the solar activity by the indicator \bar{F} (mean of F over three months) and $(F-\bar{F})$, is given by : $\Delta T = a\bar{F} + b(F-\bar{F})$ with $2.7 < a < 3.6$; $1.2 < b < 1.4$. During low solar activity \bar{F} is nearly constant and $(F-\bar{F})$ is less than 10 units, the necessary temperature variation (50K) could not be represented by this formula. Very different values of the coefficients a and b should be used for solar minimum activity. However, the values above are satisfactory for medium solar activity (for example, $\bar{F} = 140$). Other solar indicators could be also used with advantage.

Another period of 150 days following the period of Fig.2 is presented in Fig.3 and corresponds to very small variation of solar flux. The oscillations of the factors f are smaller and in several cases nonexistent. This is also the way that the observed oscillations in Fig.2 are related to the variations of solar flux.

However, all features cannot be explained by this effect; certainly other processes are needed to interpret the behaviour among the different curves in Fig.2 and Fig.3, such as diurnal and annual variation, geomagnetic activity or other phenomena. Our purpose was only to draw attention to a particular point related to the minimum of the solar activity for which empirical representation must be revised. Another purpose is also to emphasize that we need to look carefully at all these different features before revising the thermospheric model.

REFERENCES

1. L. G. Jacchia, Smithson. Astrophys. Obs., Spec. Rep. 375 (1977)
2. A. E. Hedin, J. E. Salah, J. V. Evans, C. A. Reber, G. P. Newton, N. W. Spencer, D. C. Kayser, D. Alcayde, P. Bauer, L. Cogger and J. P. McClure, J. Geophys. Res. 82, 2139 (1977)
3. A. E. Hedin, C. A. Reber, G. P. Newton, N. W. Spencer, H. C. Brinton, H. G. Mayr and W. E. Potter, J. Geophys. Res. 82, 2149 (1977)
4. U von Zahn, W. Köhnlein, K. H. Fricke, U. Laux, H. Trinks and H. Volland, Geophys. Res. Lett. 4, 33 (1977)
5. F. Barlier, C. Berger, J. L. Falin, G. Kockarts and G. Thuillier, Annls. Geophys. 34, 9 (1978)
6. W. Köhnlein, D. Krankowsky, P. Lämmerzahl, W. Joos and H. Volland, J. Geophys. Res. 84, 4355 (1979)

7. F. Barlier, C. Berger, J. L. Falin, G. Kockarts and G. Thuillier, *J. Atmos. Terr. Phys.* **41**, 527 (1979)
8. J. P. Villain, *Space Research XIX*, 231 (1979)
9. C. Berger and F. Barlier, this volume.
10. L. G. Jacchia, *Smithson. Astrophys. Obs., Spec. Rep.* **332** (1971)

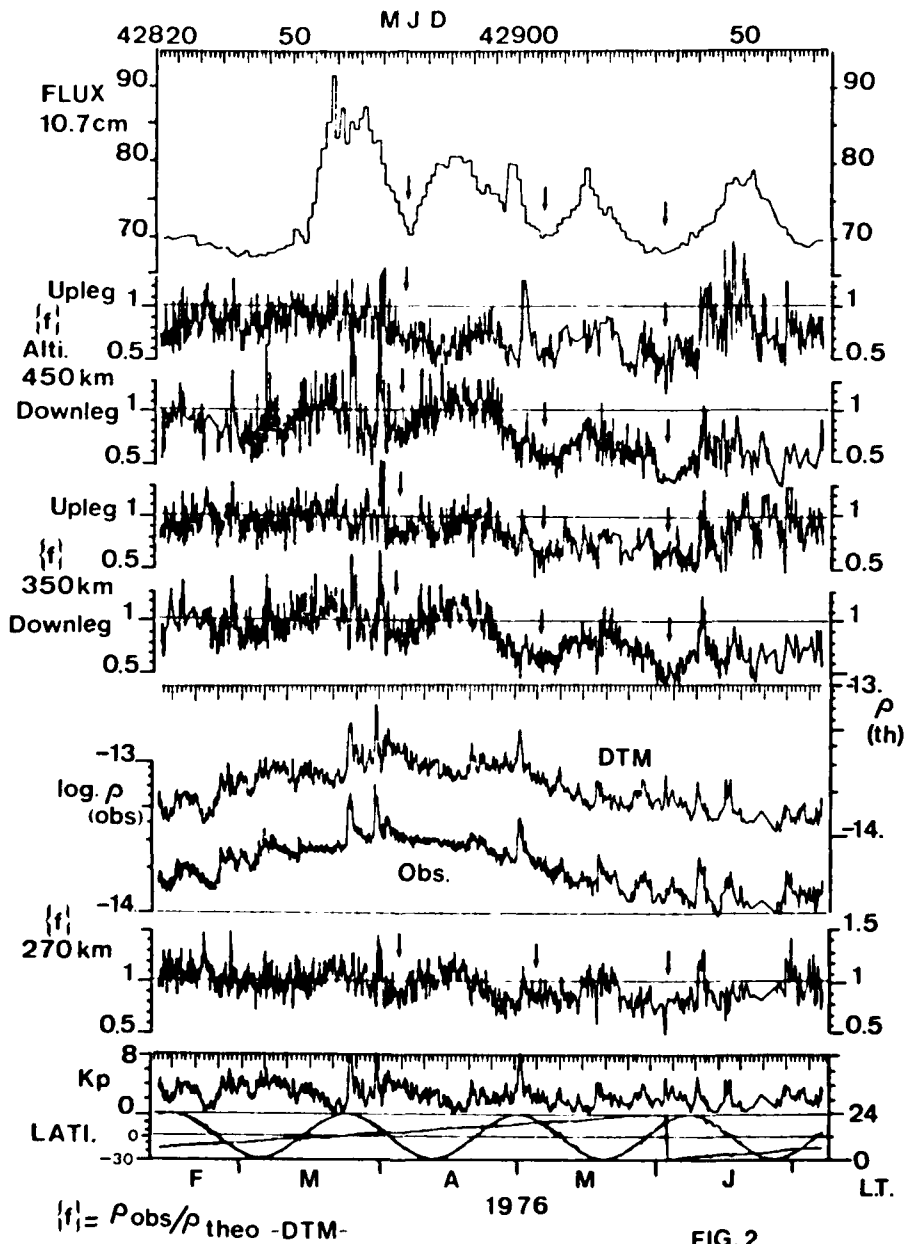


FIG. 2

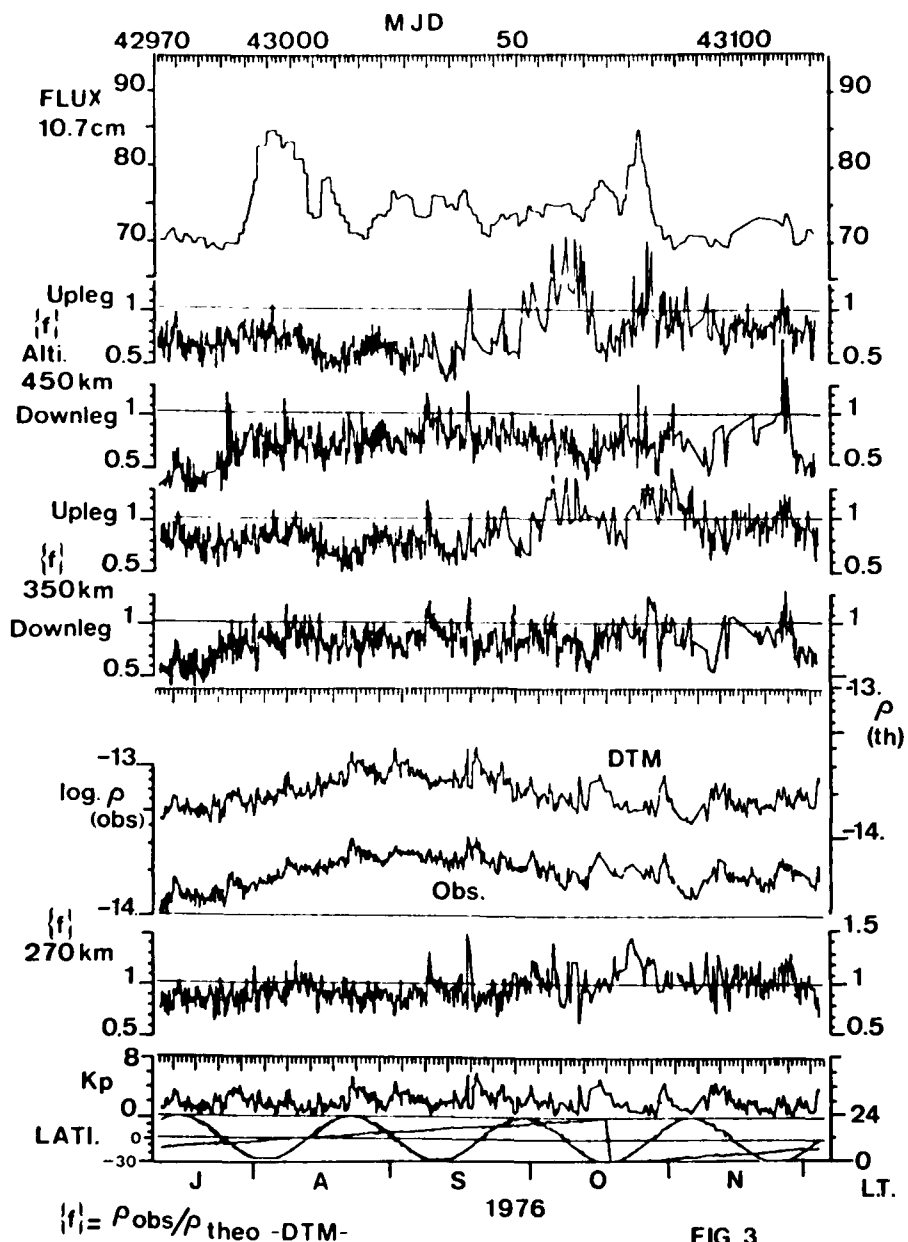


FIG. 3

VARIATIONS OF DENSITY SCALE HEIGHT BETWEEN 300 AND 400 KM

Márton J. Ill

*Observatory of the Hungarian Academy of Sciences,
Baja, Hungary*

ABSTRACT

Density data from the French CACTUS accelerometer are used to determine values of density scale height. An analysis shows a diurnal effect in the variations of scale height. There exists a correlation between geomagnetic activity and variations of scale height. Variations of the gradient of scale height are shown and analysed.

INTRODUCTION

The density scale height H_d is widely used in cases where satellite drag data are analysed to obtain atmospheric densities. Therefore it seems to be useful to study the behaviour of this scale height. Using the method described in [1] we determined more than 4500 density scale height profiles in the 300-400km height range. These profiles cover a 1.5 year interval during 1975-76. These data allow an analysis of variations of scale height as a function of time.

RESULTS

Our analysis proves that there are no significant differences between the curves referring to different altitudes of our interval, so it is sufficient to show the variations at one altitude. Therefore we present a general survey, using smoothed curves corresponding to 320km. In Figure 1 we show in 3 parts the observed variations of H_d compared with those given by CIRA 72 for the same conditions. The agreement between the values given by the model and the observed data is surprisingly good. It must be mentioned that in these curves we omitted the points referring to geomagnetically disturbed days, i.e. all cases where $K_p > 2.5$. As a result one can say that the differences with respect to the model are within 15-20%.

Inspecting the curves the most striking feature is a long-periodic variation which easily can be recognized as a diurnal effect.

The curves show 3 large maxima: in November 1975, in April 1976 and in August 1976. The maximum values of H_d are 50km in the first two cases and 46km in the last one. The strong undulation of the "observed" curve makes it difficult to determine the exact value of the maximum to minimum ratio. Accepting the extreme values of the

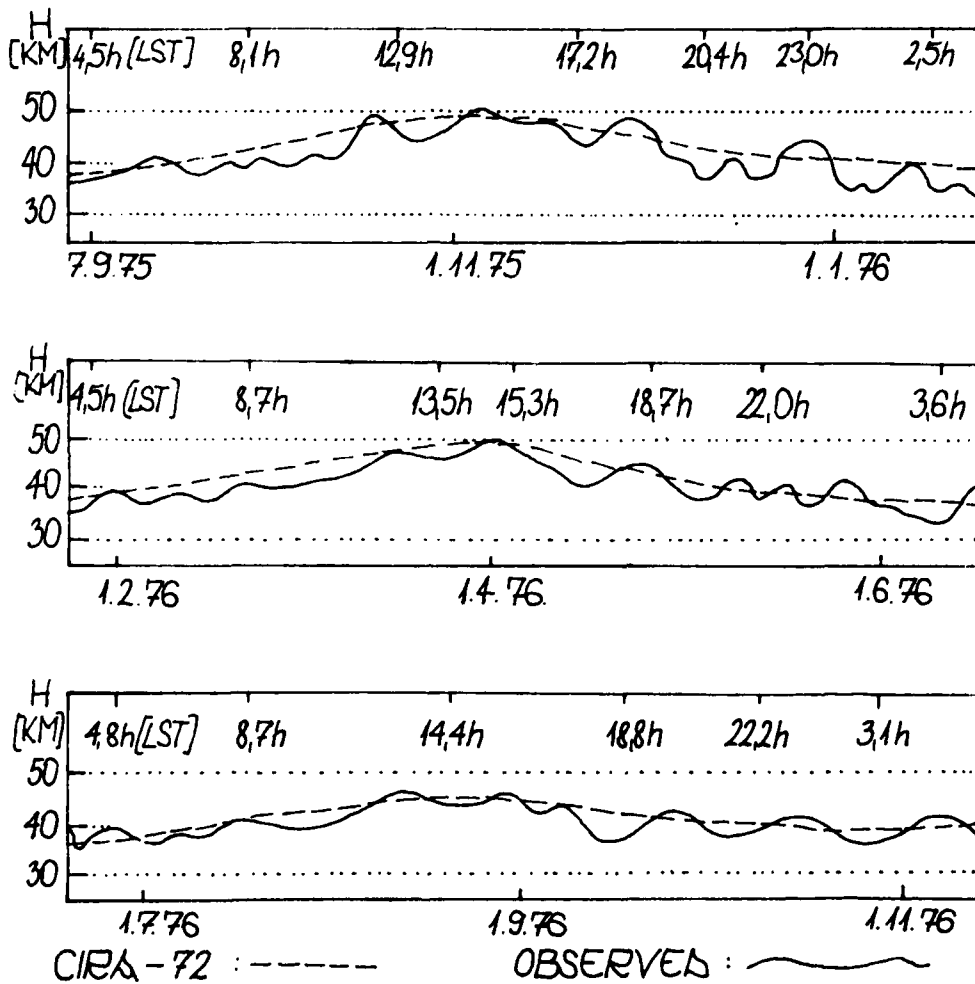


Fig.1 Variations of density scale height at 320km

curves we obtain ratios between 1.28 and 1.52. These values are about 15% higher than the corresponding values of the model. The times of the maxima are at about 15-17h LT, the minima appear around 3-4h LT.

On the whole we can establish that strong undulation is a characteristic feature of the observed curves. It is important to remark that this undulation appears simultaneously at all altitudes, with amplitudes increasing slightly with height. Just because of this simultaneity is it very conspicuous that from time to time we have some variations of H_d appearing at higher altitudes with a time-lag. However, a precise analysis revealed that this is an apparent phenomenon depending on the orbital conditions of the measuring

satellite. Considering a descending transit, i.e. the case when the satellite approaches perigee, it is clear that with decreasing altitude the corresponding local time increases. As a consequence, the satellite crosses a point at 380km with a given local time about 3 days later than the same local time at 300km. Thus we can establish that the apparently shifted variations of the scale height occur at the same local time at all altitudes and they represent an interesting feature of the diurnal effect. Since this phenomenon appears on each curve between 18-20h LT, it can be considered a sunset effect.

Examining the behaviour of the scale height it is interesting to remark that at times of geomagnetic storms the variations of scale height are in correlation with those of the geomagnetic index K_p . This correlation between K_p and H_d is usually provable when during geomagnetic storms K_p becomes larger than 3.

It is clear that the density scale height is highly variable and therefore it is useful to study the behaviour of its gradient, i.e.

$\beta = dH_d/dz$. Unfortunately, we have no analytical expression for the temperature distribution with height in the thermosphere. Therefore the gradient β must be computed from finite differences between scale heights. For a given date we calculated the gradient beginning at altitude 300km with $dz=20\text{km}$ up to 380km. We accepted the mean of the calculated values as the gradient referring to 340km. In Figure 2 we show the results obtained in this way.

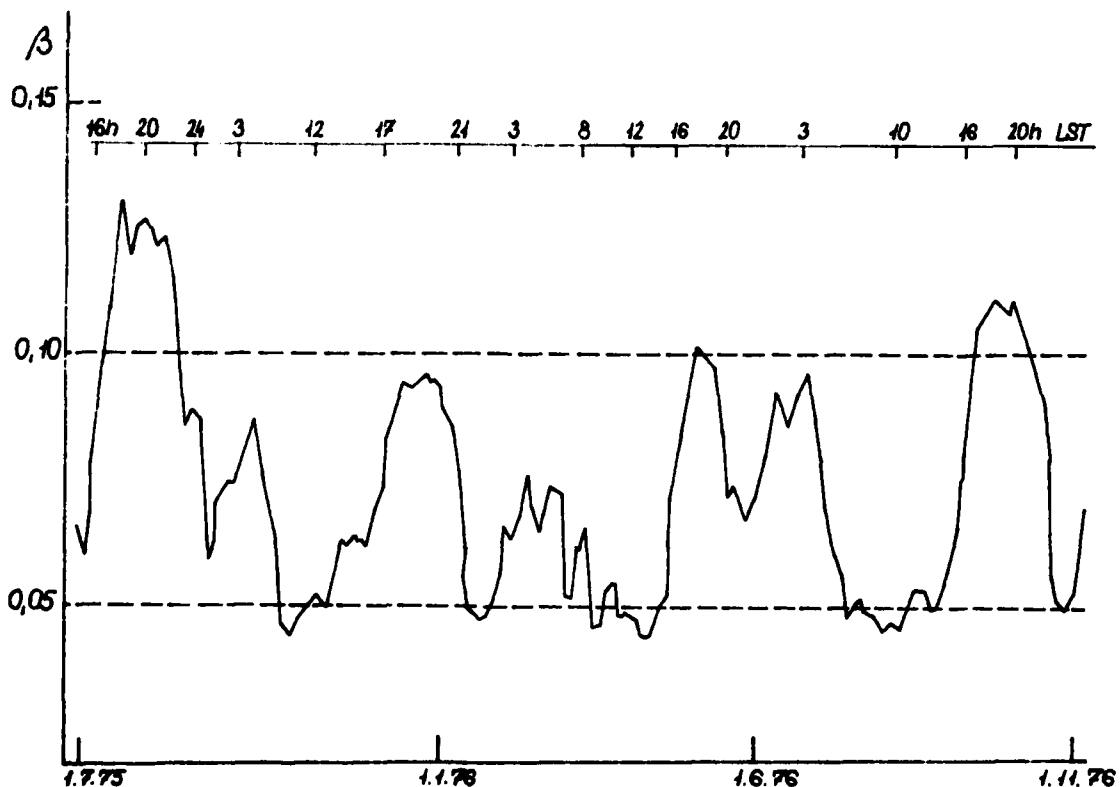


Fig.2 Variations of the gradient of density scale height

Theoretical calculations concerning the value of the gradient predict for our conditions a mean value of 0.05-0.09 with variations such that the daytime values are higher than those for night. From Figure 2 one can establish that the situation is more complicated than this. The predicted mean value [2] is in good agreement with the observed ones, but the diurnal variation cannot be represented as a simple sine wave. As we can see, between 17-21h LT we have always a maximum. The absolute minima of the curve appear between 10-14h LT. This variation is opposite that expected. It is an interesting fact that there appear secondary maxima at about 3-4h LT.

CONCLUSION

Our analysis reveals that the density scale height undergoes important variations. The most striking variation we recognized as a diurnal effect, but a strong modulation is also characteristic on all curves. The so-called sunset effect can be explained if we accept that the number densities of the different constituents do not decrease simultaneously. Accepting a time-lag of 2-3 hours between the decrease of the concentration of two major constituents we obtained curves which are very similar to the observed ones.

It is important to distinguish between the pressure scale height H_p and the density scale height H_d . Nevertheless, in the examined time interval and height range H_d was almost identical with H_p , their ratio was always between 1.05 and 1.11. As a consequence, on the basis of simple theoretical assumptions H_d can easily be transformed into H_p with an error less than 2-3%. This is important, because the variations of H_p reflect those of the T/M-ratio. But under the given conditions the temperature variations are always significantly larger than those of the mean molecular mass. As an example, we take data from CIRA 72. At an altitude of 350km we have the following parameters: at a temperature of $T = 700K$ we have a mean molecular mass $M = 15.53$ and a scale height $H_d = 40.27$. At $T = 800K$ the corresponding parameters are $M = 15.96$ and $H_d = 45.03$. As we can see, the variation of the molecular mass is very small, only 0.43, meanwhile the temperature varies 100K. At the same time the T/M-ratio varies from 45.07 to 50.13, their difference 5.06 being almost the same value as the variation of the scale height 4.76. Therefore, we can accept that the variations of the density scale height can be used to analyse the relative temperature variations in the thermosphere, if we transform them into pressure scale heights. Of course, if we wish absolute temperature variations instead of relative ones, it is necessary to take into account the variations of the mean molecular mass, on the basis of a model.

Acknowledgements

The author is deeply indebted to CERGA and to CNES for providing the accelerometer data. Grateful thanks are extended to Drs. C. Berger and F. Barlier for their valuable help in preparing this paper and for their critical comments and suggestions. This research was supported by CERGA.

References

1. M. Ill, Space Research XIX, 235 (1979).
2. G. Kockarts, Annales de Géophysique, 22, 161 (1966).

ASYMMETRICAL STRUCTURE IN THE THERMOSPHERE DURING MAGNETIC STORMS AS DEDUCED FROM THE CACTUS ACCELEROMETER DATA

C. Berger and F. Barlier

C.E.R.G.A., 06130 Grasse, France

ABSTRACT

During the last solar activity minimum, a great deal of very precise total density data was obtained in the equatorial regions from the CACTUS accelerometer experiment. Due to the eccentricity of the orbit, it is also possible to determine a density scale height by considering that the density profiles between the perigee (270 km) and 400 km are quasi-vertical. Densities and density scale heights are analysed during magnetic storms and their variations are compared with their behaviour during quiet periods. For densities as well as for scale heights, an asymmetrical structure in latitude and longitude is exhibited with respect to the magnetic equator. Their values are relatively higher in the northern hemisphere than in the southern one. The hypothesis (previously suggested) of a greater energy input in the southern hemisphere inducing asymmetrical winds, explains the results well.

INTRODUCTION

Total density data from the CACTUS accelerometer experiment [1] have been gathered in the equatorial regions during the last minimum of solar activity. The time resolution is one measurement each 2.68 seconds, the relative accuracy of the data (a few per cent) was estimated by Villain [2]. Such characteristics permit a precise study of the reaction of the thermosphere to geomagnetic activity. In this study, the data cover 2.5 years (June 1975-December 1977) and the altitude range 270 km - 600 km.

TOTAL DENSITY VARIATIONS

In Figure 1, an example is given where fine structures are evidenced, in particular, the sharp increase and relaxation time. This complex physical behaviour is not taken into account by the classical formulae of models.

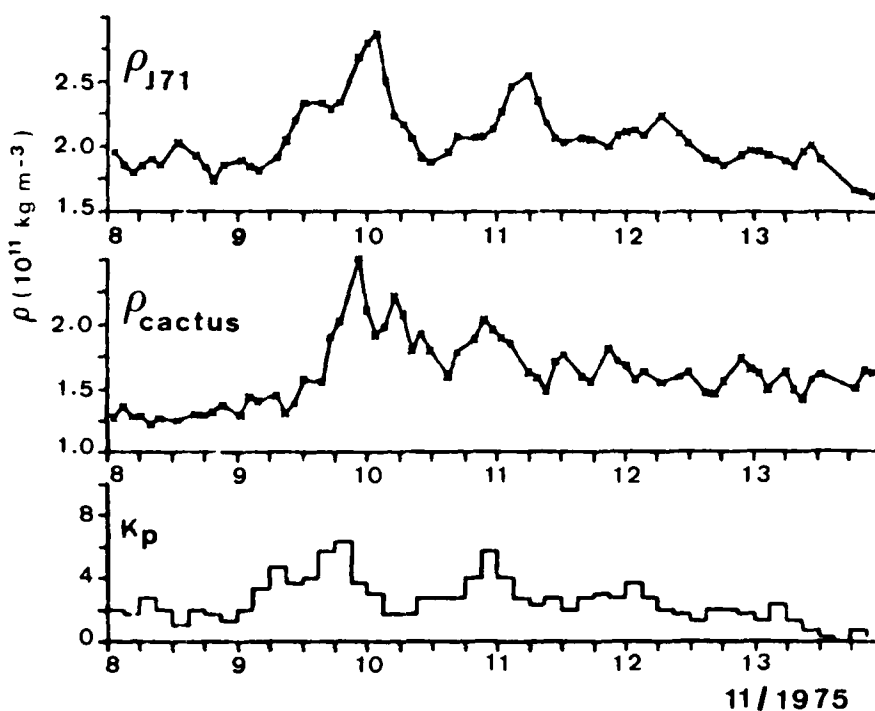


Fig. 1 Correlation between total density variations and geomagnetic activity from CACTUS data and the Jacchia 1971 model (altitude of 300 km)

However, such pure events are not numerous (about fifteen). So that, in order to use a maximum amount of data, all densities were associated with the geomagnetic planetary index K_p shifted in time by 6 hours and then statistically analysed. Our purpose is to observe if the magnetic storm structure of the thermosphere presents some asymmetries between the two hemispheres. Therefore, we have chosen as the reference model the J71 model [3] which gives a symmetrical reaction. Asymmetrical features have already been mentioned during quiet geomagnetic conditions for the December solstice [4, 5] and also during disturbed periods [6, 7].

Three geomagnetic situations have been considered :

- high activity $K_p > 5$ subdivided into two groups, $5 < K_p < 6$ and $K_p > 6$.
- medium activity $4 < K_p < 5$.
- small activity $K_p < 3$.

Three latitudinal zones have been defined : zone 20°N (30°N to 10°N), zone 0° (10°N to 10°S), zone 20°S (10°S to 30°S). We compute the ratio $f = \rho_{\text{cactus}}/\rho_{J71}$ and then take the mean values of the factors f for each geomagnetic situation and for each zone by using data in the altitude range 270 km - 400 km (Table 1a) and 400 km - 600 km (Table 1b). N is the number of data considered.

For $K_p < 3$ the f values are close to 1, but for $K_p > 4$ the f values are lower. They are the lowest in Table 1b, corresponding to higher altitudes. This fact means that the predicted temperature is overestimated when K_p is increasing. We ignore this fact here where we consider only the relative variations of the factor f in term of different parameters.

An asymmetrical behaviour between the two hemispheres appears progressively while the geomagnetic activity is increasing. It is of the same order of magnitude for both altitude zones considered.

TABLES 1a , 1b Mean Values of the $f = \rho_{\text{cactus}}/\rho_{J71}$ Ratio as a Function of Latitude and Geomagnetic Activity for Two Zones of Altitude

	$K_p < 3$			$4 < K_p < 5$			$5 < K_p < 6$			$K_p > 6$			
mean latitude	20°S	0°	20°N	20°S	0°	20°N	20°S	0°	20°N	20°S	0°	20°N	
Table 1a	N	48399	29342	52437	44497	23629	44087	11256	7118	9343	2686	2526	8872
	f	0.93	0.95	0.92	0.84	0.85	0.85	0.78	0.85	0.88	0.76	0.87	0.90
Table 1b	N	24380	14403	24922	23314	15030	18698	6888	3232	5644	1808	1112	3668
	f	0.96	0.95	0.95	0.72	0.71	0.74	0.64	0.65	0.76	0.66	0.68	0.76

A finer analysis can be attempted by drawing geographical maps using all the data (Figure 2). Asymmetries are not seen for $K_p < 3$, but develop while the geomagnetic activity is increasing. They are characterized by density gradients between the northern and southern hemisphere and by longitudinal maxima. If we consider only data covering the solstice period (± 45 days around the solstice day) such asymmetries are emphasized for the December solstice (Figure 3). They exist even for $K_p < 3$ but they are less important than for $K_p > 5$. During the June solstice no significant structure appears for $K_p < 3$, unfortunately there are not enough data for $K_p > 5$.

DENSITY SCALE HEIGHT VARIATIONS

Table 2 Mean Values of the $f = H_{\text{cactus}}/H_{J71}$ Ratio as a Function of Latitude and Geomagnetic Activity for the Altitude of 320 km

	$K_p < 3$			$4 < K_p < 5$			$5 < K_p < 6$			$K_p > 6$		
mean latitude	20°S	0°	20°N	20°S	0°	20°N	20°S	0°	20°N	20°S	0°	20°N
N	3084	1777	3177	341	172	319	100	27	78	24	15	70
f	0.98	0.99	0.98	0.93	0.93	0.95	0.90	0.97	0.94	0.88	0.93	0.94

Thanks to the high eccentricity of the trajectory (mean value in 1976 : 0.063) quasi-vertical profiles of total density can be obtained. By using the exponential decrease law and data at 310 km and 330 km altitude density scale heights (H_{cactus}) assigned to the altitude of 320 km can be determined. These determinations are processed in the same way as the density data. The results are given in Table 2.

The increase of asymmetry with geomagnetic activity appears here also, but the relative variations are smaller than that observed for total densities.

INTERPRETATION AND CONCLUSION

Asymmetries between the hemispheres are developing with geomagnetic activity for two altitude zones (270 km to 400 km and 400 km to 600 km) : the relative increase of total density is higher in the northern part and does not depend on altitude.

For the present solar conditions, atomic oxygen [O] represents almost completely the total mass density. As the relative differences between the two hemispheres are not increasing with altitude these asymmetries cannot be explained, in a first approximation, in terms of asymmetries in the thermopause temperature but more likely in terms of density variations in the lower thermosphere. Asymmetries in circulation processes can induce such variations because in the lower thermosphere [O] is very sensitive to circulation ; the lighter components are accumulated in the regions of minimum pressure (cold regions) [8]. As asymmetries are increasing with K_p an asymmetrical heating linked with geomagnetic activity in the auroral regions appears as a possible hypothesis ; it could generate an asymmetrical trans-equatorial wind. Such an hypothesis was already proposed by Mayr and Trinks [6] to interpret, for some longitudes, ESRO-4 data. In addition, it is possible to explain with this hypothesis the asymmetries observed in December even for quiet geomagnetic conditions. Indeed, at this time there is a normal circulation from the southern hemisphere (warm hemisphere) to the northern hemisphere (cold hemisphere) and the permanent heating in the auroral regions, stronger in the southern part, reinforces the normal circulation process.

It is also possible to explain by circulation processes the asymmetry in the density scale height determinations (H), (Table 2). Two factors can play a role for modifying the H parameter : temperature and mean molecular mass. Because the variations of temperature linked with K_p are small in the equatorial regions [9, 10] the effect of mean molecular mass variations is predominant. If there is a relative enhancement of atomic oxygen in the northern hemisphere a relative increase of scale height must be detected in this hemisphere, as observed.

In conclusion, asymmetrical circulation processes due to asymmetrical heating mechanisms are a plausible hypothesis in order to explain the observed total density and scale height variations with geomagnetic activity.

REFERENCES

1. J. Bouttes, M. Delattre and R. Juillerat, paper presented at Cospar Meeting, Philadelphia (1976).
2. J.P. Villain, Thèse de doctorat de 3^e cycle, Paris (1978).
3. L.G. Jacchia, Smithson. Astrophys. Observ., Spec. Rep. 332, (1971).
4. M.R. Torr and D.G. Torr, J. Atmos. Terr. Phys. 35, 2237 (1973).
5. F. Barlier, P. Bauer, C. Jaeck, G. Thuillier and G. Kockarts, J. Geophys. Res. 79, 5273 (1974).
6. H.G. Mayr and H. Trinks, Planet. Space Sci. 25, 607 (1977).
7. C. Berger and F. Barlier, to be published in J. Atmos. Terr. Phys. (1980).
8. F.S. Johnson and B. Gottlieb, Planet. Space Sci. 21, 1001 (1973).
9. G. Thuillier, J.L. Falin and C. Wachtel, J. Atmos. Terr. Phys. 39, 399 (1977).
10. A.E. Hedin, J.E. Salah, J.V. Evans, C.A. Reber, G.P. Newton, N.W. Spencer, D.C. Kayser, D. Alcaydé, P. Bauer, L. Cogger and J.P. Mc Clure, J. Geophys. Res. 82, 2139 (1977).

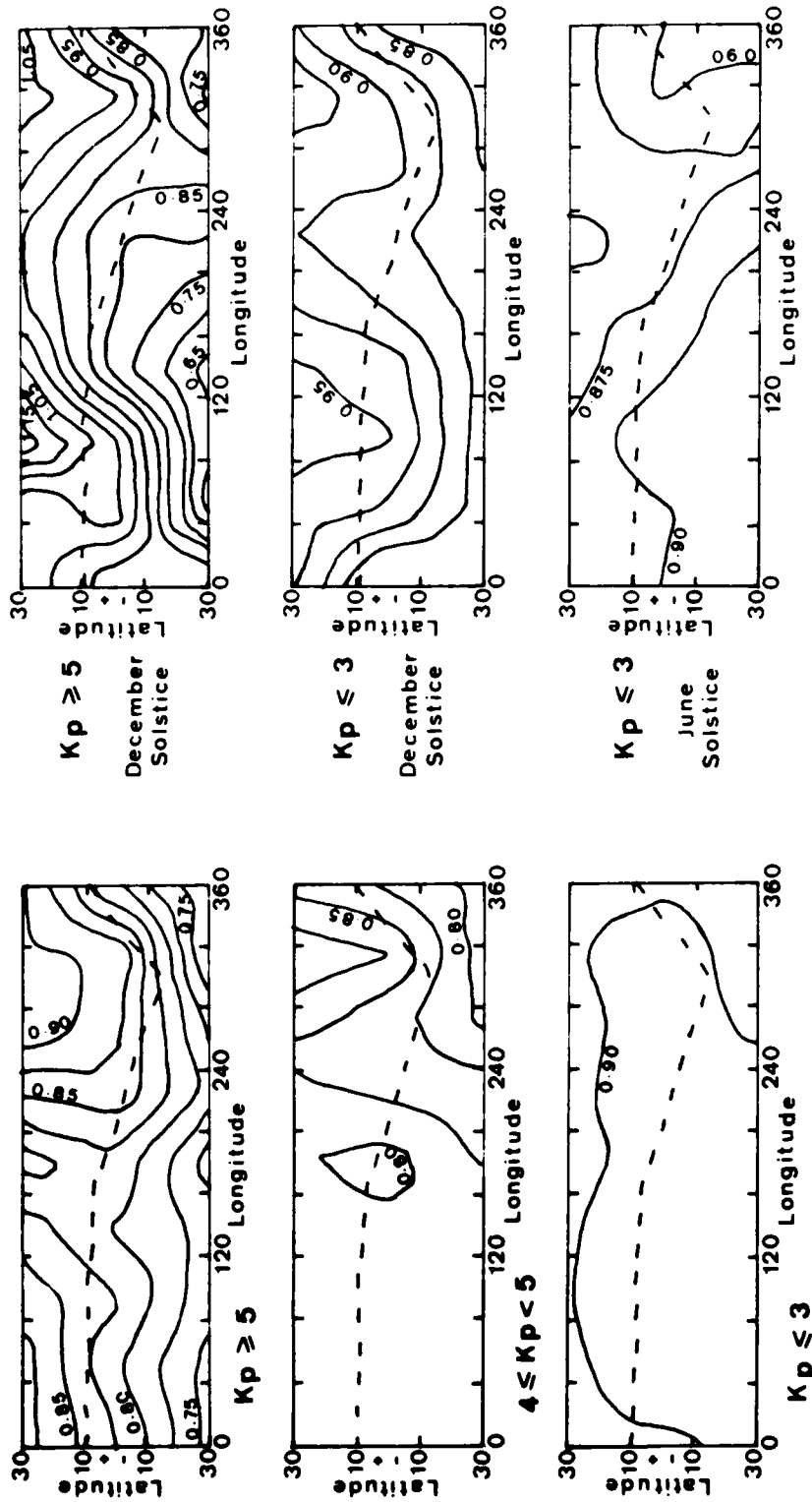


Fig. 2 Geographic maps of the $\rho_{\text{cactus}}/\rho_{\text{J71}}$ ratio for three geomagnetic conditions using data in the altitude range 270 km - 400 km.

Fig. 3 Same as Figure 2, but for the two solstice periods.

AUTHOR INDEX

- Afonin, V. 101
Antonova, L.A. 171
Apáthy, I. 101
Avdyushin, S.I. 107
- Barlier, F. 221, 231
Bencze, P. 101
Berger, C. 231
Bezrukikh, V. 101
Bleuler, E. 27
Blum, P.W. 157, 175
Brittvina, R.A. 151
Brückelman, H.C. 123
Bukusova, L.L. 107
- Champion, K.S.W. 133
Cole, K.D. 19, 65
- Falin, J.L. 221
Fedorov, V.V. 151
Feigin, V.M. 107
- Gagliardini, D.A. 35
Gaigerov, S.S. 151
Gordiets, B.F. 179
Griffis, M. 27
Gringauz, K.I. 77, 101
- Hickey, M.P. 65
Hinteregger, H.E. 39
- Illi, M.J. 227
Ivanov-Kholodny, G.S. 107
- Jacchia, L.G. 81
- Kalikhman, M.Ya. 151
Karszenbaum, H. 35
Katjushina, V.V. 171
Kazachevskaya, T.V. 107
Kidiyarova, V.G. 151
Kockarts, C. 197, 221
Kokin, G.A. 113
Kolesnik, A.G. 187
Koshelkov, Yu.P. 151
Kovács, K. 101
Kulikov, Yu.N. 179
- Markov, M.N. 179
Marov, M.Ya. 179
Martini, L. 77
- Nisbet, J.S. 27
- Offermann, D. 123
- Prölss, C.W. 31
Puolokainen, A.I. 77
- Rawer, K. 87
Richards, P.C. 53
Ryazanova, L.A. 113
- Savelyev, M.A. 107
Scherbakova, L.V. 151

- Schuchardt, K.G.H. 157, 175
Schwenn, R. 3
Shuttle, N.M. 77, 101
Slowey, J.W. 213
Szemerey, I. 101
- Vlasov, M.N. 187
Widdel, B. 123
- Tarasenko, D.A. 113, 151
Thomas, G.E. 127
Torkar, K.M. 123
Torr, D.C. 53
Torr, M.R. 53
Tulinov, V.F. 107

CORRIGENDA

Advances in Space Research Volume 1, Numbers 1 and 2 (1981)

Certain information given in Volume 1, Numbers 1 and 2 of *Advances in Space Research* has been printed erroneously, and attention is drawn to the following corrections. The Publishers regret any inconvenience caused to the relevant individuals and organizations: in all other issues of Volume 1, the information is given correctly.

In the inside front cover, in the address of Professor J. F. Denisse, Chairman of the Editorial Board, the name of the street is misspelt, and should read 61 rue Dutot, not Dudot. Of the Editorial Board Members, Professor S. A. Browhill should read Professor S. A. Bowhill; Professor W. R. Holmquist should read Dr. W. R. Holmquist; and Professor C. de Jaeger should read Professor C. de Jager.

On the second preliminary page, under "Sponsors", the order of the organizations is given incorrectly. The Committee on Space Research (COSPAR) is the principal sponsor in each case; the other sponsors are given correctly, with the Hungarian Academy of Sciences being collaborator for the whole COSPAR Twenty-third Plenary Meeting.

Also on the second preliminary page, it should be noted that K. Knott of ESA, The Netherlands, for Volume 1, Number 1, and C. T. Russell of COSPAR, USA, for Volume 1, Number 2, are the Chairmen of the respective Symposium Program Committees.

Advances in Space Research

CONTENTS OF VOLUME 1

The issues comprising Volume 1 of *Advances in Space Research* contain the proceedings of the COSPAR Twenty-third Plenary Meeting held in Budapest, Hungary, 2-14 June 1980. Symposia topics covered are:

- Physics of Planetary Magnetospheres
- Progress in Planetary Exploration
- Cosmic Rays in the Heliosphere
- Systems Performance and Early Results of Global Observing System for FGGE
- Theoretical Problems in High Energy Astrophysics
- Perspectives for Scientific Ballooning during the 1980s
- Comparative Studies of Planetary Interiors
- Active Experiments in Space Plasmas.

Also included are the Topical Sessions of the COSPAR Interdisciplinary Scientific Commissions, and the Technical Panel on Dynamics of Artificial Satellites and Space Probes, from the Meeting.

Contents Volume 1, Number 12

Proceedings of the Topical Meeting of the COSPAR Interdisciplinary Scientific Commission C (Sessions C1 and C3) of the COSPAR Twenty-third Plenary Meeting held in Budapest, Hungary, 2-14 June 1980. The papers in this issue are divided into two parts, according to their presentation at the Topical Meeting:

Part I—ISC C Session 1—Representations of Energy Sources in the Earth's Upper Atmosphere and Ionosphere	1
Section 1—Energy Sources of Solar Origin	1
Section 2—Energy Inputs and Models	63
Part II—ISC C Session 3—Models of Terrestrial Mesosphere and Thermosphere	111
Section 1—Stratosphere - Mesosphere	111
Section 2—Thermosphere—Exosphere	131
Section 3—Mesosphere—Thermosphere	195
Author Index	237

END

DATE

FILMED

9 - 81

DTIC